

## University of Southampton Research Repository

Copyright © and Moral Rights for this thesis and, where applicable, any accompanying data are retained by the author and/or other copyright owners. A copy can be downloaded for personal non-commercial research or study, without prior permission or charge. This thesis and the accompanying data cannot be reproduced or quoted extensively from without first obtaining permission in writing from the copyright holder/s. The content of the thesis and accompanying research data (where applicable) must not be changed in any way or sold commercially in any format or medium without the formal permission of the copyright holder/s.

When referring to this thesis and any accompanying data, full bibliographic details must be given, e.g.

Thesis: Author (Year of Submission) "Full thesis title", University of Southampton, name of the University Faculty or School or Department, PhD Thesis, pagination.

Data: Author (Year) Title. URI [dataset]



# **University of Southampton**

Faculty of Engineering and Physical Sciences

School of Physics and Astronomy

## **Three-dimensional materials made from engineered oligonucleotides and nanoparticles**

by

**Angela Federica De Fazio**

ORCID ID 0000-0002-9733-3981

Thesis for the degree of Doctor of Philosophy

September 2019



# University of Southampton

## Abstract

Faculty of Engineering and Physical Sciences

School of Physics and Astronomy

Thesis for the degree of Doctor of Philosophy

### **Three-dimensional materials made from engineered oligonucleotides and nanoparticles**

by

Angela Federica De Fazio

In the last decades, the ability to assemble nanoparticles into programmed 2D or 3D structures by means of synthetic oligonucleotides has resulted into the fabrication of novel nanomaterials with unique physical and chemical properties. Nuclei acids are an exceptional platform for the architecture of complex structures, allowing routes to flexible and precise placing of functional nanoparticles. The physicochemical properties of featured materials can be readily tuned by varying the constituent building blocks.

In this thesis, the advanced programming of the assembly processes was combined with the use of innovative ligation techniques. DNA-functionalised nanoparticles of different composition, size and shape were prepared and used in DNA-guided assembling processes (Chapter 3).

Furthermore, engineered synthetic DNA strands were designed and employed for the fabrication of nanoparticle assemblies with stability and resistance against DNA denaturing conditions (Chapter 4). DNA ligation was realised using a UV-sensitive molecule, the 3-cyanovinyl carbazole. Following light-stimulation, this compound allows the formation of an interstrand crosslink within a DNA duplex, providing a novel tool for the manipulation of three-dimensional nanoparticles assemblies. In contrast with other crosslinking techniques, the carbazole interstrand bond can be reversed, using a different wavelength as an external trigger. The efficient application of the 3-cyanovinyl carbazole in extended nanoparticle crystals is demonstrated for the first time.

DNA-directed heterogeneous assemblies of plasmonic and fluorescent nanoparticles were also manufactured (Chapter 5). The interplay between gold and upconversion nanoparticles within the same aggregate structure and the effect on the linear and non-linear optical properties was studied.



# Table of Contents

<b>Table of Contents</b> .....	<b>i</b>
<b>Table of Tables</b> .....	<b>v</b>
<b>Table of Figures</b> .....	<b>vii</b>
<b>Research Thesis: Declaration of Authorship</b> .....	<b>xvii</b>
<b>Acknowledgements</b> .....	<b>xix</b>
<b>Definitions and Abbreviations</b> .....	<b>xxiii</b>
<b>Chapter 1 Introduction</b> .....	<b>27</b>
1.1 Theoretical background .....	28
1.1.1 Colloidal nanoparticles .....	29
1.1.1.1 Synthesis of gold nanoparticles.....	29
1.1.1.2 Synthesis of silver nanoparticles .....	32
1.1.1.3 Optical properties of metallic nanoparticles.....	32
1.1.1.4 Synthesis and optical properties of upconversion nanoparticles .....	35
1.1.1.5 Optical properties.....	36
1.1.2 DNA nanotechnology .....	39
1.1.2.1 Structure and properties of oligonucleotides .....	39
1.1.2.2 DNA crosslinking.....	43
1.1.2.3 Strategies for oligonucleotide attachment on colloidal nanoparticles.....	45
1.1.3 Self-assembly of nanoparticles .....	48
<b>Chapter 2 Experimental Procedures</b> .....	<b>53</b>
2.1 Synthesis of Nanoparticles .....	53
2.1.1 Synthesis of 14 nm spherical gold nanoparticles.....	53
2.1.2 Synthesis of large spherical gold nanoparticles .....	53
2.1.3 Synthesis of spherical silver nanoparticles .....	54
2.1.4 Synthesis of lanthanide-doped NaYF <sub>4</sub> upconversion nanoparticles .....	54
2.1.5 Synthesis of lanthanide-doped NaY:GdF <sub>4</sub> upconversion nanoparticles .....	55
2.1.5.1 Wet annealing of upconversion nanoparticles .....	56
2.1.6 Synthesis of iron oxide nanoparticles .....	56

## Table of Contents

2.2	Oligonucleotide Functionalisation of Nanoparticles .....	56
2.2.1	Surface modification of spherical metallic nanoparticles with a dense shell of oligonucleotides.....	57
2.2.2	Surface modification of large metallic nanoparticles with a dense shell of oligonucleotides.....	58
2.2.3	Surface modification of UCNPs and IONPs with synthetic oligonucleotides ..	58
2.2.3.1	PAA ligand exchange .....	58
2.2.3.2	Carboxylation <i>via</i> silanisation and amination.....	59
2.2.4	Oligonucleotide attachment on UCNPs and IONPs .....	59
2.3	DNA-Nanoparticles Assemblies .....	60
2.3.1	Annealing at constant temperature .....	60
2.3.2	Slow cooling procedure .....	60
2.3.3	Silica embedding for imaging.....	60
2.4	Light-induced crosslinking and denaturation experiments .....	61
2.5	Characterisation Techniques .....	61
2.5.1	Spectroscopic techniques .....	61
2.5.1.1	UV-Visible spectroscopy.....	61
2.5.1.2	Oligonucleotides melting curves.....	61
2.5.1.3	DNA density on gold nanoparticles.....	62
2.5.1.4	DNA density on silver nanoparticles.....	62
2.5.1.5	Fluorescence measurements of upconversion nanoparticles.....	62
2.5.1.6	Fourier-transform infrared spectroscopy .....	63
2.5.2	Gel electrophoresis .....	63
2.5.3	Thermogravimetric analysis.....	63
2.5.4	Microscopy techniques.....	64
2.5.4.1	Transmission electron microscopy .....	64
2.5.4.2	Scanning electron microscopy .....	64
2.5.4.3	Optical microscopy.....	64
2.5.5	Scattering techniques .....	65
2.5.5.1	Zeta potential.....	65



2.5.5.1 Powder X-rays diffraction.....	65
2.5.5.2 Small-angle x-ray scattering .....	65
<b>Chapter 3 Programmed Assembly of Nanoparticles.....</b>	<b>67</b>
3.1 Synthesis of nanoparticles .....	67
3.1.1 Spherical gold nanoparticles .....	67
3.1.2 Spherical silver nanoparticles.....	70
3.1.3 Lanthanide doped NaYF <sub>4</sub> nanoparticles.....	72
3.1.4 Cubic iron oxide nanoparticles.....	80
3.2 Design and characterisation of synthetic oligonucleotides .....	82
3.2.1 DNA Melting curves.....	83
3.2.2 Polyacrylamide gel electrophoresis .....	84
3.3 Oligonucleotide functionalisation of colloidal nanoparticles .....	85
3.3.1 Loading of a dense shell of oligonucleotides on gold nanoparticles .....	85
3.3.2 Loading of a dense shell of oligonucleotides on silver nanoparticles.....	87
3.3.3 Loading of a shell of oligonucleotides on large gold and silver nanoparticles	88
3.3.4 Surface modification and oligonucleotide attachment on upconversion and magnetic nanoparticles .....	89
3.3.4.1 Phase transfer of NaYF <sub>4</sub> nanoparticles.....	91
3.3.4.2 Phase transfer of iron oxide nanoparticles .....	98
3.4 Assembly of DNA-coated nanoparticles.....	101
3.4.1 Gold nanoparticles assembly .....	101
3.4.2 Silver nanoparticles assembly .....	110
3.4.3 Upconversion nanoparticles assembly .....	116
3.4.4 Iron oxide nanoparticles assembly.....	118
<b>Chapter 4 Carbazole modification of synthetic oligonucleotides.....</b>	<b>121</b>
4.1 Carbazole modified oligonucleotide sequences .....	121
4.1.1 Polyacrylamide gel electrophoresis .....	124
4.2 Reversible photo-ligation of gold nanoparticles superlattices .....	125
4.2.1 Photo-induced decrosslinking of gold nanoparticles superlattices .....	129

## Table of Contents

4.3	Reversible photo-ligation of silver nanoparticles .....	131
4.4	Seeded growth of large superlattices .....	136
<b>Chapter 5 Optical Characterisation of Programmed Assemblies.....</b>		<b>139</b>
5.1	Fabrication of heterogeneous assemblies .....	139
5.2	UV-vis spectroscopy of heterogeneous assemblies .....	143
5.3.1	Optical characterisation of heterogeneous assemblies of 15 nm AuNPs and 45 nm UCNPs .....	148
5.3.2	Optical characterisation of heterogeneous assemblies of AuNPs and 30 nm UCNPs.....	153
<b>Chapter 6 Conclusion and Outlook.....</b>		<b>159</b>
6.1	Summary of results .....	159
6.2	Future work.....	160
<b>Appendix A</b>		<b>167</b>
A.1	List of reagents and suppliers .....	167
A.2	Description of the characterisation techniques .....	167
A.2.1	UV-Visible spectroscopy .....	167
A.2.2	Microscopy techniques.....	168
A.2.3	Transmission electron microscopy .....	168
A.2.4	Scanning electron microscopy .....	169
A.2.5	Dynamic light scattering and zeta potential.....	169
A.2.6	Powder X-rays scattering .....	170
A.2.7	Small-angle X-rays scattering.....	171
A.3	Conditions investigated for nanoparticles assemblies .....	173
<b>List of References.....</b>		<b>177</b>

## Table of Tables

<b>Table 2.1</b> DNA sequences used in this work. Molecular structures of carbazole modification (indicated as <b>Z</b> ), SH-C <sub>3</sub> H <sub>6</sub> and aminohexyl (positioning indicated as <b>X</b> ) are shown in <b>Figure 1.4</b> . .....	57
<b>Table 3.1</b> Lattice parameters and average crystallite size for hexagonal phase UCNPs. ....	78
<b>Table 3.2</b> Atomic percentages extracted from SEM-EDX spectral analysis. ....	110
<b>Table 3.3</b> SEM-EDX analysis on the sample AgNPs@Res1 + AgNPs@Res2 treated at 55 °C in 40 mM PBS buffer. Scale bar 1 μm. ....	115
<b>Table 4.1</b> DNA sequences for crosslinking. In colour, the recognition region. The 'X' denotes the position of the cyanovinyl carbazole nucleobase.....	122
<b>Table 5.1</b> Summary of the A-series samples. The number after the 'A' represents the percentage of AuNPs doping added to the UCNPs aggregate.....	141
<b>Table 5.2</b> Summary of the U-series samples. The number after the 'U' represents the percentage of UCNPs doping added to the AuNPs aggregate.....	142
<b>Table 5.3</b> Estimated spacing between two adjacent AuNPs for superlattices containing different percentages of gold, as calculated from the plasmon ruler equation. ....	147



## Table of Figures

<b>Figure 1.1</b> The localised surface plasmon resonance for gold nanoparticles. The electron cloud oscillation leads to large absorption and scattering cross section. ....	33
<b>Figure 1.2</b> Molecular structures of the DNA nucleotides. The phosphate is highlighted in blues, the deoxyribose ring is in green and the different nucleobases in black. ....	40
<b>Figure 1.3</b> Structure of the double stranded DNA. In A, the hydrogen bonds and the specific complementarity between the bases are highlighted. In B, the three-dimensional structure of the duplex conformation is shown. ....	41
<b>Figure 1.4</b> Chemical modifications to the oligonucleotide sequences. The functional groups (in red) were attached to the 5' end. Aminohexyl (A) was used in the EDC/NHS coupling, while the sulphur bridge (B) was used for Au and Ag oligo coating. ....	43
<b>Figure 1.5</b> Molecular structures and crosslink reactions for 8-Methoxypsoralen (A) and 1,3-Bis(2-chloroethyl)-1-nitrosourea (B). <sup>106</sup> .....	44
<b>Figure 1.7</b> A library of different nanostructures can be obtained from the rationally design of DNA motifs coupled with the precise synthesis of nanoparticles. Adapted from ref <sup>131</sup> . ....	49
<b>Figure 3.1</b> Representative TEM image (A) and corresponding size distribution histogram (B) calculated on over 2000 citrate coated AuNPs. The average size resulted in $14 \pm 1$ nm. Scale bar 200 nm. ....	68
<b>Figure 3.2</b> Normalised UV-vis spectrum of AuNPs 14 nm, showing a sharp and well-defined LSPR peak with maximum at 522 nm. ....	68
<b>Figure 3.3</b> Transmission electron micrographs of gold nanoparticles at different stages of the synthesis: seeds (A), after one growth step (B) and after two growth steps (C). Corresponding size distribution histograms for seeds (D, $15 \pm 1$ nm), growth 1 (E, $21 \pm 2$ nm) and growth 2 (F, $45 \pm 5$ nm). Scale bars 200 nm. ....	69
<b>Figure 3.4</b> UV-Visible spectra for gold seeds (black), first (red) and second (blue) growth nanoparticles, showing a distinct red-shift of the maximum LSPR peak. ....	70
<b>Figure 3.5</b> Representative TEM micrograph (A) and size distribution plot (C) for $15 \pm 6$ nm AgNPs. TEM micrograph (B) and size distribution plot (D) for $48 \pm 10$ nm AgNPs, after one growth step. Scalebars 50 nm. ....	71

## Table of Figures

<b>Figure 3.6</b> Normalised UV-vis spectra of 15 nm and 48 nm AgNPs, showing the maximum resonance absorbance at 406 and 423 nm respectively.....	72
<b>Figure 3.7</b> Representative TEM micrograph of NaYF <sub>4</sub> :Yb <sup>+3</sup> (20%), Er <sup>+3</sup> (2%), showing hexagonal particles with average size of 45± 2 nm (A), as depicted in the corresponding size distribution plot (B). .....	73
<b>Figure 3.8</b> Representative TEM micrograph of NaYF <sub>4</sub> :Yb <sup>+3</sup> (20%), Er <sup>+3</sup> (2%), containing 20% and 30% Gd <sup>3+</sup> ions are shown respectively in A and B. Corresponding size distribution histograms are also reported in C (for Gd <sup>3+</sup> 20%) and D (for Gd <sup>3+</sup> 30%), showing a size decrease from 27.9 ± 1.8 nm to 12.5 ± 1.5 nm. Scale bars 100 nm. ....	74
<b>Figure 3.9</b> Energy dispersive x-ray elemental analysis for NaYF <sub>4</sub> :Yb <sup>+3</sup> , Er <sup>+3</sup> . In A, the full EDX spectrum is reported. From the integration of the peaks relative to each element, the relative weight percentages were calculated. The results are summarised in B. ....	75
<b>Figure 3.10</b> Energy dispersive x-ray elemental analysis for NaY:Gd(20%)F <sub>4</sub> :Yb <sup>+3</sup> , Er <sup>+3</sup> . In A, the full EDX spectrum is reported. From the integration of the peaks relative to each element, the relative weight percentages were calculated. The results are summarised in B. ....	76
<b>Figure 3.11</b> Energy dispersive x-ray elemental analysis for NaY:Gd(30%)F <sub>4</sub> :Yb <sup>+3</sup> , Er <sup>+3</sup> . In A, the full EDX spectrum is reported. From the integration of the peaks relative to each element, the relative weight percentages were calculated. The results are summarised in B. ....	76
<b>Figure 3.12</b> X-rays diffractograms obtained from UCNPs containing 0% (red), 20% (blue) and 30% (green) Gd <sup>3+</sup> . The same hexagonal crystal lattice was obtained for the different gadolinium doping percentages. ....	78
<b>Figure 3.13</b> Fluorescence emission spectra for UCNPs containing Gd 0% (black), 20% (red) and 30% (blue). The peak positions and relative ratios are unchanged, since the percentage of erbium and ytterbium is constant in the three samples. Nanoparticles concentration 5 mg/mL. ....	79
<b>Figure 3.14</b> Representative TEM micrograph (A) and size distribution histogram (B) of 11 ± 1 nm IONPs. Scale bar 100 nm. ....	80

<b>Figure 3.15</b> XRD pattern for iron oxide nanoparticles and corresponding predicted peaks for the magnetite structure.....	81
<b>Figure 3.16</b> Energy dispersive x-rays elemental analysis for Fe <sub>2</sub> O <sub>3</sub> . In A, the full EDX spectrum is reported. From the integration of the peaks relative to each element, the relative weight percentages were calculated. The results are summarised in B. ....	82
<b>Figure 3.17</b> Average melting curves of thiol-terminated Res1+Res2, determined over three heating/cooling cycles in the range 25-90 °C. The melting curve resulted in 56.6 °C.....	83
<b>Figure 3.18</b> Polyacrylamide gel electrophoresis in native conditions to test the hybridisation efficiency of the employed oligonucleotides. Thiol-terminated Res1 and Res2 in A, while the amino-functionalised Res1 and Res2 are in B. ....	84
<b>Figure 3.19</b> (A) UV-visible spectra of gold nanoparticles covered with citrate ions (in black) or oligonucleotide ligands (in red), showing a slight red shift in the latter case. In B, zeta potentials for gold nanoparticles covered with citrate ions (in black) or oligonucleotide ligands (in red), showing a slightly less negative charge in the latter case. ....	86
<b>Figure 3.20</b> In A, UV-visible spectra of silver nanoparticles covered with tannic acid and citrate ions (in black) or oligonucleotide ligands (in red), showing a slight red shift in the latter case. In B, zeta potentials for silver nanoparticles covered with citrate ions (in black) or oligonucleotide ligands (in red), showing an increased negative charge in the latter case. ....	87
<b>Figure 3.21</b> UV-Visible spectra of AuNPs 45 nm (black) and AuNPs@DNA (red), showing a slight red shifting for the oligonucleotide-coated AuNPs. ....	88
<b>Figure 3.22</b> A graph of the zeta potential for PAA-coated UCNPs in ethanol (0.5 mg/mL). A strong negative value of -44 mV was recorded. ....	92
<b>Figure 3.23</b> Infrared spectra of oleate-capped (black) and PAA-covered (red) upconversion nanoparticles. The appearance of a strong COOH peak at 1700 cm <sup>-1</sup> is a strong confirmation of the presence of PAA molecules.....	92
<b>Figure 3.24</b> Representative TEM micrographs of different attempts of silanisation. In (A) different UCNPs clustered in the same silica shell, while in (B) the excess of silanisation	

## Table of Figures

reagents resulted into empty silica spheres. In (C) both clustered UCNPs and silica NPs are visible. Scale bars 50 nm. ....	93
<b>Figure 3.25</b> In A, the thermogravimetric analysis for as-synthesised UCNPs (solid line) and for the wet-annealed UCNPs (dotted line), showing a higher weight loss percentage for the latter case. In B, optical images of a 10 mg/mL suspension of UCNPs after annealing under white light (i) and illuminated by 980 nm laser (iii). Corresponding images of the same sample before annealing step are shown in ii and iv. ....	94
<b>Figure 3.26</b> TEM micrographs and corresponding size distribution histograms for the successful silanisation of UCNPs. In A and D, UCNPs containing 0% Gd <sup>3+</sup> are shown, with an average diameter of 53.0 ± 3.8. In B and E, UCNPs containing 20% Gd <sup>3+</sup> are reported, with an average diameter of 48.3 ± 2.8. In C and F, UCNPs containing 30% Gd <sup>3+</sup> are shown, with an average diameter of 22.2 ± 2.0. Scale bars 100 nm. ....	95
<b>Figure 3.27</b> X-ray diffraction patterns for as-synthesised UCNPs (blue) and silica-coated UCNPs (red), with corresponding planes indices, compatible with the hexagonal phase. ....	95
<b>Figure 3.28</b> Zeta potential values for silica encapsulated (red), amino-terminated (blue) and carboxy-terminated (black) UCNPs, recorded in water at a concentration of 0.5 mg/mL. ....	97
<b>Figure 3.29</b> Zeta potential measurement for DNA-coated UCNPs@SiO <sub>2</sub> (0.5 mg/mL in ultrapure water). ....	98
<b>Figure 3.30</b> Infrared spectra of oleate-capped (a) and PAA-covered (b) iron oxide nanoparticles. A small shoulder at about 1660 cm <sup>-1</sup> appeared, however, no strong peak at 1700 cm <sup>-1</sup> could be observed, suggesting that in fact the ligand exchange did not take place. ....	99
<b>Figure 3.31</b> TEM micrographs of silica coated iron oxide nanoparticles (A) and corresponding size distribution histogram (B). Scale bar 100 nm.....	100
<b>Figure 3.32</b> Zeta potential values for silica encapsulated (red), amino-terminated (blue) and carboxy-terminated (black) IONPs, recorded in water at a concentration of 0.5 mg/mL. ....	100



<b>Figure 3.33</b> Zeta potential value for IONPs covered with oligonucleotides (0.5 mg/mL in water). .....	101
<b>Figure 3.34</b> (A) SAXS profile of a AuNPs-DNA SL annealed at 54 °C in NaCl 0.3 M. (B) SAXS profile of an amorphous aggregate of gold nanoparticles annealed at 54 °C in NaCl 0.04 M. .....	102
<b>Figure 3.35</b> Structure factor profiles at different temperatures for crystals made by 14 nm AuNPs functionalised with Res1 and Res2. Temperature range from 25 to 80 °C. As the temperature is raised, the scattering peaks became broader and less intense, proving the loss of the aggregate state. ....	104
<b>Figure 3.36</b> (A) Melting curves for AuNPs 15 nm functionalised with Res1 and Res2. (B) Melting curve for AuNPs 30 nm functionalised with Res1 and Res2, recorded by monitoring the variation of absorbance at 260 nm. ....	105
<b>Figure 3.37</b> Logarithmic scattering intensities for AuNPs 14 nm samples obtained by varying the cooling rate profile. The diamond symbol indicates peaks ascribable to a crystalline lattice. ....	106
<b>Figure 3.38</b> Indexed body-centred cubic superlattice obtained from the assembly of 15 nm AuNPs. The crystallisation protocol involved a slow-cooling from 70 °C at a rate of 0.1 °C/10 min. ....	107
<b>Figure 3.39</b> Chemical structures of TMSPA and TES and reaction mechanism for the growth of a silica layer around the DNA duplex. Initially, the TMSPA electrostatically binds the negatively charged phosphate backbones of the dsDNA. This constitutes a nucleation point for the growth of a thicker layer of silica, following addition of TES. ....	108
<b>Figure 3.40</b> SEM micrograph of a 15 nm gold nanoparticles superlattice taken with increased magnification from A to C. Scale bars 100 nm. ....	109
<b>Figure 3.41</b> SEM-EDX analysis on the sample AuNPs@Res1 + AuNPs@Res2 slow cooled (0.1 °C/10 min) from 70 °C. ....	110
<b>Figure 3.42</b> Melting curves for AgNPs 15 nm functionalised with Res1 and Res2. The $T_m$ was determined at the inflection point of the ramp up cycle, and it resulted into 63.3 °C. ....	111

## Table of Figures

<b>Figure 3.43</b> Indexed structure factor of an AgNPs-DNA SL slow-cooled at 0.1 °C/10 min from 70 °C in phosphate buffer 80 mM and NaCl 0.3 M.....	112
<b>Figure 3.44</b> SEM images of an AgNPs superlattices obtained by slow (0.1 °C/10 min) cooling from 55 °C. a)-b) Tetraethylethoxysilane-coated; c)-f) Triethoxysilane-coated structures. All scale bars 1 µm. ....	113
<b>Figure 3.45</b> SAXS pattern for a silanised AgSLs. The peaks relative to the BCC pattern are still visible, even though less clearly compared to the non-silanised AgSLs.....	114
<b>Figure 3.46</b> TEM image (A) and corresponding elemental analysis spectrum, showing the presence of silver. Scale bar 2 µm. ....	116
<b>Figure 3.47</b> Logarithmic scattering intensity profiles obtained from aggregates of DNA-coated 40nm UCNPs@PAA.....	117
<b>Figure 3.48</b> Optical photographs of an assembly of IONPs subjected to a magnetic field .....	119
<b>Figure 4.1</b> Molecular structure of the 3-cyanovinyl carbazole nucleobase. ....	122
<b>Figure 4.2</b> Melting analysis for a duplex formed by Res1c and Res2c. The curve is the average result from three heating/cooling cycles. Melting temperature was determined from the inflection point and it was equal to 56 °C. ....	124
<b>Figure 4.3</b> DNA denaturing polyacrylamide gel of conventional and carbazole modified DNAs. The description of the samples loaded in each well is also included. The structures of the strands are depicted in <b>Table 2.1</b> (Res1 and Res2) and <b>Table 4.1</b> (Res1c and Res2c). ....	125
<b>Figure 4.4</b> Structure factor profile and corresponding peak indexing for a BCC SLs made from AuNPs functionalised with Res1c and Res2c.....	126
<b>Figure 4.5</b> Optical images and schematic illustrations of AuSLs assembled with conventional (A and C) or carbazole modified (B and D) oligonucleotides. In E, the UV-Vis spectrum of sample presented in C, showing a sharp plasmon peak centred at 523 nm, demonstrating the release in suspension of pristine AuNPs. ....	127
<b>Figure 4.6</b> Indexed SAXS profiles for AuSLs assembled with conventional (A and B) or engineered (C and D) oligonucleotides. ....	129
<b>Figure 4.7</b> Structure factor profiles for carbazole modified DNA AuSLs after decrosslinking with 312 nm radiation and corresponding schematic illustrations. (A) Decrosslinked	

AuSLs in native condition, (B) decrosslinked AuSLs after transfer in denaturing environment. ....	130
<b>Figure 4.8</b> Normalised UV-Visible spectrum of cyanovinyl carbazole-modified DNA-AuNPs prior to nanoparticle assembly (solid curve) and after DNA-denaturing of SLs, irradiated at 312 nm (red dotted curve). ....	130
<b>Figure 4.9</b> Structure factor profiles for carbazole-modified AuSLs. In (A), the initially synthesised AuSLs are represented; whereas in (B) the SAXS curve for the secondary AuSLs, after recrystallization from decrosslinked AuNPs. ....	131
<b>Figure 4.10</b> Structure factor profile and corresponding peak indexing for a BCC SLs made from AgNPs functionalised with Res1c and Res2c. ....	132
<b>Figure 4.11</b> Optical images and schematic illustrations of AgSLs assembled with conventional (A and C) or engineered (B and D) oligonucleotides. In E, the UV-Vis spectrum of sample presented in C, showing a sharp plasmon peak centred at 407 nm, demonstrating the release in suspension of pristine AgNPs. ....	133
<b>Figure 4.12</b> Structure factor profiles for fortified AgSLs. (A) crystallised AgSLs, photocrosslinked AgSLs in native (B) and denaturing (C) conditions are, (D) denatured decrosslinked superlattices and (E) recrystallized AgSLs. ....	134
<b>Figure 4.13</b> Normalized UV-Visible spectrum of AgNPs before assembling (solid curve) and after assembling, crosslinking, decrosslinking and de-assembling procedure (red dotted curve). ....	135
<b>Figure 4.14</b> Optical micrographs at 40X magnification of (A) an amorphous aggregate of AuNPs and (B) AuNPs crystals. Scale bars 50 $\mu\text{m}$ . ....	137
<b>Figure 4.15</b> Optical micrographs at 40X magnification of AuSLs at different growing stages. In (A) the as-synthesised AuSLs seeds and in (B) after 3 growth steps. Scale bars 50 $\mu\text{m}$ . ....	137
<b>Figure 4.16</b> Size distribution graph of the mean area variation after different growing steps. Seeds (G0) $5 \pm 6 \mu\text{m}$ , growing step 1 (G1) $12 \pm 4 \mu\text{m}$ , growing step 2 (G2) $17 \pm 8 \mu\text{m}$ and growing step 3 (G3) $43 \pm 32 \mu\text{m}$ ....	138
<b>Figure 5.1</b> Variation of the absorbance with increasing temperature. The melting temperature is defined at the inflection point of the curve and it resulted equal to 85 $^{\circ}\text{C}$ . .	140

## Table of Figures

- Figure 5.2** Optical photographs of white light scattered from gold and upconversion. On the top, pure AuSLs (sample U0), pure UC SLs (Sample A0) and a mixture of AuNPs and UCNPs (Sample U50) under ambient light, showing different hues. On the bottom, U0 (D), A0 (E) and U50 under supercontinuum laser light, showing different absorption. .... 143
- Figure 5.3** Normalised extinction spectrum of a DNA-AuNPs superlattices sample (solid line) compared to the absorbance of DNA-coated Au colloidal solution. The maximum absorbance shifted from 523 nm to 601 nm..... 144
- Figure 5.4** Offset normalised extinction spectra for superlattices containing different percentage of gold. As the amount of gold increase from 12.5% in A12.5 to 100 in U0, the maximum peak broadens and shift to longer wavelengths, as result of increased interaction between AuNPs. .... 145
- Figure 5.5** Transmission electron micrographs of UCNPs surrounded by AuNPs satellites. All scale bars 50 nm..... **Error! Bookmark not defined.**
- Figure 5.6** Representative bright field microscope images of aggregates of particles (sample U0). Scale bars 200  $\mu\text{m}$ . .... 150
- Figure 5.7** TPPL (A, C and F) and fluorescence log scale maps (B, D and F) obtained from a typical heterogeneous sample. A and B correspond to the same area, imaged with 1060 nm and 980 nm laser, similarly to C-D and E-F pairs. The bright regions in each image is thought to represent a cluster of AuNPs and UCNPs aggregates. The co-localisation of AuNPs and UCNPs is highlighted by the presence of higher intensity signals in the same regions for both lasers. .... 151
- Figure 5.8** Fluorescence to TPPL ratio for different UCNPs percentage, varying from 12.5% (sample U12.5) to 62.5% (sample A37.5). A sharp increase in the fluorescence signal takes place when the UCNPs fraction of the aggregate raised above 50%. . 152
- Figure 5.9** Representative z-stack images series for a heterogeneous aggregate of AuNPs and UCNPs and corresponding plot of the average pixel intensity for each image. The intensity increases and the background noise is reduced as the stage height approaches the laser focus. The height that maximised the pixel intensity was chosen for data collection. .... 154
- Figure 5.10** Averaged pixel intensity and corresponding dispersion of the signal for each image of A- and U-series samples. TPPL measurements for U-series and A-series samples

are represented by orange and red circles respectively. Average fluorescence intensity is symbolised by grey (U samples) and black (A samples) squares. The variation of the signal across each sample is represented by coloured bars.155

**Figure 5.11** Fluorescence to TPPL ratio against the UCNPs percentage for U-series samples (magenta diamonds) and for A-series samples (light blue triangles). A sharp increase in the fluorescence signal takes place when the UCNPs fraction of the aggregate raised above 50%.....156



## Research Thesis: Declaration of Authorship

Print name:	Angela Federica De Fazio
Title of thesis:	Three-dimensional materials made from engineered oligonucleotides and nanoparticles

I declare that this thesis and the work presented in it are my own and has been generated by me as the result of my own original research.

I confirm that:

1. This work was done wholly or mainly while in candidature for a research degree at this University;
2. Where any part of this thesis has previously been submitted for a degree or any other qualification at this University or any other institution, this has been clearly stated;
3. Where I have consulted the published work of others, this is always clearly attributed;
4. Where I have quoted from the work of others, the source is always given. With the exception of such quotations, this thesis is entirely my own work;
5. I have acknowledged all main sources of help;
6. Where the thesis is based on work done by myself jointly with others, I have made clear exactly what was done by others and what I have contributed myself;
7. Parts of this work have been published as:

### Articles in Academic Press

"Light-Induced Reversible DNA Ligation of Gold Nanoparticle Superlattices", Angela F. De Fazio, Afaf H. El-Sagheer, Jason S. Kahn, Iris Nandhakumar, Matthew Richard Burton, Tom Brown, Otto L. Muskens, Oleg Gang, and Antonios G. Kanaras, *ACS Nano* **2019** 13 (5), 5771-5777, DOI: 10.1021/acsnano.9b01294.

"Optical response of gold and upconversion nanoparticles assembled via DNA interaction," Angela F. De Fazio, Jack Haines, Alex Courtier, Otto L. Muskens, Antonios G. Kanaras, Proc. SPIE 10892, Colloidal Nanoparticles for Biomedical Applications XIV, 7 March **2019**108920A, DOI: 10.1117/12.2504970

### Abstracts, Posters and Presentations

EuroMat 2017 (Thessaloniki, September 2017)

Research Thesis: Declaration of Authorship

Gold 2018 (Paris, July 2018)

SPIE PhotonicWest 2019 (San Francisco, February 2019)

Awards

Finalist at 2019 STEM for Britain Competition

Ocean Optics Young Investigator Award, first prize (SPIE PhotonicWest)

Doctoral College Research Awards 2019, runner up

Signature:		Date:	
------------	--	-------	--



*«Poi un giorno in un libro o in un bar si farà tutto chiaro,  
capirai che altra gente si è fatta le stesse domande,  
che non c'è solo il dolce ad attenderti, ma molto d'amaro  
e non è senza un prezzo salato diventare grande...  
I tuoi dischi, i tuoi poster saranno per sempre scordati,  
lascerai sorridendo svanire i tuoi miti felici come oggetti di bimba,  
lontani ed impolverati, troverai nuove strade,  
altri scopi ed avrai nuovi amici...  
Sentirai che tuo padre ti è uguale,  
lo vedrai un po' folle, un po' saggio  
nello spendere sempre ugualmente paura e coraggio,  
la paura e il coraggio di vivere come un peso che ognuno ha portato,  
la paura e il coraggio di dire:  
" io ho sempre tentato, io ho sempre tentato... "»*



## Acknowledgements

Firstly, I would like to thank my supervisors Prof. Antonios Kanaras and Prof. Otto Muskens for providing me with the tools, advice and help to carry out my research project in the very exciting field of nanotechnology. In addition to the technical expertise, they also helped me learning new skills, including the preparation of academic papers and oral presentations, by allowing me to present my work in several international conferences. I am also grateful for the chance to carry out part of my research at the Brookhaven National Laboratory (Upton, NY). This experience boosted greatly my project and I have learned a lot from it.

I would like to thank the DSTL for funding and my technical partners, Kevin Bown and Prof. Petra Oyston, for support and encouragement during these four years. Meeting you every year at the SynBio showcase was a refreshing way to step out from my everyday research and see the bigger picture.

I would like to thank Prof. Oleg Gang and Dr. Jason Kahn for hosting me at the Brookhaven National Lab and for giving me access to Small-Angle X-ray Scattering beamline, an invaluable tool to progress with my research. A mention also to Ruipeng Li, who taught me how to process the data, while sharing some good comic books advice.

I would also like to thank Prof. Tom Brown and Dr. Afaf El-Sagheer who have synthesised all the oligonucleotides used as well as provided scientific advice in the process of oligonucleotide design. Their contribution to this project is invaluable.

A big thank you to all the present and previous members of the LICNA and the Integrated Nanophotonics groups, Maribel, Johanna, Elena, Marilena, Konstantina, Doxi and all the others I am forgetting right now. Each of you, at some point, said something that helped me and improved my work (or my mental health). A special thank you to Pete for proofreading my thesis.

A special thank you to those people that started off as co-workers and ended up being my friends: Maribel, we did not spend so much time together, but the unique connection we created makes me feel like we've known each other since ever. Konstantina and Magda: the day-to-day lab life wouldn't be bearable without you around sharing coffees and chai lattes with me! Always looking forward our next trip together. That's life!

A mention also for Rebecca and the Women Physics Network team: we supported a cause together, and while doing this I had fun and developed new skills I would have never achieved otherwise. Thank you!

## Acknowledgements

A PhD cannot be completed without a solid support network.

Thank you, Simone for showing me the nice bit of Southampton and giving me the best answer to the question “How did you ended up in Southampton?”. The dinners at yours, the CineNoce nights (not to mention the Netflix account!) are not forgotten. Thank you, Emanuela, as flatmates we survived to the deep-frying madness, with a glass of dark red wine and a TV show, seasoned with sassy comments and embarrassing playlists. Thank you Ilaria, for the trip together, for always trying to help me getting things done and for being so inspirational in spite of the struggles. Thank you Francesco, every time I speak with I learn something new, and that’s something I truly appreciate. Also, thank you for taking the time of reading my chapter.

Carina, Martina and Gabrielle: we travelled a long way around before our paths crossed, and surely we’ll travel more after they’ll diverge. But we became true friends, closer than I expected when I arrived here, when I felt “too old” to build new and deep friendships. You proved me wrong. Thank you.

Emilia, Mariarita and Maria Grazia: how long can a friendship last? You’re teaching me it can last forever (well, at least 15 years!). You know the deeps of my heart, and the peaks of my mind and, somehow, you still love me. I was just so lucky 15 years ago, when I chose sezione B of Liceo Classico Galluppi.

Davide, you are the most astounding and pure-hearted person I’ve ever met. You give me clarity when I just see fog, you put a smile on my face when I’m peevish or melancholic, and you cook me food when I’m just grumpy and tired. I couldn’t possibly ask for more.

Mamma, Papà, Manu, zia Cristina e il resto della mia famiglia: siete la migliore famiglia che potessi mai avere. Avete sempre supportato i miei sogni da quando ho iniziato a leggere, mi avete cresciuta felice a mi avete insegnato ad essere forte ed indipendente. Non sarei arrivata alla fine del dottorato senza tutto questo. Menzione d’onore a Mattia per aver mantenuto alta la mia motivazione durante l’ultimo mese di scrittura.

## Definitions and Abbreviations

A – Adenine

Abs – absorbance

AgNP – Silver nanoparticle

AuNP – Gold nanoparticle

C – Cytosine

cm – centimetre

D – dilution

DNA – deoxyribonucleic acid

EDC – 1-(3-(dimethylamino)propyl)-3-ethyl-carbodiimidemethiodide

g – gram

G – Guanine

h – hour

IONP – Iron oxide nanoparticle

L – litre

n – nano ( $10^{-9}$ )

NC – nanocrystal

nm – nanometre

NIR – near-infrared

NP – nanoparticle

NPs – nanoparticles

$\mu$  – micro ( $10^{-6}$ )

$\mu\text{m}$  – micrometre

## Definitions and Abbreviations

m – milli ( $10^{-3}$ )

M – molar

max – maximum

min – minutes

MW – molecular weight

O.D. – optical density

p – pico ( $10^{-12}$ )

PAE – programmable atom equivalent

PAGE – Polyacrylamide gel electrophoresis

PBS – phosphate buffered saline

RedOx – reduction-oxidation

Res1 – oligonucleotide sequence with thiol or amino modification (X): 3'-X-TTT TTT TTT TTT-TAA CCT AAC CTT CAT-5'

Res2 – oligonucleotide sequence with thiol or amino modification (X): 3'-X-TTT TTT TTT TTT-ATG AAG GTT AGG TTA-5'

Res1c – oligonucleotide sequence with thiol (X) and cyaniviny carbazole (Z) modifications: 3'-SH-C3H6-TTT TTT TTT TTT-TAA CCT AZAC CTT CAT-5'

Res2c – oligonucleotide sequence with thiol modification(X): 3'-SH-C3H6-TTT TTT TTT TTT-ATG AAG GTGT AGG TTA-5'

rpm – rotation per minute

s – seconds

SAXS – Small Angle X-ray Scattering

SL - Superlattice

sulfo-NHS – N-hydroxysulfosuccinimide

SPR – surface plasmon resonance

T– Thymine

TCEP - tris(2-carboxyethyl)phosphine hydrochloride

TEOS - tetraethyl orthosilicate

TES - triethylsilane

TEM – transmission electron microscopy

TMSPA - N-Trimethoxysilylpropyl-N,N,N-trimethylammonium chloride

UC – upconversion

UCNP – Upconversion nanoparticle

UV-vis – ultra-violet-visible

V – volts

W – watt

XRD – X-rays diffraction

$\xi$  – zeta

°C – degrees Celsius





## Chapter 1 Introduction

In 2009, the European Community identified a set of “Grand Challenges”,<sup>1</sup> such as climate change, tightening supplies of energy, public health and security, which will need to be faced to lead to a continuously-growing, eco-efficient European economy. In this context, nanotechnology is often addressed as the next industrial revolution, with the potential to help tackling a number of these challenges. For example, nanotechnology can enable more effective environmental and health monitoring methods, it can provide more efficient energy solutions, faster and more accurate disease diagnoses and customised medical treatments.

Nanotechnology is the science of the structures on the scale of  $10^{-9}$  m. It encompasses all the scientific fields aimed to develop new materials and devices by precise manipulation of the structure of matter at the atomic- and molecular scales. It is regarded as promising to change everything, from the medical treatments to more efficient solar cells, from new cancer therapies to pollution-eating compounds, from more durable consumer products to detectors for biohazards.

However, efficient, cost-effective and robust nanomanufacturing methods must be developed to fully realise this vast potential. As a proof of this, one could look at the funding that the nanomanufacturing sector managed to secure in the last 20 years. Under the EU Seventh Framework Programme (FP7), there were 285 nanotechnology and manufacturing projects with a European Commission (EC) contribution of over EUR 500 million, 10.8% of the total EC contribution to nanotechnology under FP7.<sup>2</sup> However, according to the estimations of the Royal Society,<sup>3</sup> nanomaterials account only for the 0.01% of the total amount of chemical production.<sup>4</sup> This confirms the need to improve the existing fabrication methods and to develop new ones. We are now under the Horizon 2020 funding program, which has the specific goal to fill the gap between nanotechnology research and markets. It aims to realise the full potential contribution of nanotechnology to sustainable growth by addressing the large scale market introduction of nano-enabled products.<sup>5</sup>

The current approaches to manufacture advanced functional materials are based on top-down techniques where the desired structures are made from the bulk, for example photolithography and milling techniques. These methods have the benefit that almost any pre-determined structure can be produced; however, they are intrinsically costly and unsuitable for the fabrication of 3D materials.

Conversely, in bottom-up strategies, smaller building blocks are assembled into larger structures by physical or chemical interactions between the units. This allows the fine control on the placement

of the single components and the fabrication of 3D structures, as well as reducing the amount of generated waste.

Amongst the bottom-up approaches, self-assembly is particularly appealing from both economic and environmental points of view, as it offers a way through which materials or product components essentially form themselves, creating less waste and using less energy. Nature is a source of inspiration for self-assembly. Evolution in the natural world has shaped an astounding variety of functional biomolecular devices. A natural tool of exceptional relevance is the deoxyribonucleic acid (DNA). DNA is capable of high selectivity and specificity for complementary sequences, allowing the fabrication of all sorts of structures.<sup>6-9</sup> As architectural material, DNA can be used on its own to build ordered static arrays of tiles,<sup>10</sup> linked rings,<sup>11</sup> and polyhedra.<sup>12</sup> Dynamic nano-devices have also been fabricated, examples include a nanomechanical switch,<sup>13</sup> a DNA-fuelled motor,<sup>14</sup> DNA-based logic gates<sup>15</sup> and circuits.<sup>16</sup> DNA can also be used in combination with inorganic components (**Figure 1.6**), and it has been extensively exploited for the organisation of colloidal particles,<sup>17-19</sup> to direct the growth of semiconductor nanocrystals,<sup>20</sup> and metal wires.<sup>21</sup>

Within this framework, the aim of this project was to advance the assembly of hybrid materials made of inorganic nanoparticles linked via DNA interactions. This thesis is organised as follows. In the next sections of this **Chapter 1**, a brief literature review of the relevant theoretical background behind this research project is given, while **Chapter 2** contains all the experimental procedures and the characterisation techniques employed in this work. **Chapter 3** discusses the synthesis of inorganic nanoparticles and the surface functionalisation with synthetic oligonucleotides as well as the formation of self-assembled three-dimensional structures. The characterisation after each step of synthesis, functionalisation and assembly is also described in this Chapter. **Chapter 4** introduces carbazole-modified oligonucleotides for the fabrication of extremely stable, light-responsive three-dimensional crystals of gold and silver nanoparticles. The reversible response to different light stimulation and the stability to unfavourable environment is thoroughly discussed. **Chapter 5** presents the fabrication of heterogeneous assemblies of nanoparticles. The linear and non-linear optical properties are investigated using both commercial and home-built setups. **Chapter 6** draws some conclusions and highlights future perspectives for the further development of the research presented in this thesis.

## 1.1 Theoretical background

In this Section, the pertinent background information about materials and techniques used in this project is introduced. **Section 1.1.1** discusses the synthesis of various colloidal nanomaterials. Their physicochemical properties are elucidated in **Section 1.1.1.3**. Oligonucleotide synthesis and

modification of nanomaterials with oligonucleotides are explained in **Sections 1.1.2**. Finally, an overview about programmed assembly of 3D nanomaterial-DNA conjugates is presented in **Section 1.1.3**.

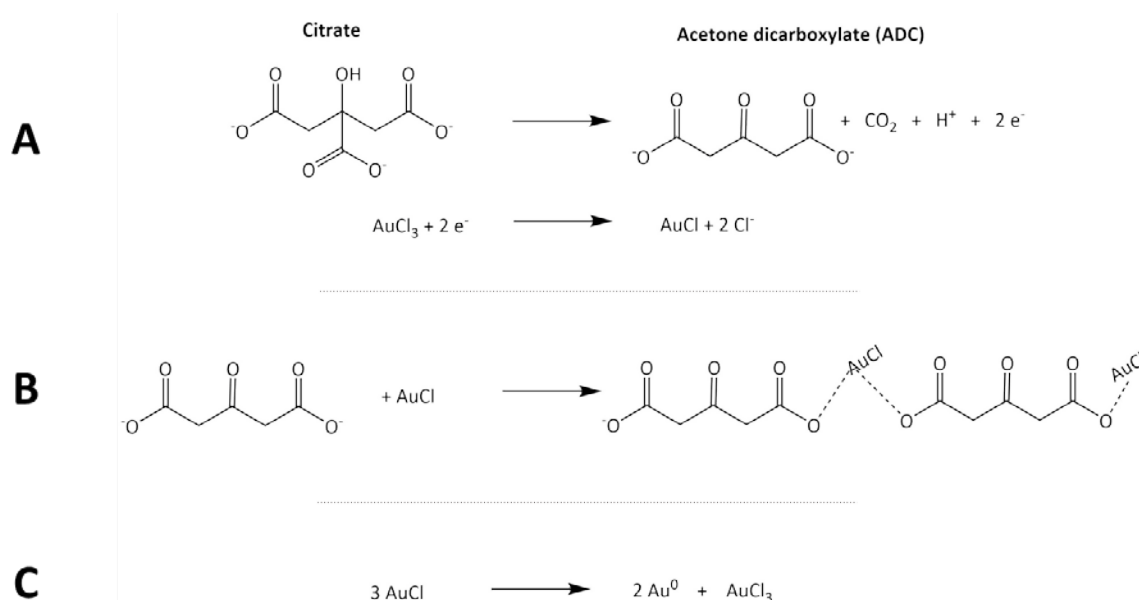
### **1.1.1 Colloidal nanoparticles**

Wet chemistry approaches provide versatile routes for the synthesis of monodispersed colloidal suspensions of nanoparticles with different compositions, sizes and shapes. In this section, the synthetic approaches and reactions involved in the synthesis of gold, silver and upconversion nanoparticles are discussed.

#### **1.1.1.1 Synthesis of gold nanoparticles**

The first known synthesis of a colloidal suspension of gold nanoparticles (AuNPs) dates back to nineteenth century, when Faraday reported a systematic study on the synthesis and optical properties of colloidal gold nanoparticles.<sup>22</sup> One century later, following Faraday study, Turkevich<sup>23</sup> developed a new procedure to synthesise AuNPs based on the reduction of gold salt with citrate, lately refined by Frens<sup>24</sup> and Schultz.<sup>25</sup> This method, with slight modifications, is still routinely used today for the synthesis of monodisperse spherical AuNPs with size ranging between 10 and 20 nm. In this strategy, two aqueous solutions of sodium tetrachloroaurate and trisodium citrate are prepared and mixed together at 100 °C. By adjusting the precursors molar ratios, the size of the resulting nanoparticles can be tuned.<sup>24</sup> In this reaction, trisodium citrate acts as both reducing agent and capping ligand, providing stabilisation to the gold colloids.<sup>26</sup> The proposed mechanism of this synthesis involves a 3-step reaction and is depicted in **Scheme 1.1**.<sup>27,28</sup>

**Scheme 1.1** Reaction mechanism for the synthesis of AuNPs from citrate reduction. In step A, the gold salt is reduced by the citrate precursor. In B, a complex between gold chloride and acetone dicarboxylate anions is formed. In step C, the disproportionation of AuCl into Au(0) and AuCl<sub>3</sub> occurs. Adapted from ref.<sup>28</sup>

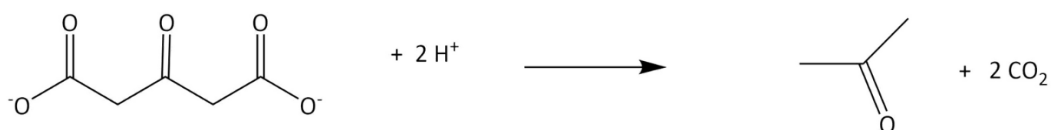


In the first step of the reaction, citrate is oxidised into acetone dicarboxylate while Au<sup>3+</sup> precursor is reduced into Au<sup>1+</sup> to form gold monochloride (AuCl) (**Scheme 1.1 Reaction A**). In an intermediate step, complexes between dicarboxylate anions and AuCl are created (**Reaction B**). Particles nuclei are then formed by coagulation of the complexes followed by disproportionation of AuCl into Au<sup>0</sup> (**Reaction C**). The nuclei promote an autocatalytic reaction with AuCl molecules, which are absorbed onto the nuclei leading to the growth of AuNPs. Excess citrate ions bind loosely the surface of the NPs, providing colloidal stability against irreversible aggregation phenomena.<sup>29</sup>

Typically, the formation of nanoparticles relies on two stages: the formation of nuclei (nucleation) followed by the growth of these nuclei into the NPs of desired diameter. A critical step to obtain narrow size distribution is the simultaneous formation of all the nuclei and avoiding the occurrence of secondary nucleation. Privman *et al.*<sup>30</sup> have shown that, in this synthesis, the AuNPs monodispersity is dependent upon the formation of gold atoms following disproportionation of aurous species. Consequently, the rapid formation of dicarboxyacetone promotes fast dismutation leading to homogeneous particles. Nevertheless, acetone dicarboxylate can also decompose into acetone (**Scheme 1.2**), which is able to reduce the gold precursor (Au<sup>3+</sup>).<sup>28</sup> This can result in secondary nucleation events, ultimately leading to particles with a wide size distribution.<sup>28</sup> However, it has

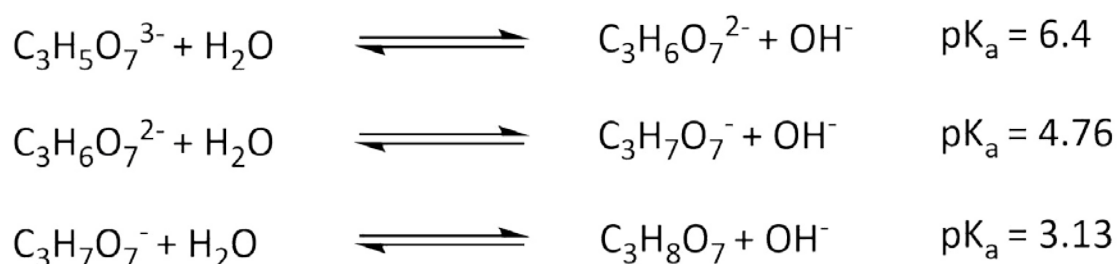
been demonstrated that this side reaction is slower compared to the citrate reaction (**Scheme 1.1 Reaction A**), thus affecting the growth process only at low citrate concentrations.<sup>27</sup>

**Scheme 1.2** Decomposition of dicarboxyacetone into acetone.



In addition to its role as reducing agent and particle stabiliser, citrate acts as pH-mediators in the reaction vessel. A systematic study by Ji *et al.*<sup>26</sup> highlighted the role of pH in the reaction kinetics. In particular, they showed pH is an important parameter of the reaction, proposing two different reaction pathways for the AuNPs formation at different pH values. At high pH the gold precursor reactivity decreases, and the particles formation follows the previously described pathway, consisting of a slow nucleation followed by a separate growth step. Also, at pH above 6.4 the citrate is completely deprotonated (**Scheme 1.3**), providing extra-stabilisation to the newly formed NPs. Conversely, at acidic pH, the nucleation is very rapid, and it results in highly reactive small nuclei that coalesce into bigger particles. This mechanism is prevalent at low pH where the citrate is fully protonated and thus its ability to bind the NPs' surface is reduced.

**Scheme 1.3** Protonation equilibrium reactions for citrate ions. Citrate can be found in different protonation states at different pH values, therefore its ability as capping agent is pH-dependent.



One major disadvantage of the Turkevich method is the loss of monodispersity in particles' shape and size when trying to increase the diameter over 20 nm. To tackle this issue, seeded-growth approaches have been developed.<sup>31-33</sup> The principle behind these methods is to isolate the nucleation from the growing step to avoid secondary nucleation and obtaining a narrow size distribution. In this approach, small particles' seeds are synthesised at 100 °C with the citrate reduction method. Following the seeds generation, the reaction temperature is lowered at 90 °C to favour the growth of larger particles over the formation of new nuclei; this occurs since the citrate

## Introduction

reduction ability is remarkably lower at temperature below 100 °C. By progressively injecting more gold and citrate precursors, they were able to synthesis AuNPs up to 200 nm with relatively small size dispersion (<10%).

### 1.1.1.2 Synthesis of silver nanoparticles

Apart from gold nanoparticles, the Turkevich method has been employed for the synthesis of silver nanoparticles (AgNPs).<sup>34–36</sup> However, the sole use of citrate as both reducing and capping agent did not yield uniform and monodisperse AgNPs. A great improvement was observed when tannic acid was introduced as nanoparticles' stabiliser.<sup>37</sup> With this approach, highly monodisperse AgNPs were obtained, with diameters ranging from 18 to 30 nm according to the amount of tannic acid employed. After this finding, Bastús *et al.*<sup>38</sup> extended the growing method they developed for the synthesis of AuNPs (**Section 1.1.1.1**), to the synthesis of AgNPs with diameters up to 200 nm. In this strategy, silver seeds are synthesised by injecting a silver precursor and tannic acid to a boiling solution of sodium citrate. Following nuclei formation, the reaction vessel temperature is lowered to 90 °C, condition in which the reductive potential of the citrate is lowered. Then, each growing step consists of the subsequent addition of citrate, silver salt and tannic acid. By tuning the ratios of the reagents, NPs up to 200 nm were produced.

### 1.1.1.3 Optical properties of metallic nanoparticles

The optical properties of nanomaterials are remarkably different from the corresponding bulk material.<sup>39</sup> Bulk materials show a continuous density of electronic states, while the states of nanoparticles are discrete, resembling those of atoms and molecules. Because of this, new, size-dependent properties arise. When the electromagnetic field interacts with metallic nanoparticles, a charge separation occurs and a dipole oscillation of the free metal electrons of the conduction band is observed. This phenomenon is called localised surface plasmon resonance (LSPR, **Figure 1.1**).

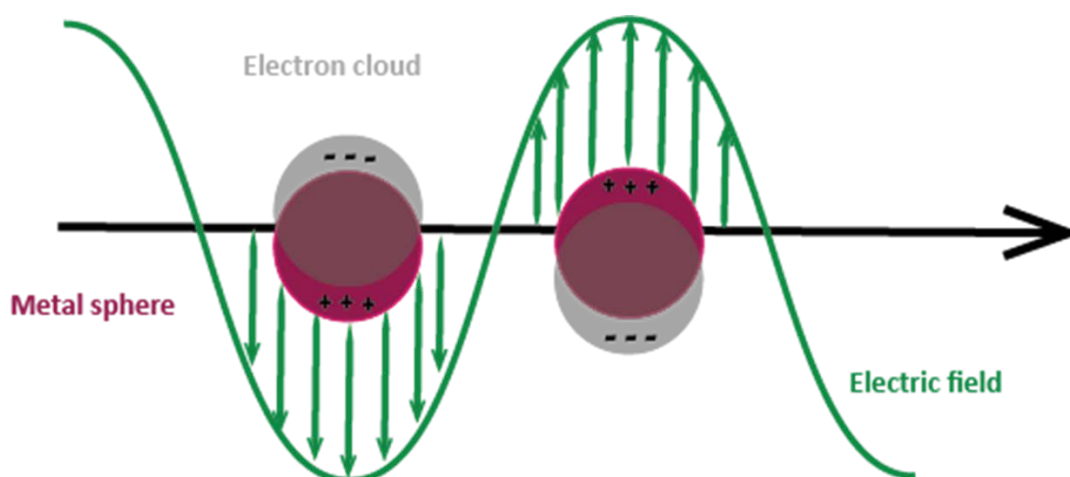


**Figure 1.1** The localised surface plasmon resonance for gold nanoparticles. When an electric field is directed at nanoparticles, the surface plasmons become excited and begin to resonate. This electric field also creates a separation of charge, that then causes a dipole oscillation in the same direction as the electric field of the incident light. The electron cloud oscillation leads to large absorption and scattering cross section.

In the case of gold and silver nanoparticles, the LSPR occurs in the visible light range, thus resulting into vivid colours varying from red to blue (AuNPs) and yellow to green (AgNPs), according to the NPs' size. While Faraday was the first one to link the size of gold colloids to their colour,<sup>22</sup> it was Gustav Mie to provide the first quantitative description of the SPR,<sup>40</sup> by solving Maxwell's equation for spherical nanoparticles. For particles with diameter below 30 nm, the electric field around a particle that is smaller than the wavelength of light can be assumed to be constant and the scattering becomes negligible (dipole approximation).<sup>42</sup> In this regime, the polarizability of the particle can be expressed with the Clausius-Mossotti equation, which links a macroscopic property (the polarizability) with the microscopic behaviour (**Equation 1.1**).

**Equation 1.1** The Clausius-Mossotti equation.  $\alpha$  is the polarizability,  $V$  is the volume of the particle,  $\epsilon_0$  is the vacuum permittivity and  $\epsilon_r(\omega) = \epsilon_r'(\omega) + i \epsilon_r''(\omega) = \epsilon_{\text{metal}}/\epsilon_{\text{medium}}$  is the complex dielectric function of the metal divided by the dielectric constant of the surrounding medium.

$$\alpha = 3\epsilon_0 V \frac{\epsilon_r(\omega) - 1}{\epsilon_r(\omega) + 2}$$

When the conduction band electrons are excited to coherently oscillate, they can relax to the ground state by either radiative or non-radiative emission (absorption or scattering). If so, the extinction cross-section can be expressed as the sum of the absorption and the scattering cross-section.<sup>41</sup> In this approximation, the extinction cross-section for a spherical NP can be written as in **Equation 1.2**.

**Equation 1.2** Dipole approximation expression for the extinction cross section of spherical nanoparticles ( $\sigma_{ext}$ ). In the equation,  $V_{NP}$  is the volume of the nanoparticle,  $\epsilon_m$  is the dielectric constant of the surround medium,  $\epsilon_i$  and  $\epsilon_{Re}$  are namely the imaginary and real part of the particles' dielectric function. Adapted from ref.<sup>43</sup>

$$\sigma_{ext} = \frac{18\pi V_{NP} \epsilon_m^{3/2}}{\lambda} \times \frac{\epsilon_i(\omega)}{(\epsilon_{Re}(\omega) + 2\epsilon_m)^2 + \epsilon_i^2(\omega)}$$

From **Equation 1.2** a few considerations can be made. First, the plasmonic properties of a material are determined by its complex dielectric function  $\epsilon$ , which corresponds to the sum of the real  $\epsilon_{Re}$  and the imaginary  $\epsilon_i$ . Second,  $\sigma_{ext}$  is maximised and a resonance occurs when the denominator in **Equation 1.2** is minimised, *i.e.* when  $\epsilon_{Re} = -2\epsilon_m$ , (Frölich condition), assuming that  $\epsilon_i$  is small or only weakly dependent on  $\omega$ .<sup>41</sup> Third, the resonance depends upon nanoparticle's shape and size, as the volume  $V_{NP}$  is present in the relation. This, however, does not predict the position of the plasmon resonance as a function of particle size. Experimental findings have shown that the LSPR blue- or red-shifts for smaller or larger particles respectively.<sup>44</sup> To take this behaviour into account, Kreibig and Genzel proposed an amendment to the dipole approximation which rendered the dielectric function size-dependent by considering the spatial constraint of electrons in small NPs.<sup>45</sup> Lastly, the SPR is also influenced by the dielectric constant of the surrounding medium  $\epsilon_m$ . This property can be used to explain shifts in the SPR as a result of changes in the medium to which nanoparticles are exposed.<sup>46,47</sup>

Apart from the LSPR, metal nanoparticles also show photoluminescence (PL). The first report of photoluminescence from gold and copper dates back to 1969.<sup>48</sup> In this seminal work, a single-photon luminescence mechanism was describes as a three-step process. First, the excitation of electrons from the d- to the sp-band generates electron–hole pairs, second, the electrons and holes scatters with partial energy transfer to the phonon lattice, and finally the electron–hole recombines resulting in photon emission.<sup>48</sup> Later, while studying the one-photon luminescence of rough gold surfaces, Boyd et al.<sup>49</sup> reported another physical process, with a quadratic dependence on the excitation energy. This phenomenon was identified as two-photon photoluminescence (TPPL). TPPL has been described as the sequential absorption of two photons of the same energy. An electron from the d band is promoted to the sp conduction band, at energy equal to twice the energy of the irradiating photons. The energy absorbed is then radiatively emitted at half the wavelength of the exciting one.<sup>49,50</sup> TPPL is a non-linear optical process. Non-linear phenomena are usually studied by means of laser light, which allows to generate high intensity of light and, consequently, high electric field amplitudes, comparable to the energies involved in electrons and atomic nuclei interactions.<sup>51</sup>



In this regime, the material polarisation  $P_i$  is not linear anymore and can be written as a function of the n-th order susceptibility  $\chi^{(n)}$ .

**Equation 1.3** Non-linear polarisation written as expansion of n-th order susceptibility  $\chi^{(n)}$ .

$$P_i = \chi_{ij}^{(1)} E_j + \chi_{ijk}^{(2)} E_j E_k + \chi_{ijkl}^{(3)} E_j E_k E_l + \dots$$

The two-photon absorption is a third-order non-parametric phenomenon, meaning that the physical mechanism for this process involves the excitement of electrons to real energy states and it is associated with the third-order  $\chi^{(3)}$ . Therefore, the intensity of the luminescence response is relatively weak but the signal can be amplified thanks to a resonant coupling with localized surface plasmons. Bouhelier *et al.*<sup>50,52</sup> showed that local field enhancement at nanoscale metal structures leads to local photoluminescence excited by two-photon absorption. This effect is known as near-field enhancement or “hot spot” effect.

Notoriously, this process has been employed as imaging tool. In 1990, Denk *et al.*<sup>53</sup> proved that the simultaneous absorption of two photons could provide three-dimensional resolution in laser scanning fluorescence microscopy. Since then, this technique has been explored as a powerful bio-imaging tool that allows for non-invasive imaging of AuNPs within cells with a higher penetration depth.<sup>54–58</sup>

#### 1.1.1.4 Synthesis and optical properties of upconversion nanoparticles

Upconversion nanoparticles (UCNPs) are another class of materials with interesting optical features. They are named after the fluorescence process known as photon upconversion. In this fluorescence mechanism, a certain frequency of light (typically in the near infrared region, NIR) is absorbed and consequently emitted at lower wavelengths (usually in the visible); hence they are able to up-convert the photons they absorb to higher energy photons (anti-Stokes process). Upconverting materials are guest-host systems where lanthanide guest ions are dispersed in a host matrix. The first report on a bulk material able to harvest and up-convert energy dates back to 1970's;<sup>59,60</sup> but it wasn't until 2003 that the observation of photon-upconversion in colloidal suspensions was reported.<sup>61</sup> Since then, a plethora of synthetic strategies sprouted for the synthesis of UCNPs with different compositions, sizes and shapes.<sup>62–66</sup>

To produce upconverting nanoparticles, a host matrix is doped with one or more rare-earth or transition metal elements. The criteria for selecting the ideal host material include: transparency in the spectral range of interest, low phonon losses, high chemical and thermal stability. A range of host lattices has been studied, examples include  $\text{LaF}_3$ ,<sup>67</sup>  $\text{Gd}_2\text{O}_3$ ,<sup>68</sup>  $\text{YF}_3$ .<sup>69</sup> Of particular relevance for

## Introduction

this work is NaYF<sub>4</sub>. NaYF<sub>4</sub> can be found in two phases:  $\alpha$  (cubic) and  $\beta$  (hexagonal).  $\beta$ -NaYF<sub>4</sub> is one of the most transparent matrices in the NIR range and with the lowest phonon losses. Additionally, it has been shown as one of the highest performing host materials for green and blue emission.<sup>62,70,71</sup>

Several synthetic strategies have been put into practice for the synthesis of NaYF<sub>4</sub> UCNPs, such as solvothermal,<sup>67,72,73</sup> microemulsion,<sup>74</sup> thermal decomposition<sup>75–77</sup> and co-precipitation<sup>78</sup> methods. Among these, the thermolysis and the co-precipitation were superior in yielding highly monodisperse, uniform and phase pure particles.

Thermolysis refers to the decomposition of one substance into two constituents due to heating. Organometallic compounds are employed as precursors, which decompose in a high boiling point organic solvent with the assistance of surfactants. After decomposition at elevated temperatures, the seeds ripen into nanoparticles assisted by the presence of a surfactant, which prevents agglomeration. This method was successfully applied to synthesise hexagonal NaYF<sub>4</sub>-based upconversion nanocrystals by different groups.<sup>75–77</sup> In these reports, uniform, small-size upconversion NaYF<sub>4</sub>:Yb,Er and NaYF<sub>4</sub>:Yb,Tm nanocrystals were obtained from the decomposition of fluoroacetate lanthanide precursors in oleylamine or in a mixture of oleylamine, oleic acid and octadecene. This strategy, however, raised safety concerns because the decomposition of the fluoride reactants creates toxic fluorinated species and even HF by hydrolysis.

At the same time, high-temperature co-precipitation methods for the synthesis of uniform, hexagonal UCNPs were reported.<sup>78–80</sup> These strategies are now considered amongst the most facile, reproducible and user-friendly to obtain phase-pure, monodispersed UCNPs of different sizes (10–70 nm)<sup>81,82</sup> and shapes (platelets, rods, cubes).<sup>83,84</sup> Generally, the initial step of this method involves the formation of an yttrium oleate precursor, followed by the addition of NH<sub>4</sub>F and NaOH. This leads to the formation of small amorphous aggregates. Treatment of these particles with elevated temperatures (~300 °C) for one hour facilitates the particle growth and generates uniform nanocrystals via an Ostwald ripening mechanism. This process is a thermodynamically-driven dissolution of small crystals or sol particles followed by the redeposition of the dissolved species on the surfaces of larger particles. This ultimately leads to the growth of larger particles on behalf of the smaller ones.

### 1.1.1.5 Optical properties of upconversion nanoparticles

The peculiar fluorescence properties of upconversion nanoparticles are due to the ions doping the transparent matrix. To facilitate the photon upconversion, a suitable dopant needs to meet specific requirements, such as long lifetimes of the excited states and a ladder-like arrangement of the

energy levels with similar spacing. These conditions are typically met by rare-earths and some transition metal elements. This is due to the long-lived metastable excited-states (up to 0.1s)<sup>85</sup> and to the high number of energy levels in the 4f-5d shells, which provide multiple energy transfer pathways for upconversion emission. By carefully choosing the dopants, a multi-colour tuning covering the entire visible spectrum can be achieved.

In a single-doped UC material, *i.e.* a material doped with only one kind of chemical element, the fluorescence emission is generated with an excited-state absorption (ESA) mechanism.<sup>64,65,85</sup> ESA (**Scheme 1.4A**) arises from the successive absorption of two photons by a single electron of the doping ion. The electron is sequentially excited from a ground state to an intermediate energy level (E1) and afterwards from E1 to a higher energetic level E2. The emission will occur from the radiative relaxation from E2 level, thus resulting in the emission of a photon with higher energy than the exciting one.

Nonetheless, the intra-atom f–f transitions of lanthanide ions typically show low extinction coefficients with narrow bandwidth. This feature, combined with the lack of fully matched absorption bands between different lanthanide ions, impedes effective excitation of different lanthanide activators under a single wavelength. This issue is normally overcome using indirect excitation by introducing a co-dopant. In this configuration, the doping ions consist of a sensitizer, which acts as an antenna harvesting the incident energy. The sensitizer ion is brought into a metastable excited state (E1). This energy is then transferred to the activator, which is excited to its first excited state while the sensitizer relaxes back to its ground state (G). Several of these energy transfers lead to the excitation of the emitter to higher states (E2), resulting into multiple emissions at different wavelengths (**Scheme 1.4B**). This mechanism is known as energy transfer upconversion (ETU).

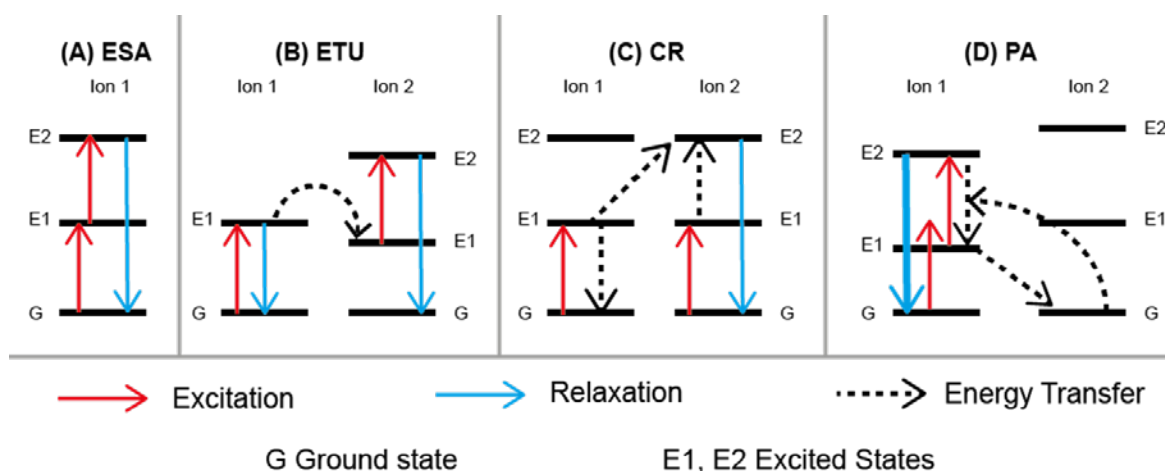
Other two complementary mechanisms are the cross relaxation (CR) and the photon avalanche (PA) processes. CR (**Scheme 1.4C**) results from an inter-ions interaction typically occurs when the two ions have similar energy levels. In their excited state E, both ions can absorb the incident radiation. This energy is then transferred from one ion to the other, and it is radiatively emitted. The efficiency of the CR process is in close relation with the dopant concentration and it usually occurs as complementary mechanism to existing ones (such as ETU or PA).

PA (**Scheme 1.4D**) is a more complex looping process that requires multiple excited state absorptions followed by cross-relaxation. Initially, the first excited level (E1) of ion 1 is occupied, followed by the population of higher energy levels through ESA. When electrons relax from E2 they can either emit light or transfer energy to the ion 2. If a transfer occurs, it can create an energy loop that increases the chance of promoting more electrons in high energy levels (pumping process).

## Introduction

Consequently, in optimal conditions, PA can facilitate the emission of light from a low-power excitation source and maximise the energy-to-emission turnover ratio. Therefore, this mechanism is highly desirable for UC lasers.<sup>86</sup>

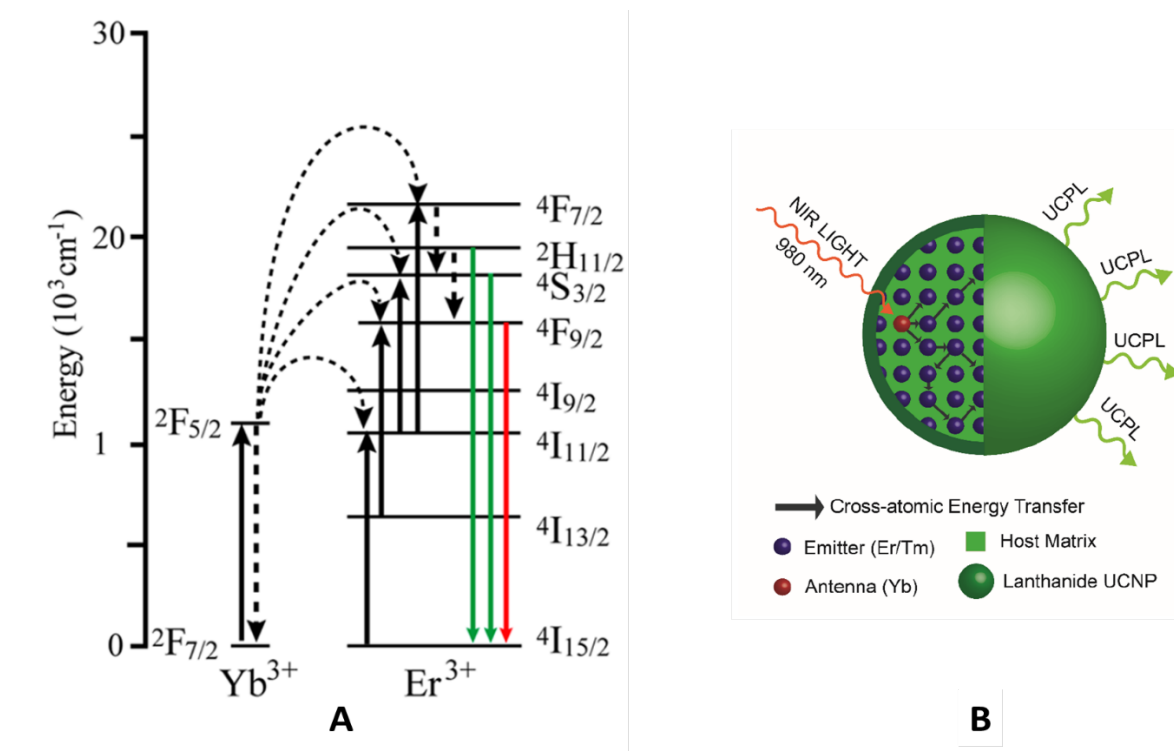
**Scheme 1.4** Upconversion mechanisms for UCNPs doped with one or two lanthanide ions. excited-state absorption (A), energy transfer upconversion (B), cross-relaxation (C) and photon avalanche (D).



Amongst the elements tested as antennas, ytterbium is particularly relevant for a number of reasons.<sup>69,87</sup> First,  $\text{Yb}^{3+}$  has a large absorption cross-section; therefore, it will absorb the majority of the incident light, which can be transferred to the activators. Second, it has only one transition, the  ${}^2F_{7/2} \rightarrow {}^2F_{5/2}$ , which is opportunely resonant with many f–f transitions of  $\text{Er}^{3+}$ ,  $\text{Tm}^{3+}$ , and  $\text{Ho}^{3+}$ , thus facilitating efficient energy transfer from  $\text{Yb}^{3+}$  to these ions. Lastly, ytterbium transition can be easily excited by means of an inexpensive, low power, continuous wave laser (980 nm).

On the other side, an ideal emitter would possess similar energy gaps between three or more subsequent energy levels, so that sequential excitations are possible with a single monochromatic light source. Rare-earth ions with an energy-level structure suitable for this type of excitation include  $\text{Er}^{3+}$ ,  $\text{Tm}^{3+}$  and  $\text{Ho}^{3+}$ , which are currently the most common emitters (activators) in upconversion phosphors. In particular,  $\text{Er}^{3+}$  has at least three different transitions induced by IR photons of the same energy, thus leading to emission of green and red light (**Scheme 1.5**).

**Scheme 1.5** (A) Energy levels for  $\text{Yb}^{3+}$  and  $\text{Er}^{3+}$  ions, which acts as antenna and emitter, respectively. In B, an illustration of the UC working principle within a particle. Within the host matrix (in green), the antenna (red ion) harvests the incoming photon and it transfers it to the emitter (blue ions). Adapted from refs.<sup>66,85</sup>



### 1.1.2 DNA nanotechnology

In recent years, DNA has emerged as a powerful tool to generate nano-patterned materials, in one, two or three dimensions.<sup>88</sup> The ability to precisely tailor DNA nanostructures has paved the way to new and exciting applications in the areas of nanofabrication, chemical sensing, imaging, and gene regulation. In this section, the structure and properties of synthetic oligonucleotides are explored (**Section 1.1.2.1**). A brief overview of the relevant chemical modification for self-assemble nanostructures is given in **Section 1.1.2.2**.

#### 1.1.2.1 Structure and properties of oligonucleotides

Deoxyribonucleic acid (DNA) is a biological macromolecule, which encodes all the genetic information in living organisms. It is a linear polymer formed by nucleotide monomers.<sup>89</sup> Each monomer consists of a pentose sugar (deoxyribose), a phosphate group and a nitrogenous base. The naturally occurring bases in DNA are the pyrimidines Cytosine (C) and Thymine (T) and the purines Guanine (G) and Adenine (A) (**Figure 1.2**). Each nucleobase is linked to a deoxyribose, and

## Introduction

the deoxyribose molecules are linked to each other by a phosphodiester bond (phosphate backbone). At  $\text{pH} > 2$  phosphate groups are negatively charged, resulting in DNA being a highly charged anionic polymer. It should be noted that each ribose is oriented in the same fashion, the phosphodiester linkage is created between the 5'-phosphate group of one nucleotide to the 3'-hydroxyl group of another. This characteristic endows each oligonucleotide with specific directionality.

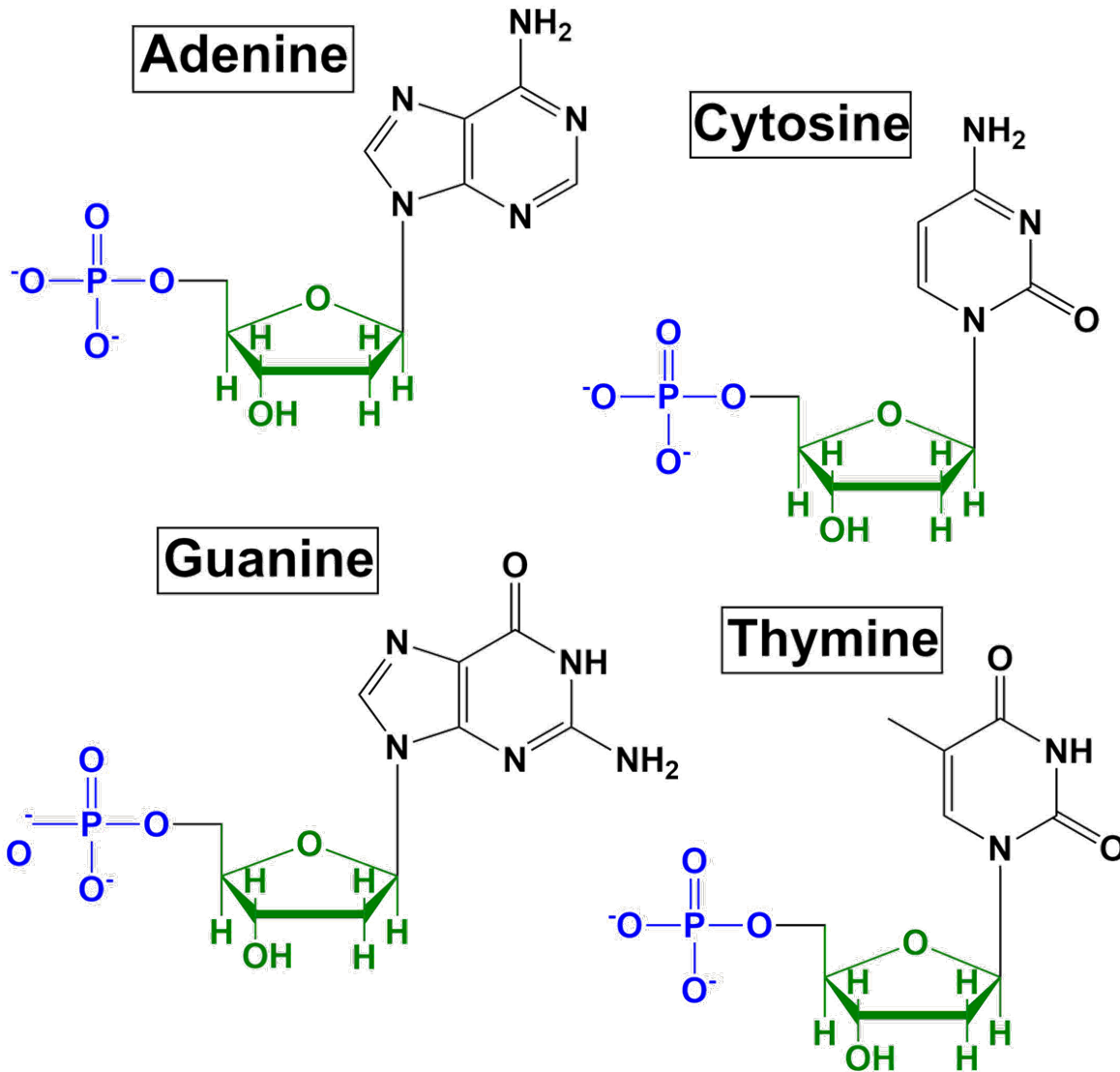


**Figure 1.2** Molecular structures of the DNA nucleotides. The phosphate is highlighted in blues, the deoxyribose ring is in green and the different nucleobases in black.

In 1953, Rosalind Franklin, James Watson and Francis Crick revealed that oligonucleotides are usually arranged in a three-dimensional double helix formed by two intertwined single strands.<sup>90</sup> In solution, the double-stranded DNA (dsDNA) is organised such that the negatively-charged pentose-phosphate backbone lies on the outside and the hydrophobic bases on the inside. This arrangement is driven by the binding between base pairs (bp) *via* hydrogen bonds. In order to maximise the

number of hydrogen bonds, guanine pairs with cytosine (G-C), while adenine pairs with thymine (A-T). These interactions are selective and highly specific. Within a duplex, the strands are arranged in an anti-parallel manner, with the 5'-end of an ssDNA facing the 3'-end of the complementary one (Figure 1.3).

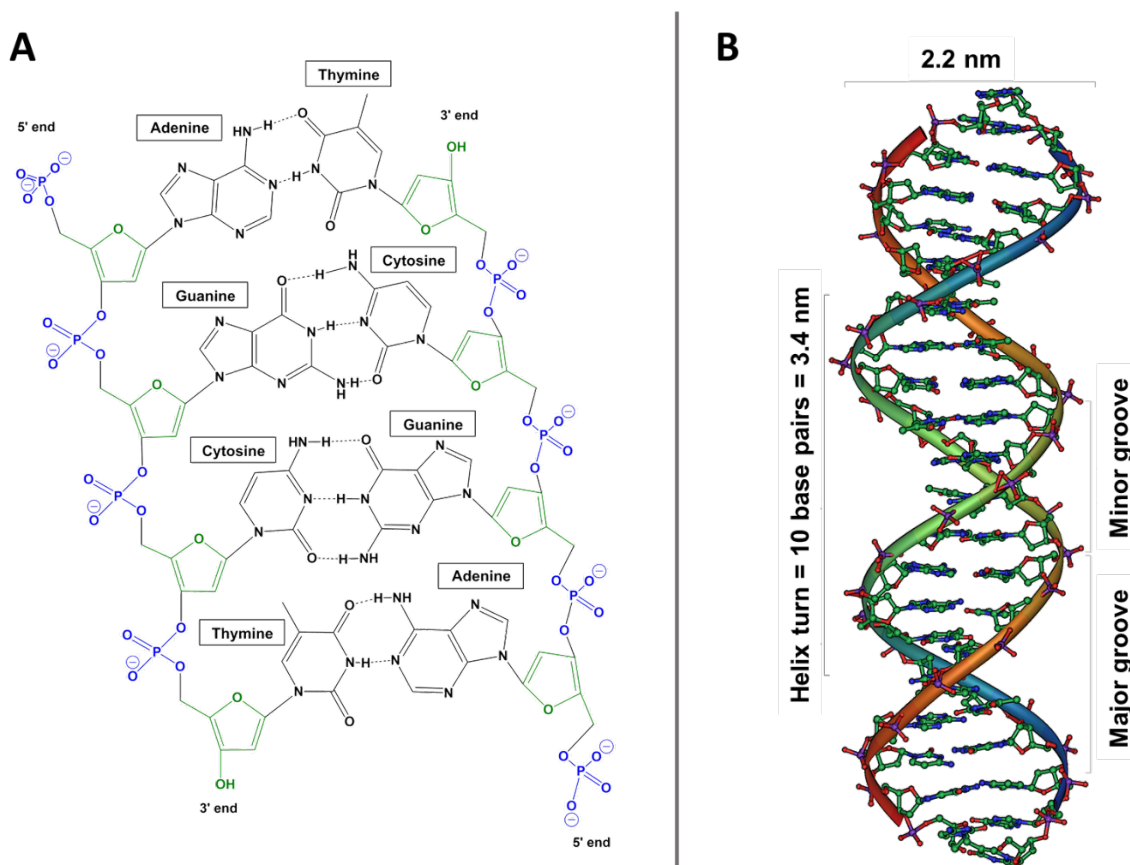


**Figure 1.3** Structure of the double stranded DNA. In A, the hydrogen bonds and the specific complementarity between the bases are highlighted. In B, the three-dimensional structure of the duplex conformation is shown.

Apart from the hydrogen bonding between complementary bases, the dsDNA stability is also ensured by  $\pi$ -stacking between adjacent nucleoside. This interaction arises from instantaneous dipoles due to electron density fluctuations between the electron-rich nitrogenous rings of the bases.

Nonetheless, the negatively charged backbones generate repulsive forces, making the duplex sensitive to the environment conditions (temperature, pH, ionic strength). To facilitate the double helix formation (hybridisation process) the charges are usually screened by means of positively charged ions (e.g.  $\text{Mg}^{2+}$ ,  $\text{Na}^+$ ). Another parameter to consider is the pH of the surrounding medium, as it will affect the protonation of the nucleobases and hence the hydrogen bonding within the

## Introduction

duplex. For this reason, the pH of a dsDNA solution is usually controlled by means of buffer solutions.

Besides, also the temperature is a key parameter. High temperatures will cause the DNA to unfold (dehybridisation process) by breaking the hydrogen bonds between bases. To monitor this variable, a dsDNA melting temperature  $T_m$  is defined as the temperature at which 50% of the dsDNA are dehybridised. This value can be experimentally determined for any oligonucleotide pairs by exploiting the different UV absorption of ssDNA and dsDNA. As the duplex is denatured into two single strands, the  $\pi$  interactions between the nucleotide bases are broken; this allows for a stronger UV absorption (hyperchromic effect). This gives rise to a characteristic sigmoidal shape of a DNA melting curve. The melting temperature is found at the inflection point of the curve. This value depends on the number of pairing bases and for sequences longer than 13 bases can be calculated according to **Equation 1.3**. Examples of melting curves can be found in **Figure 3.17**.

**Equation 1.4** 4 Melting temperature operative formula for oligonucleotides composed by more than 13 bases.<sup>91</sup>

$$T_m = 64.9 + 41 \times \frac{yG + zC - 16.4}{wA + xT + yG + zC}$$

Pre-programmed, customised synthetic DNA sequences can be produced by automated solid phase phosphoramidite synthesis.<sup>92-94</sup> Furthermore, a wide range of functional groups can be either incorporated via a functionalized column used for solid phase synthesis (for 3' modifications only) or by utilization of pre-modified nucleoside phosphoramidite monomers.<sup>95</sup> The addition of functional groups within synthetic oligonucleotides may serve different aims: anchoring on surfaces, introduction of labelling agents, and introduction of new chemical functionalities.

In this work, two different modifier groups were employed to attach multiple ssDNA on the surface of nanoparticles. In the case of gold and silver a thiol group was chosen, as the efficiency of the linkage Au-SH and Ag-SH is well-established in the literature.<sup>96-98</sup> For other kind of particles, such as UCNPs, amino-modifiers were chosen instead. An amino group can covalently bound a carboxy termination placed on the surface of the NPs, providing efficient loading of oligonucleotides.<sup>99</sup> Details of the anchoring group structures are reported in **Figure 1.4** and reaction mechanisms can be found in **Section 1.1.2.3**.



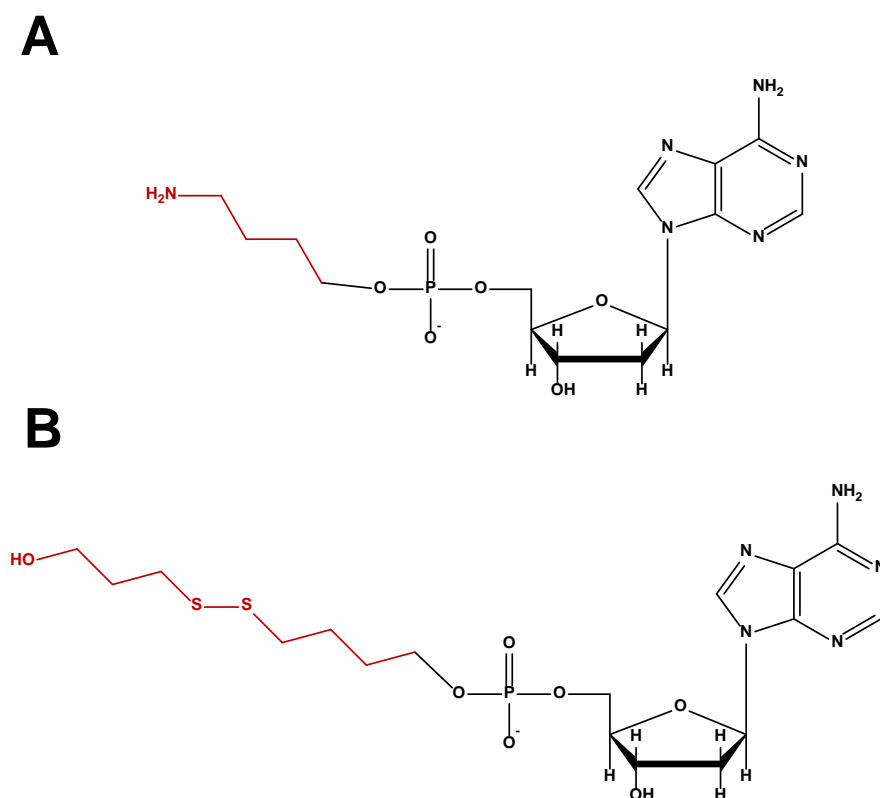


**Figure 1.4** Chemical modifications to the oligonucleotide sequences. The functional groups (in red) were attached to the 5' end. Aminohexyl (A) was used in the EDC/NHS coupling, while the sulphur bridge (B) was used for Au and Ag oligo coating.

Another type of modification relevant for the present work, is the introduction of engineered nucleobases able to introduce novel functionalities in the DNA strands. For the present work, a particularly relevant example is the 3-cyanovinyl carbazole nucleobase. This compound can be precisely positioned in an oligonucleotide sequence during the synthesis. It is able to create a reversible covalent bond between two complementary strands, following appropriate light stimulation.<sup>100–103</sup> An extended discussion can be found in the following **Section 1.1.2.2**.

### 1.1.2.2 DNA crosslinking

As discussed earlier in this Chapter, the dsDNA is held together by weak forces which require specific environment condition to retain their structure. To tackle this problem, crosslinking approaches to create covalent bonds within dsDNA have been developed. Crosslinking between two complementary strands can be promoted by the introduction of an intercalator, for example 8-Methoxypsoralen (8-MOP) and 1,3-Bis(2-chloroethyl)-1-nitrosourea (BCNU).<sup>104–106</sup> These compounds diffuse in gaps between base-pairs in dsDNA. Following permeation, these molecules can undergo [2+2]-photoaddition with a thymine (8-MOP) or guanine (BCNU) This approach has been recently used for the crosslinking of DNA-Nanoparticles superlattices.<sup>107</sup> However, an effective crosslinking within a duplex can only happen if the intercalator is found between two opposite

## Introduction

thymines, in the case of 8-MOP, or between a guanine and a cytosine, in the case of BCNU.<sup>104</sup>

Molecular structures and crosslinking reactions are detailed in **Figure 1.5**.

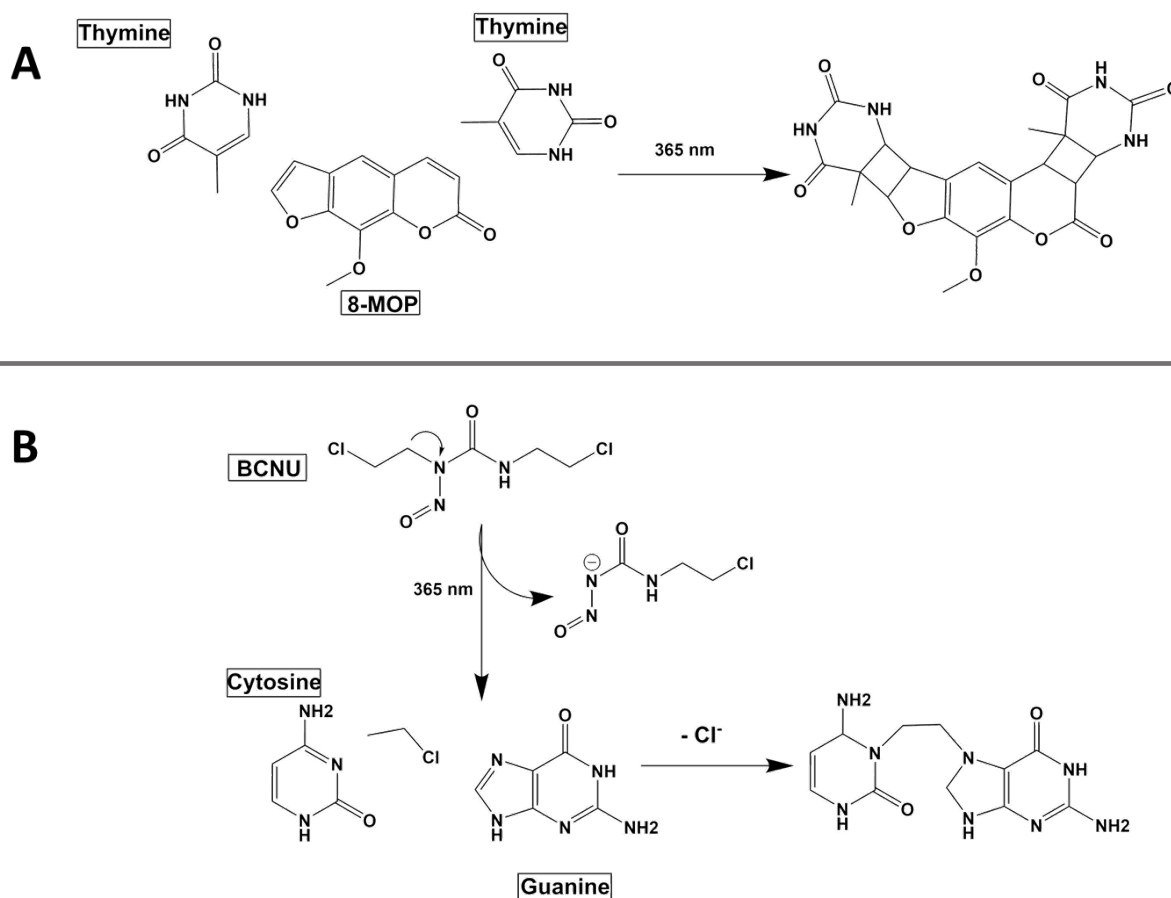
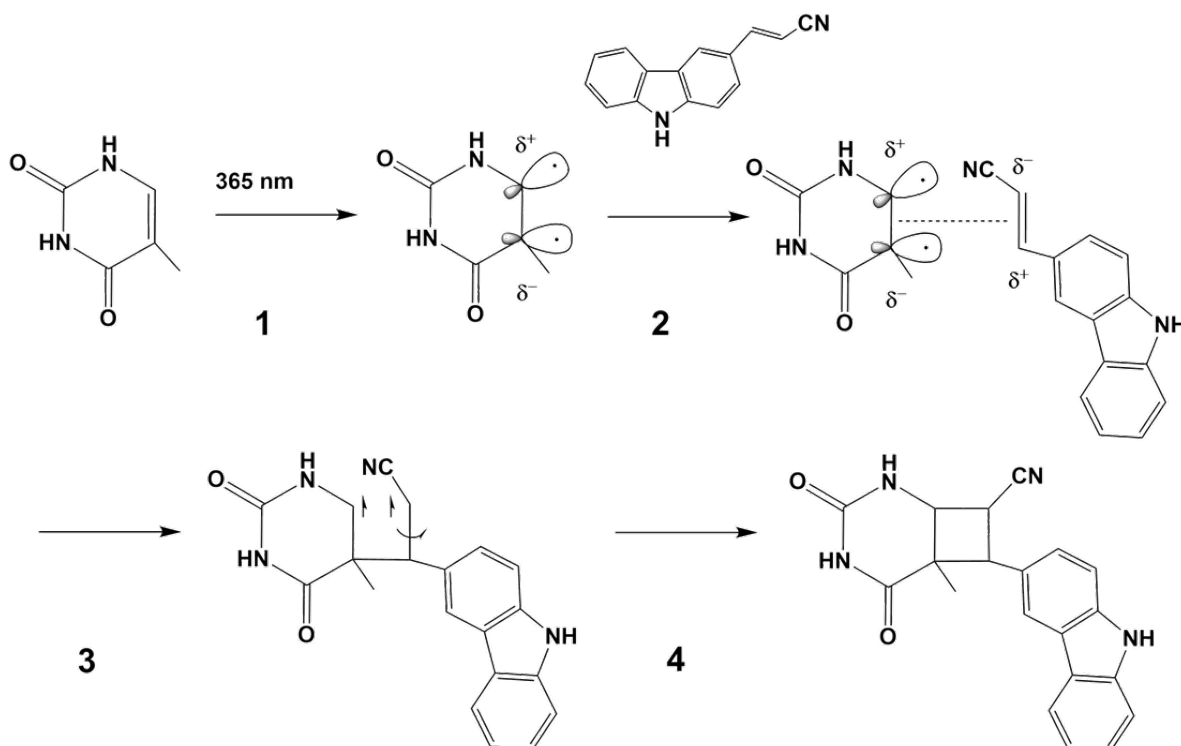


**Figure 1.5** Molecular structures and crosslink reactions for 8-Methoxypsoralen (A) and 1,3-Bis(2-chloroethyl)-1-nitrosourea (B).<sup>106</sup>

A different strategy to promote covalent ligation with a duplex envisages the introduction of a modified nucleobase in the DNA sequence. As mentioned in **Section 1.1.2.1**, in this work a 3-cyanovinyl carbazole nucleobase was employed. This molecule was developed by Fujimoto *et al.*<sup>100–102</sup> as efficient light-induced crosslinker of DNA. This reaction is a [2+2]-photocycloaddition between an electron-rich double bond and an opposite thymine base, which leads to the formation of a cyclo-butane ring. The reaction steps are illustrated in **Scheme 1.6**. In step 1, the highly energetic UV light excites an electron from the highest occupied molecular orbital (HOMO) to the lowest unoccupied molecular orbital (LUMO). Following re-arrangement of electrons (steps 2 and 3), a new bond is then formed with the double bond of the cyanovinyl group (step 4). In addition to the covalent ligation, another novel feature is the possibility to efficiently de-crosslink the dsDNA by irradiation with UV-B light. Light irradiation at 312 nm can be used to open the cyclobutane ring and to yield the pristine cyano-ethylene group and thymine base.

**Scheme 1.6** Reaction mechanism for the [2+2]-photocycloaddition between a thymine and a cyanovinyl carbazole. In the first step, the double bond of a thymine base is brought to an excited state. An excited complex is formed with the cyanovinyl moiety of the carbazole nucleobase (steps 2 and 3). Finally, a cyclobutane is formed (step 4).<sup>108</sup>



In the past, this exceptional functionality has been used to assemble oligomers of gold nanoparticles.<sup>103</sup> In this work, the efficacy of this linkage was extended to three-dimensional assemblies of thousands of particles.<sup>109</sup> An extended discussion on this can be found in **Section 1.1.3**.

### 1.1.2.3 Strategies for oligonucleotide attachment on colloidal nanoparticles

Functionalization of nanoparticles is necessary for their stability, functionality, and biocompatibility. The precise control on the surface chemical composition and its modification are of utmost importance for added value applications concerning nanoparticles. The creation of specific surface sites on nanoparticles for selective molecular attachment is considered a promising approach for their applications in nanofabrication, nanopatterning, self-assembly, nanosensors, nanomedicine.

A special role amongst the surface ligands is played by DNA. DNA modification provides the nanoparticle with functional properties intrinsic to the DNA ligand, such as chemical recognition, target specificity, biocompatibility. In particular, gold nanostructures functionalised with ssDNA

## Introduction

have become increasingly important building blocks for applications in sensing and nanomedicine,<sup>110</sup> metamaterials,<sup>111,112</sup> nano-optics,<sup>113–117</sup> and nanoelectronics.<sup>118,119</sup>

In 1996, the first evidences of successful attachment of oligonucleotides on AuNPs were reported. Specifically, Mirkin and co-workers showed that gold nanoparticles can be modified with a dense shell of oligonucleotides,<sup>18</sup> while Alivisatos and co-workers revealed that it was equally feasible to conjugate discrete number of ssDNA on the surface of AuNPs.<sup>17</sup>

The attachment of ssDNA on gold surface is now a well-established method due to employment of thiol-terminated oligonucleotides (**Section 1.1.2.1**), and a number of strategies have been developed for the conjugation of a large number of oligonucleotides onto a citrate-coated gold nanosphere.

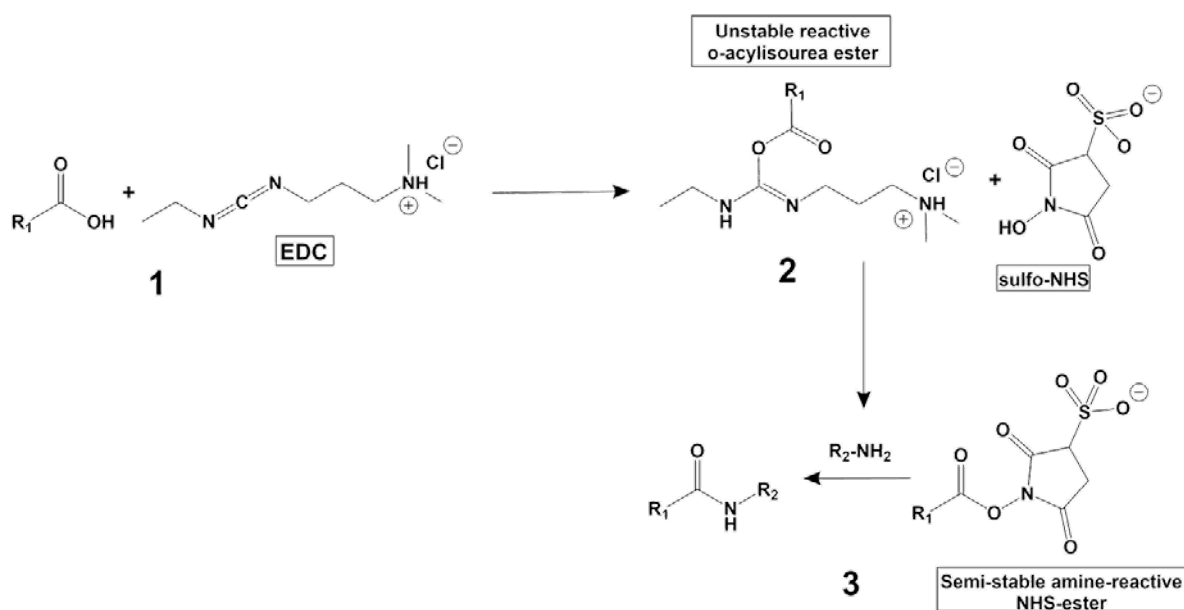
In general, to achieve a high loading of oligonucleotides on the NP's surface is necessary to screen the repulsive charges between the gold nanoparticle surface and the negatively charged phosphate backbone on the DNA, as well as the charges between individual DNA strands.<sup>120</sup> This can be obtained by increasing the concentration of screening ions in solution. This, however, may result in irreversible nanoparticles aggregation.<sup>121</sup> To prevent NPs precipitation, the ionic strength of the DNA-NPs solution must be gradually increased. A common strategy to achieve this result is the so-called salt-aging protocol. In this method, NaCl is gradually added to a suspension containing NPs and thiol-modified ssDNA. The slow addition of Na<sup>+</sup> ions screens the charges between the citrate-coated AuNPs and the oligonucleotides, and few ssDNA are able to bind the surface of the NP. As this occurs, the NPs stability increases, allowing the addition of more cations without causing aggregation. This, eventually, results in a dense layer of oligonucleotides on the gold nanoparticle surface.<sup>122</sup> A similar strategy was reported by Kanaras *et al.* In their work, they obtained a similar result using a vacuum centrifugation method in which the ionic strength and concentrations of oligonucleotides and AuNPs are gradually increased as a result of an overall decreasing reaction volume.<sup>9</sup>

A completely different strategy was recently reported by Zhang and collaborators using a pH-assisted route.<sup>123</sup> The quantitative DNA functionalisation was achieved in few minutes by adding a citrate buffer at pH 3 to an AuNPs-ssDNA suspension. Another novel approach was developed by Liu *et al.* In their work, they obtained densely-functionalised DNA-AuNPs by freezing and thawing without the addition of any salt or buffer.<sup>124</sup>

All these methods work well for AuNPs since they rely on the bond affinity of sulphur for gold and, to a lesser extent, for silver.<sup>125,126</sup> For particles with a different composition, the conjugation of oligonucleotides is not equally straightforward. In many cases, inorganic nanoparticles are

stabilized by polymers containing variable functional end-groups such as hydroxyl, carboxyl, amine, alkyne, azide or aldehydes, which complicate the development of a general strategy for covalent DNA conjugation.<sup>121</sup> Nevertheless, when the surface of particles contains carboxyl groups, amine-terminated oligonucleotides can be conjugated via the use of well-established EDC/sulfo-NHS coupling strategy.<sup>99,127</sup> EDC (1-ethyl-3-(3-dimethylaminopropyl) carbodiimide hydrochloride) is a commonly used cross-linking reagent employed for the coupling of a primary amine with a carboxylic group. Sulfo-NHS (N-hydroxy sulfosuccinimide) is used to increase the stability of active intermediates in coupling reactions via the formation of active ester functional groups with carboxylates. The general reaction mechanism is outlined in **Scheme 1.7**. The reaction involves the coupling of a primary amine with a carboxylic acid in presence of 1-Ethyl-3-(3-dimethylaminopropyl)carbodiimide (EDC) and N-hydroxysulfosuccinimide (sulfo-NHS); the mechanism is depicted in **Scheme 1.7**. Initially, the carboxylic acid is activated by EDC to form a highly reactive intermediate (**Scheme 1.7, step 1**). Due to the tendency of this intermediate to hydrolyse, the overall yield of the coupling reaction may decrease; for this reason sulfo-NHS is employed to form an active ester (**Scheme 1.7, step 2**), which has a higher selectivity to react with primary amine to form an amide bond (**Scheme 1.7, step 3**). Using this method, Alonso-Cristobal *et al.* showed that the surface of upconversion nanoparticles coated with a carboxy-rich silica shell could also be successfully conjugated with amine-terminated DNA strands.<sup>99</sup>

**Scheme 1.7** EDC/sulfo-NHS coupling reaction scheme. In the first step, the carboxylic acid is activated by EDC to form a highly reactive intermediate. Sulfo-NHS is employed to form an active ester (step 2), which selectively reacts with a primary amine to form an amide (step 3).



## Introduction

Following on these reports, Au and AgNPs used in this work were functionalised with thiol-terminated ssDNA using a progressive salt aging method. Carboxyl-functionalized nanomaterials employed in this project (UCNPs, Iron Oxide NPs) were conjugated to amine-terminated DNA using EDC/sulfo-NHS coupling. Experimental details of these procedures can be found in **Section 2.2**, while results are discussed in **Section 3.3**.

### 1.1.3 Self-assembly of nanoparticles

Apart from manipulating the morphologies at the individual level, to realize the full potential of nanomaterials it is of utmost importance to control the precise positioning and orientation of these nanomaterials in the three-dimensional space. Moreover, it is critical to exert selective and dynamic control over the assembly-disassembly process in response to specific stimuli. To meet these requirements, directed-assembly methods relying on external variables, such as concentration, reaction time, pH, and solution temperature are often employed.<sup>128–130</sup>

A different strategy is the template-directed self-assembly approach. A template is any object acting as a scaffold onto which different particles can be arranged into a structure with a morphology that is complementary to that of the template. Thus, a broad variety of elements, such as single molecules, microstructures (e.g. carbon nanotubes), block copolymers, rigid scaffold (such as zeolites) can serve as templates. In this framework, a role of special relevance is played by DNA (**Figure 1.6**). The high selectivity and specificity for complementary sequence, the versatility in the structures that can be constructed and the tunability of the available chemical modification leveraged the assembly NPs into many exotic structures.<sup>44</sup>

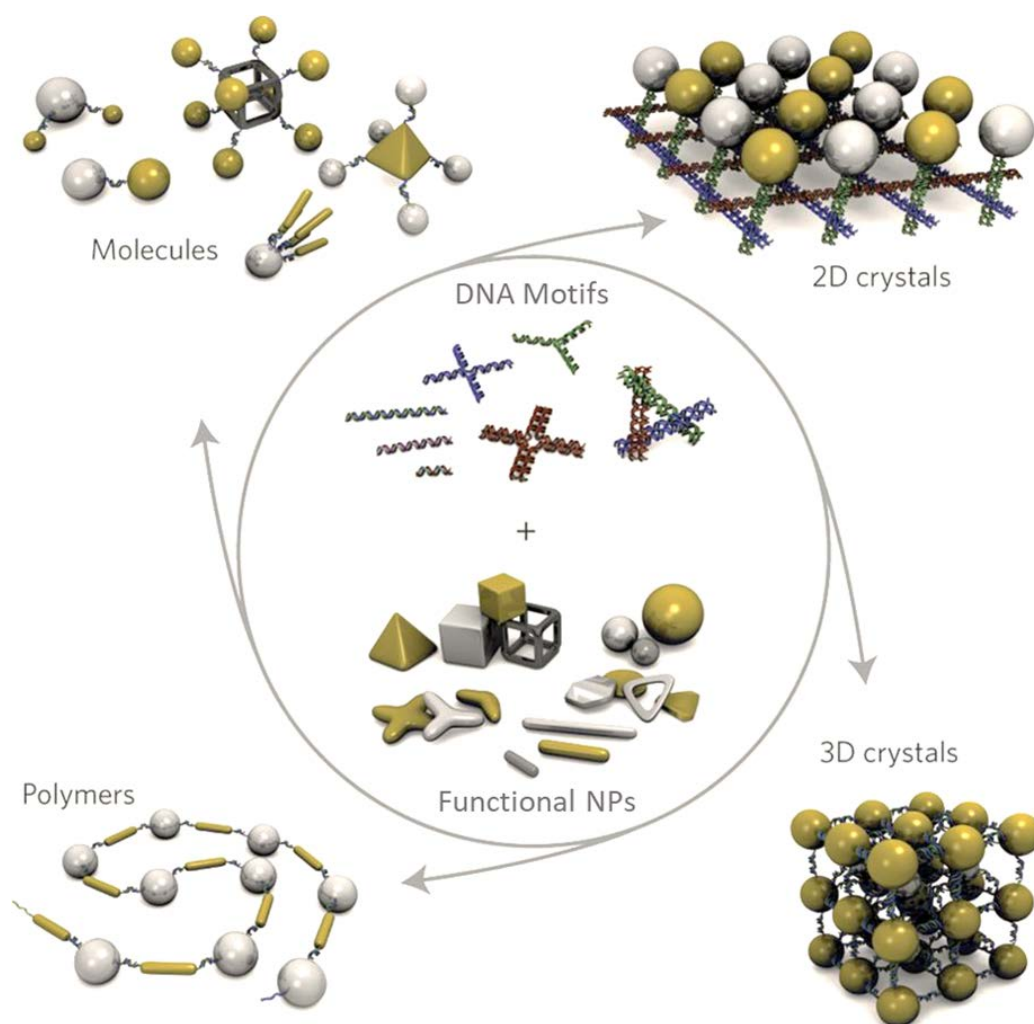


**Figure 1.6** A library of different nanostructures can be obtained from the rationally design of DNA motifs coupled with the precise synthesis of nanoparticles. Adapted from ref <sup>19</sup>.

Pioneering work from Mirkin and collaborators showed that two batches of particles with complementary DNA are reversibly forming aggregates depending on the temperature. This approach was initially used for the amorphous aggregation of a large number of nanoparticles; then, in 2008, the possibility to assemble DNA-coated AuNPs in an extended crystal habit (superlattices) through DNA hybridisation was independently proved by Mirkin<sup>131</sup> and Gang<sup>132</sup> research groups. In their work, the annealing of two batches of NPs coated with complementary ssDNA at a constant temperature resulted into the formation of polycrystalline superlattices. By appropriate design, body centred cubic (BCC) and face-centred cubic (FCC) geometries were synthesised via self-assembly, exploiting the self-recognition ability encoded in the properly designed DNA strands.

The possibility to fabricate heterogeneous superlattices was firstly shown by Sun and Gang in 2011, who reported the formation of BCC structures of gold nanoparticles and quantum dots. In their

## Introduction

work, they also demonstrated that nanoparticles of different sizes can be assembled together in an ordered structure.<sup>133</sup>

In 2013, Mirkin group reported the first single crystal of DNA-coated AuNPs.<sup>134</sup> To favour the formation of a structure with well-defined crystal facets, a slow-cooling assembly strategy was preferred. In this approach, rather than annealing at a fixed temperature, the NPs were heated up above the DNA melting temperature and allowed to slowly cool down to RT. In addition to this new crystallisation protocol, the silanisation of the structures allowed the visualisation by scanning electron microscopy.<sup>135</sup> Since then, research has been focusing to extend the programmability and tunability of AuNP-DNA superlattices,<sup>136</sup> studying the thermodynamics and kinetics of formation,<sup>137–139</sup> and expanding the library of available structures.<sup>140</sup>

In 2010<sup>141</sup> anisotropic AuNPs (nanorods, triangular prisms, octahedrons) were firstly employed within a superlattice. In this work, they shown that, being equal the DNA strands used, the shape of the colloidal building blocks has strong influence in determining the most stable configuration, directly affecting the lattice parameters, crystal structures and crystallisation conditions. Later<sup>142</sup> NPs with different shapes were mixed, showing the principle of the maximisation of hybridisation events, thus favouring the formation of long-range distance ordered structures composed by complementary-shaped NPs (e.g. concave-convex cubes). Simultaneously, the increased level of complexity in DNA engineering allowed for the formation of more exotic and even reconfigurable structures. Examples of this include a system composed by hairpin strands, able to switch between two different crystal lattices.<sup>139</sup> Another example includes the first diamond lattice made by AuNPs and DNA, using DNA origami tetrahedron cages to encapsulate the NPs and then assembling them in a diamond structure.<sup>143</sup>

More recently, research has focussed on the attempt of producing very large superlattices, as this is envisioned to facilitate the physical characterisation of the system.<sup>144</sup> In their work of 2019, Seo *et al.*, explored the possibility to use extremely high salt concentration (up to 1 M), to facilitate the growth of a single NPs crystal of about 10  $\mu\text{m}$ . However, this strategy yielded only one crystal in this size range.

In parallel, a strategy to obtain small but highly homogeneous crystals has been reported.<sup>145</sup> In this method, the suspension containing AuNPs functionalised with complementary ssDNA was deposited on a layer of dextran sulfate. When the crystals grow and reach a critical mass, they become heavier than the dextran layer, and precipitate at the bottom of it. At this point, the growth of the precipitated SLs is quenched as the dextran separate them from the solution containing free DNA-NPs. In this way, AuSLs with significantly narrower size distribution were achieved.



However, the inherent instability of DNA duplexes currently limits the application capability of these materials. DNA strands can hybridise (and stay hybridised) only in presence of cations, able to intercalate the double helix and screen the negatively charged phosphate backbones.<sup>135</sup> An attempt to solve this problem consisted in the growing of a silica shell through sol-gel chemistry around the crystals<sup>135</sup>, thus encapsulating the superlattice in a rigid and stable shell. Other attempts to tackle this issue have focused mainly on the intercalation of molecules<sup>146</sup> or ions<sup>147</sup> within the DNA duplex.

The successful achievement of self-assembled NPs-DNA superstructures suggested the conceptual assembly of a new periodic table<sup>148</sup> based on nucleic acid-nanoparticle conjugates acting as atom equivalents (often referred as programmable atom equivalents, PAEs) to build higher ordered materials through pre-programmed hybridisation events. Nucleic acids play the role of the electrons connecting the atom equivalents to form artificial “molecules”. This new paradigm in combination with a set of design rules for the self-assembly, facilitates the systematic investigation of novel materials and may help to predict properties of certain nanoparticle combinations.

Altogether, there has been a tremendous development in the field of self-assembling nanostructures in the last decade which led to interesting and promising new materials. In this work, DNA-directed assembly of three-dimensional plasmonic and fluorescent nanoparticles is investigated and a novel tool for the reversible cross-linking of ordered superlattices with 3-cyanovinyl carbazole is presented.



## Chapter 2 Experimental Procedures

This Chapter includes all the experimental procedures used in this work. Protocols for the synthesis and surface modification of nanoparticles and their assembly can be found in **Sections 2.1, 2.2** and **2.3**. Characterisation techniques are described in **Section 2.5**.

### 2.1 Synthesis of Nanoparticles

Nanoparticles with different size, shapes and composition were synthesised according to well-established wet chemistry protocols. Corresponding characterisation can be found in **Section 2.5**.

#### 2.1.1 Synthesis of 14 nm spherical gold nanoparticles

Spherical gold nanoparticles of  $14 \pm 1$  nm were synthesised following a citrate reduction method, developed by Turkevich<sup>23</sup> and modified by Frens<sup>24</sup>. In detail, an aqueous solution of sodium tetrachloroaurate (100 mL, 1 mM) was heated to 100 °C whilst under gentle stirring. Once boiling, trisodium citrate (5 ml, 2% wt in water) was sharply injected under vigorous stirring and a colour change from yellow to colourless was immediately observed. After the colour turned to red, the solution was left to stir at 100 °C for additional 15 minutes. Subsequently, the suspension of AuNPs was left to cool down overnight under mild stirring. Finally, the NPs were purified by filtration over a 0.45 µm syringe filter and stored at 4 °C for further characterisation and use.

#### 2.1.2 Synthesis of large spherical gold nanoparticles

Large AuNPs (> 20 nm) are synthesised according to a seed-mediated protocol. In this synthetic protocol two stages are required: in the first, the gold seeds are synthesised, in the second one, the growing occurs in multiple steps, according to the targeted size.

A solution of sodium citrate in Milli-Q water (150 mL, 2.2mM) was heated for 15 min under vigorous stirring. Afterwards NaAuCl<sub>4</sub> (1 mL, 25 mM) was injected. A colour change from yellow to grey and then to light red was observed within 10 min. The solution was cooled to 90 °C and two further injections of NaAuCl<sub>4</sub> (1 mL, 25 mM) were carried out at 30-minute intervals. Afterwards, the sample was diluted by extracting 55 mL of sample and adding of Milli-Q water (53 mL) and of sodium citrate (2 mL, 60mM). This solution was then used as a seed solution, and the process was repeated again. This process was repeated in order to produce AuNPs of increasing sizes. After production of NPs with the desired size, the heating mantle was removed, and the suspension was allowed to

## Experimental Procedures

cool at room temperature. The nanoparticles were purified by filtration over a 0.45  $\mu\text{m}$  syringe filter and stored at 4  $^{\circ}\text{C}$  for further characterisation and use.

### 2.1.3 Synthesis of spherical silver nanoparticles

The synthesis of  $15\pm 6$  nm AgNPs was performed with slight modifications of a previously reported protocol.<sup>38</sup> Sodium citrate (1 mL, 5 mM) and tannic acid (1 mL, 0.025 mM) were added to 98 mL of ultrapure water. Once boil had started,  $\text{AgNO}_3$  (1 mL, 25 mM) was injected to the boiling solution, which became bright yellow. The reaction was left to stir for additional 15 minutes. The so-obtained seeds can be used to grow different generation of particles with increasing size. Each growth step consisted in the extraction of 19.5 mL of the starting solution, followed by sequential addition of ultrapure water (16.5 mL), tannic acid (1.5 mL, 2.5 mM), sodium citrate (0.5 mL, 25 mM) and silver nitrate (1 mL, 25 mM). After a colour change is observed, the mixture is left to react for further 15 minutes. This growth step can be repeated until the desired NP size is reached. After the achievement of the target size, the NPs were purified by centrifugation (10000 rpm, 20 min, 3x), dispersed in 5 mL of ultrapure water and stored at 4  $^{\circ}\text{C}$ .

### 2.1.4 Synthesis of lanthanide-doped $\text{NaYF}_4$ upconversion nanoparticles

Lanthanide upconversion nanoparticles were synthesized according to minor modifications to a previously reported thermal decomposition protocol.<sup>80</sup> The crystalline matrix was created by using yttrium(III) chloride hexahydrate, sodium hydroxide and ammonium fluoride. Ytterbium(III) chloride hexahydrate, was used as the sensitizer and erbium(III) chloride hexahydrate as emitter. The ratio of yttrium/ytterbium/erbium salts was kept as 78%:20%:2%.

Yttrium(III) chloride hexahydrate (236 mg, 0.78 mmol), ytterbium(III) chloride hexahydrate (77 mg, 0.20 mmol) and erbium(III) chloride hexahydrate (8 mg, 0.02 mmol) salts were dissolved with oleic acid (6 mL, 19 mmol) and 1-octadecene (15 mL) in a three-necked round-bottom flask. The flask was placed in a heating mantle equipped with a temperature probe and heated at 150  $^{\circ}\text{C}$  for 1 h and 30 minutes under argon flow to allow the solubilisation of the salts. Then, the solution was cooled down to room temperature and a solution of methanol (10 mL) containing sodium hydroxide (100 mg, 2.5 mmol) and ammonium fluoride (148 mg, 4 mmol) was added dropwise to the reaction under vigorous stirring. This mixture was slowly heated to 110 $^{\circ}\text{C}$  for 1 h under argon gas at atmospheric pressure and then 30 more minutes under vacuum. Next, the temperature was raised to 310  $^{\circ}\text{C}$  and left to react for 1 h and 10 min. Subsequently, the mixture was left to cool to room temperature, and the  $\text{NaYF}_4:\text{Yb}^{3+},\text{Er}^{3+}$  nanoparticles were collected by precipitation in ethanol and centrifugation (8000 rpm, 10 min). The supernatant was removed and the pellet redispersed in

ethanol and centrifuged again (5000 rpm, 15 min). This process was repeated three times, after which the precipitate was left to dry overnight. The weight of the resulting nanoparticles was measured, and the particles (10 mg/mL) were stored in hexane at room temperature until further use.

#### 2.1.5 Synthesis of lanthanide-doped NaY:GdF<sub>4</sub> upconversion nanoparticles

To modulate the size of the matrix, gadolinium was used to replace part of the Y in the lattice. Gadolinium-doped UCNPs were synthesised by modifying the amounts used in the synthesis reported above (**Section 2.1.4**). The amount of Y was decreased while the Gd was increased accordingly, keeping the ratios of Gd/Y to 20%/80% or to 30%/70%, while the other salts were kept unvaried to ytterbium/erbium 20%/2% of the combined matrix ions Gd<sup>3+</sup> and Y<sup>3+</sup>.

Specifically for UCNPs 20%Gd: yttrium(III) chloride hexahydrate (180 mg, 0.59 mmol), gadolinium (III) chloride hexahydrate (74 mg, 0.20mmol), ytterbium(III) chloride hexahydrate (77 mg, 0.20 mmol) and erbium(III) chloride hexahydrate (8 mg, 0.02 mmol) salts were weighted.

For UCNPs 30%Gd: yttrium(III) chloride hexahydrate (142 mg, 0.47 mmol), gadolinium (III) chloride hexahydrate (116 mg, 0.31 mmol), ytterbium(III) chloride hexahydrate (77 mg, 0.20 mmol) and erbium(III) chloride hexahydrate (8 mg, 0.02 mmol) salts were weighted.

After weighing the appropriate amount of compounds for the desired concentration, the salts were dissolved with oleic acid (6 mL, 19 mmol) and 1-octadecene (15 mL) in a three-necked round-bottom flask and placed in a heating mantle equipped with a temperature probe. The temperature was raised to 150 °C under argon flow to allow complete solubilisation. After 1h and 30 minutes, the solution was cooled down to room temperature and a solution of methanol (10 mL) containing sodium hydroxide (100 mg, 2.5 mmol) and ammonium fluoride (148 mg, 4 mmol) was injected dropwise to the reaction while stirring. This mixture was slowly heated to 110°C for 1 h under argon gas at atmospheric pressure and then 30 more minutes under vacuum. Finally, the temperature was raised to 310 °C and left to react for 1 h and 10 min. Subsequently, the mixture was left to cool to room temperature, and the NaY:GdF<sub>4</sub>:Yb<sup>3+</sup>,Er<sup>3+</sup> nanoparticles were collected by precipitation in ethanol and centrifugation (8000 rpm, 10 min). The supernatant was removed and the pellet redispersed in ethanol and centrifuged again (5000 rpm, 15 min). This process was repeated three times, after which the precipitate was left to dry overnight. The weight of the resulting nanoparticles was measured, and the particles (10 mg/mL) were stored in hexane at room temperature until further use.

### 2.1.5.1 Wet annealing of upconversion nanoparticles

The dispersibility of the UCNPs was improved increasing the amount of oleic acid molecules surrounding each nanoparticle; this was done *via* a wet annealing protocol.

UCNPs (10 mg/mL in hexane, 10 mL) were added to 20 mL of 1-octadecene and 15 mL of oleic acid in a three-neck flask placed in a heating mantle and equipped with a temperature probe and connected to an argon gas line. The temperature was raised to 80 °C and kept for 1 hour to allow complete evaporation of the hexane under Ar flow. Next, the temperature was increased to 240 °C to allow the surface coverage of the oleic acid ligands. After 2 h, the reaction was cooled down to room temperature and the particles were purified by centrifugation in ethanol (5000 rpm, 15 min, 3x) and allowed to dry.

### 2.1.6 Synthesis of iron oxide nanoparticles

The synthesis of iron oxide nanoparticles was performed in two steps following a literature protocol.<sup>149</sup> First, the precursor Fe(oleate)<sub>3</sub> was synthesised. FeCl<sub>3</sub> (324 mg, 2mmol) was placed in a three-neck round bottom flask and solubilised in a mixture of water and ethanol (ratio 3:4, 6 mL and 8 mL respectively), and then oleic acid (1.9 mL, 6 mmol) and hexane (14 mL) were added. The mixture was left to stir at room temperature for 30 min under Ar flux. The flask was placed in a heating mantle equipped with a probe and a temperature controller. Solid NaOH (240 mg, 6 mmol) was added and the temperature was raised to 70 °C. After four hours, the heating mantle was removed and, upon cooling, the product was isolated using a separating funnel and washed three times with hexane. The so-obtained brown slurry was transferred in octadecene (12.5 mL) and oleic acid (0.5 mL, 1.58 mmol) was added. After solubilisation at room temperature for 30 minutes, the reaction was initiated by increasing the temperature to 320 °C and allowing a reaction time of 1 hour. After cooling, the particles were purified by centrifugation (5000 rpm, 15 min, 3x) and allowed to dry.

## 2.2 Oligonucleotide Functionalisation of Nanoparticles

The different protocols to create a dense layer of single stranded DNA sequences on the surface of gold and silver nanoparticles is reported in the following **Sections 2.2.1** and **2.2.2**. The oligonucleotide attachment on NaYF<sub>4</sub> and Fe<sub>2</sub>O<sub>3</sub> nanoparticles is illustrated in **Sections 2.2.3** and **2.2.4**. Oligonucleotides used in this work are reported in **Table 2.1** below.

**Table 2.1** DNA sequences used in this work. Molecular structures of carbazole modification (indicated as **Z**), SH-C<sub>3</sub>H<sub>6</sub> and aminohexyl (positioning indicated as **X**) are shown in **Figure 1.4**.

Abbreviation	Sequence and Modification
Res1	3'-X-TTT TTT TTT TTT TTT-TAA CCT AAC CTT CAT-5'
Res2	3'-X-TTT TTT TTT TTT TTT-ATG AAG GTT AGG TTA-5'
Res1c	3'-SH-C <sub>3</sub> H <sub>6</sub> -TTT TTT TTT TTT TTT-TAA CCT AZAC CTT CAT-5'
Res2c	3'-SH-C <sub>3</sub> H <sub>6</sub> -TTT TTT TTT TTT TTT-ATG AAG GTGT AGG TTA-5'

### 2.2.1 Surface modification of spherical metallic nanoparticles with a dense shell of oligonucleotides

15 nm gold and silver NPs were functionalised with a dense layer of synthetic oligonucleotides using a well-established salt-aging protocol.<sup>120</sup> The first step of this procedure required the deprotection of the thiol termination of the synthetic oligonucleotides. The DNA strands (8 nmol, 27  $\mu$ L, molar ratio with nanoparticles equal to NP/ssDNA=1/800) were incubated with TCEP (0.5 M, 5  $\mu$ L) for two hours in ice. After this, the excess TCEP was removed via spin-column chromatography using Sephadex G-25 columns pre-equilibrated in distilled water containing 0.05% Kathon CG/ICP Biocide. The purified and deprotected DNA strands were incubated with gold or silver NPs (1 mL, 10 nM) for additional two hours, followed by the addition of phosphate buffer (0.1 M, pH 7.4) to achieve a final concentration of 0.01 M. The mixture was left to equilibrate in a revolving shaker overnight. A solution of NaCl (2 M) was gradually added (6 additions of 30  $\mu$ L each over 8 hours) to the DNA and NPs mixture to achieve a final concentration of 0.3 M. Each addition was followed by 60 seconds of ultrasonication. The DNA-coated NPs were left shaking overnight and purified by centrifugation in ultrapure water (16400 rpm, 20 min, 3x). After the last centrifugation step, they were dispersed in water or phosphate buffer for further use.

### 2.2.2 Surface modification of large metallic nanoparticles with a dense shell of oligonucleotides

Large (>15 nm) gold and silver nanoparticles were functionalised with a shell of thiol-modified ssDNA, using a salt-aging protocol.<sup>120</sup> In the first step of this procedure the deprotection of the thiol termination of the synthetic oligonucleotides was carried out. The DNA strands (32 nmol, 108  $\mu$ L, molar ratio with nanoparticles equal to NP/ssDNA=1/3200) were incubated with TCEP (0.5 M, 5  $\mu$ L). After two hours in ice, the excess TCEP was removed *via* spin-column chromatography using Sephadex G-25 columns pre-equilibrated in distilled water containing 0.05% Kathon CG/ICP Biocide. The purified and deprotected DNA strands were incubated with gold or silver NPs (1 mL, 10 nM) for additional two hours, followed by the addition of phosphate buffer (0.1 M, pH 7.4) to achieve a final concentration of 0.01 M. The mixture was left to equilibrate in a revolving shaker overnight. A solution of NaCl (2 M, 30  $\mu$ L) was added to the spinning suspensions of NPs in phosphate buffer. After 2 hours, 10 further additions of NaCl (2 M, 30  $\mu$ L) were completed over 8 hours to achieve a final concentration of 0.3 M. Each addition was followed by 60 seconds of ultrasonication. The DNA-coated NPs were left shaking overnight and purified by centrifugation in ultrapure water (10000 rpm, 20 min, 3x). After the last centrifugation step, they were dispersed in water or phosphate buffer for further use.

### 2.2.3 Surface modification of UCNPs and IONPs with synthetic oligonucleotides

After the synthesis, lanthanide-doped NaYF<sub>4</sub> and iron oxide NPs are covered with a layer of oleic acid molecules. To attach DNA on the NPs surface, nanoparticles should be water-soluble and have availability of COOH ends on their surface to allow for an EDC/NHS coupling reaction to occur (**Section 2.2.4**). To achieve these requirements, two different chemical strategies were employed: the ligand exchange with the hydrophilic polymer polyacrylic acid, PAA (**Section 2.2.3.1**) and the surface carboxylation *via* previous silanisation and amination steps (**Section 2.2.3.1**).

#### 2.2.3.1 PAA ligand exchange

The oleic acid ligands on the surface of UCNPs and IONPs were replaced by the multidentate hydrophilic polymer polyacrylic acid (PAA) following previously reported protocols.<sup>99,150</sup> PAA (250 mg, MW  $\approx$  1.8 kDa) was dissolved in 3 mL of THF, added to a stirring solution of nanoparticles in THF (10 mg/mL, 5 mL) and left to mix for 96 hours. Purification was performed by three rounds of centrifugation (16400 rpm, 15 min) in ethanol. The particles were stored in borate buffer (1 mM, pH 8.5) to a final concentration of 2 mg/mL at 4 °C.



### 2.2.3.2 Carboxylation *via* silanisation and amination

The first step of the functionalisation is the silica coating of the NPs' surface via base-catalysed polymerisation of tetraethyl orthosilicate (TEOS) in reverse water-in-oil microemulsion. Initially, the surfactant IGEPAL CO-520 (500 mg, MW) was dissolved *via* sonication in 10 mL of hexane containing nanoparticles (40 mg). Subsequently an ammonium hydroxide solution (100  $\mu$ L, 35% v/v) was added and the solution was sonicated until a clear homogeneous suspension was obtained. TEOS (75  $\mu$ L) was added to the emulsion, which was left to stir overnight. The silica-coated NPs were centrifuged and washed with ethanol (5000 rpm, 15 min, 3x) to remove excess reagents.

In the second step, the NPs@SiO<sub>2</sub> were chemically modified with amino groups on the surface. The amino-enriched silane reagent (APTMS, 150  $\mu$ L, 0.068 mmol) was added to a suspension of the NPs@SiO<sub>2</sub> in ethanol (10 mg/mL, 4 mL) and allowed to react overnight. Three rounds of centrifugation in ethanol (5000 rpm, 15 min) were performed to remove excess reagents.

For the third stage, the NPs@SiO<sub>2</sub>-NH<sub>2</sub> were dispersed in dry DMF (2 mg/mL, 5 mL) and 3 mL of succinic anhydride (150mg, 1.5 mmol in dry DMF) was added dropwise. The reaction was left stirring overnight under Ar. Three centrifuge rounds in ethanol (5000 rpm, 20min) were performed and the NPs@SiO<sub>2</sub>-COOH were either stored in ethanol or dispersed in borate buffer (1 mM, pH 8.5) at a concentration of 2 mg/mL for further functionalisation.

### 2.2.4 Oligonucleotide attachment on UCNPs and IONPs

Oligonucleotide attachment on UCNPs and IONPs was carried out exploiting the NHS-EDC coupling chemistry (more discussion on this can be found in **Sections 3.3.4.1.4** and **3.3.4.2.4**). 1-Ethyl-3-(3-dimethylaminopropyl)carbodiimide (EDC) (1.15 mg, 191.70 g/mol) was dissolved in MES buffer (20 $\mu$ L, 0.1 M, pH 6) to a final concentration of 0.3 M and in a separate vial N-hydroxysulfosuccinimide sodium salt (Sulfo-NHS, 2.6 mg, 217.13 g/mol) was dissolved in MES buffer (40  $\mu$ L, 0.1 M, pH 6) also to a final concentration of 0.3 M. Both solutions were mixed, sonicated and added to a borate buffer solution of nanoparticles (2 mg/mL, 1 mL). The mixture was shaken for 1 h and the oligonucleotide of choice was added in excess (15 nmol, 40  $\mu$ L). The reaction was left to shake overnight and subsequently purified by centrifugation in ultrapure water (16400 rpm, 15 min, 3x). The pellet was collected and dispersed in ultrapure water (1 mg/mL) and stored at 4 °C.

## 2.3 DNA-Nanoparticles Assemblies

Nanoparticles were assembled by modifying previously reported literature protocols.<sup>133,134</sup> Two approaches were exploited: the annealing at constant temperature (**Section 2.3.1**) and the slow cooling procedure (**Section 2.3.2**).

### 2.3.1 Annealing at constant temperature

In this protocol, the DNA hybridisation is allowed by keeping the DNA-coated NPs at a constant temperature slightly below or above the DNA duplex melting temperature (see **Section 1.1.2.1** for further details). Two batches of NPs (10 pmol, 1 mL each) functionalised with complementary DNA strands were incubated in a NaCl solution (1 mL, 0.3 M). They were pre-annealed above the DNA melting temperature for 20 minutes and then let cool overnight. After that, the suspensions were annealed at constant temperature (ranging from 45 to 65 °C) close to the melting temperature for two hours in a thermomixer and then removed. After particles' assembly at the bottom of the tube, the supernatant was removed and fresh NaCl (1 mL, 0.3 M) was added.

### 2.3.2 Slow cooling procedure

Two batches of NPs (10 pmol, 1 mL each) decorated with complementary DNA strands were incubated in hybridization buffer (10 mM Phosphate buffer, NaCl 0.3 M) at a temperature above the melting temperature of the DNA duplex (typically 70°C) and slowly cooled down to 25°C using a programmable Applied BioSystems ProFlex™ PCR thermal cycler (0.1°C/10 min). When a pellet was present, the supernatant was removed and fresh NaCl (1 mL, 0.3 M) was added.

### 2.3.3 Silica embedding for imaging

To prevent the collapse of the nanostructure during SEM imaging, DNA-NPs crystals were encapsulated in a silica shell.<sup>135</sup> The as-synthesised SLs were transferred in a 1.5 mL tube and the volume was brought 1 mL with NaCl 0.3 M. N-Trimethoxysilylpropyl-N,N,N-trimethylammonium chloride (TMSPA, 50% methanol, 2 µl) was added to the shaking (700 rpm) suspension of SLs, to allow the electrostatic binding of the ammonium to the negatively-charged phosphate backbone of the DNA. After 20 minutes, a silica growing agent, either triethylsilane, TES, or tetraethyl orthosilicate, TEOS, was added (4 µl, 99% v/v). After four days of shaking, the supernatant containing excess of silica was very carefully removed, and the mixture was purified by three rounds of centrifugation (700 rpm, 5 minutes) and redispersed in 1 mL of water.

## 2.4 Light-induced crosslinking and denaturation experiments

DNA crosslinking was performed by transferring 200  $\mu\text{l}$  of assembled DNA-NPs SLs on a plate in an ice-bath and placed under UV-A light (centred at  $\lambda = 365 \text{ nm}$ ) for 30 minutes at a power of 50  $\text{mW}/\text{cm}^2$  and at a distance of 4 cm from the UV lamp. DNA de-crosslinking was carried out under UV-B irradiation (centred at  $\lambda = 312 \text{ nm}$ , power 50  $\text{mW}/\text{cm}^2$ , 30 min). The de-crosslinked SLs samples were transferred to DNA denaturing conditions by addition of urea (7 M, 200  $\mu\text{l}$ ) followed by ultrasonication and heating above the DNA melting temperature (70  $^{\circ}\text{C}$ ). The decrosslinking/denaturing step was repeated twice to allow full dissolution of the crystals. DNA-functionalized NPs obtained from the decrosslinking/DNA denaturation procedure were purified by centrifugation (16400 rpm, 10 min).

## 2.5 Characterisation Techniques

DNA, nanoparticles, DNA-coated nanoparticles and their assemblies were characterised using a variety of spectroscopies (**Section 2.5.1**), structural (**Sections 2.5.2** and **2.5.5**) and morphological (**Section 2.5.4**) analytic techniques.

### 2.5.1 Spectroscopic techniques

#### 2.5.1.1 UV-Visible spectroscopy

The concentrations of gold and silver NPs were determined by monitoring the absorption maximum over a wavelength range of 200 to 800 nm. Spectra were collected using a black low volume quartz cuvette (optical path length 1 cm) using a 2600 Shimadzu UV-vis spectrophotometer.

#### 2.5.1.2 Oligonucleotides melting curves

The DNA melting temperatures were determined by monitoring the variation of the absorbance at 260 nm for the dehybridisation/hybridisation of a DNA duplex (see **Section 1.1.2.1** for theoretical background). Two complementary oligonucleotides (10 pmol each) were mixed in hybridisation buffer (1 mL, phosphate buffer 0.01 M, NaCl 0.3 M) and transferred in a Suprasil quartz absorption cuvette. Using a Cary 300 Bio UV-Vis spectrophotometer equipped with a thermal cell connected to an external controller (Agilent Technologies), the temperature was firstly raised to 90  $^{\circ}\text{C}$  and then decreased to 25  $^{\circ}\text{C}$  (rate 1  $^{\circ}\text{C}/\text{min}$ ) and the variation of the absorbance at 260 nm was monitored.

### 2.5.1.3 DNA density on gold nanoparticles

After the functionalisation of the AuNPs, the number of successfully attached thiol-modified nucleotides was quantified by dissolution of the gold core. A solution of KI/I<sub>2</sub> (ratio of I<sub>2</sub> to KI 1:6, 5 µL) was slowly added to the ssDNA-coated AuNPs to induce the dissolution of the core until a colour change from wine red to bright yellow was visible. The solution was then made up to 1 mL using ultrapure water and loaded onto a NAP 10 desalting column. After 1 mL of the solution had entered the column it was eluted using an additional 1 mL of ultrapure water and 1.5 mL were collected for UV analysis. The oligonucleotide optical density (O.D.) was measured at 260 nm on a DeNovix DS – 11 spectrophotometer and the concentration calculated using the Beer-Lambert Law.

### 2.5.1.4 DNA density on silver nanoparticles

The number of oligonucleotides attached to spherical AgNPs was determined *via* dissolution of the metal core. A solution of KCN (0.1 M, 5 µL) was slowly added (1 µL per addition) to the oligonucleotide-coated silver suspensions (100 nM, 100 µL) until the dissolution of silver was testified by the disappearance of the yellow colour to yield a colourless solution. The solution was brought to an overall volume of 1 mL using ultrapure water and loaded onto a NAP 10 desalting column. After 1 mL of the solution had entered the column it was eluted using an additional 1 mL of ultrapure water and 1.5 mL were collected for UV analysis. The oligonucleotide optical density (O.D.) was measured at 260 nm on a DeNovix DS – 11 spectrophotometer and the concentration calculated using the Beer-Lambert Law.

### 2.5.1.5 Fluorescence measurements of upconversion nanoparticles

Upconversion fluorescence of a suspension of UCNPs was measured in a manually aligned setup with a continuous wave 980 nm 300mW diode laser (Thorlabs) as excitation source, a SpectraSuite Spectrometer (OceanOptics, USA) and a single photon counting avalanche detector (id100, ID-Quantique, Switzerland). The emitted fluorescence was collected at an angle of 180° to the excitation beam using a 35mm focal length lens and was analysed using a fibre-coupled grating spectrometer (USB4000, OceanOptics, USA). A short pass IR-blocking filter (FGS900) and a narrowband optical filter centred at 545nm (Thorlabs) were used to suppress scattered excitation light and select only the fluorescence emission. Specimen samples were prepared by transferring 1 mL of UCNPs (1 mg/mL in hexane) in a quartz cuvette and each measurement was performed with 1 second of integration time and 10 scans to average and at least three independent datasets were collected. A schematic drawing of the set-up can be found in **Section 5.3**.

### 2.5.1.6 Fourier-transform infrared spectroscopy

The successful ligand exchange and DNA attachment via EDC/sulfo-NHS coupling on UCNPs and IONPs was confirmed *via* Attenuated Total Reflectance Fourier Transform infrared (ATR-FTIR) spectroscopy. In detail, 5 mg of PAA-coated NPs and DNA-coated NPs were analysed on a Nicolet iS5 FT-IR Spectrometer (Thermo Fisher). Each spectrum was taken at room temperature, 10 seconds scan time.

### 2.5.2 Gel electrophoresis

Native 8 % polyacrylamide gels were prepared by mixing acrylamide monomer solution (10.5 mL, 40% wt/V), TBE buffer (14 mL, 5x) and ultrapure water (45.5 mL). N, N, N', N'-tetramethylethylene diamine (56  $\mu$ L) was added as a catalyst and amine persulfate (560  $\mu$ L, 10 % wt/V) as an initiator. Denaturing 8% polyacrylamide gels were made by adding urea (29.4 g, 8 M) to an acrylamide monomer solution (14 mL, 40% wt/V), TBE buffer (14 mL, 5 x) and ultrapure water (up to 70 mL). The polymerisation was then initiated by adding N,N,N',N'-tetramethylethylenediamine (45  $\mu$ L) as a catalyst and amine persulfate (450  $\mu$ L, 10 % wt/V) as an initiator. The gels mixture was quickly casted between two glass plates and a comb was inserted to create wells. After 2 hours of polymerisation, the gel was placed in a bath of 1 x TBE running buffer, the comb was removed and the wells were filled with running buffer. Electrodes of the PROTEAN II xi Cell from BioRad were connected and samples prepared as following were loaded in the gel's wells. Samples were prepared by mixing an equimolar ratio of the desired DNA strands in buffer (10 $\mu$ L, phosphate buffer 0.01 M, NaCl 0.3 M or MgCl<sub>2</sub> 15 mM) in a final volume of 50  $\mu$ L. The hybridisation was conducted by heating up the mixture for 5 minutes at 75 °C and cooling down to room temperature. When using denaturing conditions after hybridisation, samples were mixed with a solution of formamide (1/2 of the final volume) and heated up to 75 °C for 10 minutes before being chilled in an ice bath. A solution of ficoll, high-mass polysaccharide (20  $\mu$ L, 15% in 3x TBE), was added to increase the density of the samples. Samples were loaded and the gel was run at 110 W for 2 h. To visualise the strands, the gel was immersed in 200  $\mu$ L of ultrapure water containing the Diamond™ Nucleic acid dye (20  $\mu$ L). After 10 minutes, the gel was rinsed with water and imaged using the Gel Doc EZ system from Bio-Rad.

### 2.5.3 Thermogravimetric analysis

Thermogravimetric analysis was performed using a TG 209 F1 Libra (Netzsch). In a typical experiment, ~ 10 mg of a dried sample were loaded in an alumina crucible and heated from room

## Experimental Procedures

temperature to 900°C at a rate of 10°C/min under an air atmosphere (flow 50 mL/min) and the mass variation was measured with the in-built scale.

### **2.5.4 Microscopy techniques**

The morphology of the synthesised materials was analysed by Transmission Electron Microscopy (TEM) and Scanning Electron Microscopy (SEM). Details about these techniques can be found in section.

#### **2.5.4.1 Transmission electron microscopy**

For TEM imaging of the synthesised nanoparticles, a diluted specimen droplet was deposited and evaporated on a 400 Mesh Copper grid coated with a Formvar and a carbon film to make the surface hydrophobic. Visualisation of gold nanoparticles and their assemblies was performed using a Hitachi H7000 TEM, operating voltage: 75kV or Hitachi H7700, operating voltage 100kV. Images of the particles were analysed using the ImageJ software and the data were plotted using Origin software to obtain size distribution histograms.

#### **2.5.4.2 Scanning electron microscopy**

SEM images of the superlattices were obtained either on a Jeol JSM 7500F Field-Emission Gun SEM, with resolution of 1 nm at 15kV, operating between 0.5 and 30kV, or on a JEOL JSM 6500F Field-Emission Gun SEM, with resolution of 1.5 nm at 15kV, operating between 0.5 and 30kV. The instrument is equipped with an Oxford Instruments INCAx-act x-ray detector, which allows for Energy-Dispersive X-Ray Spectroscopy.

Samples were prepared by dropcasting a droplet (ca. 10  $\mu$ L) of the specimen onto a silicon wafer chip (Agar Scientific) and allowed to dry.

In some cases, to facilitate the visualisation, a thin layer of metallic gold was spin coated onto the silicon chip using a Quorum Mini Sputter Coater/Glow Discharge System SC7620, operating at 18 mA for 30 seconds to obtain a layer thickness of  $\sim$ 5 nm.

#### **2.5.4.3 Optical microscopy**

Optical microscope images were obtained on a Bresser Biolux NV 20x-1280x Microscope, equipped with 3 objectives (4x, 10x and 40x) and 2 changeable wide field eyepieces (5x and 16x) which allow to achieve a magnification range from 20x to 1280x. The white light source was a 6-step dimming LED, which included a condenser lens.

## 2.5.5 Scattering techniques

### 2.5.5.1 Zeta potential

Electrophoretic mobility and zeta potential measurements were performed using a Malvern Zetasizer Nano ZS with a He-Ne light source at 633 nm wavelength and collection angle 173°. Each measurement was performed loading 1 mL of the colloidal sample in a disposable folded capillary cell and recording 10 sub-runs for three times.

### 2.5.5.1 Powder X-rays diffraction

Powder X-rays diffraction data were collected on a Bruker D2 phaser in the angular range  $2\theta = 20\text{--}80^\circ$  with an angular accuracy of  $\pm 0.02^\circ 2\theta$ . A copper detector is used with the Cu  $K\alpha$  at a wavelength of 0.15418 nm. The generated X-Rays were filtered using a nickel  $K\beta$  filter to obtain monochromatic X-rays with only  $K\alpha$  wavelength. The beam of electrons was accelerated in the vacuum tube at a potential of 30 kV with a 10 mA value of current. The  $2\theta$  values were scanned from  $20^\circ$  to  $80^\circ$  with a  $0.02^\circ$  increment and 2 s step time. In a typical experiment,  $\sim 10$  mg of powdered sample were smeared on a glass sample holder, assuring a flat upper surface. The sample was placed on a motorised stage in a chamber and the intensity of diffracted X-rays was continuously recorded as the sample and detector rotated through their respective angles. A peak in intensity occurs when the powder contains lattice planes with d-spacings appropriate to diffract X-rays at that value of  $\theta$  (**Appendix A.2.6** for the theoretical explanation).

### 2.5.5.2 Small-angle x-ray scattering

Small-angle X-Ray scattering was used to characterise the nanoparticles arrangement of the superlattices (see **Appendix A.2.7** for the relevant theory behind this technique).

SAXS measurements were performed at the Complex Materials Scattering (CMS) beamline of the National Synchrotron Light Source II (NSLS-II, Brookhaven National Lab, Upton, USA). Samples in buffer solution were loaded into glass capillaries and set onto a sample stage for scattering under ambient conditions and an exposure time of 30 s. The SAXS detector was a Pilatus 2M detector from Dectris, the detector distance was 5.02 m, the wavelength used was 0.918 Å with current at 13.5 KeV. The scattering angle was calibrated using silver behenate as a standard. The scattering data were converted to 1D scattering intensity vs. wave vector transfer,  $q$ . The structure factor  $S(q)$  was calculated as the ratio between the background corrected 1D scattering intensities extracted by angular averaging of CCD images for assembled systems and dissociated particles.





## Chapter 3 Programmed Assembly of Nanoparticles

Over the last decades, the fabrication of functional materials has been greatly enabled by the capability to synthesise and assemble different nanoparticles with precise control over shape, size and surface chemistry. The ability to direct the organisation of colloidal nanomaterials has been significantly boosted using DNA as a scaffold to arrange particles into complex assemblies.

In the following chapters, DNA-directed, light-stimulated extended superlattices of gold or silver NPs are synthesised and characterised (**Chapter 4**), along with heterogeneous assemblies of gold nanoparticles with lanthanide-doped NaYF<sub>4</sub> (**Chapter 5**).

This Chapter includes the results and discussion for i) the synthesis of the various types of nanoparticles (**Section 3.1**), ii) their functionalization with oligonucleotides (**Section 3.3**), iii) the self-assembly of nanoparticle superlattices driven by nucleic acids (**Section 3.2**) and iv) the characterisation of these mesoscale materials (**Section 3.4**).

### 3.1 Synthesis of nanoparticles

#### 3.1.1 Spherical gold nanoparticles

Spherical gold nanoparticles with an average size of 14 nm were synthesised according to the Turkevich method.<sup>23,24</sup> This method is based on the reduction of Au(III) to metallic Au(0) by trisodium citrate, which acts both as reducing and stabilising agent. AuNPs of size ranging between 10 to 20 nm can be obtained (**Sections 2.1.1** and **2.1.2**). **Figure 3.1** shows a representative transmission electron micrograph of gold nanoparticles. Size distribution of  $14 \pm 1$  nm was obtained by analysing  $\approx 2000$  particles over multiple high resolution TEM images using ImageJ software and plotted as histograms with OriginLab software.

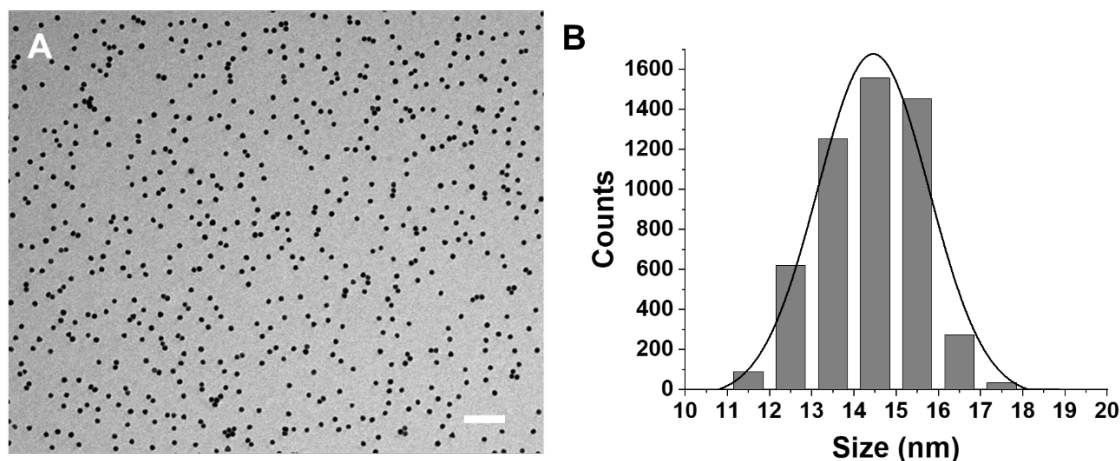


**Figure 3.1** In (A) a representative low magnification TEM image shows the uniformity of size and shape of citrate-coated AuNPs. The size distribution histogram (B) was calculated by measuring >2000 citrate coated AuNPs over multiple high resolution micrographs. The average size resulted in  $14 \pm 1$  nm. Scale bar 200 nm.

UV-Vis spectroscopy was used to monitor the stability and monodispersity of nanoparticles, as well as to calculate the concentration of every freshly synthesised batch of particles. In **Figure 3.2**, the spectrum of AuNPs is displayed, showing a narrow LSPR peak at 522 nm, characteristic for 14 nm NPs.<sup>151</sup>

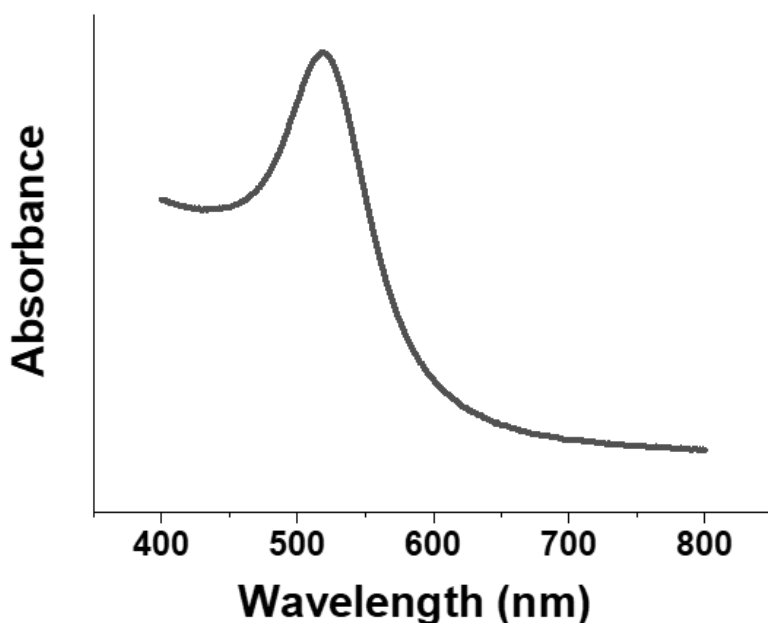


**Figure 3.2** Normalised UV-vis spectrum of AuNPs 14 nm, showing a sharp and well-defined LSPR peak with maximum at 522 nm.

Larger gold nanoparticles were also synthesised via a seed-mediated growth approach (experimental in **Section 2.1.2**). In this strategy, gold seeds are firstly synthesised by citrate reduction of Au(III) at 100 °C; next, the temperature is lowered to 90 °C and more gold and citrate precursors are added.<sup>33</sup> By lowering the temperature, the formation of new seeds is prevented and, consequently, the growth of the existing ones is favoured. **Figure 3.3** shows AuNPs at different growth stages: the initial seeds (**A**), the first generation (**B**) and the second generation (**C**). The average size distributions were measured and corresponding histograms are reported in **Figure 3.3**, showing an average size of  $15 \pm 1$  nm for the seeds,  $21 \pm 2$  nm for the first growth and  $45 \pm 5$  nm for the second growth, calculated on  $\approx 1000$  NPs from multiple high resolution TEM images.

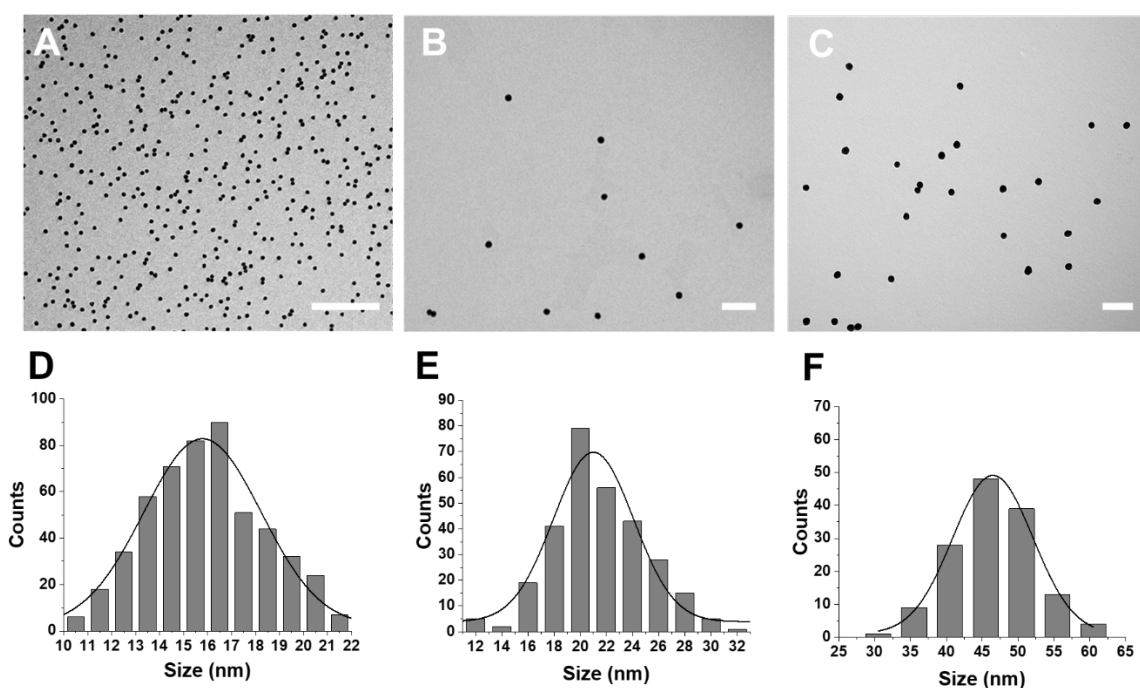


**Figure 3.3** Transmission electron micrographs of gold nanoparticles at different stages of the synthesis: seeds (**A**), after one growth step (**B**) and after two growth steps (**C**). Corresponding size distribution histograms for seeds (**D**,  $15 \pm 1$  nm), growth 1 (**E**,  $21 \pm 2$  nm) and growth 2 (**F**,  $45 \pm 5$  nm). Scale bars 200 nm.

The growth of AuNPs was also followed by UV-Vis spectroscopy (**Figure 3.4**). As thoroughly discussed in **Section 1.1.1.3**, the LSPR shows a red-shift as the average diameter of the particles increases.<sup>152</sup> The absence of shoulders or secondary peaks confirmed the synthesis of spherical and homogeneous nanoparticles.

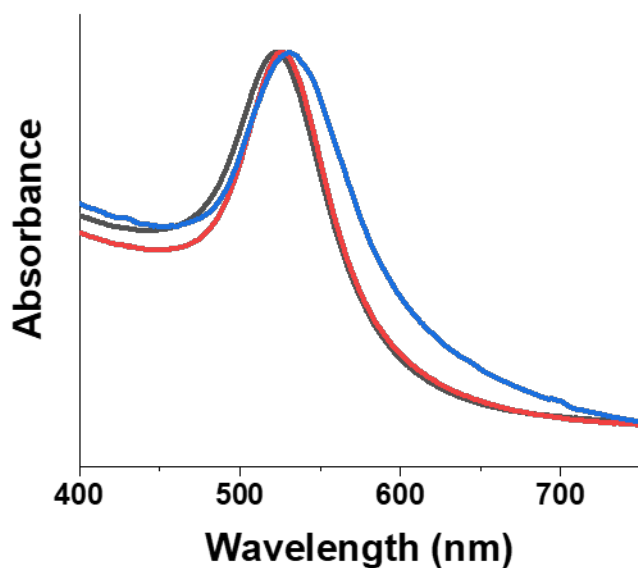


**Figure 3.4** UV-Visible spectra for gold seeds (black), first (red) and second (blue) growth nanoparticles, normalised to the maximum. A distinct red-shift of the maximum LSPR peak is observed as the average size of the AuNPs is increased.

### 3.1.2 Spherical silver nanoparticles

Colloidally stable spherical silver nanoparticles were synthesised using a recently published protocol.<sup>38</sup> In this approach, AgNPs seeds are obtained using trisodium citrate to reduce a Ag(I) salt, and stabilised by addition of tannic acid. By tuning the amount of citrate and tannic acid, silver seeds between 10 and 20 nm can be obtained. **Figure 3.5** shows a representative TEM image and size distribution of a sample of  $15 \pm 6$  nm AgNPs. Size histogram was obtained by analysing  $\approx 600$  NPs over multiple high resolution TEM images.

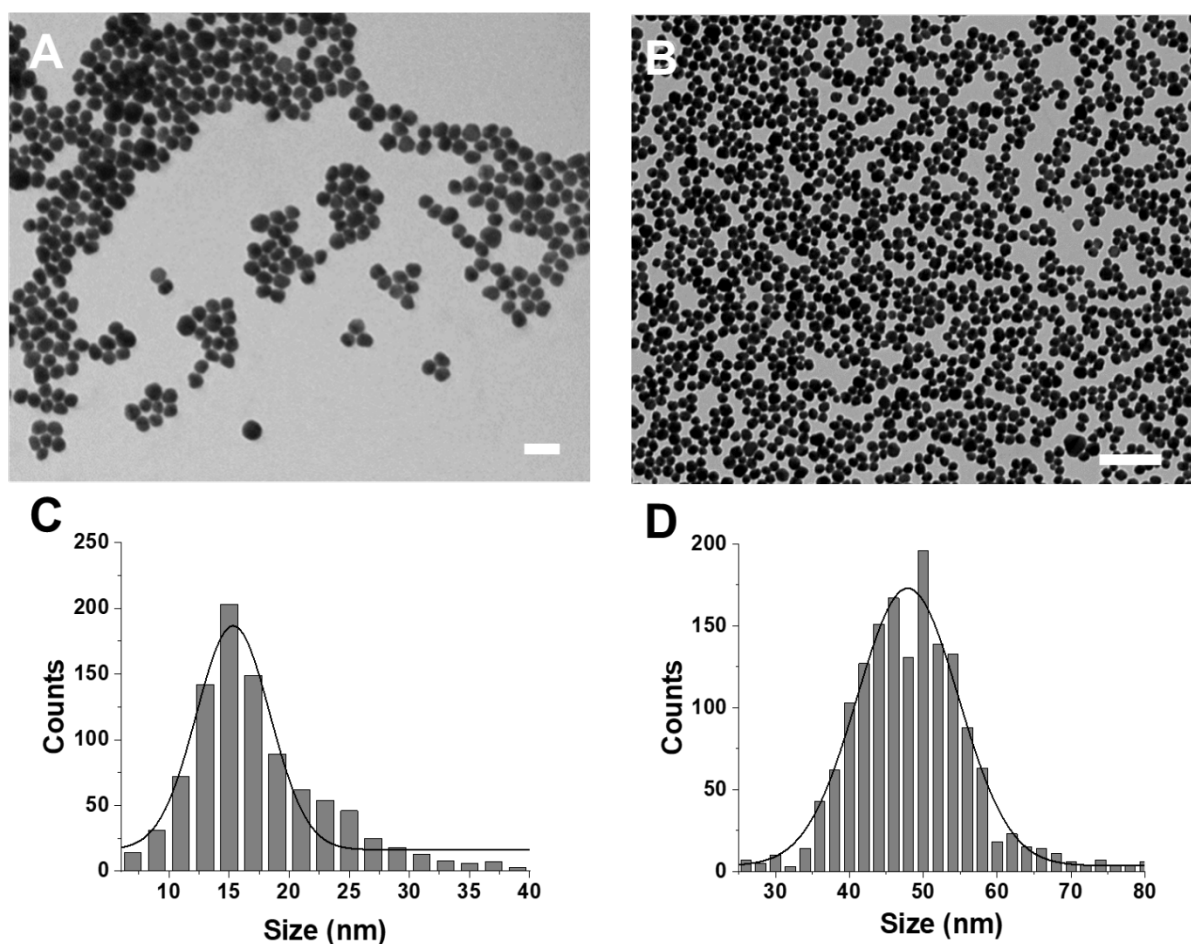


**Figure 3.5** Representative TEM micrograph (A) and size distribution plot (C) for  $15 \pm 6$  nm AgNPs. TEM micrograph (B) and size distribution plot (D) for  $48 \pm 10$  nm AgNPs, after one growth step. Scalebars 50 nm.

The so-obtained AgNPs were used as seeds to grow a first generation of larger particles, executing a single growth step following the experimental protocol reported in **Section 2.1.3**. Representative TEM micrograph of AgNPs after one growth step and corresponding size distribution histogram are reported in **Figure 3.5**. From the measurements of over 500 particles, an average size of  $48 \pm 10$  nm was calculated for spherical silver NPs.

Similar to gold nanoparticles, AgNPs exhibit a strong plasmon resonance in the visible region, which can be used to assess stability, degree of monodispersity and concentration of a batch of AgNPs. In **Figure 3.6**, the relevant normalised UV-vis spectra for seeds and particles after one growth step are reported. The LSPR peak maxima showed a red-shift as the size of the AgNPs increased, moving from 405 nm (Ag seeds) to 413 nm (AgNPs growth 1), in agreement with previous reports.<sup>37</sup>

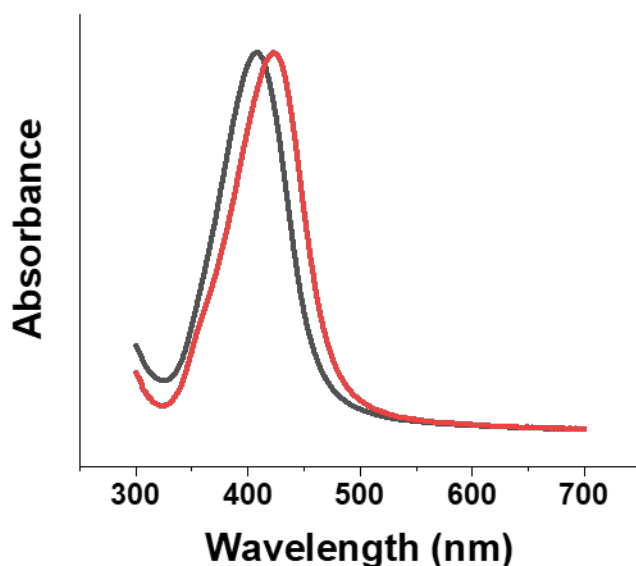


**Figure 3.6** Normalised UV-vis spectra of 15 nm and 48 nm AgNPs, showing the maximum resonance absorbance at 406 and 423 nm respectively.

### 3.1.3 Lanthanide doped NaYF<sub>4</sub> nanoparticles

Lanthanide-doped upconversion nanoparticles (UCNPs) are fluorescent materials made of a host matrix (NaYF<sub>4</sub> or NaY:GdF<sub>4</sub>) intercalated by doping ions (Yb<sup>3+</sup> and Er<sup>3+</sup>). A thorough explanation of their composition and how this affects the optical properties and can be found in **Section 1.1.1.4**. In the present work, UCNPs of different sizes were prepared following a reported coprecipitation protocol<sup>153</sup> with slight modifications (details can be found in **Sections 2.1.4** and **2.1.5**). In the first step of the synthesis, the chloride salts of yttrium, ytterbium, gadolinium and erbium are dissolved in oleic acid and octadecene at 140 °C. During this step is critical to work under argon flow to minimise the oxidation of the oleic acid due to air and allow the formation of the oleate forms of the precursors. After solubilisation, the reaction was allowed to cool to room temperature. Meanwhile, NaOH and NH<sub>4</sub>F were dissolved in dry methanol and added to form the host matrix together with yttrium and gadolinium. This addition is done at RT for multiple reasons. First, it reduced the risk of producing fluorinated compounds, and secondly, to obtain phase-pure β-UCNPs (hexagonal phase).<sup>80</sup> As discussed in **Section 1.1.1.4**, pure β-UCNPs can be produced with high degree of monodispersity and they show superior optical properties in comparison with the cubic α-UCNPs. Methanol was evaporated at 80 °C and the mixture was degassed in vacuum at 100 °C for 30 minutes to ensure the evaporation of any humidity trace. This step is of utmost importance to prevent the oxidation of the oleates, which would change the number of oleic ligands available to bind the surface of the nanoparticles once formed. Oleic acid ligands influence the final morphology of the nanoparticles. In our experiments, the concentration of oleic acid used was selected with the

aim to promote the formation of hexagonal platelet shape nanoparticles. Regulation of the oleic acid concentration can lead to the formation of rods and cubes.<sup>84</sup> The oleic acid ligands are a key factor in controlling the shape of the particles as they are able to direct the preferential growth of specific facets. The shape control of nanocrystals (NCs) during growth is a kinetically controlled process: at high growth rates, ligands that selectively bind a specific NP facet decrease their energy and slow their growth.<sup>154</sup> High-energy facets grow faster than low-energy facets in this kinetic regime and vanish as the NC grows, leading to NCs that are terminated by slow-growing low-energy facets.<sup>155</sup> Different ligand coverages on different NC facets can lead to anisotropic interactions between NCs by changing their effective shape.

After thorough degassing, the solution is quickly (10 °C/min) heated up to 310 °C, to allow the homogeneous growth of the seeds and avoid the creation of secondary nuclei. In **Figure 3.7** a representative TEM image of NaYF<sub>4</sub>:Yb<sup>3+</sup>(20%), Er<sup>3+</sup>(2%) shows the high uniformity in shape and size of the produced hexagonal platelets. Size distribution was evaluated by measuring ≈ 200 particles over multiple TEM images.

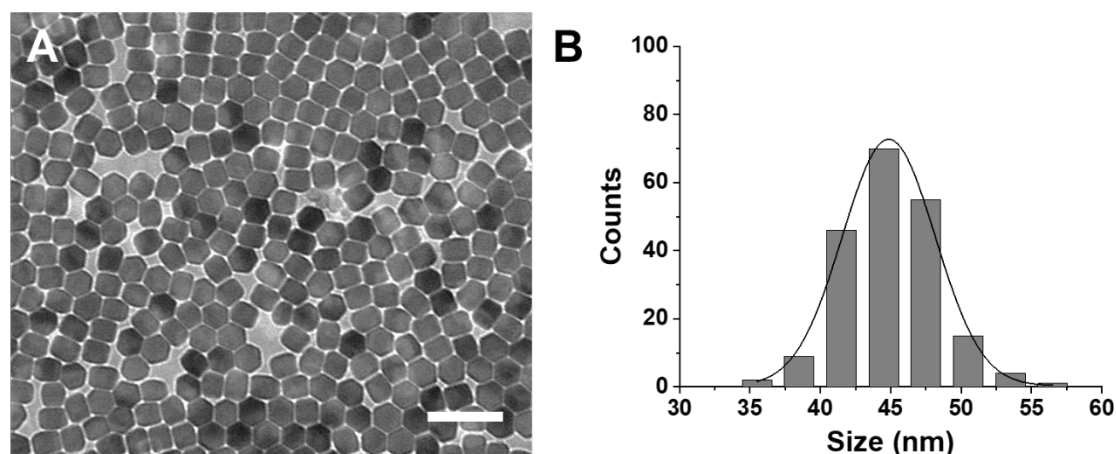


**Figure 3.7** Representative TEM micrograph of NaYF<sub>4</sub>:Yb<sup>3+</sup> (20%), Er<sup>3+</sup> (2%), showing hexagonal particles with average size of 45± 2 nm (A), as depicted in the corresponding size distribution plot (B).

In prevision of combining UCNPs with 15 nm gold nanoparticles in DNA-NPs assemblies, the average size and morphology of UCNPs was tuned by introducing Gd ions in the crystalline matrix to replace part of the yttrium. In **Figure 3.8**, TEM images and corresponding size distributions for NaY(80%)Gd(20%)F<sub>4</sub>:Yb<sup>3+</sup>(20%), Er<sup>3+</sup>(2%) are reported, as well as TEM micrograph and size histograms for NaY(70%)Gd(30%)F<sub>4</sub>:Yb<sup>3+</sup>(20%), Er<sup>3+</sup>(2%). From these, it is clear that if all other factors are kept constant, the introduction of Gd<sup>3+</sup> in different percentages causes a reduction of the size of the single NP. This finding is supported by the literature,<sup>156</sup> where sub-10 nm NPs were synthesised with a matrix of pure gadolinium ions. By replacing the 20% of Y<sup>3+</sup> with Gd<sup>3+</sup> in the crystal lattice, the

## Programmed Assembly of Nanoparticles

average size of NPs decreased from  $44.9 \pm 3.3$  nm to  $27.9 \pm 1.8$  nm (over 250 particles analysed). The size distribution was shifted to even smaller values by replacing 30% of  $Y^{3+}$  with the same amount of  $Gd^{3+}$ , resulting in an average size of  $12.5 \pm 1.5$  nm, calculated by measuring  $\approx 300$  particles over multiple TEM images. The size decrease of UCNPs in presence of gadolinium was attributed to the strong effect of ion on crystal growth rate through surface charge modification. Theoretical calculations<sup>83</sup> have shown that the electron charge density of the crystal surface increases when a  $Gd^{3+}$  ion replaces a  $Y^{3+}$  ion in the crystal lattice. This increased negative charge on the surface of the small nucleation seeds slows down the diffusion of negatively charged  $F^-$  ions to the surface. Consequently, the growth rate is reduced, and this results in a drop of the nanocrystal size, which can be regulated by varying the amount of constituent matrix ions.<sup>83</sup>

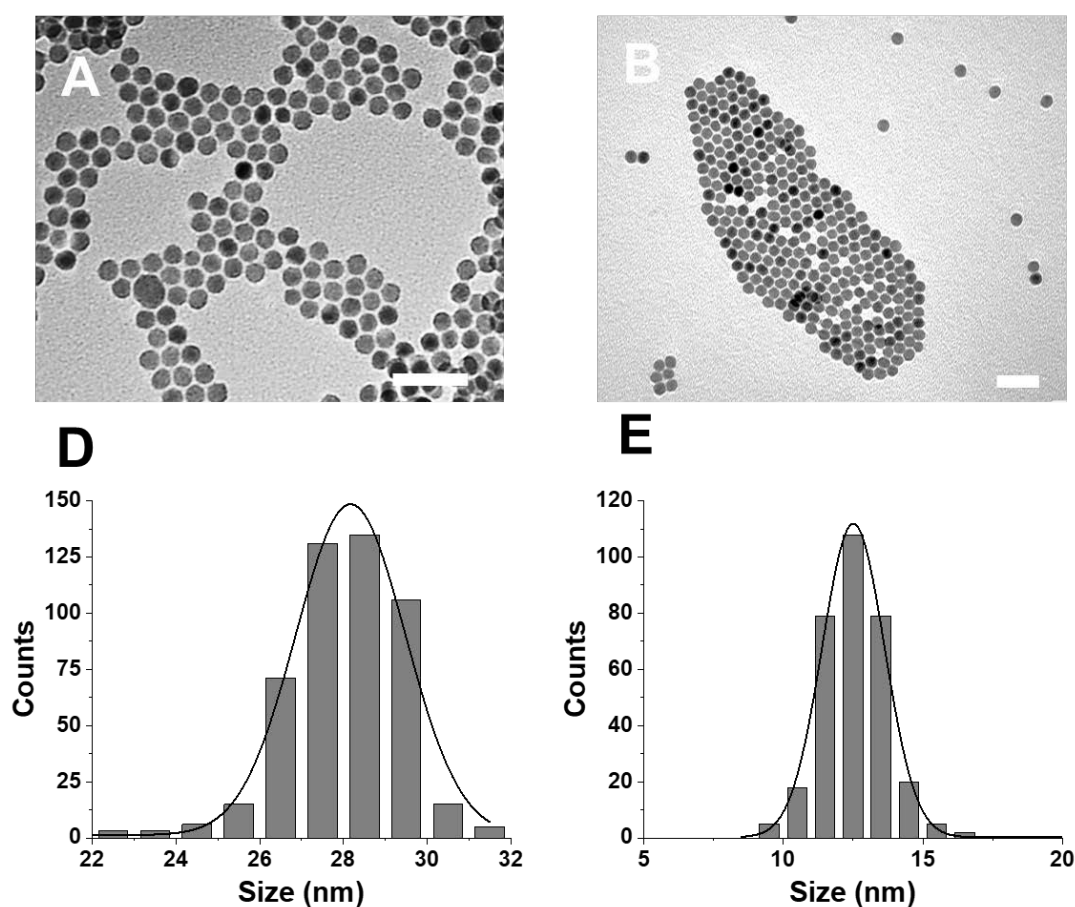


**Figure 3.8** Representative TEM micrograph of  $NaYF_4:Yb^{3+}$  (20%),  $Er^{3+}$  (2%), containing 20% and 30%  $Gd^{3+}$  ions are shown respectively in A and B. Corresponding size distribution histograms are also reported in C (for  $Gd^{3+}$  20%) and D (for  $Gd^{3+}$  30%), showing a size decrease from  $27.9 \pm 1.8$  nm to  $12.5 \pm 1.5$  nm. Scale bars 100 nm.

The presence of  $Gd^{3+}$  in the UCNPs was confirmed by Energy-Dispersive X-ray Spectroscopy (EDX or EDS). This technique is coupled with an electron microscope and allows to reveal the elemental composition of a sample. The spectra obtained from UCNPs  $Gd^{3+}$  0%,  $Gd^{3+}$  20% and  $Gd^{3+}$  30% are



shown in **Figure 3.9**, **Figure 3.10** and **Figure 3.11**. The characteristic energy peaks can be easily identified as following: the matrix elements Y appears with two peaks at 1.9 and 14.968 keV, while Gd can be found at 6.056 keV. The lighter Na and F appear with a single peak (at 1.04 keV and 0.677 keV, respectively), the dopants Yb at 1.526 keV and 7.4 keV, and Er at 1.404 keV and 6.949 keV. In addition to the NCs elements, other peaks attributed to O (0.525 keV), Cu (8.046 keV) and C (0.277 keV) were detected and were attributed to the grid. From the integration of the areas under the corresponding peaks, the weight percentage for each element was calculated. The percentages of the antenna and emitter ions (ytterbium and erbium) remained fairly constant in the three different samples and close to the targeted percentages (20% for ytterbium and 2% for erbium). Conversely, the percentage of the matrix ions varied significantly. The simultaneous addition of gadolinium and subtraction of yttrium during the synthesis, is well represented by the measured percentages, where the amount of  $Gd^{3+}$  increased from 0%, to 23.2% and 28%.

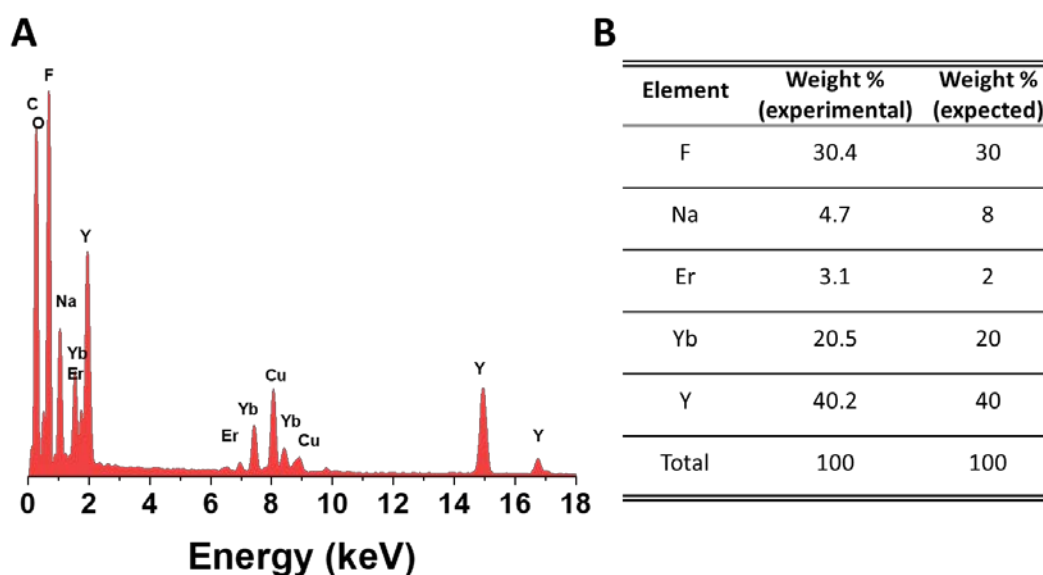


**Figure 3.9** Energy dispersive x-ray elemental analysis for  $NaYF_4:Yb^{+3}, Er^{+3}$ . In A, the full EDX spectrum is reported. From the integration of the peaks relative to each element, the relative weight percentages were calculated. The results are summarised in (B), showing a very good agreement with the expected values (also reported in table B).

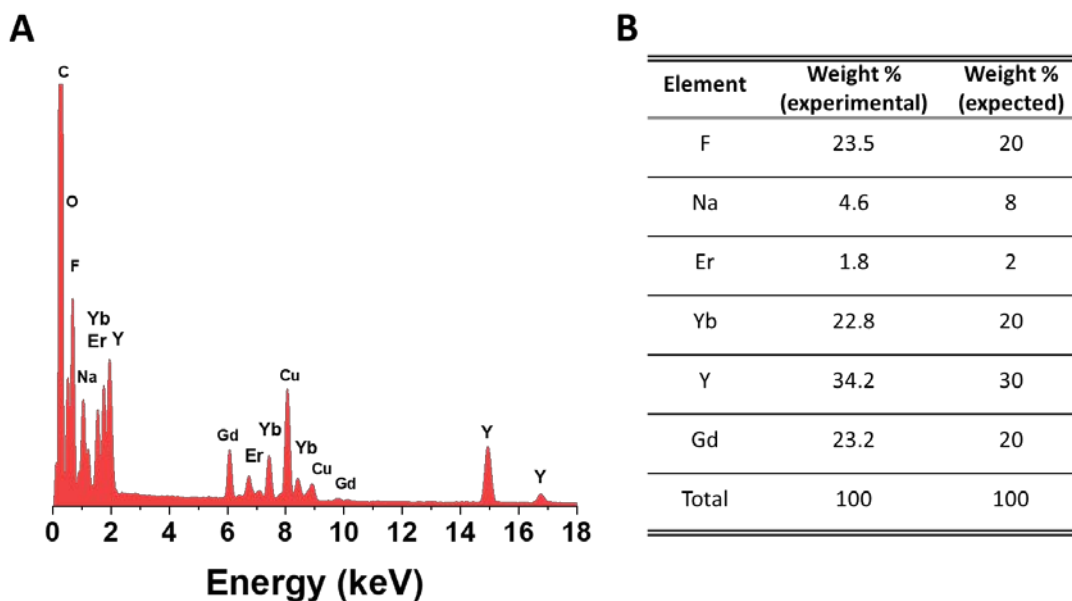


**Figure 3.10** Energy dispersive x-ray elemental analysis for NaY:Gd(20%)F<sub>4</sub>:Yb<sup>+3</sup>, Er<sup>+3</sup>. In A, the full EDX spectrum is reported. From the integration of the peaks relative to each element, the relative weight percentages were calculated. The results are summarised in (B), showing a very good agreement with the expected values (also reported in table B).

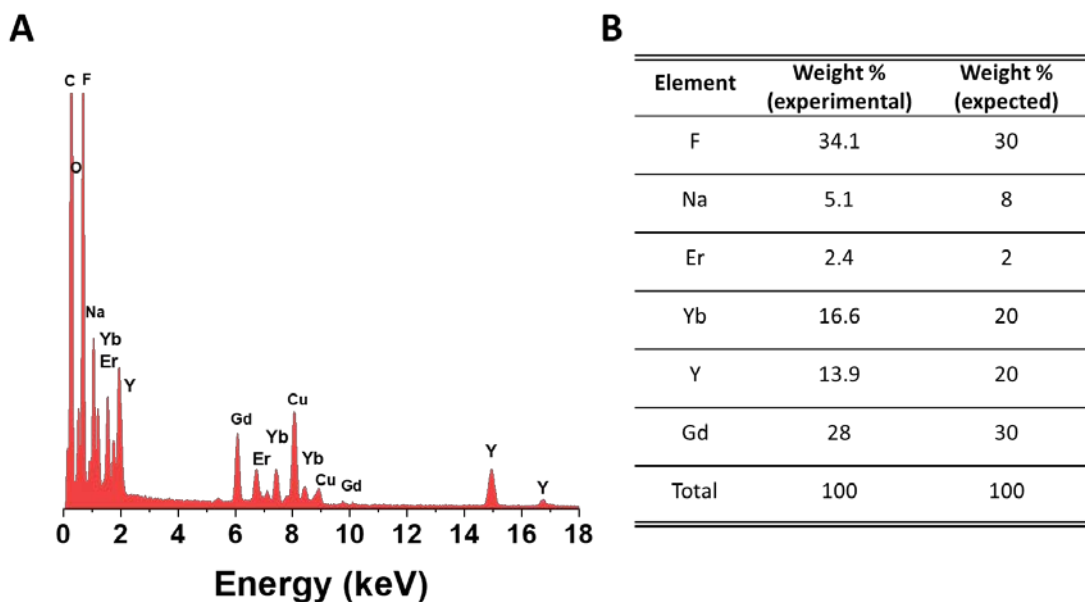


**Figure 3.11** Energy dispersive x-ray elemental analysis for NaY:Gd(30%)F<sub>4</sub>:Yb<sup>+3</sup>, Er<sup>+3</sup>. In A, the full EDX spectrum is reported. From the integration of the peaks relative to each element, the relative weight percentages were calculated. The results are summarised in (B), showing a very good agreement with the expected values (also reported in table B).

X-ray diffraction (XRD) was carried out on the NPs with different percentages of Gd. **Figure 3.12** shows the diffraction patterns for NPs containing 0%, 20% and 30% Gd<sup>3+</sup>, featuring the crystalline planes. In all experiments the crystal lattice was hexagonal, the Bragg spacing between crystal planes was calculated from **Equation 3.1** as an average from three different peaks (*hkl* 200, 111 and 201). From these, the lattice parameters *a* and *c* were calculated rearranging **Equation 3.2**. The obtained lattice parameters are shown in **Table 3.1**. The obtained values are moderately constant, demonstrating that the structure is not affected by the introduction of the gadolinium in the matrix.

**Equation 3.1** Bragg equation for the calculation of the interplane distances. In the equation,  $\lambda$  is the x-rays wavelength (in this case 0.154 nm),  $\theta$  is the Bragg angle at which the peak is found and *hkl* are the corresponding Miller indices.

$$d_{hkl} = \frac{\lambda}{2\sin\theta}$$

**Equation 3.2** The lattice parameters *a* and *c* for an hexagonal lattice can be calculated from the geometry of the unit cell by employing the  $d_{hkl}$  value obtained from Bragg equation. For a plane where the index *l* is equal to zero, the term  $l^2/c^2$  is zero and the parameter *a* can be extrapolated. The obtained value can be then implemented in the equation to calculate *c*.

$$\frac{1}{d_{hkl}^2} = \frac{4(h^2 + hk + k^2)}{3a} + \frac{l^2}{c^2}$$

The size of the smallest crystal domain within the nanoparticle (crystallite) was also calculated from the Debye-Scherrer formula (**Equation 3.3**). The full width half maximum was measured for each well-defined peak in the diffractogram, and the average crystallite size was calculated by averaging the *D* values obtained from different peaks. The size obtained decreased from 20.3 nm (UCNPs 0%Gd<sup>3+</sup>), to 16.3 nm (UCNPs 20%Gd<sup>3+</sup>) and 11.6 nm (UCNPs 30%Gd<sup>3+</sup>). This observation is consistent with the overall nanoparticle shrinkage with increasing gadolinium fraction in the lattice.

**Equation 3.3** Debye-Scherrer formula for the calculation of the crystallite size. *K* is a dimensionless shape factor with a value close to unity (typically 0.9);  $\lambda$  is the x-ray wavelength;  $\beta$  the full width half maximum of a peak and  $\theta$  is the Bragg angle.

$$\tau = \frac{k\lambda}{\beta\cos\theta}$$

**Table 3.1** Lattice parameters and average crystallite size for hexagonal phase UCNPs.

Sample	Lattice parameters (nm)		Crystallite size (nm)
	a	c	
$\text{NaYF}_4:\text{Yb}^{3+}, \text{Er}^{3+}$	$0.68 \pm 0.07$	$0.24 \pm 0.02$	$20.3 \pm 4.3$
$\text{NaY}(80\%)\text{Gd}(20\%)\text{F}_4:\text{Yb}^{3+}, \text{Er}^{3+}$	$0.68 \pm 0.07$	$0.24 \pm 0.02$	$16.3 \pm 1.1$
$\text{NaY}(70\%)\text{Gd}(30\%)\text{F}_4:\text{Yb}^{3+}, \text{Er}^{3+}$	$0.33 \pm 0.07$	$0.26 \pm 0.05$	$11.6 \pm 2.0$

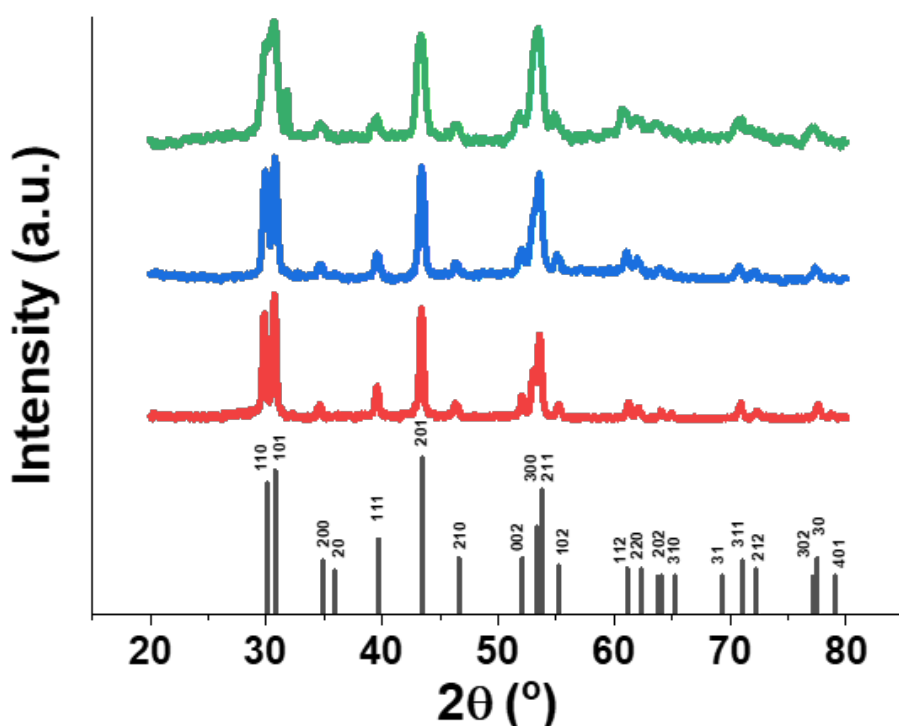


**Figure 3.12** X-rays diffractograms obtained from UCNPs containing 0% (red), 20% (blue) and 30% (green) Gd<sup>3+</sup>. The same hexagonal crystal lattice was obtained for the different gadolinium doping percentages.

Alongside with playing a major role in the size tuning of the NPs, the replacement of yttrium with gadolinium ions also affected the upconversion fluorescence of the NPs. In **Figure 3.13** the spectra for NPs Gd<sup>3+</sup> 0%, 20% and 30% are shown. No peak shifting was observed, proving that the introduction of a different ion did not affect substantially the energy level distribution for the

NaYF<sub>4</sub>:Yb<sup>3+</sup>,Er<sup>3+</sup> NPs. As detailed in the theoretical background **Section 1.1.1.5**, fluorescence phenomena rely mostly on the sensitizer/emitter combination. The antenna of choice, ytterbium (Yb<sup>3+</sup>) is a highly efficient photo-sensitizer with high absorption at 976 nm (transition  $^2F_{7/2} \rightarrow ^2F_{5/2}$ ). The absorbed energy is then transferred to Er<sup>3+</sup>, an activator within the matrix which emits the energy in the visible spectrum, with emissions in the green at 522 nm and 541 nm, corresponding to the transitions  $^4H_{11/2} \rightarrow ^4I_{15/2}$  and  $^4S_{3/2} \rightarrow ^4I_{15/2}$ , and an emission peak in the red at 652 nm ( $^4F_{9/2} \rightarrow ^4I_{15/2}$  transition). In gadolinium-doped systems, the lowest excited level ( $^6P_{7/2}$ ) of Gd<sup>3+</sup> is situated in the ultraviolet region, remarkably higher than most excited levels of ytterbium and erbium ions involved in the upconversion processes. Hence, excitation energy loss through energy transfer from Yb<sup>3+</sup> and Er<sup>3+</sup> to 4f levels of Gd<sup>3+</sup> can be avoided.<sup>157</sup> Besides, the intensity ratio of green and red emission demonstrated a remarkable change as a result of the incorporation of Gd<sup>3+</sup> ions into NaYF<sub>4</sub>:Yb<sup>3+</sup>, Er<sup>3+</sup> host lattice. With increasing percentage of Gd<sup>3+</sup> doping, the UC luminescence efficiency is decreased at 540 nm and 520 nm and enhanced at 656 nm, compared to those without doping. A possible explanation can be provided considering the local distortion induced by the Gd<sup>3+</sup> doping in crystal lattice, thus reducing the site symmetry of the activators. Therefore, the probabilities of different pathways in the ETU process could be changed due to the modified lattice symmetry, unit cell parameters and intra-4f transition probability.

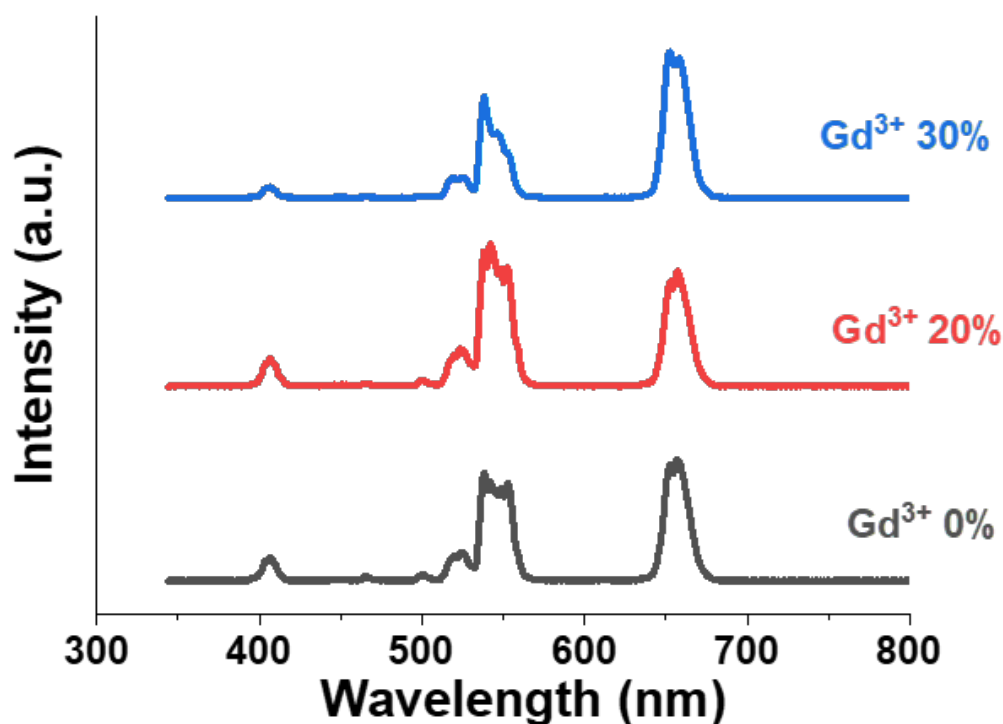


**Figure 3.13** Fluorescence emission spectra for UCNPs containing Gd 0% (black), 20% (red) and 30% (blue). The peak positions and relative ratios are unchanged, since the percentage of erbium and ytterbium is constant in the three samples. Nanoparticles concentration 5 mg/mL.

### 3.1.4 Cubic iron oxide nanoparticles

Fe<sub>2</sub>O<sub>3</sub> nanocubes were synthesised using a thermal decomposition strategy.<sup>158–160</sup> Following this protocol, the iron-oleate precursor was synthesised in a water/hexane mixture, starting from the solubilisation of FeCl<sub>3</sub> in water and sequentially adding ethanol, hexane, oleic acid and NaOH. The mixture was allowed to vigorously stir for 4 hours under controlled argon atmosphere. The iron-oleate complex was formed and it was transferred to the non-polar organic phase (hexane). The complex was purified by extracting the organic phase. The Fe-oleate complex was then decomposed at 320 °C, yielding monodisperse nanocubes. **Figure 3.14** TEM shows images of iron oxide nanoparticles (IONPs) and the corresponding size distribution, calculated by measuring  $\approx 200$  particles over multiple TEM images. The average size of the particles was  $11 \pm 2$  nm (size variation 15%). A variety of crystal structures are available for iron oxide particles, and for this reason a diffraction analysis was carried out.

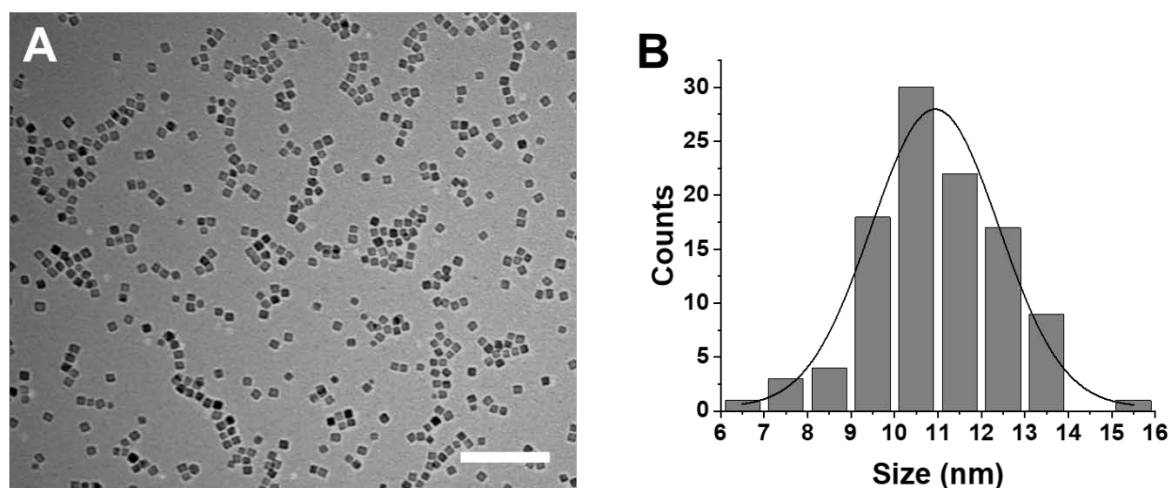


**Figure 3.14** Representative TEM micrograph (A) and size distribution histogram (B) of  $11 \pm 1$  nm IONPs. Scale bar 100 nm.

**Figure 3.15** shows the electron diffraction profile for IONPs. The characteristic peaks for the cubic spinel structure of magnetite were obtained. The average crystallite size was estimated to be  $6 \pm 1$  nm using the Debye-Scherrer formula (**Equation 3.3**). This value is reasonably close to the size measured from TEM images, suggesting that each nanocube constitutes a single crystal domain. This is of special interest as superparamagnetism phenomena are usually observed for single-domain iron oxide nanocrystals.<sup>161,162</sup>

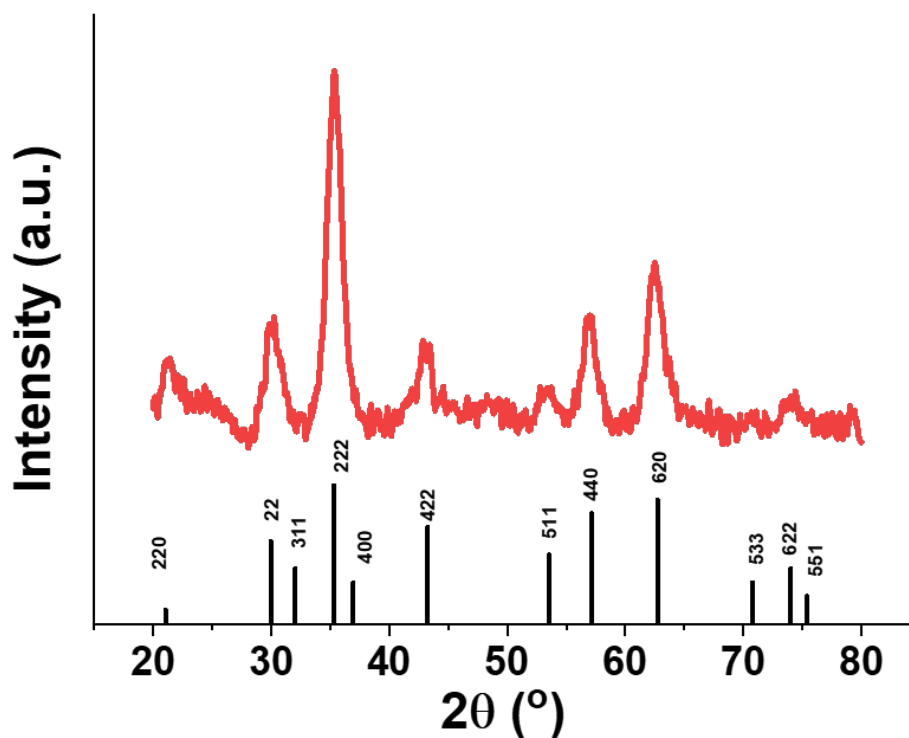


**Figure 3.15** XRD pattern for iron oxide nanoparticles and corresponding predicted peaks for the magnetite structure.

EDX spectroscopy was also performed (**Figure 3.16**). An intense peak appeared at 6.4 keV, confirming the presence of an elevated fraction of iron. The calculated percentage of oxygen is unexpectedly low (4%); this finding was justified considering the close proximity with a secondary peak of Fe, which may have rendered correct integration and evaluation techniques challenging.

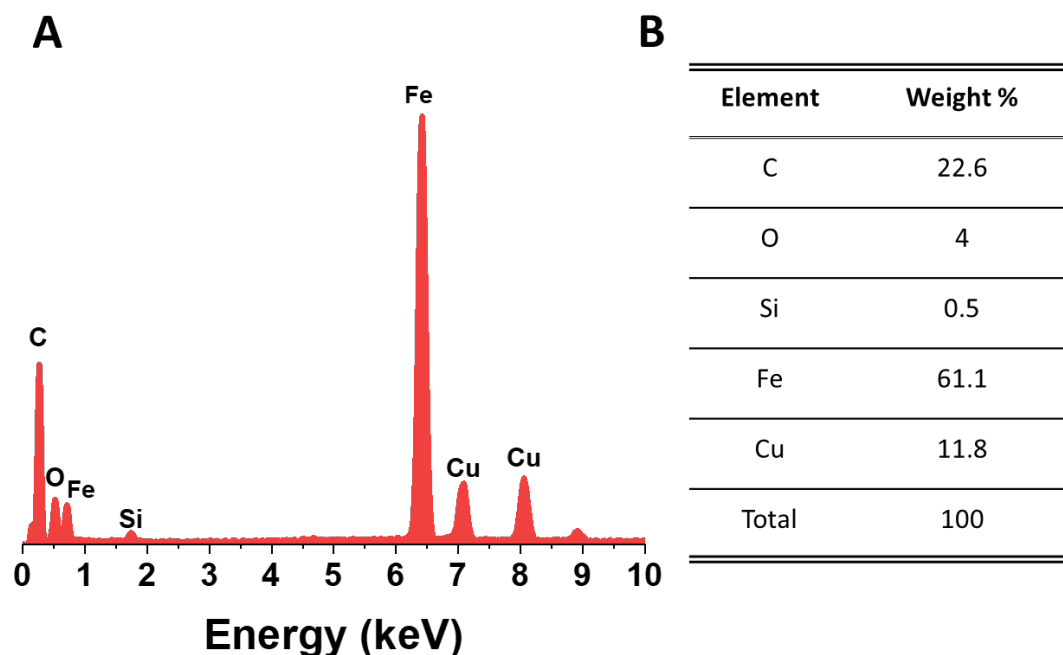


**Figure 3.16** Energy dispersive x-rays elemental analysis for  $\text{Fe}_2\text{O}_3$ . In A, the full EDX spectrum is reported. From the integration of the peaks relative to each element, the relative weight percentages were calculated. The results are summarised in B.

### 3.2 Design and characterisation of synthetic oligonucleotides

For this work, two sets of complementary DNA strands were designed and used to assemble NPs of different chemical compositions. Each oligonucleotide sequence was designed following previously reported experiments to attach the oligos to the various types of nanoparticles and guide their self-assembly in ordered superlattices. The sequences were designed to include an anchoring group in order to bind to the nanoparticle surface. Here, thiol modified oligonucleotides (**Table 2.1**) were employed to bind to the gold or silver nanoparticles' surface and an amine modified oligos were employed to bind to magnetic and upconversion nanoparticles utilizing EDC coupling chemistry (**Section 1.1.2.3**).

The overall length of the strand was tuned according to the NPs size. For example, nanoparticles larger in size required longer oligonucleotide strands to ensure the colloidal stability of the nanoparticle. However very long sequences provided the nanoparticles with a high degree of freedom prohibiting the effective formation of ordered superlattices. It has been experimentally shown that the ideal sequence length for producing crystals has to be comparable with the nanoparticles core diameter.<sup>163</sup>



The complementary region of two oligonucleotides was designed short enough to allow the DNA to hybridise and de-hybridise multiple times in low temperatures. Reconfiguration of nanoparticles allows a higher degree of organization during the formation of superlattices.

Prior attachment on the inorganic cores, the designed DNA strands were characterised by UV-Vis Spectroscopy (**Section 3.2.1**) and polyacrylamide gel electrophoresis (**Section 3.2.2**).

### 3.2.1 DNA Melting curves

The characteristic absorption band of oligonucleotides in the UV region was used to check the duplex formation of complementary single stranded DNA. Specifically, the absorption cross section of DNA duplexes is lower than the corresponding single stranded DNA due to  $\pi$ -stacking of bases in the double helix; this behaviour is known as hyperchromicity effect.<sup>164</sup> A detailed discussion can be found in **Section 1.1.2.1**.

UV melting experiments were performed on DNA strands Res1 and Res2 (30 base pair). Experimentally,  $T_m$  was determined during three heating/cooling cycles in phosphate buffer 0.1 M and NaCl 0.3 M (see **Section 2.5.1.2** for experimental protocol). **Figure 3.17** presents the melting profile for Res1+2, resulting in 56.6 °C, a value in good agreement with the predicted 54.5 °C, calculated by using the nearest neighbour approximation of the OligoCalc tool (<http://biotools.nubic.northwestern.edu/OligoCalc.html>).

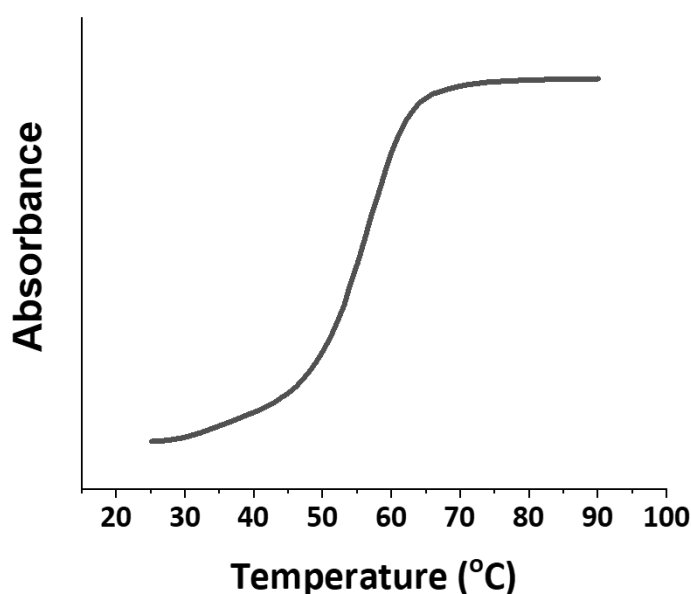


**Figure 3.17** Average melting curves of thiol-terminated Res1+Res2, determined over three heating/cooling cycles in the range 25-90 °C. The melting curve resulted in 56.6 °C.

### 3.2.2 Polyacrylamide gel electrophoresis

After determining the oligonucleotide stability and hybridisation properties using UV Visible spectroscopy, the hybridisation of oligonucleotides was characterized using polyacrylamide (PA) gel electrophoresis (GE). PAGE gels are widely employed to characterise DNA, RNA and proteins. In this technique, a polymer matrix with a specific pore size is prepared. The DNA samples are loaded into the matrix by placing them into pre-casted wells. The application of an electric field induces the migration of the molecules inside the matrix which are then separated accordingly to their size and net charge.<sup>165</sup>

PAGE analysis in DNA native conditions was conducted. For each gel shown in **Figure 3.18**, three samples were prepared and loaded, one containing a mixture of previously hybridised complementary ssDNA (lane 1), and the other two the corresponding single stranded oligonucleotides (lane 2 and lane3).

In **Figure 3.18** PA gel in phosphate buffer 0.1 M and NaCl 0.3 M (native conditions) for Res1 and Res2 is reported. In A, lane 1 contains pre-hybridised sample of thiol Res1+Res2, while lanes 2 and 3 correspond to Res1 and Res2 respectively. In case of successful hybridisation between the complementary strands, the band containing the pre-hybridised sample should run slower through the gel matrix, compared to the corresponding ssDNAs, whose bands should run further. Indeed, as expected, band in lane 1 run slower than Res1 and Res2 alone, confirming the efficient hybridisation between these two strands. **Figure 3.18B** shows PA gel in native conditions for pre-hybridised amino-terminated Res1+Res2 (lane 1), Res1 (lane 2) and Res2 (lane 3). Also in this case, the band in lane 1 run slower, thus endorsing the efficiency of the hybridisation between Res3 and Res4.

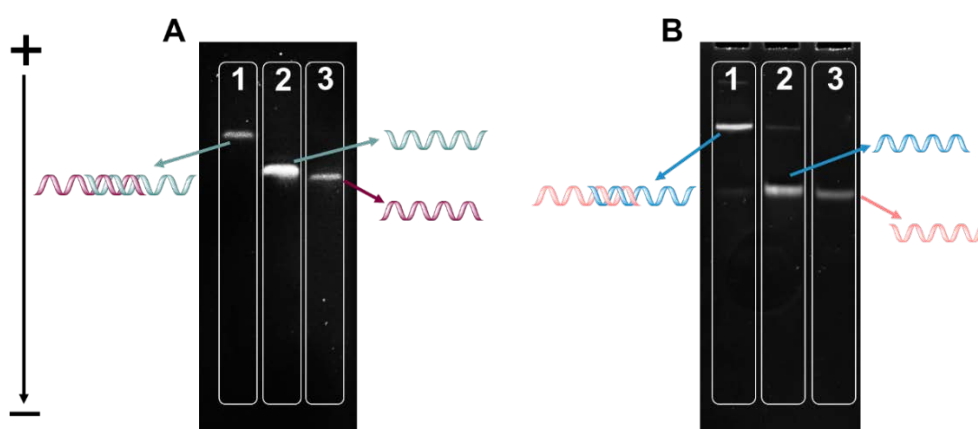


**Figure 3.18** Polyacrylamide gel electrophoresis in native conditions to test the hybridisation efficiency of the employed oligonucleotides. Thiol-terminated Res1 and Res2 in A, while the amino-functionalised Res1 and Res2 are in B.

### 3.3 Oligonucleotide functionalisation of colloidal nanoparticles

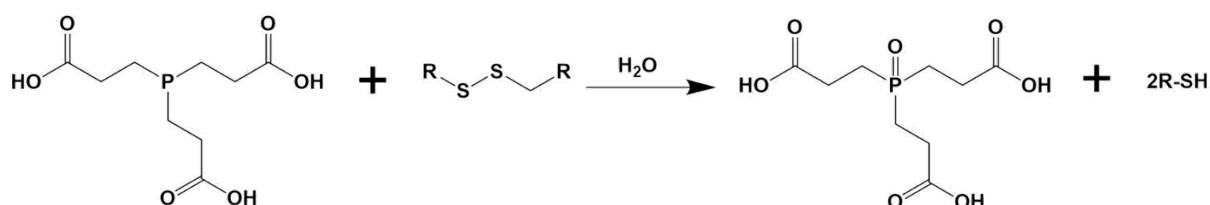
A dense layer of oligonucleotides was covalently attached on the surface of gold, silver, lanthanide-doped NaYF<sub>4</sub> and iron oxide nanoparticles. In the case of AuNPs and AgNPs, direct attachment of single stranded DNA (ssDNA) was achieved by covalent binding between thiol-terminated ssDNA and the gold or silver surface (experimental details in **Sections 2.2**, discussion of results in **Sections 3.3.1** and **3.3.2**, respectively).

For functionalization of the iron oxide nanoparticles and the upconversion nanoparticles with DNA, the particles must first be transferred in water. Two different approaches were employed to bring nanoparticles in water. The first approach involves the ligand exchange with polyacrylic acid and the second approach is the coating of nanoparticles with a silica shell and the surface modification with carboxylic groups (experimental details in **Section 2.2.3**). The results from these strategies are detailed in **Section 3.3.4.1** for UCNPs and **Sections 3.3.4.2** for IONPs.

#### 3.3.1 Loading of a dense shell of oligonucleotides on gold nanoparticles

Oligonucleotides can be conjugated to AuNPs by using a thiol modification to either the 5' or 3' end. Thiols have a very strong affinity for gold where a S-Au bond is thought to be chemically and energetically equivalent to an Au-Au bond.<sup>96</sup> The thiol modification at the 3' end of a DNA sequence is highly reactive towards the formation of S-S bridges, for this reason they are usually synthesised with a disulfide at the termination to avoid unwanted side reactions. The first step of oligonucleotide attachment on NPs was the cleavage of this S-S bond to yield a SH termination. Thus, the chosen oligonucleotide in an excess ratio of ssDNA/AuNPs=800/1 was incubated with the reducing agent TCEP for two hours in ice (reaction mechanism detailed in **Scheme 3.1**).<sup>166</sup>

**Scheme 3.1** Reaction mechanism for the TCEP cleavage of a disulphide bond.



Tris(2-carboxyethyl)phosphine

A low temperature was necessary to decrease the reactivity of the thiol end once deprotected. After activation, the sequence was rapidly purified via spin column chromatography and incubated with citrate-coated AuNPs, to allow non-specific binding of the DNA on the surface of NPs. This step

is necessary to stabilise the NPs as in the following stages phosphate buffer and sodium chloride will be added, which otherwise would cause irreversible aggregation of citrate NPs. After overnight equilibration of the NPs with DNA in phosphate buffer, small aliquots of NaCl were added over the course of 8 hours to a final concentration of 0.3 M. This slow addition has a dual role: firstly, adding small amounts of salt does not cause particles' aggregation but instead helps the DNA strands to attach the NPs surface; secondly, when higher concentrations of salt are added, the packing of DNA on the NPs is also optimised as the increase of ions effectively screens the repulsive force between negatively charged DNA.<sup>120</sup> UV-vis spectroscopy and zeta potential measurements were used to qualitatively assess the DNA conjugation on 14 nm AuNPs (**Figure 3.19**). A slight red-shift of about 4 nm was observed at the nanoparticles spectrum, which was attributed to the change in the refractive index in the immediate surroundings of the NPs.<sup>40,167</sup>

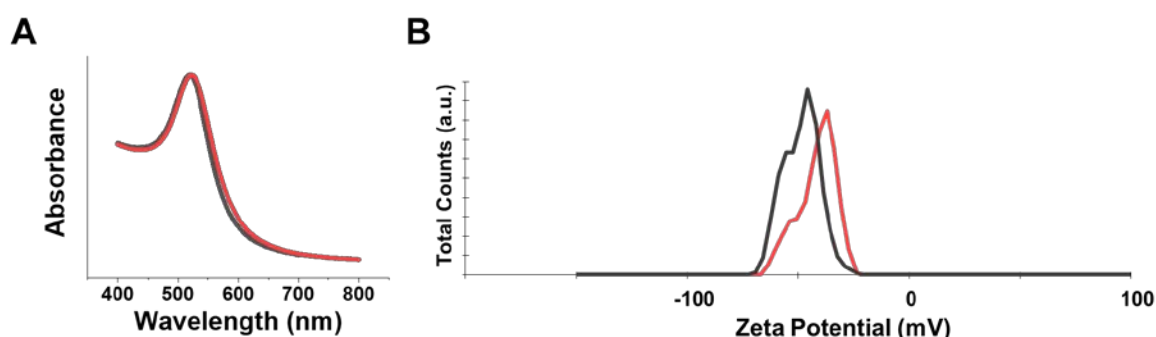
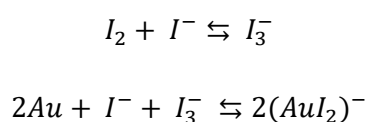


**Figure 3.19** (A) UV-visible spectra of gold nanoparticles covered with citrate ions (in black) or oligonucleotide ligands (in red), showing a slight red shift in the latter case. In B, zeta potentials for gold nanoparticles covered with citrate ions (in black) or oligonucleotide ligands (in red), showing a slightly less negative charge in the latter case.

The number of loaded strands per particles can be evaluated by dissolving the metal core of DNA-functionalised AuNPs, which results into the release in solution of the attached oligonucleotides (see **Sections 1.1.2.1** and **2.2.1** for theoretical background and experimental procedure). Au(0) is oxidised to Au(I) in a redox reaction with KI/I<sub>2</sub> highlighted in **Equation 3.4**.<sup>168–170</sup> The Au ions were removed from the solution *via* column chromatography using a Nap10 column. The eluted solution is collected, and a UV-vis measurement is performed. From the absorbance at 260 nm the DNA concentration could be calculated using the Beer law, resulting in an average of 112±4 strands per 14 nm gold particle (0.19 strand/nm<sup>2</sup>) calculated over three independent measurements.

**Equation 3.4** Redox reaction leading to the dissolution of AuNPs.



### 3.3.2 Loading of a dense shell of oligonucleotides on silver nanoparticles

Similarly to the AuNPs, the oligonucleotides are conjugated to AgNPs via a thiol group. Even if not as strong as in the case of gold, thiols have an affinity for silver. Theoretical calculations have shown that the affinity between a thiol and a gold cluster is in the range of -22 to -34 kcal/mol, while for SH and Ag clusters the binding energy spans between -11 and -16.<sup>125</sup> As discussed previously (**Section 3.3.1**), the first step of oligonucleotide attachment on NPs is the cleavage of this S-S bond to yield SH terminations *via* TCEP reduction. After overnight incubation with the deprotected oligos, small aliquots of NaCl were added over the course of 8 hours to a final concentration of 0.3 M to allow the progressive loading of the strands on the NPs without causing irreversible aggregation of the particles. UV-vis spectroscopy and zeta potential measurements were complementarily used to qualitatively assess the DNA-NPs conjugation (**Figure 3.20**). The spectra of citrate and DNA coated AgNPs are nearly superimposable, confirming the absence of aggregation. A minor red-shift of about 4 nm was observed, attributed to a change in the refractive index in the immediate surroundings of the NPs.<sup>167</sup> As in the case of AuNPs, the zeta potential shifted to more negative values for AgNPs@DNA, compatible with the replacement of the citrate ions with the more negatively charged DNA.

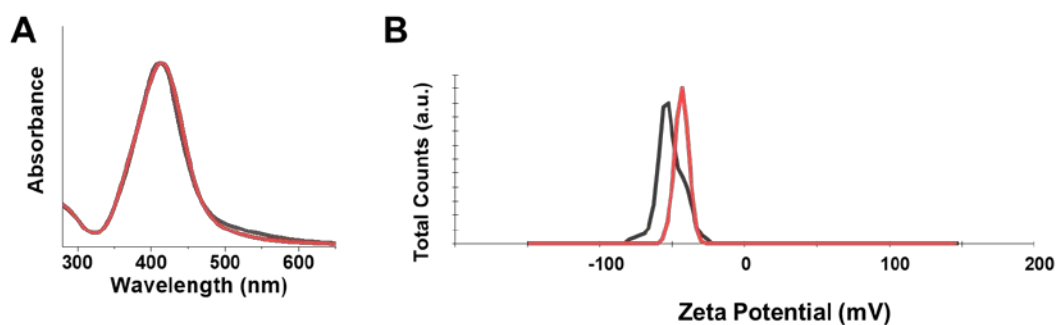
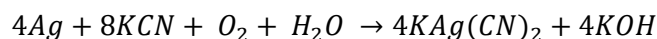


**Figure 3.20** In A, UV-visible spectra of silver nanoparticles covered with tannic acid and citrate ions (in black) or oligonucleotide ligands (in red), showing a slight red shift in the latter case. In B, zeta potentials for silver nanoparticles covered with citrate ions (in black) or oligonucleotide ligands (in red), showing an increased negative charge in the latter case.

Quantification of the number of DNA strands was assessed *via* etching of the silver core followed by UV-Vis spectroscopy. Ag(0) from the NPs is oxidised to Ag(I) in a redox reaction with KCN (**Equation 3.5**).<sup>123,171</sup> The solution was purified from Ag salt *via* column chromatography on NAP10 column and the concentration of DNA was calculated from the absorbance at 260 nm, resulting in an average of  $132 \pm 7$  strands per 15 nm AgNPs ( $0.15 \text{ strand/nm}^2$ ).

**Equation 3.5** Chemical reaction for the dissolution of the AgNPs core with KCN.



### 3.3.3 Loading of a shell of oligonucleotides on large gold and silver nanoparticles

A salt-aging strategy was also employed for the surface functionalisation of larger AuNPs and AgNPs, (experimental in **Section 2.2.2**). Compared to 15 nm NPs, a larger excess of oligonucleotides was added to the suspension of NPs (NPs to ssDNA ratio 1/3200 rather than 1/800). Secondly, the first addition of NaCl 2 M was followed by two hours of shaking before carrying on with the following additions, to allow more time for weak DNA binding on the NPs' surface. In **Figure 3.21** the UV-Vis spectra for 45 nm AuNPs with citrate (black curve) and with DNA (grey profile) are reported, showing a similar absorption band in terms of width, but with a slight red shift ( $\sim 3$  nm) for the AuNPs@DNA, ascribable to the slight difference in the refractive index surrounding the NPs coated with oligonucleotides.

The salt aging protocol resulted in the loading of  $658 \pm 10$  ssDNA per 45 nm AuNPs, corresponding to a surface density of  $0.10$  strand/nm<sup>2</sup>, calculated from three independent measurements. The number of loaded strands per particles was determined by releasing the ssDNA from the NPs' surface and monitoring the DNA absorbance at 260 nm to calculate DNA concentration. The attached oligonucleotides were released in solution by etching the gold core in a redox reaction with KI/I<sub>2</sub> (see **Equation 3.4**). The density of oligonucleotides loaded on larger AuNPs is lower compared to the loading density on smaller AuNPs ( $0.10$  versus  $0.19$  strand/nm<sup>2</sup>). A possible explanation for this observation is that the amount of ssDNA initially added during the salt aging procedure was not enough to maximise the loading. Alternatively, one could consider that the maximum packing on the surface of large NPs required a greater amount of salt ions to screen the increased negative charge, due both to the larger surface area of big NPs and to the higher number of ssDNA in solution.

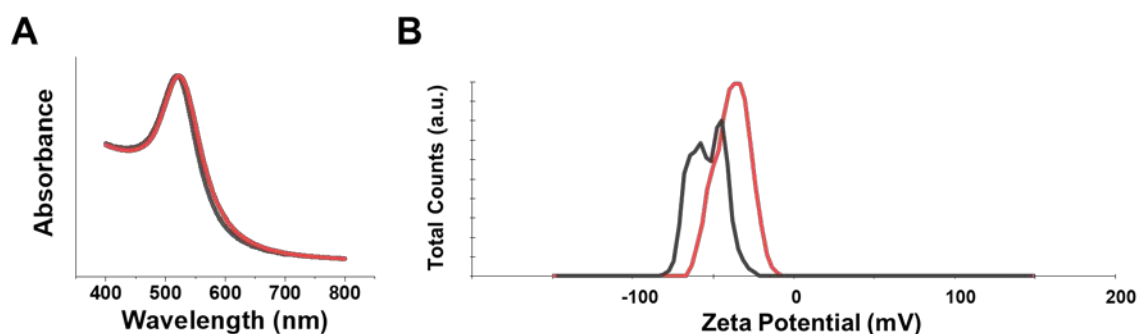


**Figure 3.21** UV-Visible spectra of AuNPs 45 nm (black) and AuNPs@DNA (red), showing a slight red shifting for the oligonucleotide-coated AuNPs. In B, zeta potentials for 45 nm Au nanoparticles

covered with citrate ions (in black) or oligonucleotide ligands (in red), showing an increased negative charge in the latter case.

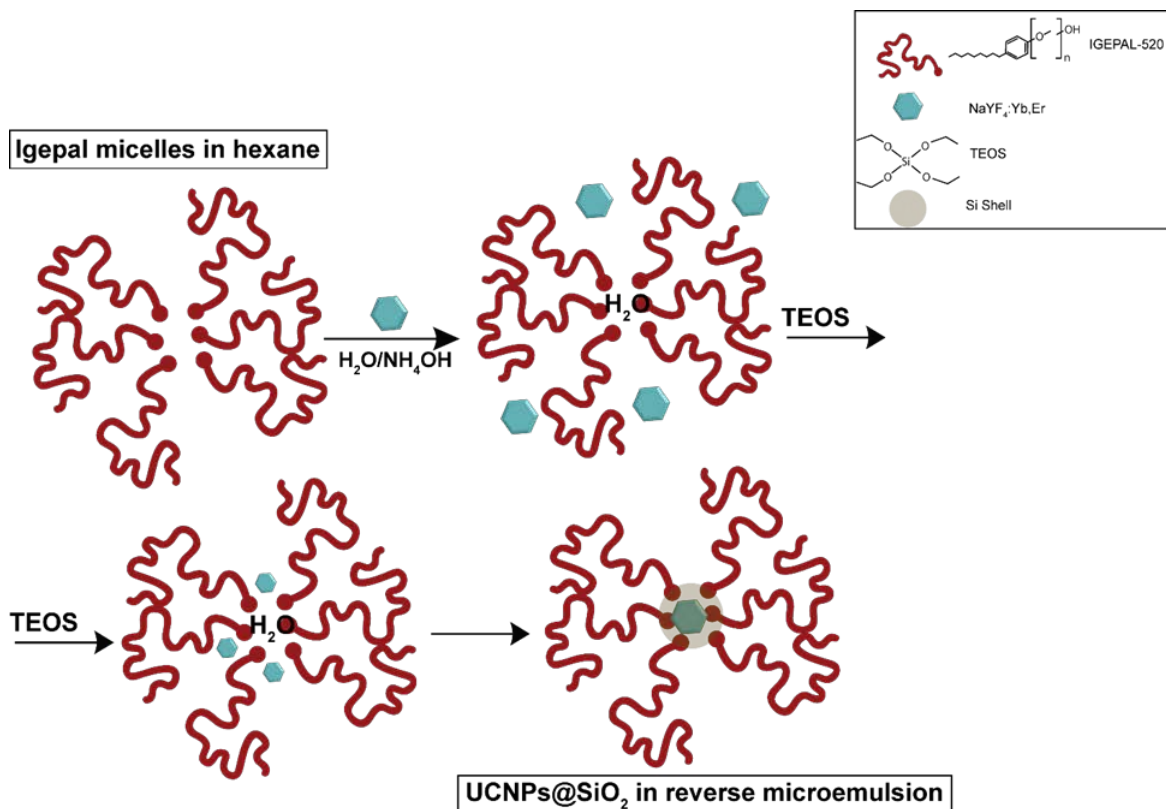
Similarly to the large AuNPs, the functionalisation of 48 nm AgNPs with ssDNA was carried out by following the same salt-aging protocol. It resulted in the attachment of  $732 \pm 21$  strand ( $0.09$  strand/nm<sup>2</sup>), calculated over three independent experiments. Each experiment consisted in the dissolution the metal core to release the oligonucleotides attached on the silver surface (**Equation 3.5**), followed by UV-Vis spectroscopy to measure the DNA absorbance at 260 nm. As in the case of large AuNPs, the density of oligonucleotides loaded on bigger AgNPs is lower compared to the loading density on smaller AgNPs ( $0.09$  versus  $0.15$  strand/nm<sup>2</sup>), reinforcing the explanations given for AuNPs 45 nm. In particular, the loading density on large Au and AgNPs is essentially the same, suggesting that a higher surface coverage could be achieved by tuning either the number of added oligonucleotides or the final NaCl concentration.

### 3.3.4 Surface modification and oligonucleotide attachment on upconversion and magnetic nanoparticles

In contrast with silver and gold, NaYF<sub>4</sub> and Fe<sub>3</sub>O<sub>4</sub> do not show any affinity for typical DNA-terminations like thiol groups. Furthermore, they are not readily dispersible in water due to the presence of organic hydrophobic ligands such as oleic acid. For these reasons they require additional steps before being attached to ssDNA. For this aim, two well-known approaches were adapted and used in this work: the silanisation<sup>172</sup> and the ligand-exchange.<sup>99</sup>

The silanisation of nanoparticles consists in coating the nanoparticles' surface using an alkoxy silane compound (such as TEOS). The alkoxy silane molecules are anchored to the surface of the nanoparticles using a reverse microemulsion method and the respective silicate groups are hydrolysed to create a silica shell. **Scheme 3.2** shows the silanisation mechanism *via* water-in-oil microemulsion.<sup>172</sup>

**Scheme 3.2** Schematic drawing of the silica encapsulation via reverse microemulsion, adapted from ref.<sup>172</sup> The silanisation includes a first step in which the Igepal surfactant forms the micelles. After addition of aqueous ammonia and TEOS, the UCNPs diffuse in the micelles and a silica coating around individual NPs is formed.

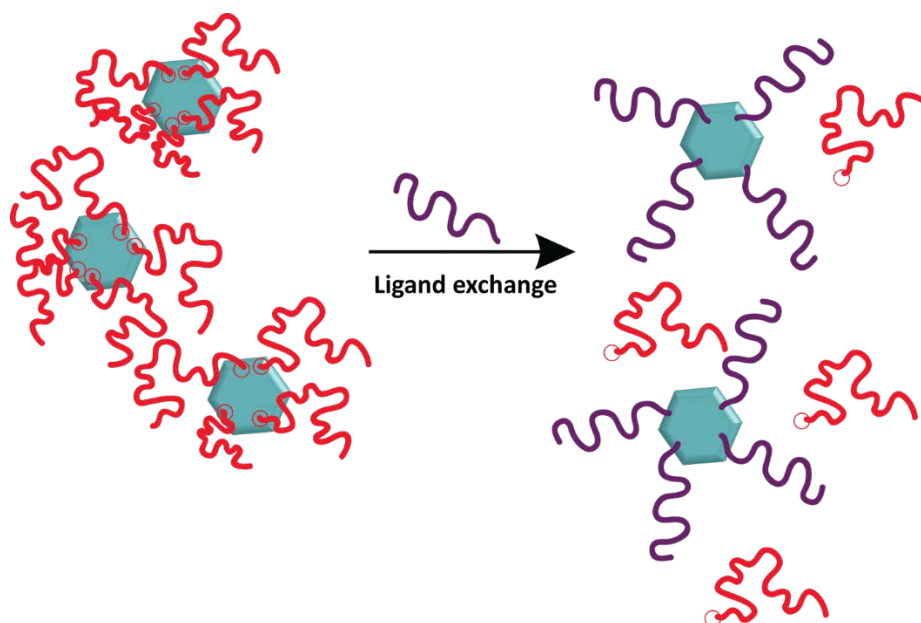


On the other hand, a ligand-exchange method consists in the replacement of the capping molecules on the nanoparticles' surface with another set of ligands which have higher affinity for the nanoparticles' surface (**Scheme 3.3**). In this work, the oleic acid ligands on the UCNPs surface were exchanged with the multi-dentate polymer polyacrylic acid (PAA).

Following either silanisation or ligand exchange, the nanoparticles were suspended in water and the carboxy groups were used to attach amine-terminated oligonucleotides via EDC coupling chemistry.



**Scheme 3.3** Ligand exchange mechanism, adapted from ref.<sup>99</sup> In this mechanism, the ligands on the surface of the NPs are replaced with another set of molecules with a higher affinity for the nanoparticles' surface.



#### 3.3.4.1 Phase transfer of NaYF<sub>4</sub> nanoparticles

Either a ligand exchange or a silanisation approach was used to modify the surface of UCNPs. The ligand-exchange is a facile, one-step approach to bring nanoparticles in water and render them ready for EDC/NHS coupling with amine-modified ssDNA.

On the other side, silanisation is rather lengthy as to make the NPs available for the coupling with the DNA, two additional steps are required after the silanisation: the amination and the carboxylation of the silica surface. Furthermore, the formation of a silica shell around a single particle is challenging as it demands accurate calibration of the amount of precursors used. However, the encapsulation in a silica shell guarantees stability overtime and at elevated temperatures.

##### 3.3.4.1.1 Polyacrylamide functionalisation of upconversion nanoparticles

PAA and oleate-UCNPs were mixed together in tetrahydrofurane (THF) and left to stir for four days. Afterwards, three rounds of centrifugation and washing in ethanol were carried out to remove the unbound PAA. The accomplishment of the ligand exchange was verified by zeta potential measurements and FTIR spectroscopy. **Figure 3.22** shows the zeta potential after ligand exchange, revealing a strong negative charge due to the presence of PAAs.

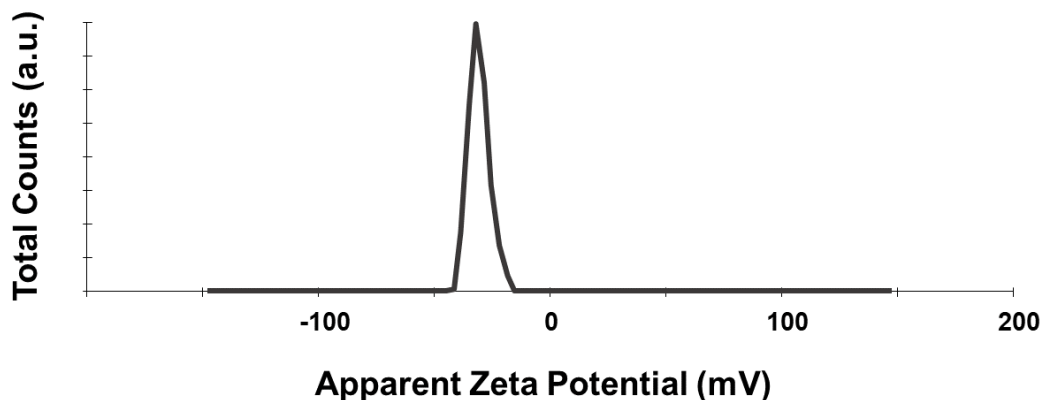


**Figure 3.22** A graph of the zeta potential for PAA-coated UCNPs in ethanol (0.5 mg/mL). A strong negative value of -44 mV was recorded.

The infrared spectra for oleate- and PAA-capped UCNPs are reported in **Figure 3.23**. It clearly shows the appearance of a strong peak at  $\sim 1700\text{ cm}^{-1}$  typically attributed to carboxylic groups, hence compatible with the presence of PAA on the NPs.

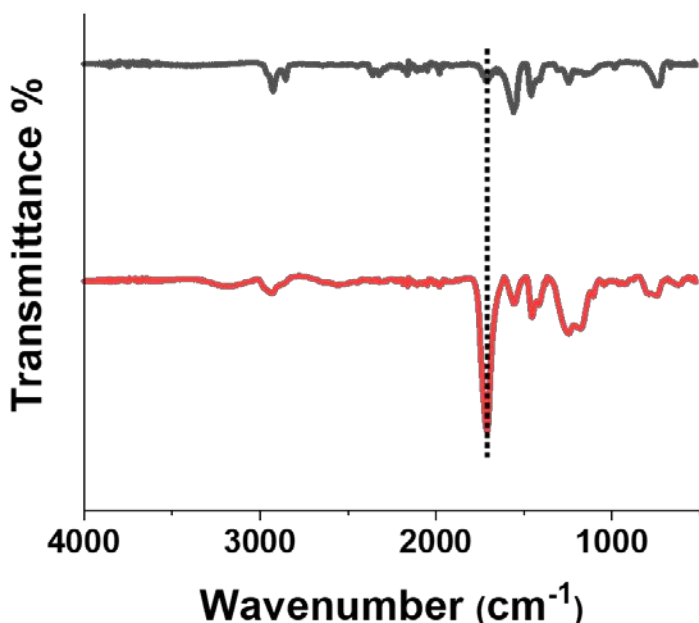


**Figure 3.23** Infrared spectra of oleate-capped (black) and PAA-covered (red) upconversion nanoparticles. The spectra were offset for better visualisation. The appearance of a strong COOH peak at  $1700\text{ cm}^{-1}$  is a strong confirmation of the presence of PAA molecules.

### 3.3.4.1.2 Silanisation of upconversion nanoparticles

Following the synthesis, UCNPs in hexane were mixed with Igepal and ammonia during sonication to allow the formation of a microemulsion. The silanisation agent (TEOS) was later added and they were left to age overnight under magnetic stirring. To optimize the silanisation of individual NPs, the ratios of NPs/ammonia/TEOS were varied. **Figure 3.24** displays different TEM micrographs showing various cases of unsuccessful coatings.

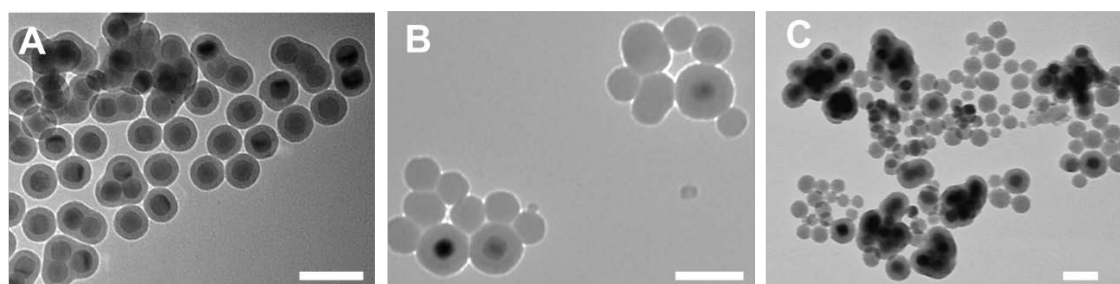


**Figure 3.24** Representative TEM micrographs of different attempts of silanisation. In (A) different UCNPs clustered in the same silica shell, while in (B) the excess of silanisation reagents resulted into empty silica spheres. In (C) both clustered UCNPs and silica NPs are visible. Scale bars 50 nm.

The lack of colloidal stability lead to the clustering of more than on NP in each silica shell. To tackle this issue, a wet annealing protocol was used to load more oleic acid ligands on the NPs' surface and increase their dispersibility (experimental in **Section 2.1.5.1**). A visual proof of this is given in **Figure 3.25B**, where the same batch of UCNPs is shown before and after the wet annealing procedure. A transparent suspension was obtained for annealed NPs (i and iii), proving that a more efficient dispersion was achieved, in comparison with the highly scattering suspension of NPs before annealing (ii and iv) which looked fairly turbid. **Figure 3.25A** shows the thermogravimetric analysis of the nanoparticles. The residual inorganic mass of the as-synthesised UCNPs (solid line) corresponds to the 94% of the initial total mass, while for the annealed sample the residual mass was 89%. This difference was attributed to the different number of organic ligands bound on the NPs' surface, corresponding to 6% and 11% respectively for pre- and post-annealed samples, confirming that the difference in the quality of the dispersion was due to a different loading of oleic acid molecules.

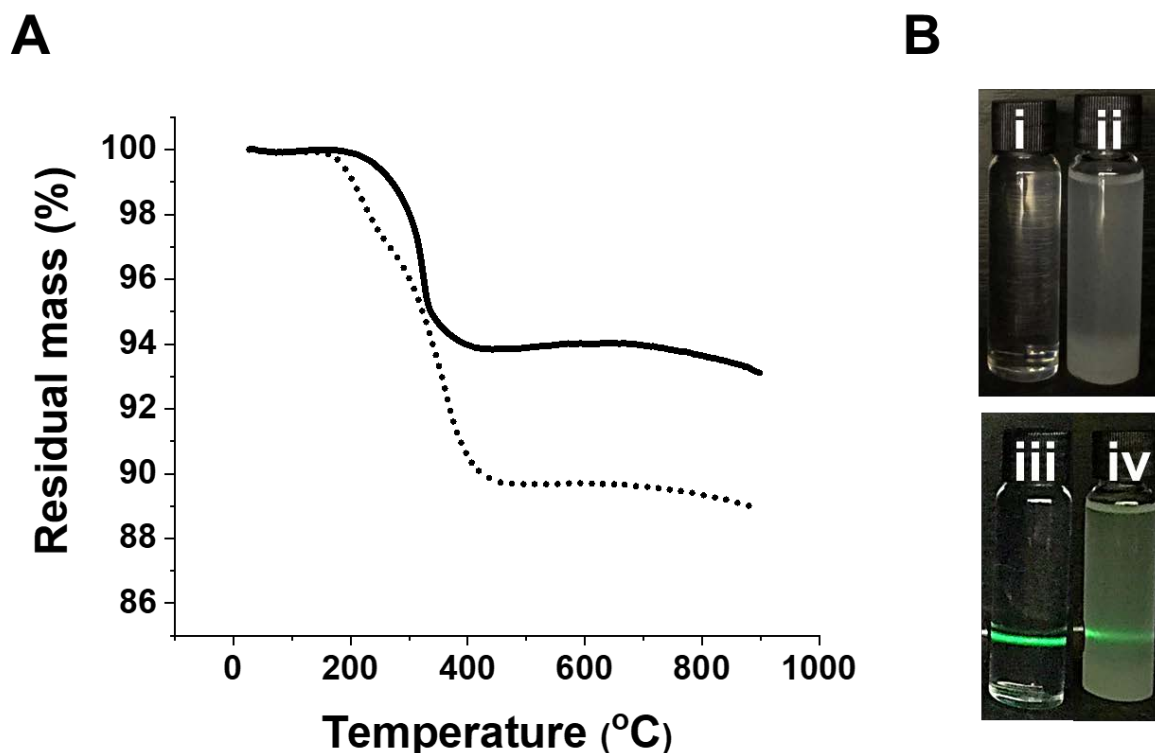


**Figure 3.25** In A, the thermogravimetric analysis for as-synthesised UCNPs (solid line) and for the wet-annealed UCNPs (dotted line), showing a higher weight loss percentage for the latter case. In B, optical images of a 10 mg/mL suspension of UCNPs after annealing under white light (i) and illuminated by 980 nm laser (iii). Corresponding images of the same sample before annealing step are shown in ii and iv.

Following efficient dispersion of UCNPs in hexane, the effective encapsulation of individual NPs in silica shell was also accomplished for different sized UCNPs. **Figure 3.26** shows representative TEM images of UCNPs:Gd<sup>3+</sup> 0%, UCNPs:Gd<sup>3+</sup> 20% and UCNPs:Gd<sup>3+</sup> 30%, and corresponding size histograms of the encapsulated NPs. As a result of the silica shell, the size of the nanoparticles increased from  $44.9 \pm 3.3$  nm to  $53.0 \pm 3.8$  nm for NPs with Gd 0%, and from  $27.9 \pm 1.8$  nm to  $48.3 \pm 2.8$  nm for Gd 20% and from  $12.5 \pm 1.5$  nm to  $22.2 \pm 2.0$  nm for Gd 30%.

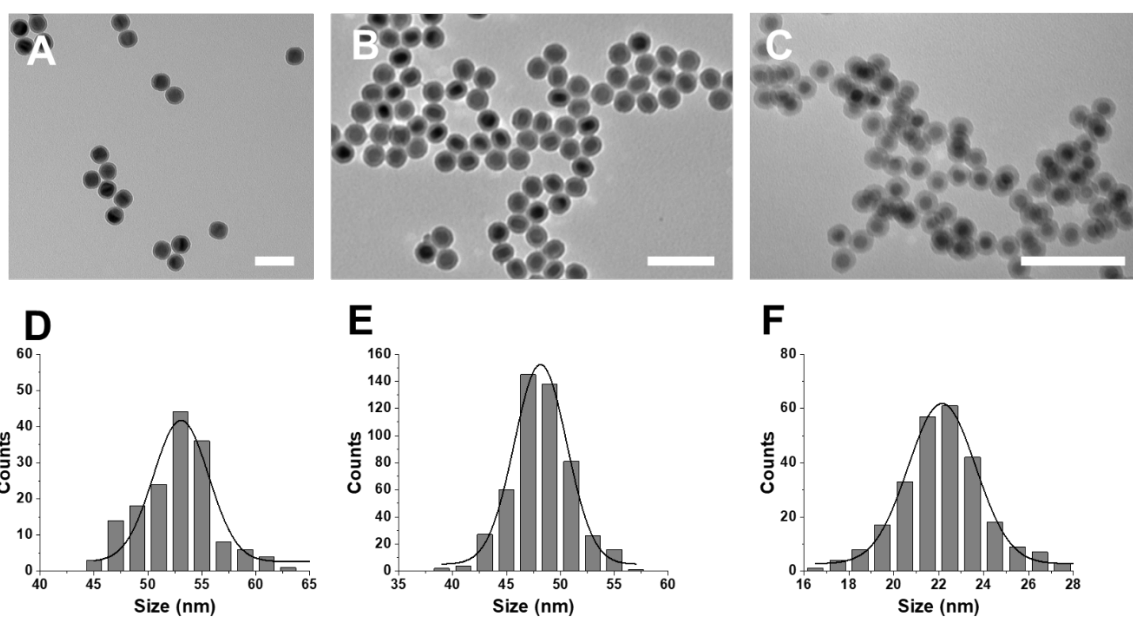


**Figure 3.26** TEM micrographs and corresponding size distribution histograms for the successful silanisation of UCNPs. In A and D, UCNPs containing 0% Gd<sup>3+</sup> are shown, with an average diameter of  $53.0 \pm 3.8$ . In B and E, UCNPs containing 20% Gd<sup>3+</sup> are reported, with an average diameter of  $48.3 \pm 2.8$ . In C and F, UCNPs containing 30% Gd<sup>3+</sup> are shown, with an average diameter of  $22.2 \pm 2.0$ . Scale bars 100 nm.

Analysis of X-ray diffraction patterns for UCNPs prior and after silanisation was also carried out. In **Figure 3.12** the diffraction patterns are observed, and the peaks were assigned to the predicted reflections for the hexagonal phase.

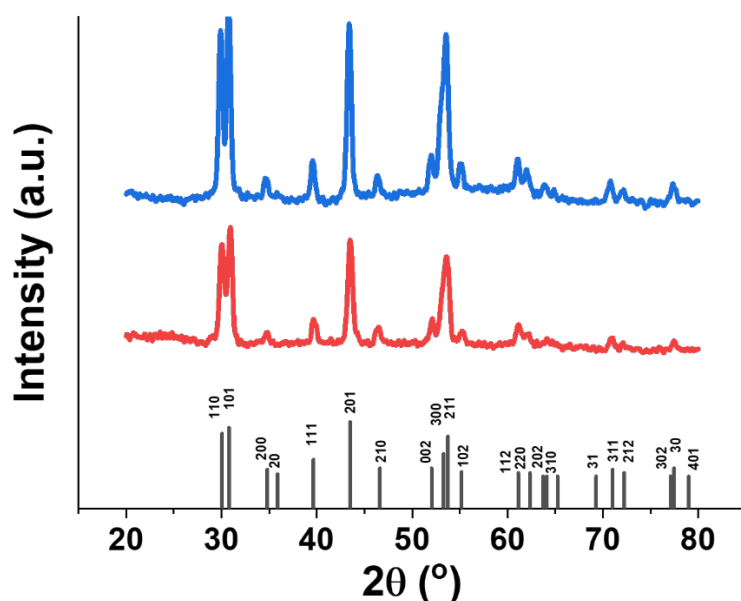
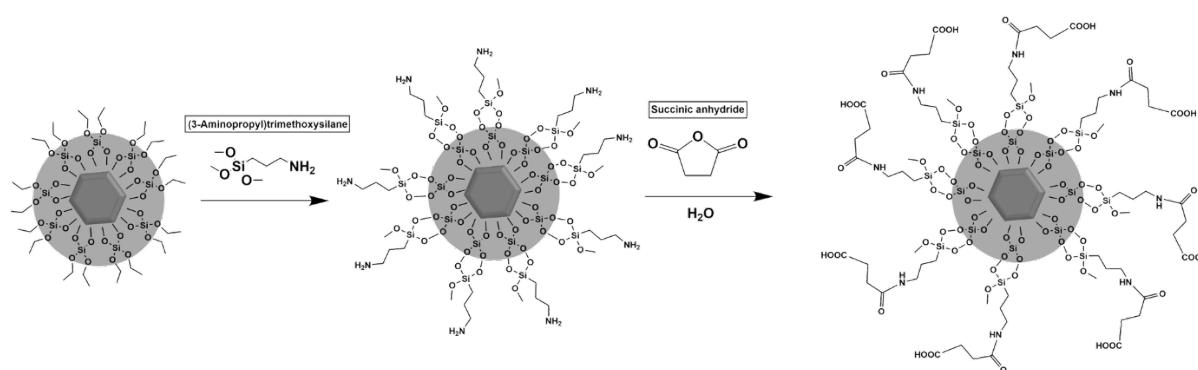


**Figure 3.27** X-ray diffraction patterns for as-synthesised UCNPs (blue) and silica-coated UCNPs (red), with corresponding planes indices, compatible with the hexagonal phase.

### 3.3.4.1.3 Amination and carboxylation of UCNPs

Following successful silanisation, the UCNPs@SiO<sub>2</sub> were chemically modified for ssDNA attachment *via* EDC/NHS coupling. For this goal, carboxylic groups were added to their surface with a two-step process. In the first step, an amino enriched silano compound (3-(aminopropyl)trimethoxysilane, APTMS, **Scheme 3.4**) was attached on the silica-coated UCNPs through silica dioxide bonds.

**Scheme 3.4** Reaction mechanism for the carboxylation of the UCNPs' surface. In the first step, the 3-(aminopropyl)trimethoxysilane is added to the silica-coated UCNPs. In the second step, following the hydrolysis and consequent ring opening, the succinic anhydride attacks the amino termination on NPs forming an amide bond. Reaction mechanisms adapted from ref.<sup>108</sup>



APTMS contains a secondary amine termination, susceptible to attack by a carboxylic group to form an amide. Therefore, in the second step, the amine-modified UCNPs@SiO<sub>2</sub> reacted with succinic anhydride (**Scheme 3.4**, step 2). The ring opening of the anhydride yields a linear chain with two -COO<sup>-</sup> terminations, available to react with the amine modified UCNPs. The reaction between the COOH and the amino groups on the UCNPs surface led to the formation of an amide bonding. The whole process was monitored using zeta-potential measurements (**Figure 3.28**). Upon conversion nanoparticles encapsulated in a silica shell showed a negative potential of  $-32 \pm 3$  mV, attributed to the presence of SiO<sup>-</sup> and Si-OH. The potential shifted to positive values ( $+23 \pm 5$  mV) after reaction with APTMES, due to the presence of amines. Finally, as expected, the potential returned to negative values ( $-35 \pm 6$  mV) after the carboxylation step.

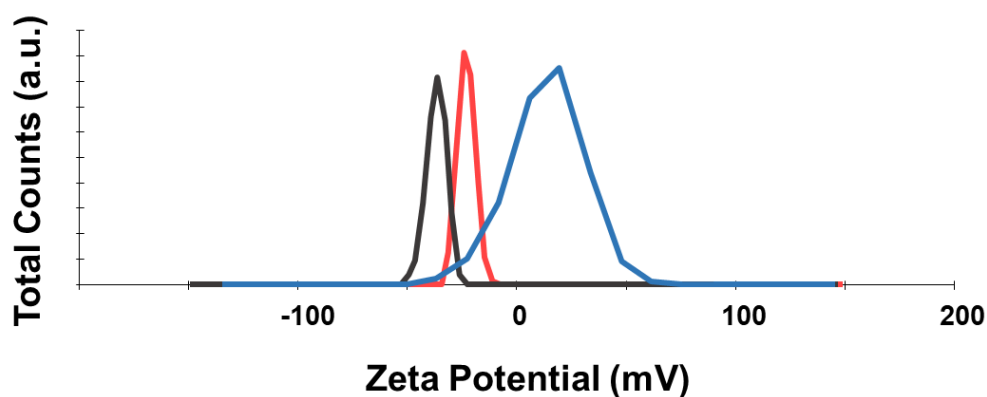


**Figure 3.28** Zeta potential values for silica encapsulated (red), amino-terminated (blue) and carboxy-terminated (black) UCNPs, recorded in water at a concentration of 0.5 mg/mL.

#### 3.3.4.1.4 Oligonucleotide attachment on $\text{NaYF}_4$ nanoparticles *via* NHS/EDC coupling

After the carboxylation of their surface, the UCNPs were finally ready to be functionalized with amino-modified ssDNA using EDC/sulfo-NHS chemistry. This method has already been successfully applied<sup>99</sup> and has been proved to be highly effective. The details of the reaction mechanisms involved in the NHS/EDC coupling are reported in **Section 1.1.2.3**.

Using this strategy, amino-modified Res1 and Res2 (sequences in **Table 2.1**) were loaded onto UCNPs' surface. Initially, the UCNPs were incubated with EDC and NHS to allow the formation of the reactive intermediate in **Scheme 3.2b**. After  $\sim 30$  minutes, the oligonucleotide of choice was added. Purification by centrifugation in Milli-Q water was carried out after overnight shaking, yielding a white pellet, which showed prolonged stability when dispersed in water.

As expected, the zeta potential measurements (**Figure 3.29**) of UCNPs@DNA showed that the particles were negatively charged (-25 mV, 0.5 mg/mL in water).

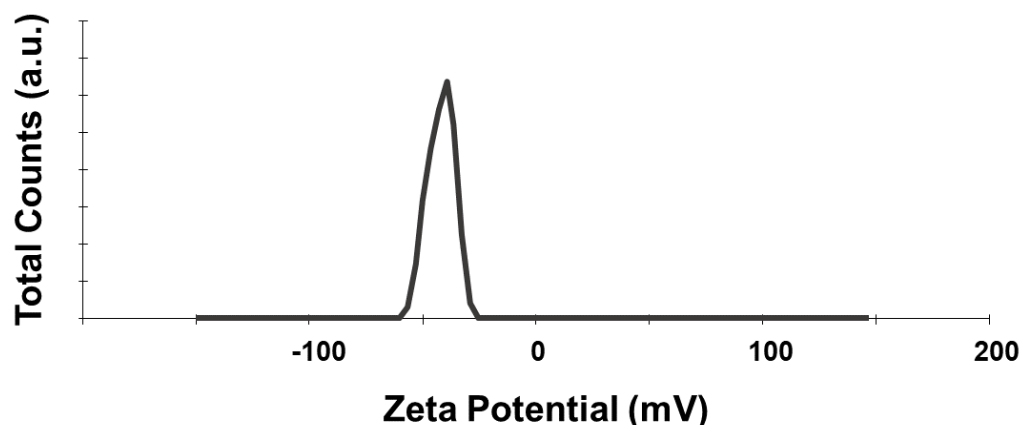


**Figure 3.29** Zeta potential measurement for DNA-coated UCNP@SiO<sub>2</sub> (0.5 mg/mL in ultrapure water).

#### 3.3.4.2 Phase transfer of iron oxide nanoparticles

Analogously to the UCNP, the as-synthesised IONPs are stabilised by a shell of hydrophobic ligands. To facilitate the phase-transfer to aqueous solution, the silanisation and the ligand exchange strategies were tested.

##### 3.3.4.2.1 Poliacrylamide functionalisation of iron oxide nanoparticles

The replacement of the oleic ligands with PAA molecules was easily performed by dispersing the IONPs in THF and adding an excess of PAA, also dissolved in THF. The mixture was left to stir at RT over 4 days to ensure full replacement of the oleic acid and it was then purified by repeated centrifugations and washing steps. The particles were characterized by FT-IR spectroscopy. In **Figure 3.30**, the infrared spectra of IONPs before (red) and after (black) incubation with PAA shows no differences in the location and intensity of the peaks, suggesting in fact that the ligand exchange did not occur. The reasons for the unsuccessful ligand exchange are not clear at this stage. However, based upon the results obtained from UCNP, more effort was devoted to the silanisation of IONPs, which appeared more promising towards the application in superlattices assembly.



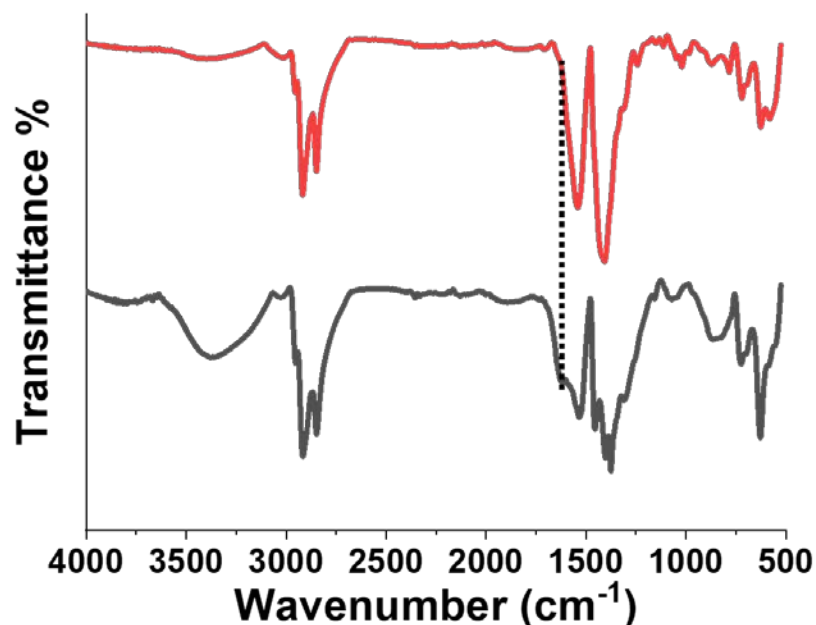


**Figure 3.30** Infrared spectra of oleate-capped (red) and PAA-covered (grey) iron oxide nanoparticles. The spectra were offset for better visualisation. A small shoulder at about 1660 cm<sup>-1</sup> appeared, however, no strong peak at 1700 cm<sup>-1</sup> could be observed, suggesting that in fact the ligand exchange did not take place.

### 3.3.4.2.2 Silanisation of IONPs

The coating of IONPs with silica was achieved similar to the case of UCNPs, following a recently published protocol,<sup>160s</sup>. **Figure 3.31** shows the transmission electron micrographs of the silanised IONPs, which demonstrate the efficacy of the protocol in yielding individually silica-coated NPs. The average diameter of silica-coated IONPs was determined by measuring over 200 NPs and it resulted into  $40 \pm 4$  nm.

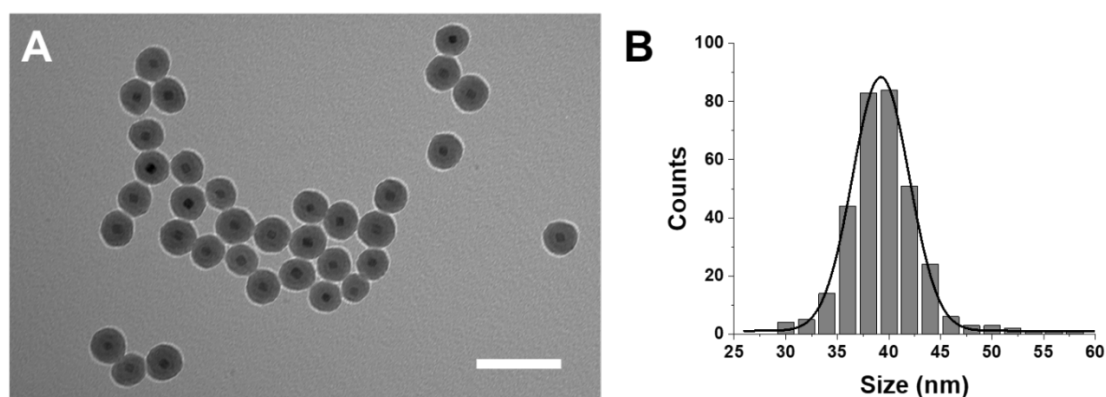


**Figure 3.31** TEM micrographs of silica coated iron oxide nanoparticles (A) and corresponding size distribution histogram (B). Scale bar 100 nm.

### 3.3.4.2.3 Amination and carboxylation of IONPs

Similarly to the UCNPs, the IONPs@SiO<sub>2</sub> required further manipulation *via* EDC/NHS coupling to obtain carboxylic termination on the surface of the NPs susceptible of attachment with amino-ssDNA.

The whole process was monitored using  $\zeta$ -potential (**Figure 3.32**). Silica-coated IONPs had a negative potential of  $-23 \pm 5$  mV, attributed to the presence of SiO<sup>-</sup> and Si-OH. The amination of the surface led to a potential shifted to positive values ( $+18 \pm 5$  mV). The reaction with succinic anhydride brought the potential back to negative values ( $-35 \pm 6$  mV) as a result of the introduction of -COOH terminations.

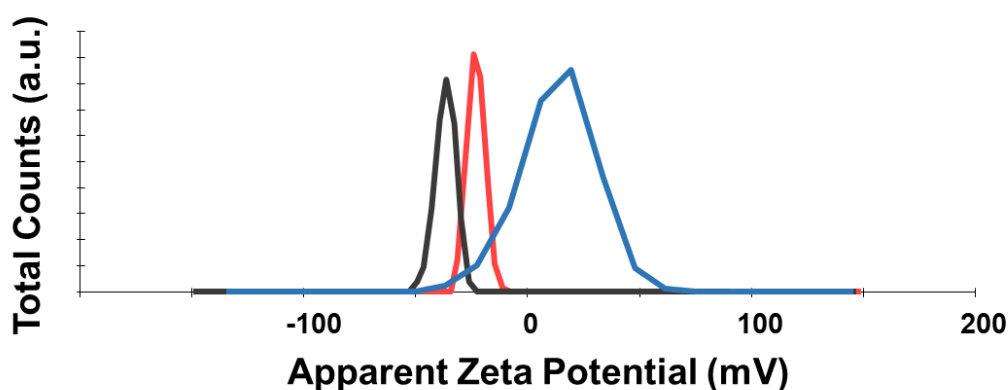


**Figure 3.32** Zeta potential values for silica encapsulated (red), amino-terminated (blue) and carboxy-terminated (black) IONPs, recorded in water at a concentration of 0.5 mg/mL.

### 3.3.4.2.4 Oligonucleotide attachment on iron oxide nanoparticles *via* NHS/EDC coupling

Following the carboxylation of the surface, the IONPs could be functionalized with amino-terminated ssDNA *via* EDC/sulfo-NHS chemistry. As for the UCNPs (**Section 3.3.4.1.4**), the reaction involves the coupling of a primary amine with a carboxylic acid in presence of EDC and sulfo-NHS mediators (detailed description can be found in **Section 3.3.4.1.4** accompanied by the reaction **Scheme 1.7**). This strategy allowed to attach amino-terminated Res3 and Res4 (sequences in **Table 2.1**) onto IONPs' surface. The zeta potential measurement of IONPs@DNA resulted into  $-41 \pm 2$  mV.

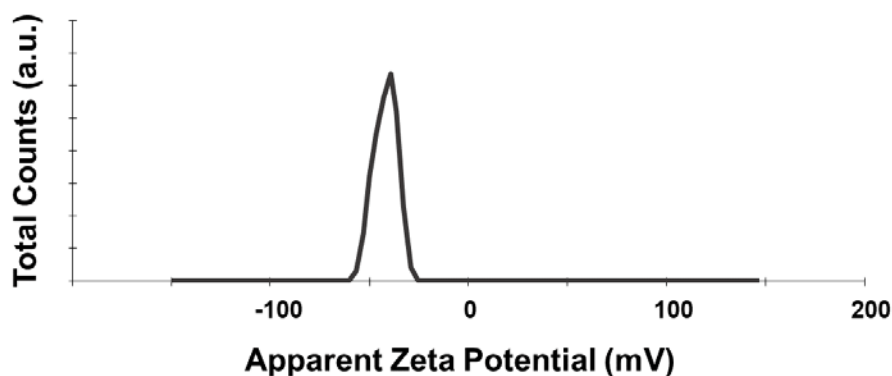


**Figure 3.33** Zeta potential value for IONPs covered with oligonucleotides (0.5 mg/mL in water).

### 3.4 Assembly of DNA-coated nanoparticles

In the previous sections, the synthesis, functionalisation and characterisation of different nanoparticles were discussed. The efficient hybridisation of the designed DNA strands was proved via melting analysis and gel electrophoresis. In this section, the assembly of DNA-coated NPs is presented

#### 3.4.1 Gold nanoparticles assembly

Assembly of gold dimers, trimers and various oligomers using DNA have been widely explored within our group and others.<sup>103,173–177</sup> Because of the well-known surface chemistry and reactivity, AuNPs are the optimal candidates for an initial study on the crystallisation process with prescribed oligonucleotides. To avoid the formation of amorphous aggregates, the ideal conditions to favour the accurate positioning of the particles within a network must be explored.

Following literature reports,<sup>131,132</sup> a constant temperature annealing approach was firstly used. In this protocol two batches of particles functionalised with the complementary ssDNA Res1 and Res2 were mixed in equimolar amounts in a buffered solution and placed in a thermal mixer (without shaking) and kept at a temperature near to the melting temperature of the DNA strands employed, (see **Section 3.2.1**). The annealing temperature was chosen in consideration of the melting temperature of the DNA duplex. If the temperature was kept above the  $T_m$  the DNA would not hybridise. However, if the temperature was kept too low, the energy provided would not be sufficient for the NPs to arrange in a crystalline fashion, which is the thermodynamically most

favourable configuration.<sup>163</sup> When the assembly process is kinetically driven, it leads to the formation of amorphous aggregates. To avoid this, enough energy in the form of heat must be provided. Another parameter to consider is the salt concentration, as the presence of cations is essential to allow the DNA hybridisation. An oligonucleotide is a strongly negatively charged molecule, due to the abundance of phosphate groups in the polymer backbone. For this reason, in order to be able to hybridise in a duplex efficiently, some form of charge screening between two strands is needed; this is usually achieved by adding inorganic salts (e.g. NaCl, MgCl<sub>2</sub>).

Various combinations of the two key parameters have been tested and the results are summarised in **Appendix A.3**. After two hours of annealing at constant temperature, followed by rapid cooling at RT, no aggregates were observed at low salt concentration. This confirmed that the salt concentration required for the assembly of a large number of particles needs to be higher than what usually employed for nanoparticles oligomers. Annealing at a fixed temperature above the dsDNA  $T_m$  followed by immediate cooling at room temperature also resulted in absence of precipitates. Concentrations between 0.1 and 0.3 M of salt and annealing temperatures between 50 and 54 °C yielded black aggregates that precipitated out of the solution. To distinguish between amorphous and crystalline aggregates, structural analysis was carried out. Small-Angle X-ray Scattering (SAXS) is a synchrotron technique that allows the structural characterisation of materials in the nano-scale (more information about SAXS can be found in the **Appendix A.2.7**). **Figure 3.34** shows the scattering intensity patterns for a crystalline sample (A) of gold nanoparticles, compared to the profile of an amorphous aggregate (B). The presence of an ordered lattice is shown by a series of peaks with various intensity ratios and relative positions  $q$  ( $q$  is a quantity proportional to the scattering angle, defined in **Section A.2.7**).

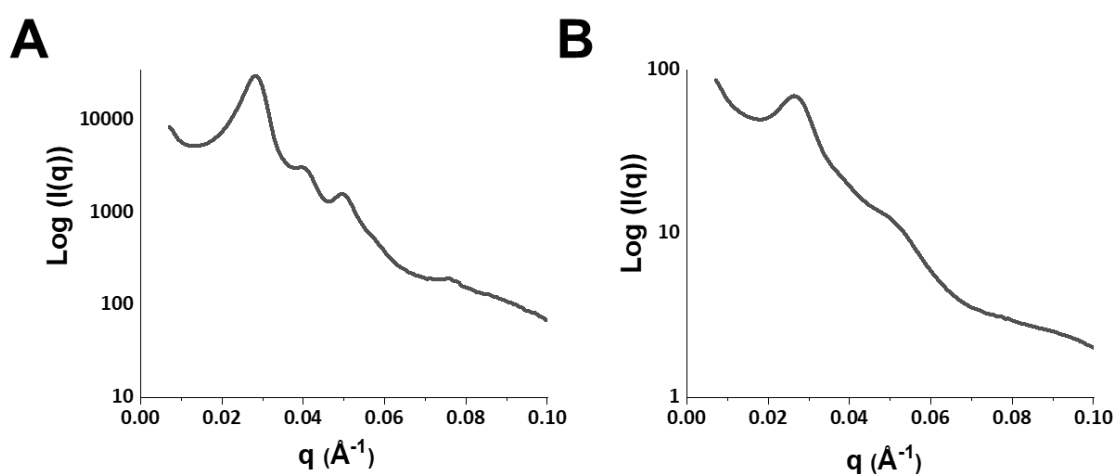


**Figure 3.34** (A) SAXS profile of a AuNPs-DNA SL annealed at 54 °C in NaCl 0.3 M. (B) SAXS profile of an amorphous aggregate of gold nanoparticles annealed at 54 °C in NaCl 0.04 M.

Along with the constant temperature annealing, a slow cooling strategy was also investigated. The first approach is the most common and it has been extensively used for the fabrication of different SLs (see **Section 1.1.3**), but the second one has been proved as the most efficient way to obtain single crystal lattices arranged in polyhedra of few microns with well-defined facets.<sup>178</sup>

In a typical experiment, two batches of AuNPs functionalised with the complementary strands Res1 and Res2 were incubated together in a ratio 1:1. Sodium chloride was added to screen the negative charge of the DNA backbones and facilitate the DNA hybridisation. The samples were transferred in a thermal cycler, an apparatus which permits the accurate control over applied temperature gradients. Then, the samples were brought to a temperature above the  $T_m$ . **Figure 3.35** shows the SAXS patterns for 14 nm AuNPs functionalized with Res1 and Res2 and incubated at 56 °C. During the experiment, the capillary containing the superlattices (SLs) was placed in a thermal cell and the temperature was externally controlled. The sample was heated to the specified temperature value, kept for 10 minutes and then the scattering pattern was collected. A series of 10 scattering patterns were recorded at temperatures varying from 25 °C to 80 °C. When kept at RT (25 °C), the sample showed sharp peaks compatible with a crystalline structure. However, as expected, while the temperature was increased, a progressive broadening of the peaks was observed, leading to a complete melting at 80 °C. To evaluate if this caused the DNA detachment from the nanoparticles, the sample was cooled down to 25 °C *in situ*. Upon cooling, the pattern returned to the initial BCC shape, showing the ability of the DNA-coated NPs to hybridise. This thus confirmed that the NPs@DNA system was not degraded by heating up to 80 °C.

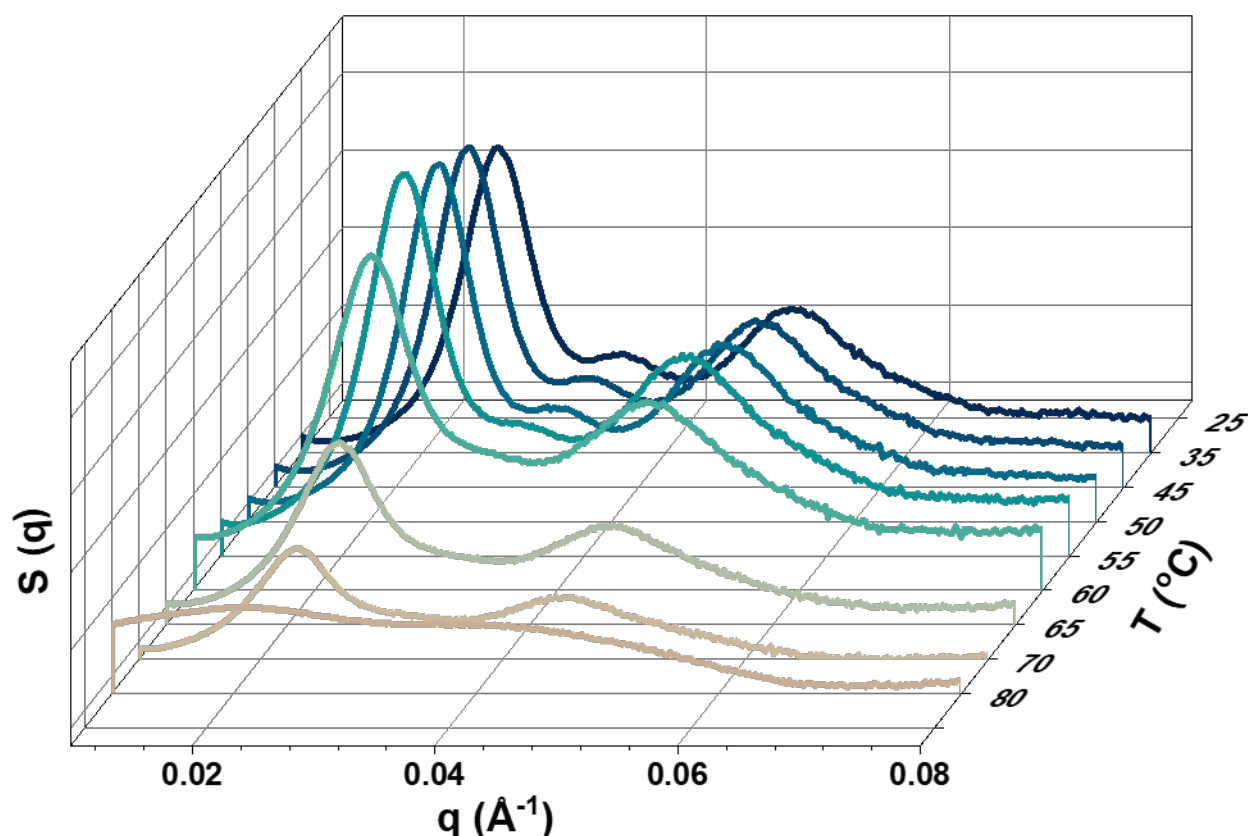


**Figure 3.35** Structure factor profiles at different temperatures for crystals made by 14 nm AuNPs functionalised with Res1 and Res2. Temperature range from 25 to 80  $^{\circ}\text{C}$ . As the temperature is raised, the scattering peaks became broader and less intense, proving the loss of the aggregate state.

In addition to the structural monitoring of the lattice, the crystal disassembly was also followed by UV-Vis. The lattice disassembly due to DNA dehybridisation under heating was followed by monitoring the variation in absorbance at 260 nm, analogously to the melting curves registered for the dsDNA alone (**Section 3.2.1**). **Figure 3.36** shows that in the presence of NPs, the melting temperature is shifted to higher values (60-65  $^{\circ}\text{C}$ ) compared to the DNA alone (56  $^{\circ}\text{C}$ ), as observed previously by SAXS (**Figure 3.34**). This finding can be justified considering that the presence of AuNPs at the ssDNA ends increases the steric hindrance and thus more energy is required to hybridise the DNA (higher energy barrier). However, after the hybridisation step, the overall stability of the system is enhanced, and the energy of the final state is remarkably lower.

As for free oligonucleotides, the characteristic sigmoidal shape was observed also for DNA-NPs. However, unlike the case of the DNA by itself, the temperature-up cycle curve follows a sharper path than the temperature down cycle. This is due to the rate of mass transport processes. When

the temperature is raised, the melting (i.e. DNA dehybridisation) and the diffusion of non-aggregated DNA-AuNPs in solution is a rapid process. This results in a sharp transition, and the hyperchromic effect is observed within 2-3 °C span. Conversely, the reassembling and the sedimentation of the aggregate are much slower processes, which originates a smoother absorbance decrease. For this reason, the data collection was carried out by slowing down the scan rate; this allowed enough time to the system to aggregate during the cooling down cycle and diffuse in solution during the heating up cycle. This asymmetric behaviour was reproduced in every melting/cooling cycle performed.

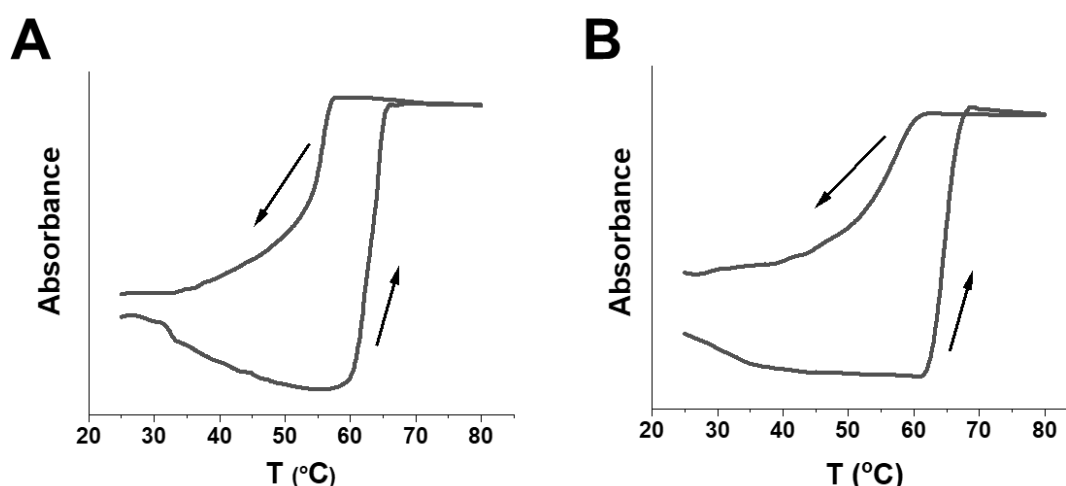


**Figure 3.36** (A) Melting curves for AuNPs 15 nm functionalised with Res1 and Res2. (B) Melting curve for AuNPs 30 nm functionalised with Res1 and Res2, recorded by monitoring the variation of absorbance at 260 nm.

Another factor to be considered is how fast the samples are brought back to room temperature. For the constant temperature annealing the samples were simply removed from the thermal mixer and allowed to cool naturally, in the case of the slow cooling procedure a different approach was preferred. To favour the most thermodynamically stable form, the crystallisation process needs to be thermodynamically-driven, rather than kinetically; for this reason, enough time needs to be given to the particles to reconfigure within the crystal. Consequently, different cooling rates profiles were tested, resulting in 5 to 7 days long crystallisation processes. **Figure 3.37** shows the scattering patterns as logarithm of the intensity vs  $q$ . All the samples were prepared starting from AuNPs 14 nm functionalised either with Res1 or Res2, mixed together in buffered solution with NaCl 0.3 M. They were then transferred to a thermal cycler and then two different cooling profiles were applied: for sample (a) represented by the black profile, the temperature was raised to 70 °C and cooled down to 25 °C at a steady rate of 0.1 °C/10 min. Instead, the rate applied to the sample (b) represented by the red profile was slower: the temperature was raised to 70 °C, firstly cooled down to 60 °C at a rate of 0.1 °C/10 min, then cooled down to 40 °C with a slower rate of 0.1 °C/20 min

and finally brought to RT at a rate of 0.1 °C/10 min. In the temperature profile applied to (b), a particularly slow rate was chosen around the melting temperature of the system (40-60 °C); this was done considering this stage as the most critical for an optimal arrangement of the particles. The data show that for (b) the peaks are slightly sharper than for (a). This suggested that increasing the time the sample was kept at its melting point had a little effect on the overall crystallinity.

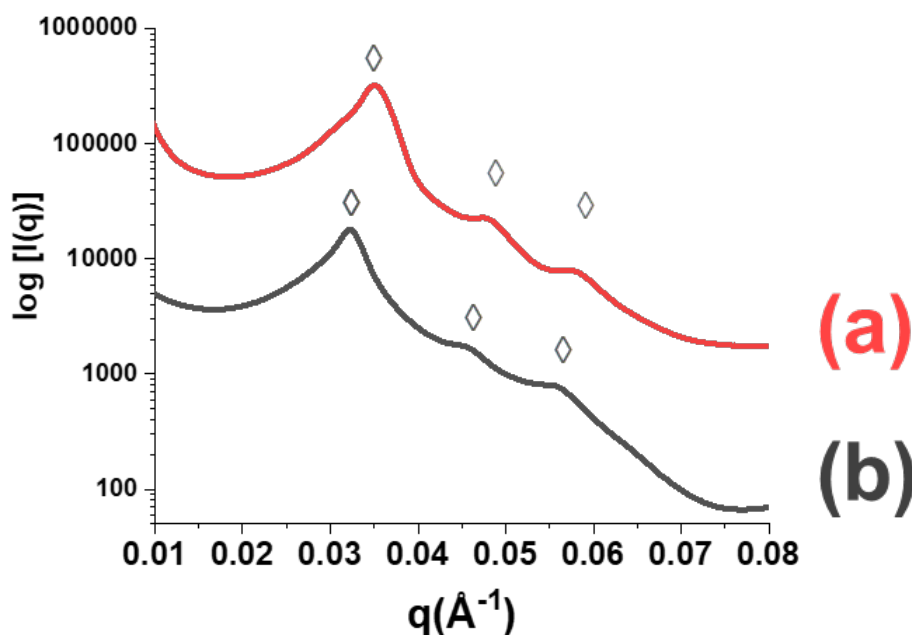


**Figure 3.37** Logarithmic scattering intensities for AuNPs 14 nm samples obtained by varying the cooling rate profile. The diamond symbol indicates peaks ascribable to a crystalline lattice.

Well-defined crystals of AuNPs were obtained using 0.3 M NaCl and by cooling down from 70 °C with a constant rate of 0.1 °C/10 min. These peaks were assigned to a body-centred cubic geometry (BCC) by calculating the theoretical SAXS patterns using the PowderCell software (available free of charge from the Federal Institute for Materials Research and Testing at [http://www.ccp14.ac.uk/ccp/web-mirrors/powdcell/\\_v/v\\_1/powder/e\\_cell.html](http://www.ccp14.ac.uk/ccp/web-mirrors/powdcell/_v/v_1/powder/e_cell.html)). This software is normally employed for the simulation of atomic scattering patterns, but it provides a good approximation of SAXS patterns from nanoparticle lattices as well. For NPs SLs, the attribution to a specific lattice and corresponding planes is performed considering the intensities ratios and relative positions  $q_{hkl}$  of the peaks. The position of the peaks on the  $q$  axis is dictated by the interparticle distance, which is dependent on the NPs' size. The relative distances between peaks is dictated by the geometry of the structure. Therefore, the interplane distance  $d_{hkl}$  can be calculated rearranging the Bragg Law as  $d_{hkl} = 2\pi/q_{hkl}$ , and obtaining the lattice parameter  $a$  as  $a = d_{hkl}\sqrt{h^2 + k^2 + l^2}$ . Finally, the nearest neighbour distance  $d_{nn}$  for a BCC spatial arrangement is equal to  $\sqrt{3}/2$ , resulting in 27 nm for the samples in **Figure 3.38**. For a lattice formed by AuNPs functionalised with Res1 and Res2,



the theoretical core-to-core nearest neighbour distance was calculated considering two 14 nm AuNPs linked by two DNA strands of overall length  $\approx 15$  nm. It resulted in 29 nm and the experimental value of 27 nm is in excellent agreement.

**Scheme 3.5** Schematic illustration of the theoretical core-to-core distance between two 14 nm NPs linked by 45 base pairs DNA strands.

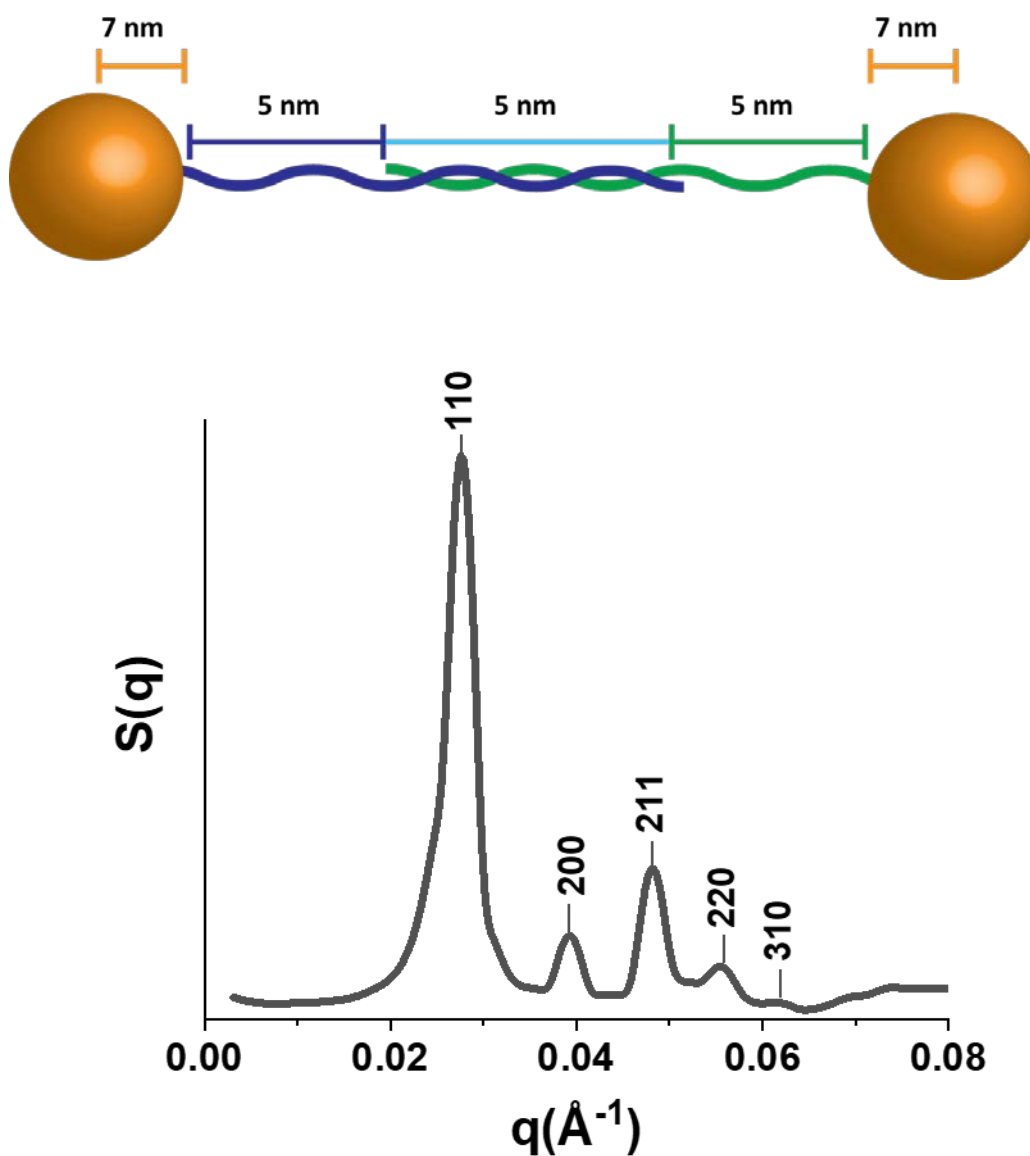


**Figure 3.38** Indexed body-centred cubic superlattice obtained from the assembly of 14 nm AuNPs. The crystallisation protocol involved a slow-cooling from 70 °C at a rate of 0.1 °C/10 min.

To allow imaging under vacuum and avoiding the collapse of the crystal in those conditions, the superlattices were silanised (see experimental in **Section 2.3.3**). In the first step of this procedure TMSPA is added to a shaking suspension of the as-synthesised SLs, where TMSPA was present in large excess relative to the number of phosphate groups on the DNA. This reagent is formed by a

positively charged moiety, a trimethyl ammonium quaternary salt, linked with a propyl to a trimethoxy silyl group (structure and working mechanism in **Figure 3.39**). The ammonium's role is to electrostatically bind the DNA phosphate backbone while the silyl group serves as co-condensation site for a silica growing agent subsequently added to promote the silica condensation. As a growing reagent, two different molecules were tested (Tetraethylethoxysilane, TEOS, and Triethoxysilane, TES). These precursors have different reactivity, typically a thicker layer of silica is grown with tetraethylethoxysilane. This molecule has four ethoxy groups that can act as nucleation point for the growth of  $\text{SiO}_2$ , while the triethoxysilane only has three: this forms a thinner silica shell that allows a better visualisation of the nanoparticle features in the crystals.

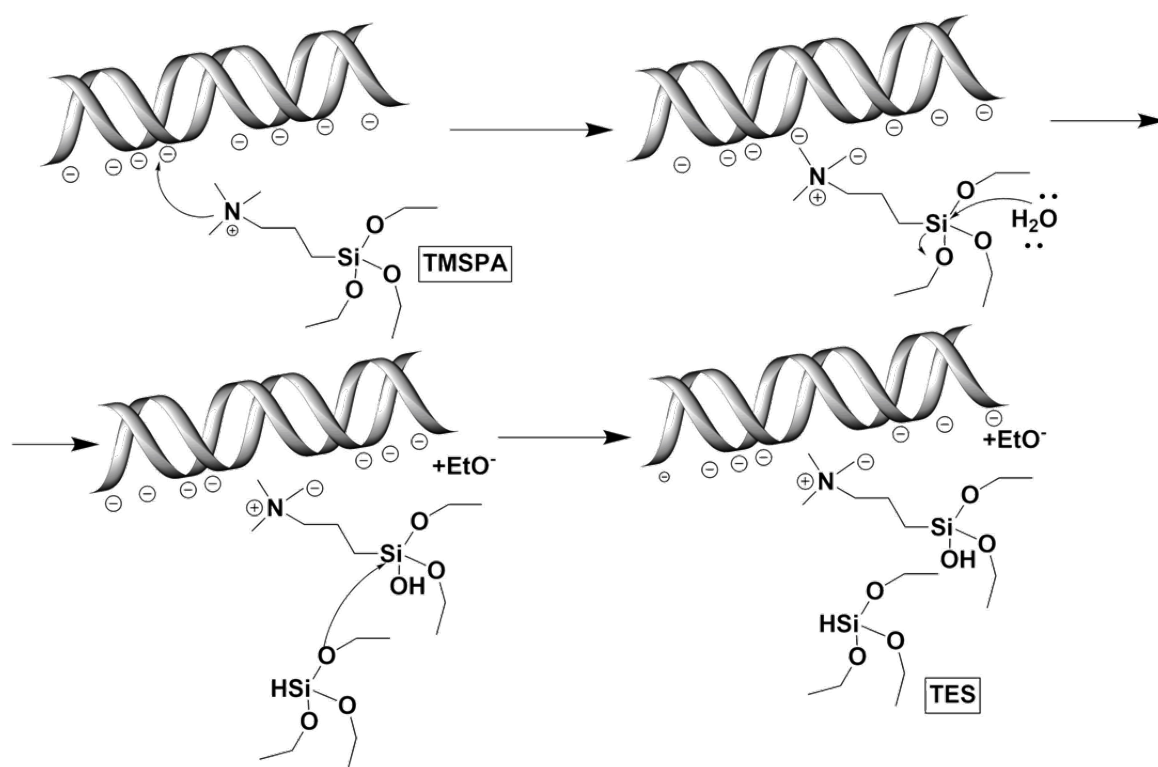


**Figure 3.39** Chemical structures of TMSPA and TES and reaction mechanism for the growth of a silica layer around the DNA duplex. Initially, the TMSPA electrostatically binds the negatively charged phosphate backbones of the dsDNA. This constitutes a nucleation point for the growth of a thicker layer of silica, following addition of TES.

This procedure presented several experimental challenges: first of all, it is challenging to know the number of crystals formed during the crystallisation. Thus, it is difficult to choose the amount of silica reagents to be used. An estimation of the needed silanisation reagents was made by assuming the same number of ssDNA on each AuNPs and considering that all the AuNPs participate in the SLs assembly. Another issue is the overall poor control over silica growth, which leads to the formation of amorphous silica structures as by-products. An attempt to mitigate this problem consisted in

carrying out the reaction at a neutral pH to slow down the condensation step.<sup>172</sup> Despite these difficulties, the silica encapsulation is currently the best option to obtain images of the samples.

In **Figure 3.40** scanning electron micrographs of different magnifications are shown. In particular, in **Figure 3.40C** shows the ordered arrangement of the individual nanoparticles can be appreciated.

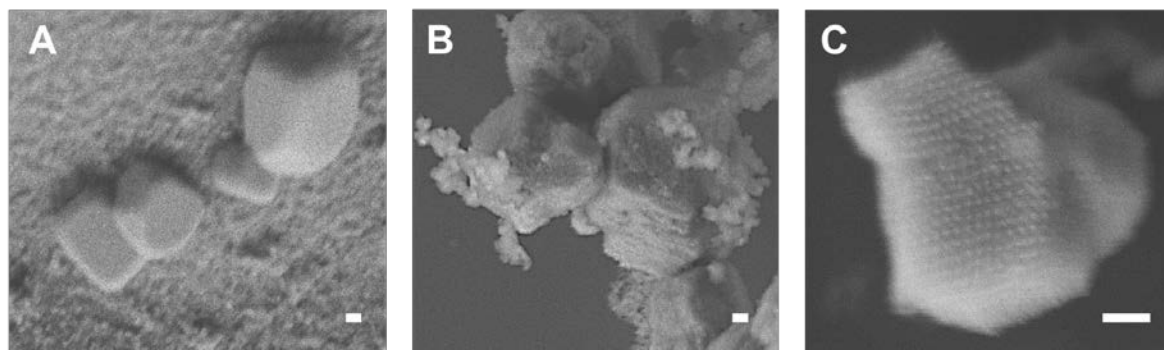


**Figure 3.40** SEM micrographs of a 15 nm gold nanoparticles superlattice taken with increased magnification from A to C. Scale bars 100 nm.

In order to confirm the presence of gold, elemental analysis coupled with SEM imaging was performed. **Figure 3.41** shows the EDX spectra of a chosen area of the sample. **Table 3.2** summarises the quantification of the atomic percentages extracted from the EDX spectra. A large amount of silicon and oxygen was found, due both to the silica encapsulation and to the sample support. The silicon to oxygen ratio was 1:2, in agreement with their presence in the form of  $\text{SiO}_2$ . Along with silica, also  $\text{Na}^+$  and  $\text{Cl}^-$  ions were present, as NaCl was used during the assembly step to control the ionic strength of the suspension. Gold was also detected (*circa* 10%), even if in a lower amount than  $\text{SiO}_2$ . This finding was justified considering the abundance of silica due both to the sample holder and the excess of silica produced during the crystals silanisation protocol.

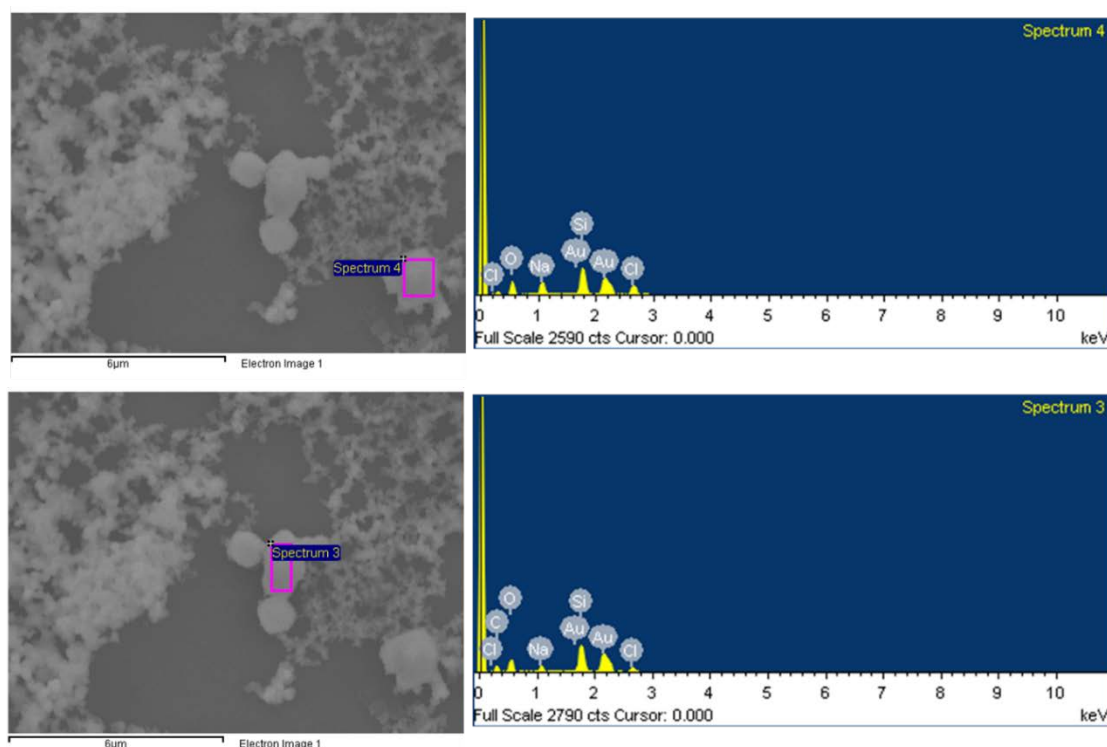


**Figure 3.41** SEM-EDX analysis on the sample AuNPs@Res1 + AuNPs@Res2 slow cooled (0.1 °C/10 min) from 70 °C.

**Table 3.2** Atomic percentages extracted from SEM-EDX spectral analysis.

Spectrum	Si (%)	O (%)	Cl (%)	Na (%)	Au (%)	Total
Spectrum 3	17.00	30.35	5.24	3.36	8.72	100.00
Spectrum 4	23.15	38.47	15.42	11.82	11.14	100.00
Mean	20.08	34.41	10.33	7.59	9.93	-
Std. deviation	3.08	4.06	5.09	4.23	1.21	-

### 3.4.2 Silver nanoparticles assembly

The assembly of silver nanoparticles *via* DNA interactions was also investigated. Building upon the previous studies performed on AuNPs 3D assembly (**Section 3.4.1**), the annealing at constant

temperature was not employed in this case. Instead, the slow cooling protocol was preferred as a result of the better crystal quality obtained for AuNPs. Different temperature profiles and inorganic salt concentrations were tested. Typically, two batches of AgNPs functionalised with the complementary strands Res1 and Res2 were incubated together in a ratio 1:1, to form a BCC lattice. Next, sodium chloride was added to screen the negative charge of the DNA backbones and allow the hybridisation. The samples were placed in a thermal cycler machine, to allow the accurate control over applied temperature gradients. The samples were then brought to a temperature above the DNA  $T_m$  and allowed to cool with a controlled rate. A UV melting analysis was carried out to investigate the temperature-resolved assembly/disassembly process (**Figure 3.42**). The  $T_m$  was determined at the inflection point of the curve obtained during the ramp up cycle, and it resulted into 63.3 °C.

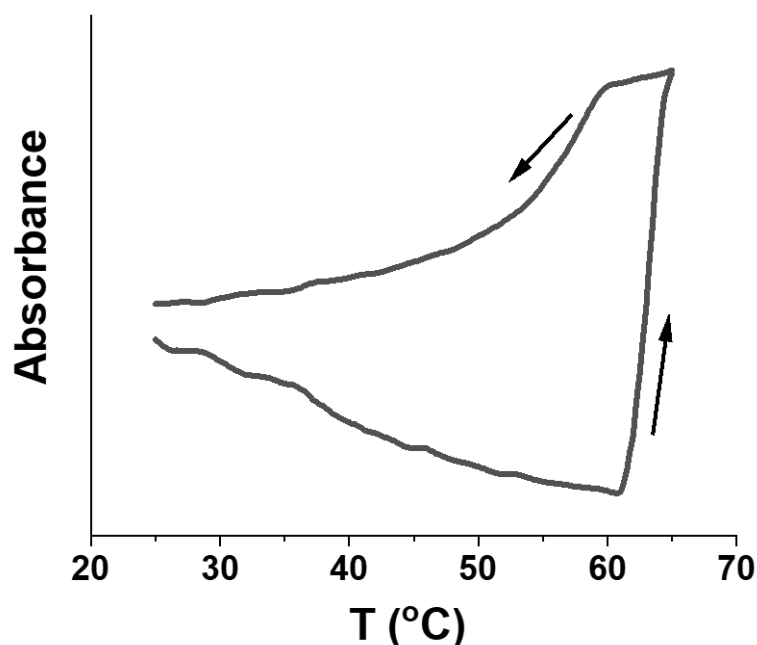


**Figure 3.42** Melting curves for AgNPs 15 nm functionalised with Res1 and Res2. The  $T_m$  was determined at the inflection point of the ramp up cycle, and it resulted into 63.3 °C.

Well-defined crystals of AgNPs were obtained working in phosphate buffer 80 mM and NaCl 0.3 M, at a cooling rate of 0.1 °C/10 min from a starting temperature of 70 °C. Corresponding SAXS with coherent indexing is reported in **Figure 3.43**, where the expected peaks for a BCC lattice emerged.

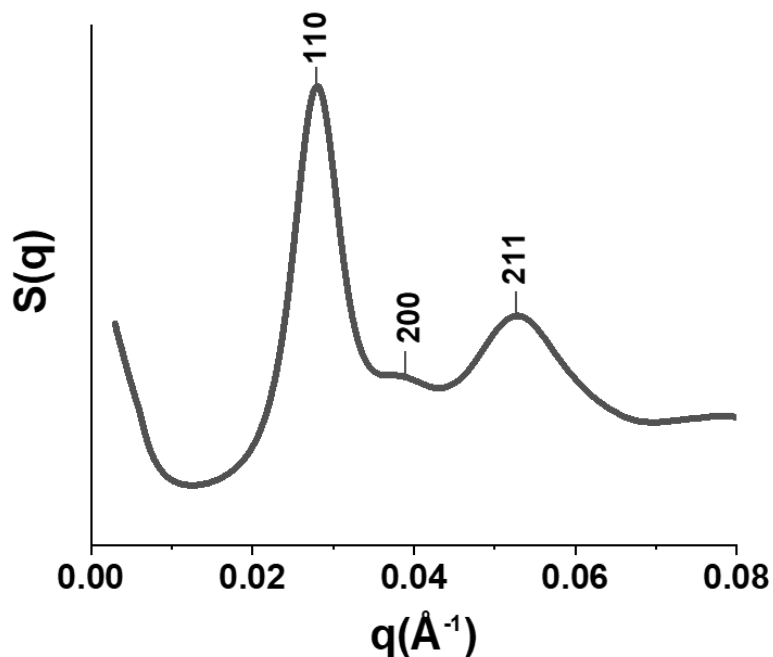


**Figure 3.43** Indexed structure factor of an AgNPs-DNA SL slow-cooled at 0.1 °C/10 min from 70 °C in phosphate buffer 80 mM and NaCl 0.3 M.

From the SAXS profile in **Figure 3.43**, the interplane distance  $d_{hkl}$  was calculated by rearranging the Bragg Law (see **Section 3.4.1**). For a lattice formed by 15 nm AgNPs functionalised with Res1 and Res2, the theoretical nearest neighbour distance was predicted to be 26 nm and the experimental value was 28 nm (calculated from  $q_{110}$ ).

To be able to image the structures under vacuum, a silica layer was grown on the crystalline structures (see experimental in **Section 2.3.3** and detailed discussion in previous **Section 3.4.1**). SEM images of silica-coated SLs are shown in **Figure 3.44**. Typically, a thicker layer of silica is grown with tetraethylethoxysilane (**Figure 3.44A-B**). When triethoxysilane is employed (**Figure 3.44C-F**) the layer is thinner and less homogeneous, allowing the visualisation of finer details.

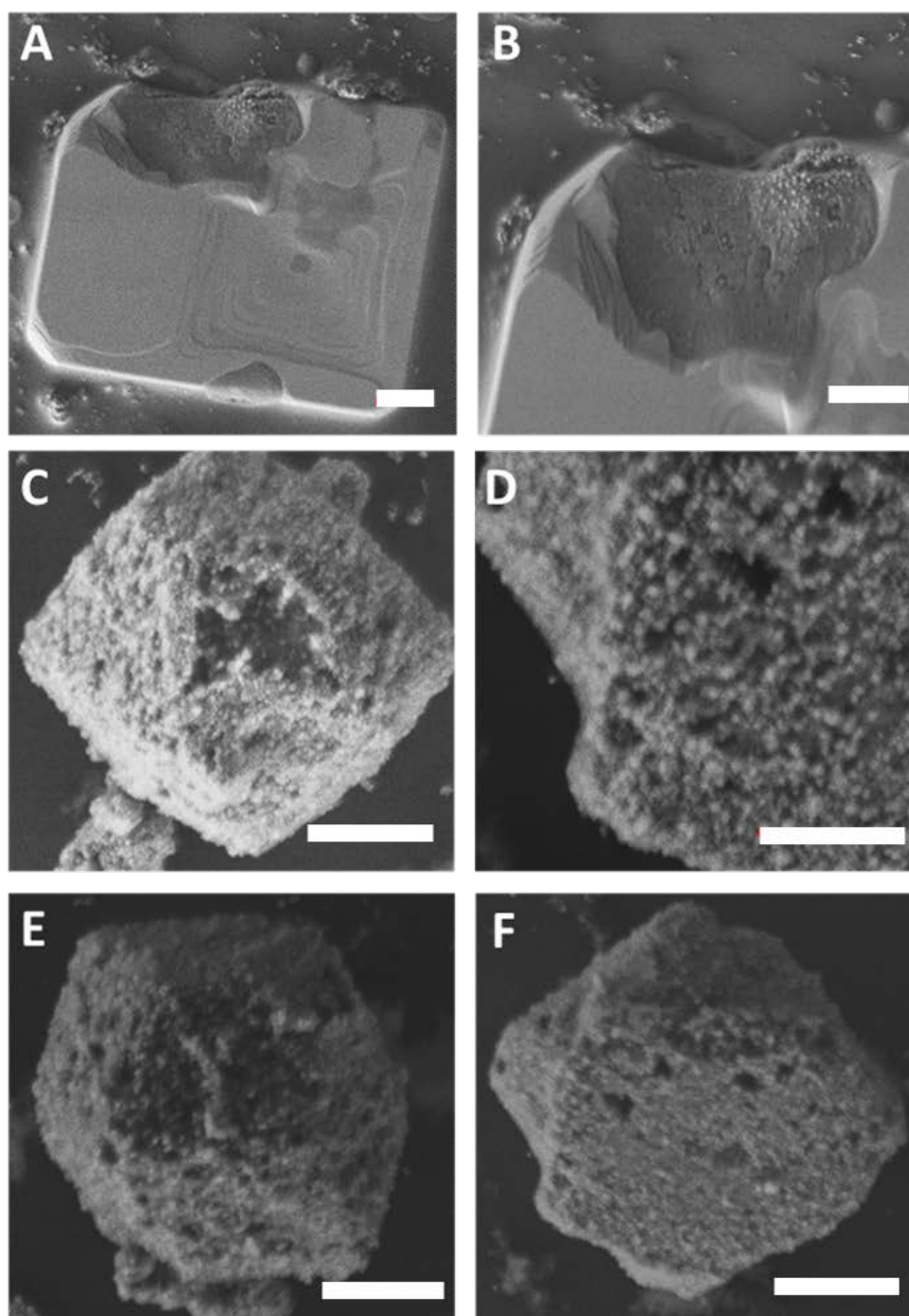


**Figure 3.44** SEM images of AgNPs superlattices obtained by slow ( $0.1\text{ }^{\circ}\text{C}/10\text{ min}$ ) cooling from  $55\text{ }^{\circ}\text{C}$ . A)-B) Tetraethylethoxysilane-coated; C)-F) Triethoxysilane-coated structures. All scale bars  $1\text{ }\mu\text{m}$ .

SAXS measurements were also recorded for the silanised AgSLs (**Figure 3.45**). Due to a large amount of amorphous silica in the sample, the diffraction peaks are less accentuated but still visible and compatible with a BCC lattice, confirming that after silanisation the BCC structure was retained

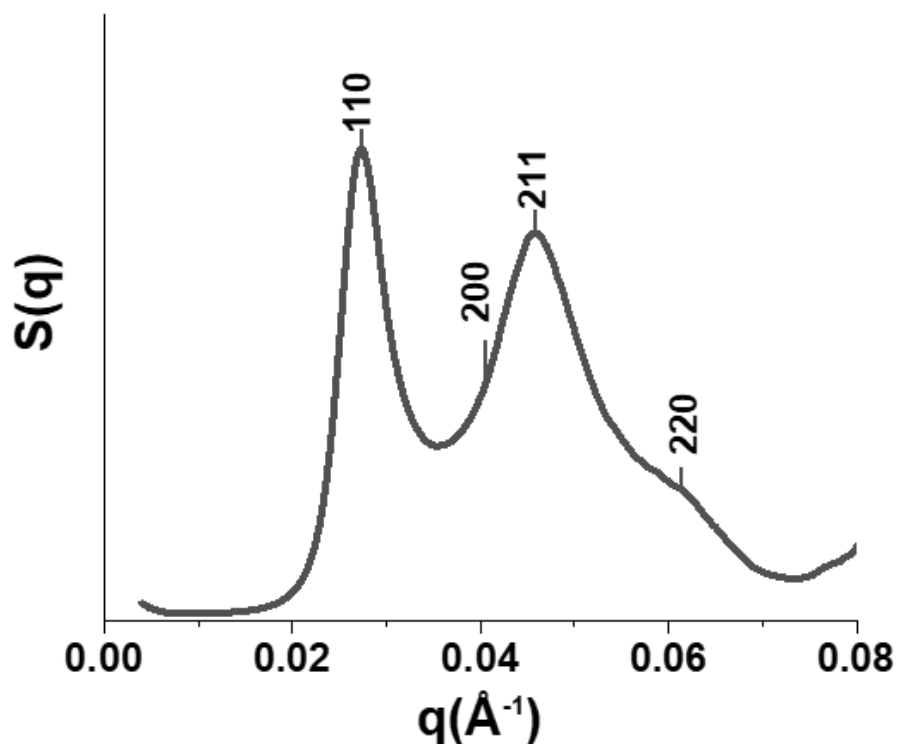


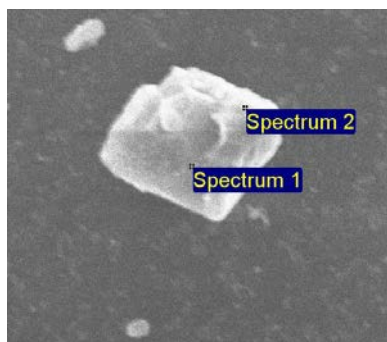
**Figure 3.45** SAXS pattern for a silanised AgSLs. The peaks relative to the BCC pattern are still visible, even though less clearly compared to the non-silanised AgSLs.

Elemental analysis in conjunction to SEM and TEM imaging was also carried out, and it showed an abundance of silver (over 70%) in the structures. Silicon due to both the encapsulation and to the substrate was also detected, in addition to Cl, due to the presence of sodium chloride. Interestingly, no Na or O was sensed, while they were detected in the case of AuSLs (**Table 3.2**). This dissimilarity lead also to different percentages of the metal content. This apparent incongruence was attributed to a different sensitivity of the instrument used to analysed AgSLs compared to the one used for the AuSLs.



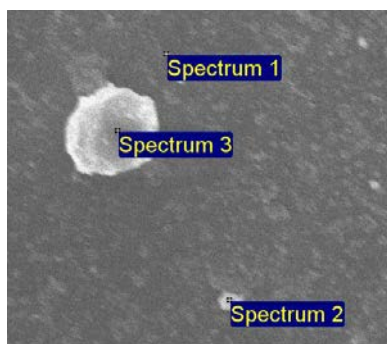
**Table 3.3** SEM-EDX analysis on the sample AgNPs@Res1 + AgNPs@Res2 treated at 55 °C in 40 mM PBS buffer. Scale bar 1  $\mu$ m.

**Image 1**



Spectrum	Si	Cl	Ag	Total
Spectrum 1	6.25	20.45	73.30	100.00
Spectrum 2	9.42	17.99	72.59	100.00
Mean	7.84	19.22	72.94	100.00
Std. deviation	2.24	1.74	0.50	

**Image 2**



Spectrum	Si	Cl	Ag	Total
Spectrum 1	100.00			100.00
Spectrum 2	27.39		72.61	100.00
Spectrum 3	3.62	19.18	77.20	100.00
Max.	100.00	19.18	77.20	
Min.	3.62	19.18	72.61	

EDX spectroscopy was employed in combination with TEM imaging, to further confirm the presence of silver in the cubic structure visible at low magnification. In addition to the Ag contained in the crystal structure, also Si and Cl were detected, as already highlighted by SEM-EDX. The presence of copper was attributed to the substrate used for TEM imaging.

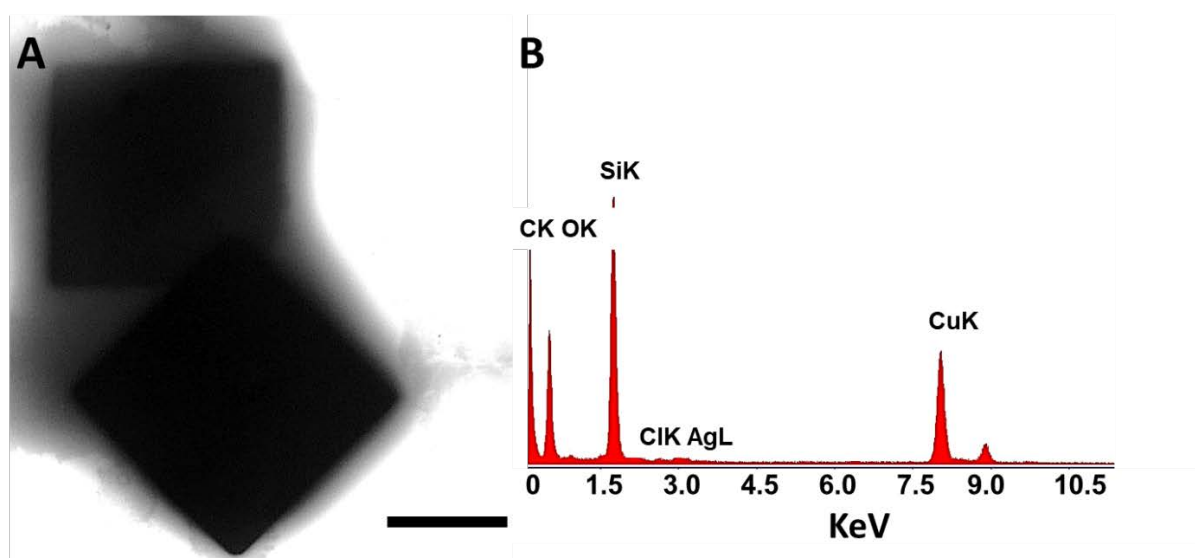


**Figure 3.46** TEM image (A) and corresponding elemental analysis spectrum, showing the presence of silver. Scale bar 2  $\mu\text{m}$ .

### 3.4.3 Upconversion nanoparticles assembly

The three-dimensional assembly of UCNPs of different sizes and compositions, functionalised with either the PAA method or the silanisation approach was carried out. In a typical experiment, two batches of UCNPs functionalised with the amino-terminated complementary strands Res1 and Res2 were mixed in equimolar amounts. Unlike gold and silver, UCNPs do not have a UV-Vis band that can be used to precisely calculate the molar concentration; to overcome this issue a mathematical model based on the geometry and size of the system was employed.<sup>179</sup> According to this model, 1 mg of UCNPs@DNA corresponds to *circa* 10 pmol, hence 1 mg of each UCNPs@Res1 and UCNPs@Res2 were employed for the assembly. The mixture was transferred in a thermal cycler and allowed to cool down from a temperature above the  $T_m$  at a constant rate of 0.1  $^{\circ}\text{C}/10$  min (duration 5 days). The crystallisation procedure was performed both on 45 nm PAA-coated UCNPs and on 45 nm and 12 nm silica coated UCNPs NPs.

The so-obtained samples were characterised by SAXS and SEM imaging. **Figure 3.47** shows, the SAXS patterns obtained from DNA-directed aggregates of 40 nm UCNPs@PAA. Multiple peaks of decreasing intensity as  $q$  increases emerged. It was not possible to assign this pattern to any crystal configuration, which suggests that the particles were not organized in a crystalline structure. A hypothesis is that the prolonged time at relatively high temperature may cause the release of the physisorbed PAA ligands from the UCNPs' surface and the consequent loss of the ssDNA coupled to the PAA. The absence of oligonucleotides on the NPs prevents the self-assembly and causes the destabilisation of the UCNPs in aqueous solution, which irreversibly aggregate. Moreover, the anisotropy of the particles may have played a role as well. The anisotropy of the system may give

rise to a different forms of assembly due to the directionality of the bond.<sup>141</sup> In particular, due to high aspect ratio, one can expect that the majority of the DNA interactions between two UCNPs will be face to face. This is due to the significantly reduced surface area along the edges of the prisms. Compared to the large hexagonal faces, the edges accommodate fewer DNA strands able to participate in hybridization events, thus the face-to-face binding is more likely. A previous work<sup>141</sup> reported the presence of lines of gold triangular nanoprisms, showing a scattering pattern akin to the one reported in **Figure 3.47**.

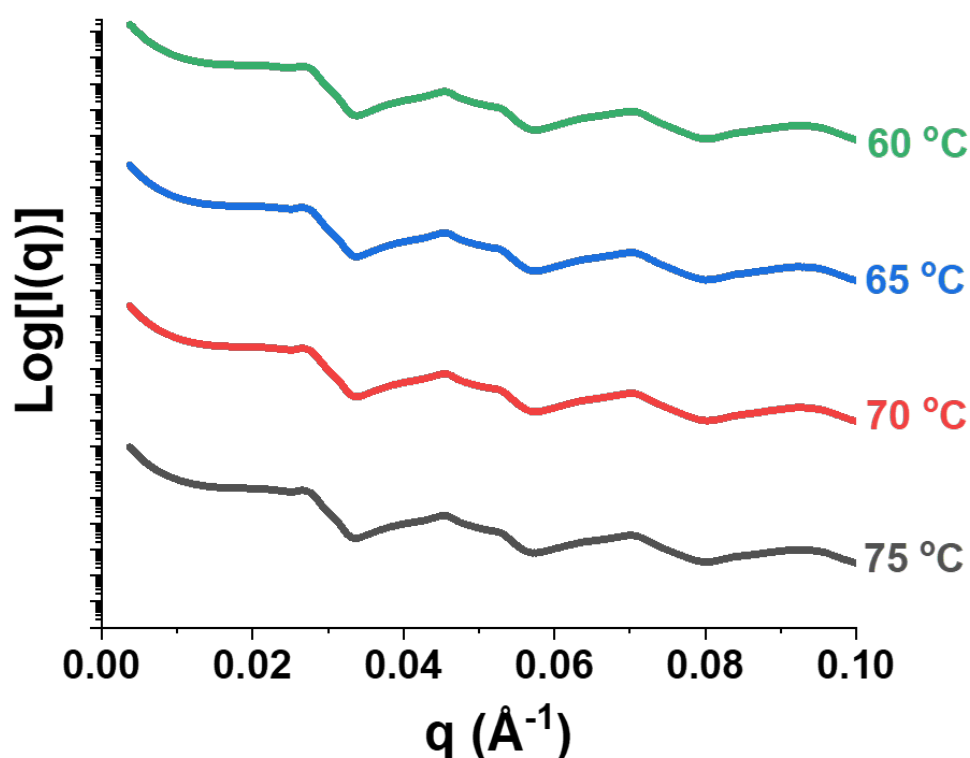


**Figure 3.47** Logarithmic scattering intensity profiles obtained from aggregates of DNA-coated 40nm UCNPs@PAA.

Silica coated upconversion nanoparticles were also employed to make crystals instead of PAA-coated UCNPs. Thanks to the presence of a rigid coating on the NPs' surface available for oligonucleotide attachment, we predicted that the overall stability of the UCNPs@ssDNA system would improve by preventing the release of the oligonucleotide from NPs' surface during the crystallisation.

On the other side, to address the anisotropy matter, smaller UCNPs were prepared. In fact, the reduction of the size of the NPs translated in an increased aspect ratio, hence the number of ssDNA that could be accommodated on the prisms' edges was closer to the number of strands ligated to the surface, thus minimising the preferentiality for the face-to-face interaction.

## Programmed Assembly of Nanoparticles

SAXS analyses are currently being undertaken at the NSLS-II synchrotron facility at Brookhaven National Lab (Upton, USA).

### 3.4.4 Iron oxide nanoparticles assembly

Silica-coated IONPs functionalised with complementary DNA strands NH<sub>2</sub>-Res1 and NH<sub>2</sub>-Res2 were used to attempt the fabrication of a three-dimensional magnetic assembly. In a typical experiment, two batches of IONPs functionalised with the complementary strands were mixed in equimolar amounts. Similarly to UCNPs, IONPs do not have a UV-Vis band that can be used to precisely calculate the molar concentration; to overcome this issue a mathematical model previously used for the UCNPs based on the geometry and size of the system was adapted to the IONPs.<sup>179</sup> According to this model, 3 mg of IONPs@DNA corresponds to *circa* 10 pmol, hence 3 mg of each IONPs@Res3 and IONPs@Res4 were employed for the assembly. The mixture was transferred in a thermal cycler and allowed to cool down from a temperature above the T<sub>m</sub> at a constant rate of 0.1 °C/10 min. The resulting samples resulted into a brownish aggregate at the bottom of colourless solution. To check if the sample had retained any magnetic property, a neodymium magnet was used to gather the assembly, resulting in an aggregated collected in proximity of the magnet. Interestingly, after the removal of the magnet, the free IONPs rapidly returned to their initial state, while the aggregates retained the memory of the magnetic field.

Structural analyses *via* SAXS are currently being undertaken at the NSLS-II synchrotron facility at Brookhaven National Lab (Upton, USA).

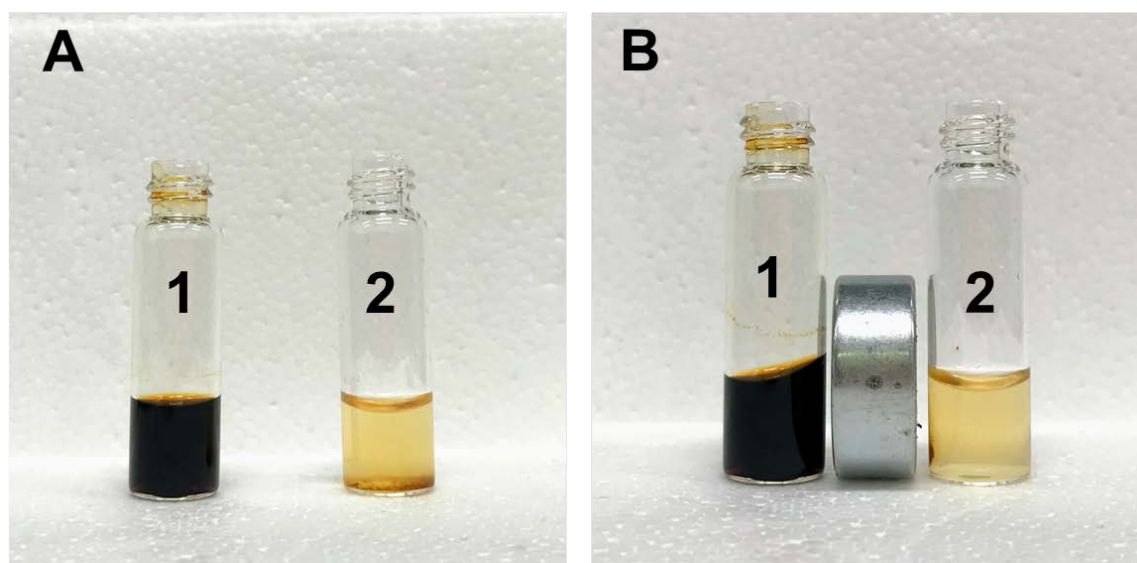


**Figure 3.48** Optical photographs of free IONPs (A.1) and DNA-assembled IONPs (A.2). In this latter case, brown aggregates can be noticed at the bottom of the vial. Following application of a magnetic field (B), both free IONP (B.1) and the aggregates (B.2) are rapidly attracted to the magnet.



## Chapter 4 Carbazole modification of synthetic oligonucleotides

In **Chapter 4**, the synthesis, functionalization and assembly of different types of nanoparticles are discussed. A new method to ligate DNA gold or silver nanoparticles using light is also presented here.

DNA is an exceptional platform for the directed assembly of NPs; however, it is intrinsically sensitive to DNA-denaturing conditions, which leads to the dehybridisation of dsDNA into its component strands. This instability represents a challenge for a thorough characterisation of three-dimensional assemblies of DNA and NPs, as it can prompt the dissolution of the superlattices (SLs). DNA-nanoparticle SLs are disassembled in conditions that induce DNA dehybridisation, such as elevated temperatures, low ionic strengths and other harsh environments such as low or high pH.<sup>107</sup>

To tackle this issue, fortified three-dimensional SLs have been fabricated by employing a chemically-modified DNA sequence to assemble nanoparticles. The chemical modification is a cyanovinyl carbazole molecule (shown in **Figure 4.1**), which photo-reacts with an adjacent base and creates a covalent chemical bond. The photochemical ligation of DNA provides enhanced stability of the DNA-nanoparticle assemblies under DNA denaturing conditions.

The chapter is organised as follows: in **Section 4.1** the oligonucleotides sequences are described and characterised. The assembly of AuNPs and AgNPs with the carbazole modified DNA strands is presented in **Sections 4.2** and **4.3** respectively. Finally, crosslinked SLs are employed to attempt the growth of microscale crystal structures (**Section 4.4**).

Parts of this Chapter have been published in “Light-Induced Reversible DNA Ligation of Gold Nanoparticle Superlattices”, Angela F. De Fazio, Afaf H. El-Sagheer, Jason S. Kahn, Iris Nandhakumar, Matthew Richard Burton, Tom Brown, Otto L. Muskens, Oleg Gang, and Antonios G. Kanaras, *ACS Nano* **2019** *13* (5), 5771-5777, DOI: 10.1021/acsnano.9b01294.

### 4.1 Carbazole modified oligonucleotide sequences

In this work, the fabrication of fortified crystals of DNA-coated NPs was achieved by introducing a cyanovinyl carbazole nucleobase in the DNA strands design. The carbazole-modified nucleobase reacts with an adjacent thymine located in the complementary DNA strand to form an interstrand covalent bond. Molecular structure of the carbazole modification is illustrated in **Figure 4.1** and detailed sequences are reported in **Table 4.1**. Each strand had a total length of 31 bases, containing

## Carbazole modification of synthetic oligonucleotides

a polyT spacer and a 15-base recognition region. The direction of the complementary section was designed such that 5' and 3' were reversed to allow the hybridisation. Every oligonucleotide was modified at the 3' end with a disulphide linker to facilitate the attachment onto gold and silver surfaces. One of the strands (Res1c) contained a nucleobase modified with a 3-cyanovinyl carbazole moiety, whereas the complementary strand (Res2c) did not contain any engineered nucleobase.

**Table 4.1** DNA sequences for crosslinking. In colour, the recognition region. The 'X' denotes the position of the cyanovinyl carbazole nucleobase.

Abbreviation	Sequence and Modification
Res1c	3'-SH-C <sub>3</sub> H <sub>6</sub> -TTT TTT TTT TTT TTT-TAA CCT AXAC CTT CAT-5'
Res2c	3'-SH-C <sub>3</sub> H <sub>6</sub> -TTT TTT TTT TTT TTT-ATG AAG GTGT AGG TTA-5'

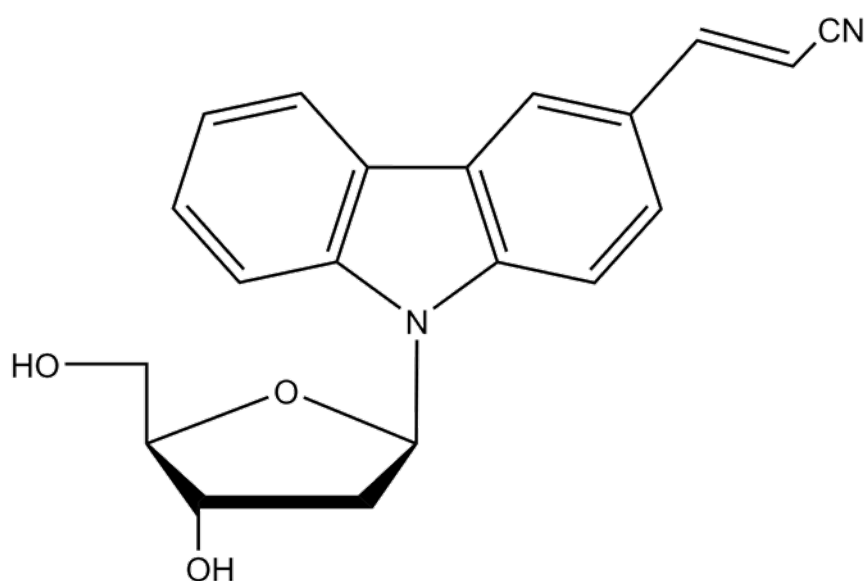


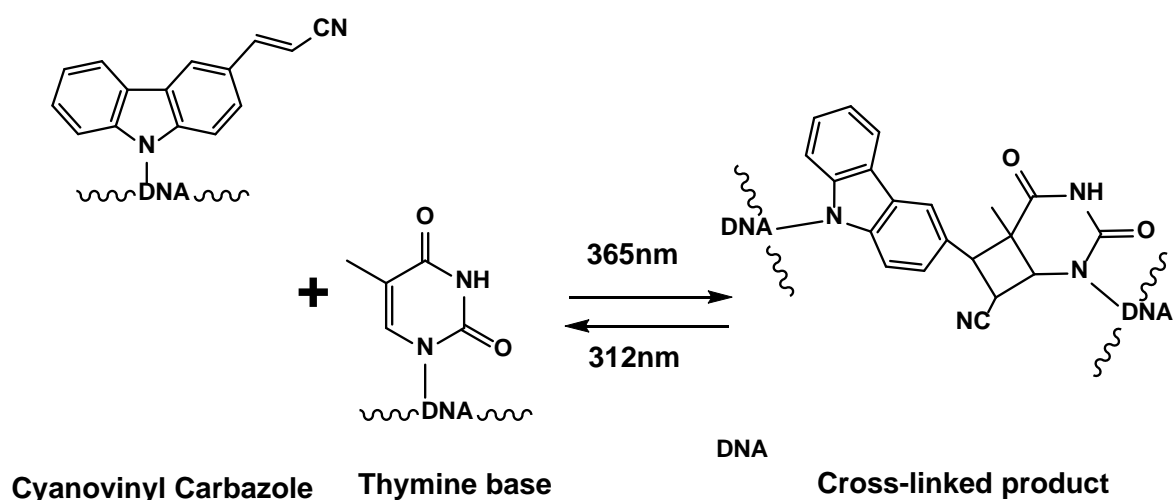
**Figure 4.1** Molecular structure of the 3-cyanovinyl carbazole nucleobase.

The position of the carbazole nucleobase within Res1c was carefully designed so that it would lay in the middle of the recognition region and it would diagonally face a thymine base. These two conditions are put into place to maximise the yield of the crosslinking reaction with the complementary DNA strand. In **Scheme 4.1**, a simplified reaction scheme for the photo-induced crosslinking reaction mechanisms between the 3-cyanovinyl carbazole and a thymine is illustrated (a detailed mechanisms and explanation can be found in **Scheme 1.6** and **Section 1.1.2.2**). When irradiated with 365 nm UV light, a thymine base is brought to an excited state. The C5-C6 double bond can now react with the electron withdrawing double bond of the cyanovinyl carbazole in the



opposite strand which eventually leads to the formation of a cyclo-butane.<sup>100,101</sup> In order for this reaction to happen, specific positioning of the cyanovinyl moiety with respect to the double bond is required; in particular, the reaction has a higher yield when the carbazole base faces diagonally the thymine base.<sup>102</sup> This occurs because the diagonal arrangement optimises the *p* orbitals overlap and reduces the cyclo-butane strain.<sup>108</sup> To allow the correct positioning of the thymine with respect to the carbazole, the strands need to be hybridised before the photocrosslinking is executed.

**Scheme 4.1** Reaction for the reversible [2+2] photocycloaddition. The double bond of a thymine base is brought to an excited state by irradiation at 365 nm. A concerted rearrangement of the electrons leads to the cyclobutane formation.



To test the effective hybridisation between Res1c and Res2c, a melting analysis was carried out by monitoring the characteristic DNA absorbance at 260 °C over three heating/cooling cycles. In this experiment, 200 pmol of each nucleotide were mixed together in phosphate buffer containing NaCl 0.3 M and the melting behaviour was monitored by UV spectroscopy (experimental procedure can be found in **Section 2.5.1.2**). **Figure 4.2** shows the variation in the absorbance at 260 nm over a temperature range spanning from 25 to 80 °C. In the graph the typical sigmoidal curve predicted for effective DNA dehybridisation can be observed, proving the hybridisation efficacy of the designed sequences. The melting temperature was determined at the inflection point of the sigmoid, resulting in 56 °C. This experimentally found value is in good agreement with the value calculated according to theory (54 °C) using the nearest neighbour approximation (see **Section 1.1.2.1**).

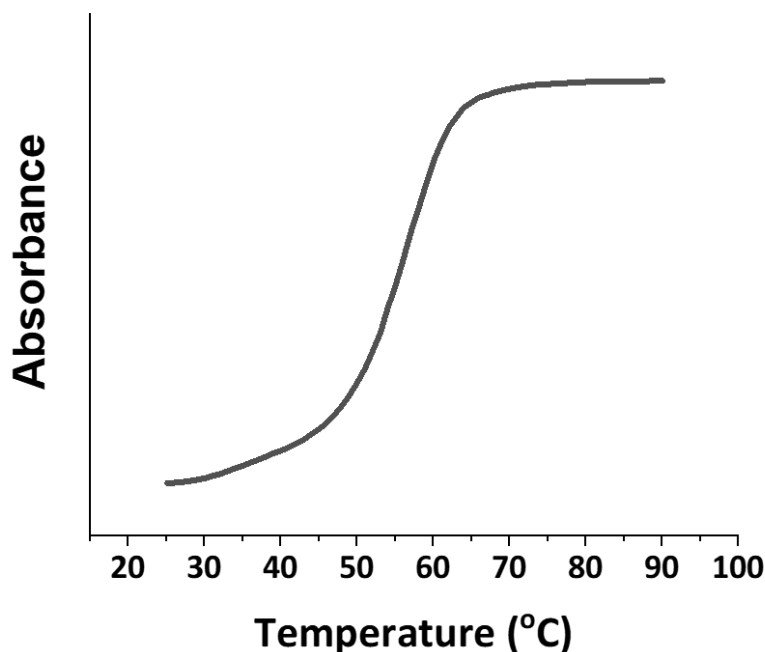


**Figure 4.2** Melting analysis for a duplex formed by Res1c and Res2c. The curve is the average result from three heating/cooling cycles. Melting temperature was determined from the inflection point and it was equal to 56 °C.

The difference of *circa* 2 °C is small considering the presence of the carbazole nucleotide in the middle of the complementary region of the sequence. The chemically modified adenine does not hybridise with the thymine adjacent nucleobase, thus resulting into an interruption of the complementarity, which could potentially cause a disruption during nanoparticle assembly. The melting analysis suggested that the designated positioning of the carbazole had little effect on the hybridisation efficiency of the dsDNA, thus validating the chosen sequence design.

#### 4.1.1 Polyacrylamide gel electrophoresis

In order to confirm the photoligation of two DNA strands after irradiation with 365 nm light a denaturing polyacrylamide (PA) gel was prepared by addition of urea in the polymer matrix (method in **Section 2.5.2**). Urea lowers the melting point of the dsDNA by breaking the interactions between the nucleobases. Thus, the incorporation of urea in the gel matrix causes the dsDNA to dehybridise into the corresponding ssDNAs while running through the gel. When denaturation occurs efficiently, the band corresponding to the dehybridised dsDNA will migrate at the same level of the corresponding single strands.

DNA duplexes of conventional oligonucleotides (Res1 and Res2) and photoligated carbazole-modified sequences (Res1c and Res2c) were monitored using DNA denaturing polyacrylamide gel

electrophoresis. Each sample was prepared in phosphate buffer 0.1 M and NaCl 0.3 M. Photoligated DNA was not affected by the denaturing conditions (lane 7). Conversely, non-photocrosslinked carbazole dsDNA was dehybridised (lane 6). **Figure 4.3** shows that, as expected, the conventional dsDNA (lane 3) migrated at the same height with the corresponding ssDNAs (lanes 1 and 2, respectively). On the other hand, the photoligated DNA (lane 7) was delayed compared to the corresponding ssDNAs (lanes 4 and 5 respectively), suggesting that the duplex form was retained. This proved that the photocrosslinked dsDNA was unaffected by the denaturing condition. For comparison, carbazole-modified dsDNA not exposed to UV light was also run (lane 6). When the photoligation step was not performed, the dsDNA containing the carbazole was denatured (lane 7).

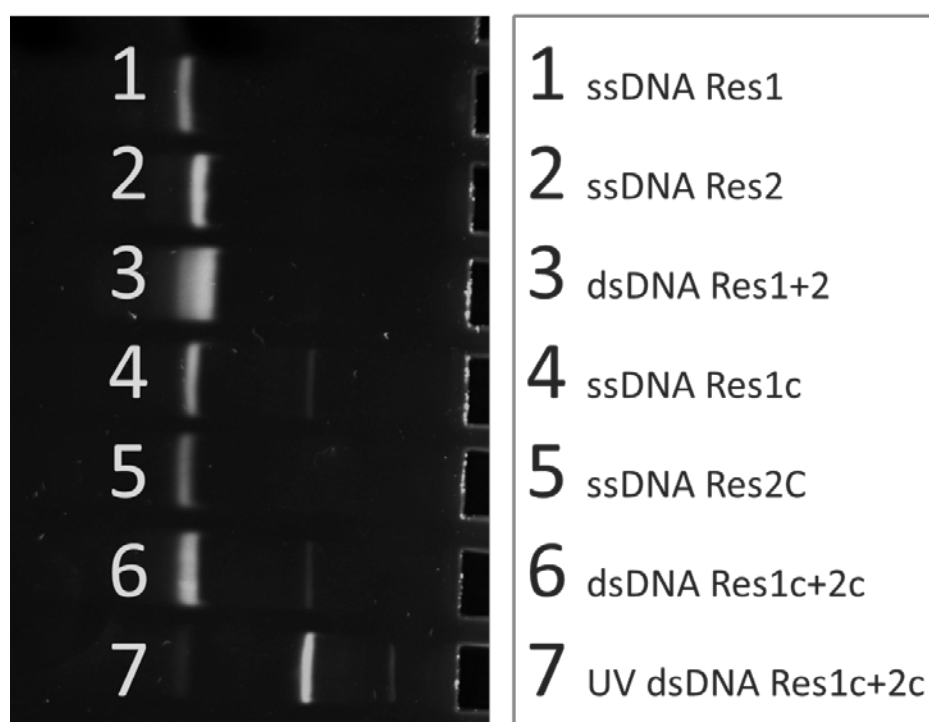


**Figure 4.3** DNA denaturing polyacrylamide gel of conventional and carbazole modified DNAs. The description of the samples loaded in each well is also included. The structures of the strands are depicted in **Table 2.1** (Res1 and Res2) and **Table 4.1** (Res1c and Res2c).

## 4.2 Reversible photo-ligation of gold nanoparticles superlattices

After testing the efficacy of photoligation, the carbazole-modified DNA strands Res1c and Res2c were used to assemble three-dimensional superlattices of gold nanoparticles. Two batches of AuNPs functionalised with Res1c and Res2c were mixed in equimolar amounts (for experimental details, see **Section 2.2** and **2.3**). Next, the DNA hybridisation was facilitated by addition of NaCl 0.3 M and the samples were placed in a thermal cycler. The crystallisation was promoted by heating

up the samples above the  $T_m$ , followed by the slow cooling at room temperature (cooling rate 0.1 °C/10 min). Detailed discussion about the crystallisation procedure can be found in **Section 3.4.1**.

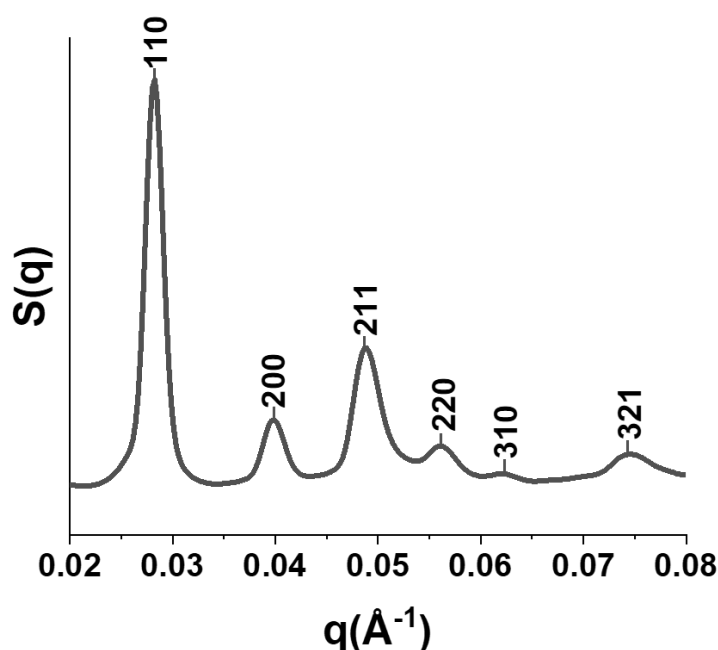


**Figure 4.4** Structure factor profile and corresponding peak indexing for a BCC SLs made from AuNPs functionalised with Res1c and Res2c.

**Figure 4.4** shows SAXS pattern for AuSLs obtained from the cyanovinyl carbazole-modified oligonucleotides prior to any light exposure. From the relative intensity and the position of the peaks it is possible to assign the pattern to a body-centred cubic configuration. The lattice parameter  $a$  was calculated from the relation with the interplane distance  $d_{hkl}$  as  $a = d_{hkl}\sqrt{h^2 + k^2 + l^2}$ . In turn,  $d_{hkl}$  was calculated from Bragg's Law as  $d_{hkl} = 2\pi/q_{hkl}$ . The nearest neighbour distance  $d_{nn}$ , core-to-core, was obtained from the cubic geometry of the unit cell and it was found to be 27 nm, in agreement with the predicted value (28 nm) based on the NP diameters and the DNA length. An average crystallite size of  $\sim 0.4 \mu\text{m}$  was estimated from the scattering correlation length  $\xi \approx 2\pi/\Delta q$ .

Following successful crystallisation of SLs with the carbazole-modified sequences, the effectiveness of the photoligation was investigated. **Figure 4.5** shows a visual comparison between NPs assembled using conventional (Res1 and Res2) and carbazole-modified oligonucleotides (Res1c and Res2c). After the slow-cooling procedure, both set of strands yielded a black sediment at the bottom of the capillary (**Figure 4.5A** and **B**). The SLs were then placed approximately 5 cm under the UV lamps and irradiated with  $\lambda = 365 \text{ nm}$  for 30 minutes at a power of  $50 \text{ mW/cm}^2$ . A 7 M urea solution was added, and the samples were heated to  $70 \text{ }^\circ\text{C}$  to induce DNA dehybridisation. In this condition, the aggregated state was retained exclusively for the assemblies composed by the

cyanovinyl carbazole-modified DNA strands, as proved by the black pellet observed at the bottom of the capillary tube (**Figure 5.5C**). This was further confirmed by the absence of black aggregates in the capillary containing the particles previously assembled with the set of conventional strands and also by a colour change of the solution from colourless to red that suggests the release of gold nanoparticles. This solution was analysed via UV-vis spectroscopy (**Figure 4.5E**). A sharp peak appeared at 523 nm, confirming the presence of well-dispersed 15 nm AuNPs.

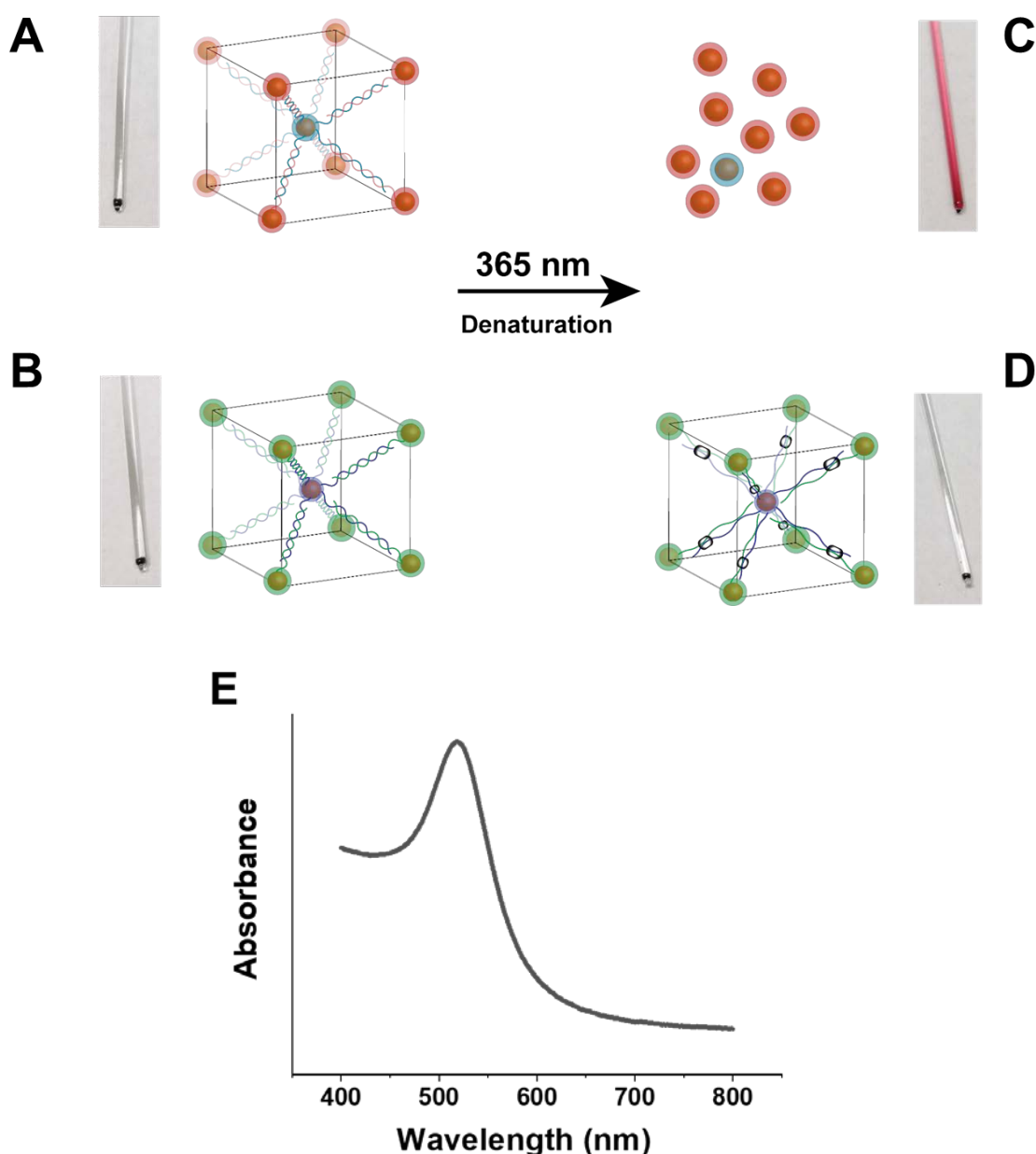


**Figure 4.5** Optical images and schematic illustrations of AuSAs assembled with conventional (A and C) or carbazole modified (B and D) oligonucleotides. In E, the UV-Vis spectrum of sample presented in C, showing a sharp plasmon peak centred at 523 nm, demonstrating the release in suspension of pristine AuNPs. Different colours code for different oligonucleotides sequences.

This hypothesis was further confirmed by scattering analysis. The SAXS profiles of crystals formed by conventional and modified DNA strands are reported in **Figure 4.6**. In **Figure 4.6A** the SAXS profile for SLs obtained from Res1 and Res2 in native condition (phosphate buffer 0.1 M and NaCl 0.3 M) shows the characteristic peaks for a BCC lattice, as previously discussed (**Figure 3.34**). To verify whether the assembly state was preserved under DNA denaturation conditions, urea (7 M) was added to the sample and the tube was heated to 70 °C for 5 minutes to prompt dehybridisation. In **Figure 4.6B**, the SAXS of the sample made from conventional strands displays no signs of ordered structures after light irradiation at 365 nm and the application of DNA denaturation conditions (urea 7 M, followed by heating at 60 °C). This confirmed that in the absence of the carbazole modification, irradiating with UV light did not induce DNA crosslinking or breaking and thus all crystalline ordering was lost upon DNA dehybridisation. In contrast, the SAXS for SLs made with the carbazole-modified photoligated sequences showed the same number and intensity ratio of the peaks before (**Figure 4.6C**) and after (**Figure 4.6D**) DNA denaturing, demonstrating the integrity of the crystal structure for a BCC lattice.

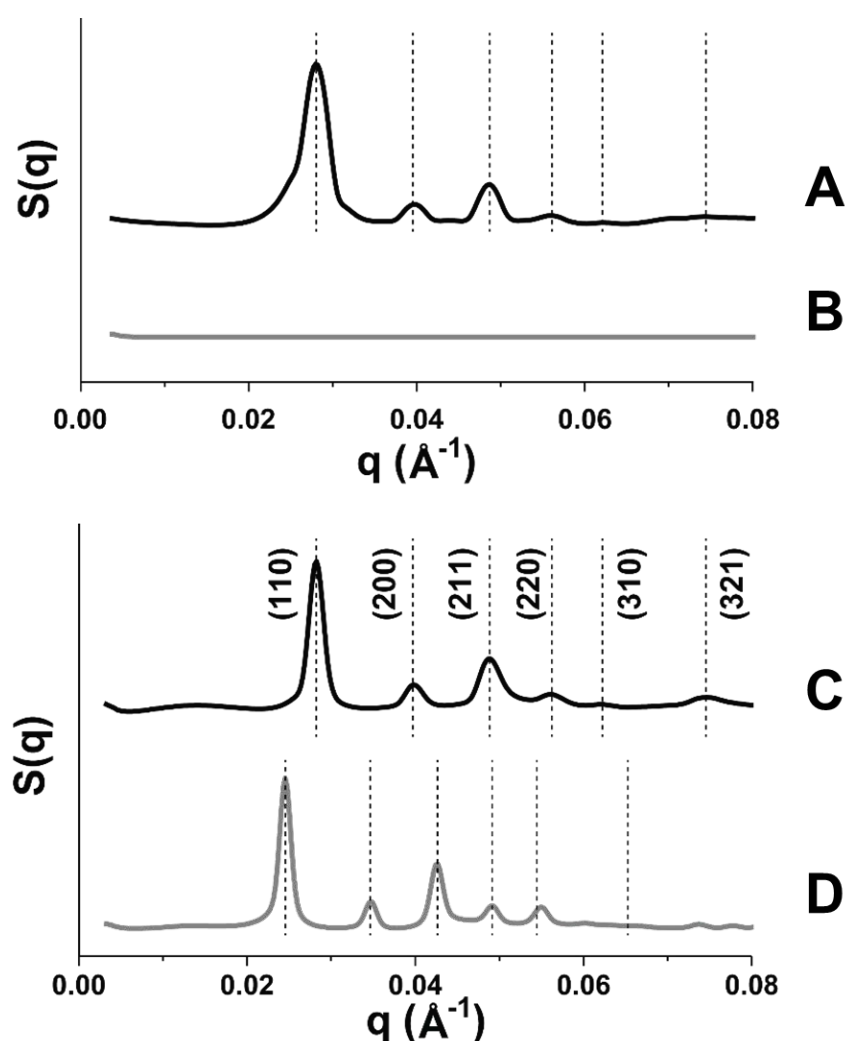


**Figure 4.6** Indexed SAXS profiles for AuSLs assembled with conventional (A and B) or engineered (C and D) oligonucleotides. In A and C the SLs were in native condition (phosphate buffer 0.1 M and NaCl 0.3 M), prior to irradiation, showing the characteristic peaks for a body-centred cubic lattice. Following irradiation and transfer to DNA-denaturing condition (urea 7M), the ordered structure is completely lost in the case of SLs assembled with conventional DNA strands (C). Conversely, peaks attributable to the cubic lattice could still be observed of the carbazole-modified SLs (D).

Interestingly, a noticeable shift of the peaks towards lower  $q$  values was observed for the carbazole-modified SLs after DNA denaturation. This finding implied a wider distance between NPs in the lattice; in fact, the nearest neighbour distance was shifted from 27 nm in native conditions to 31 nm for SLs in DNA denaturing conditions (“breathing” effect). Due to the denaturing environment, the oligonucleotide strands relaxed while the NPs were still held together by the crosslinking between the oligonucleotide strands. Consequently, the ordered structure was still maintained (as proved by the scattering signals) but the interparticle distance increased due to strand relaxation.

Often, DNA intercalators are used to increase the duplex stability by raising the  $T_m$  and thus preventing the dehybridisation at the working conditions. Instead, the carbazole create a covalent bond which does not prevent the dehybridisation but ligates the duplex, which is now found in a locked conformation.

#### 4.2.1 Photo-induced decrosslinking of gold nanoparticles superlattices

An interesting feature of the photoaddition of a cyanovinyl carbazole to a double bond is the reversibility of the reaction.<sup>100,101</sup> Irradiation at 312 nm induces the opening of the cyclobutane ring to yield the pristine reagents.

The carbazole-containing samples were illuminated with  $\lambda=312$  nm for 30 minutes at 50 mW/cm<sup>2</sup> to induce the cyclobutane ring opening. Structure factors of the decrosslinked aggregates in both native and DNA denaturing environment are depicted in **Figure 4.7**. In both cases, no interstrand covalent bond was present, but while in pattern labelled **A** the sample was in an environment favourable to DNA hybridisation, in **B** the conditions were switched to DNA denaturing ones. The BCC features are still visible in the pattern **A** because the UV irradiation only caused the ring opening, without prompting any dsDNA dehybridisation. Conversely, after transfer to DNA denaturing conditions, all the BCC features were lost, due to DNA dehybridization.

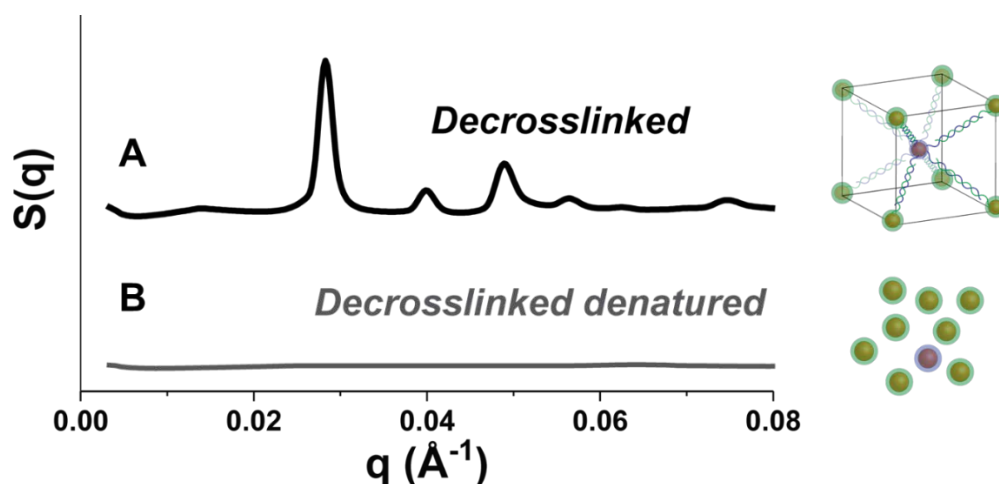


**Figure 4.7** Structure factor profiles for carbazole modified DNA AuSLs after decrosslinking with 312 nm radiation and corresponding schematic illustrations. (A) Decrosslinked AuSLs in native condition, (B) decrosslinked AuSLs after transfer in denaturing environment.

Furthermore, the disassembled particles were optically characterised, and their spectrum was compared to that of the AuNPs coated with oligonucleotides, recorded prior to the initial step of crystallization. As shown in **Figure 4.8**, the two spectra are superimposable, with no peak shift or broadening observed for the DNA-coated nanoparticles after UV light exposure.

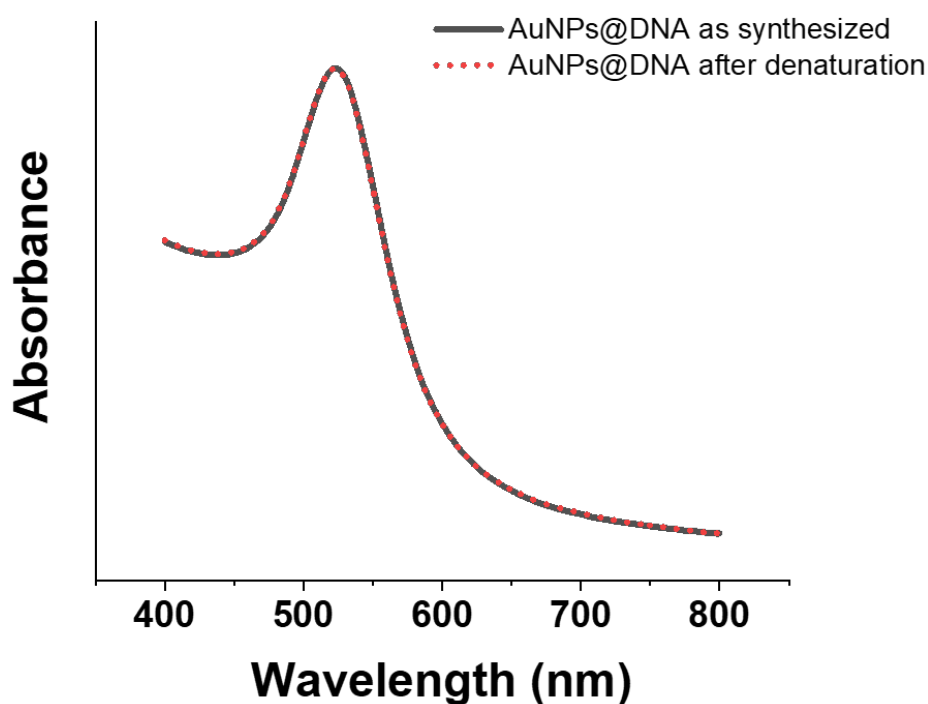


**Figure 4.8** Normalised UV-Visible spectrum of cyanovinyl carbazole-modified DNA-AuNPs prior to nanoparticle assembly (solid curve) and after DNA-denaturing of SLs, irradiated at 312 nm (red dotted curve).



This finding indicated that (i) the employed UV irradiation did not affect the integrity of the DNA-coated nanoparticles and (ii) the DNA-coated NPs were still intact after a full cycle of crystallisation, UV exposure and DNA denaturation. To confirm this last hypothesis and verify the full functionality of the oligonucleotides on the NPs' surface, a second crystallisation procedure was carried out. The NPs were transferred in phosphate buffer 0.1 M containing NaCl 0.3 M and placed in a thermal cycler. The sample was heated up to 70 °C and cooled down at a rate of 0.1 °C/10 min. After reaching room temperature, a black precipitate was observed. Scattering analysis confirmed that it was a BCC crystal with a lattice parameter and crystallinity comparable to the crystal fabricated in the previous steps. In **Figure 4.9**, SAXS profiles for the crystals obtained initially (**A**) is compared with the pattern obtained from the second crystallisation stage (**B**). No detectable differences in peaks number, intensity ratio or position were observed, confirming the full functionality of the oligonucleotide-coated NPs. This proved the complete reversibility of the cyanovinyl carbazole.

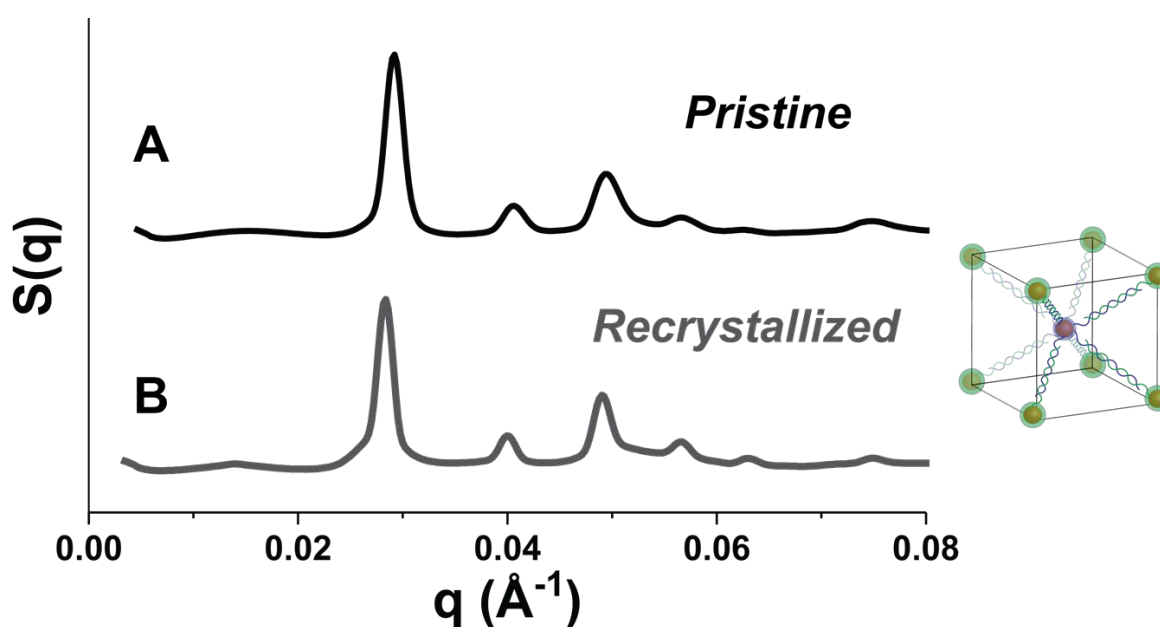


**Figure 4.9** Structure factor profiles for carbazole-modified AuSLs. In (A), the initially synthesised AuSLs are represented; whereas in (B) the SAXS curve for the secondary AuSLs, after recrystallization from decrosslinked AuNPs.

### 4.3 Reversible photo-ligation of silver nanoparticles

The functionality of the carbazole-modified DNA strands was further verified by using them to assemble silver nanoparticles.

First, crystals made with carbazole-modified (Res1c and Res2c) strands were synthesised using a controlled slow-cooling method (**Section 2.3.2** for experimental protocol and **Section 3.4.1** for discussion). Briefly, silver nanoparticles were functionalised with a dense shell of Res1c or Res2c and mixed in equimolar amounts in phosphate buffer 0.1 M and NaCl 0.3 M. The crystallisation was performed by placing the samples in a thermal cycler and slowly cooling down at a controlled rate (0.1 °C/10 min).

**Figure 4.10** shows the SAXS pattern for the AgSLs obtained from engineered DNA strands with corresponding peak attribution. As for the crystals assembled with Res1 and Res2 (**Section 3.4.2**), the AgNPs were arranged in a BCC lattice with a nearest neighbour distance of 26 nm (for calculations, see **Section 4.2**). The  $d_{nn}$  was in good agreement with the predicted value of 30 nm, estimated considering AgNPs of 15 nm in diameter and a DNA duplex of *circa* 15 nm in length when hybridised.

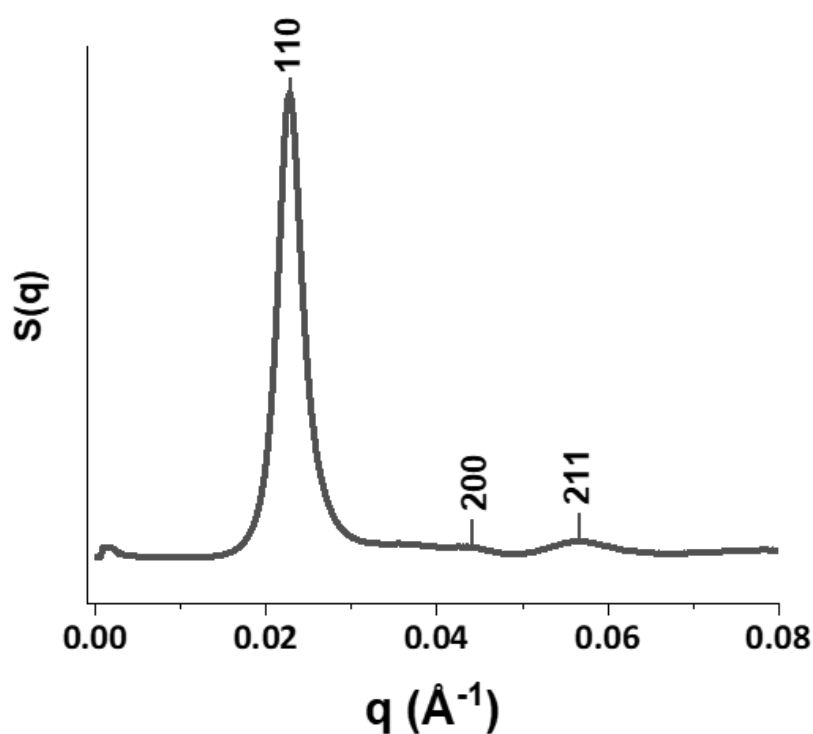


**Figure 4.10** Structure factor profile and corresponding peak indexing for a BCC SLs made from AgNPs functionalised with Res1c and Res2c.

After successful crystallisation, the photoligation was performed. **Figure 4.11** displays digital images of capillaries containing assemblies made from conventional (**B** and **D**) and modified (**A** and **C**) strands, before (**A** and **B**) and after (**C** and **D**) denaturation. As previously discussed (**Section 4.2**), the slow cooling procedure yielded a black sediment at the bottom of the capillary for both engineered and conventional strands (**Figure 4.11A** and **B**, respectively). The SLs were then exposed

to  $\lambda = 365$  nm for 30 minutes at a power of  $50 \text{ mW/cm}^2$  and transferred to denaturing environment. Upon denaturation, the aggregated state was preserved solely for the assemblies containing the cyanovinyl carbazole, as attested by the presence of the dark precipitate (**Figure 4.11C**). On the contrary, particles previously assembled with the set of conventional strands were readily dispersed in solution upon denaturation. The resuspension of the AgNPs was demonstrated by (i) the absence of the black aggregate and (ii) by a colour change of the solution from colourless to yellow (**Figure 4.11D**). A UV-Vis absorbance measurement was carried out on sample represented in **D** and it is shown in **Figure 4.11E**. The presence of a sharp and well-defined peak at 407 nm confirmed the presence of well-suspended AgNPs.

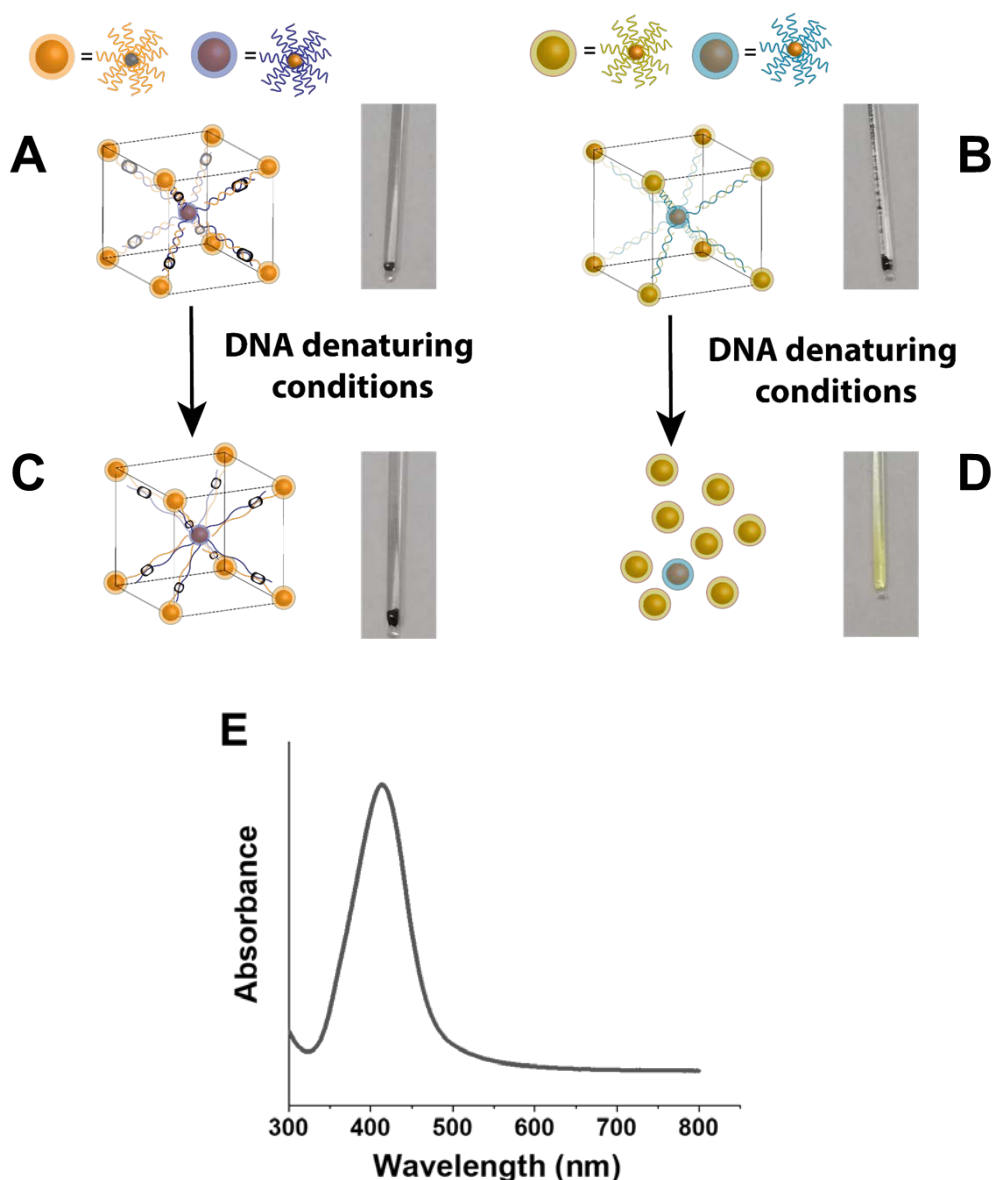


**Figure 4.11** Optical images and schematic illustrations of AgSLs assembled with conventional (A and C) or engineered (B and D) oligonucleotides. In E, the UV-Vis spectrum of sample presented in C, showing a sharp plasmon peak centred at 407 nm, demonstrating the release in suspension of pristine AgNPs.

Furthermore, AgSLs were characterized by SAXS measurements that are reported in **Figure 4.12** for both native and DNA denaturing environment, labelled respectively as (B) and (C). As previously observed (**Section 4.2**), although the BCC lattice structure was preserved, the application of DNA denaturing conditions caused the dehybridisation of the DNA strands as previously observed in **Section 4.2**. This resulted in an enlargement of the unit cell size, and the lattice parameter varied from 29 nm to 33 nm.

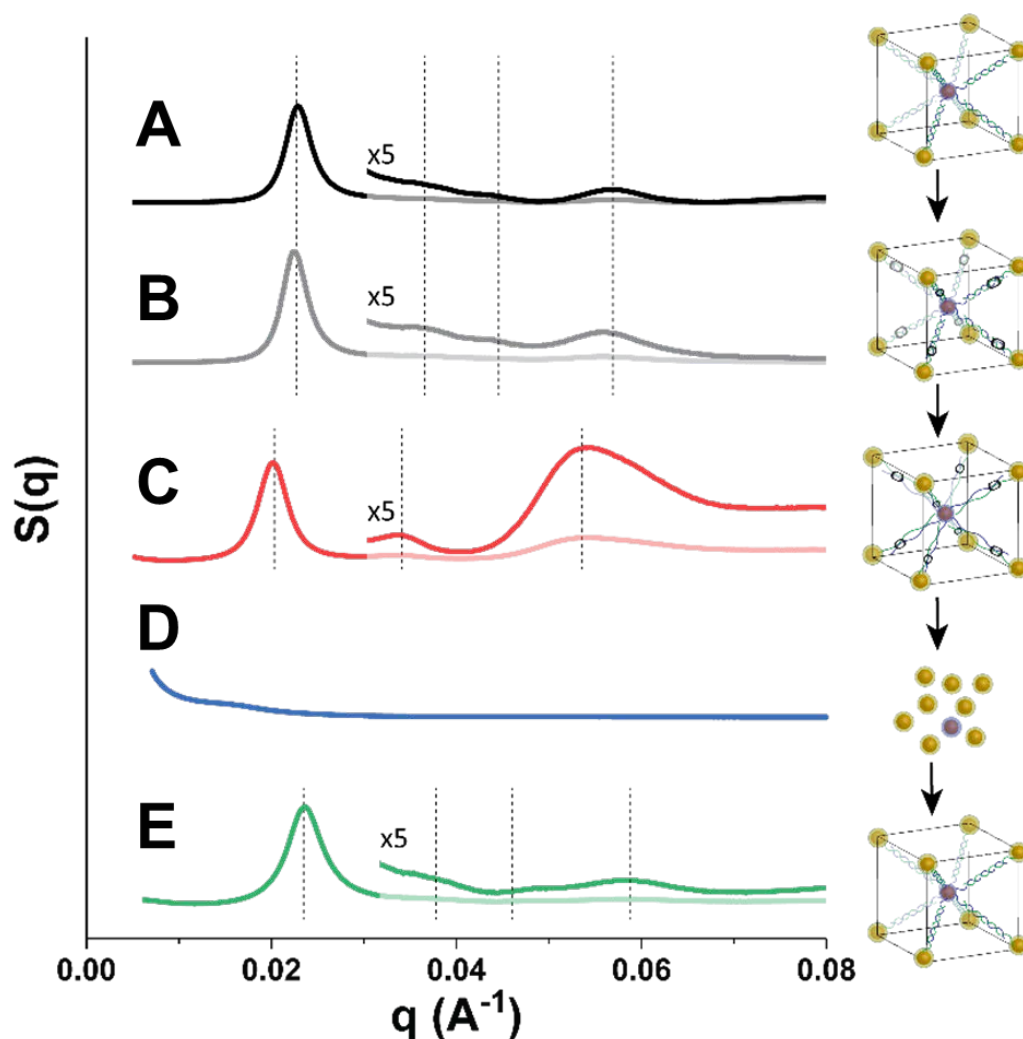


**Figure 4.12** Structure factor profiles for fortified AgSLs. (A) crystallised AgSLs, photocrosslinked AgSLs in native (B) and denaturing (C) conditions are, (D) denatured decrosslinked superlattices and (E) recrystallized AgSLs.

Following the photoligation, the reverse reaction was tested. The carbazole-containing AgSLs were exposed to  $\lambda=312$  nm for 30 minutes at  $50$  mW/cm<sup>2</sup> to induce the cyclobutane ring opening. Structure factor of the decrosslinked aggregates in denaturing environment is reported in **Figure**

**4.12D.** As predicted, after decrosslinking and transfer to denaturing conditions, all the BCC features were lost, due to the absence of any form of ligation between the oligonucleotides.

To verify whether the employed UV irradiation had caused any damage on the DNA-coated NPs, UV-visible spectroscopy was used to monitor the LSPR of AgNPs. In **Figure 4.13**, the spectrum of freshly synthesised DNA-functionalised AgNPs (solid line) is compared to the one recorded after denaturing cycle steps (dashed line). The maximum absorbance in both cases was found at 412 nm and no peak broadening was detected for the AgNPs after the photoligation procedure. To check the integrity of Res1c and Res2c, the recrystallization of the NPs was attempted. After this second slow-cooling step, peaks ascribable to a BCC lattice reappeared in the SAXS pattern (**Figure 4.12E**). This series of experiments confirmed what was previously found for AuNPs, that the carbazole technology is highly effective in providing robustness to NPs SLs without altering the DNA-NPs functionality.

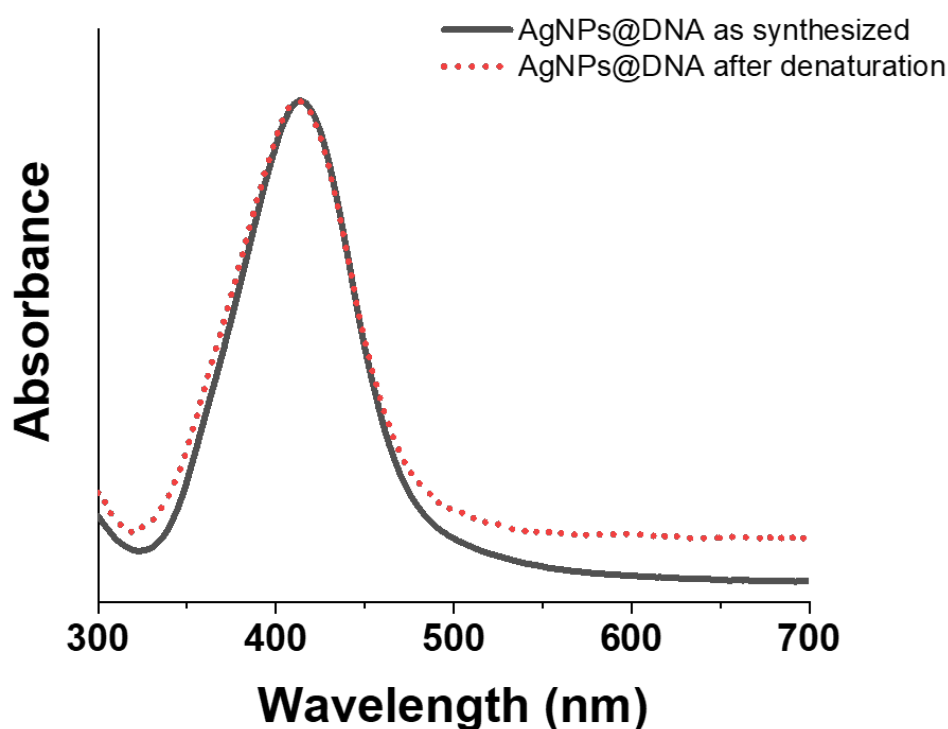


**Figure 4.13** Normalized UV-Visible spectrum of AgNPs before assembling (solid curve) and after assembling, crosslinking, decrosslinking and de-assembling procedure (red dotted curve).

## 4.4 Seeded growth of large superlattices

Part of the work presented in this section has been done in collaboration with Mr Joseph Cook and Miss Doxi Misatziou.

The presence of a robust interstrand ligation within the crystal structure could enable the fabrication of previously unachievable structures, such as core-shell or crystals of tens of micrometres.

In this project, preliminary work towards the fabrication of extended crystals has been carried out. Photocrosslinked gold superlattices were used as seeds to mediate the growth of larger structures by progressive addition of DNA-AuNPs. To help the preferential growth of existing crystals rather than the formation of new ones, some precautions in designing the experiment were taken. First, a gentle shaking was applied to disperse the existing crystals in the AuNPs suspension and make them available for uniform NPs attachment via DNA hybridisation. Secondly, to favour the growth of existing seeds, the operating conditions must be such that the energy provided to the system does not overcome the energy barrier for the formation of new nuclei. For this reason, the experiment was carried out at a temperature below 70 °C, *i.e.* the temperature used for the initial crystallisation process. Specifically, the growth was attempted at room temperature and at 50 °C.

In a typical experiment, the as-synthesised crystals were photocrosslinked by exposure to 365 nm light (30 minutes, 50 mW/cm<sup>2</sup>). Equimolar amounts of freshly synthesised AuNPs functionalised with Res1c or Res2c were added to the crystals. The ionic strength of the suspension was adjusted by adding NaCl 2 M to a final concentration of 0.3 M or 0.5 M. The sample was transferred to a tube and left to shake in a thermal shaker (250 rpm). The crystals were left to grow for 24 to 48 hours, until no free AuNPs were present in suspension, testified from a colour change from red to colourless. This step was repeated multiple times to attempt visible growth in larger crystals. Optical microscopy was used to image the crystals to verify whether a significant growth of the superlattices had been achieved.

**Figure 4.14** shows optical images of amorphous (**A**) and crystalline (**B**) samples prior to any growth step. In (**A**) big clusters of aggregated gold are clearly visible everywhere on the specimen. Conversely, the AuNPs in (**B**) were more homogeneously dispersed in smaller aggregates.

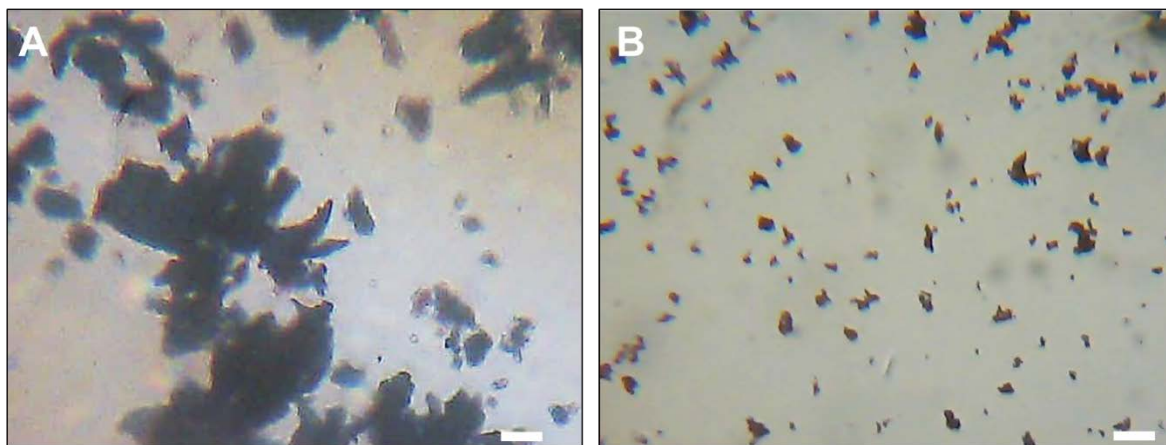


**Figure 4.14** Optical micrographs at 40X magnification of (A) an amorphous aggregate of AuNPs and (B) AuNPs crystals. Scale bars 50  $\mu\text{m}$ .

A comparison between two samples at different growing stages is shown in **Figure 4.15**. In (A), AuSLs were imaged after a single addition of DNA-coated AuNPs, whereas in (B) 3 additions were executed. The mean area of the aggregates was measured, and the results are summarised in the size distribution graph in **Figure 4.16**. The measured mean area steadily increased from the seeds (G0) to the following growing steps (G1, G2 and G3), varying from  $5 \pm 6 \mu\text{m}$  to  $45 \pm 32 \mu\text{m}$  after 3 growing steps. The dispersion around the mean area also increased, suggesting that secondary nucleation of amorphous aggregates may occur, along with the agglomeration of different aggregates. However, from the images it was not possible to determine if single crystals or aggregates of polycrystalline material was being observed. SAXS analysis are currently in progress to investigate the crystallinity of the grown samples.

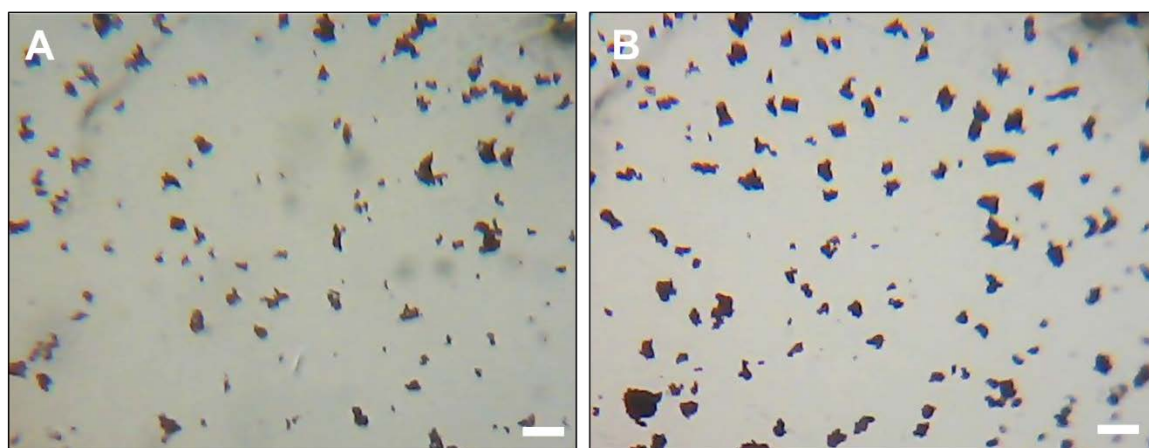


**Figure 4.15** Optical micrographs at 40X magnification of AuSLs at different growing stages. In (A) the as-synthesised AuSLs seeds and in (B) after 3 growth steps. Scale bars 50  $\mu\text{m}$ .

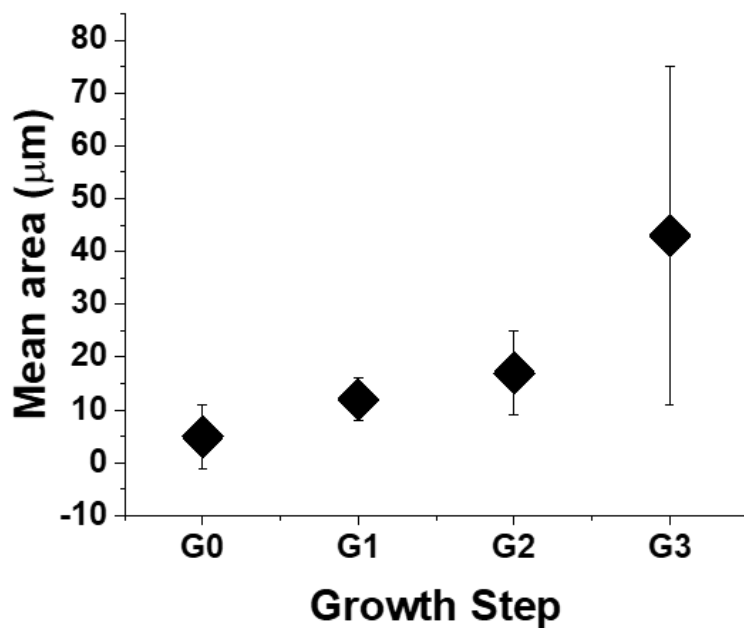


**Figure 4.16** Size distribution graph of the mean area variation after different growing steps. Seeds (G0)  $5 \pm 6 \mu\text{m}$ , growing step 1 (G1)  $12 \pm 4 \mu\text{m}$ , growing step 2 (G2)  $17 \pm 8 \mu\text{m}$  and growing step 3 (G3)  $43 \pm 32 \mu\text{m}$



## Chapter 5 Optical Characterisation of Programmed Assemblies

In the literature, the plasmon enhancement of fluorescence signal is a well-known process. Typically, there are two strategies that can be put in place to increase the fluorescence emission: either by intensifying the incident illumination flux or by increasing the radiative decay rate. Both can be done using plasmonic NPs. When light couples to LSPR, it can become highly confined near the interface, leading to enhanced electromagnetic fields that result in increased absorption cross sections. Fundamentally, the plasmonic structures behave as optical nanoantennas.<sup>180</sup> The antenna acts in three different ways, first it locally concentrates the incident field and enhances absorption. Secondly, the antenna can also enhance emission by increasing the emitter's radiative decay rate. However, the antenna can also quench the emission by increasing the nonradiative decay rate. The balance of these three processes relies on various parameters, such as spectral overlap between the resonances and absorption/emission frequencies, field overlap, polarization, antenna material, and pump power.<sup>180</sup>

In this work, preliminary studies on the interplay between gold and upconversion nanoparticles within the same aggregate structure were studied. First, the fabrication of mixed aggregates of AuNPs and UCNPs is described (**Section 5.1**). The effect of increasing amount of UCNPs in an AuNPs aggregate on the gold plasmon resonance was investigated (**Section 5.2**). Next, the effect of the synergy between gold and upconversion on the non-linear optical properties was explored in **Section 5.3**. Part of the work presented in this Chapter was carried out in collaboration of Mr Ahmad Azizan, Mr Alexander Courtier and Mr Jack Hynes.

### 5.1 Fabrication of heterogeneous assemblies

Assemblies with heterogeneous composition were prepared using DNA-functionalised gold and upconversion nanoparticles. Particles with narrow size distribution were synthesised as previously discussed (experimental in **Sections 2.1.1** and **2.1.4**, detailed discussion in **Sections 3.1.1** and **3.1.3**) and functionalised with the appropriate oligonucleotides (Experimental in **Section 2.2** and discussion in **3.3**). Specifically, AuNPs were functionalised with Res1 or Res2 modified with a thiol group, while UCNPs were functionalised with Res1 or Res2 modified with an amino termination (sequences in **Table 2.1**).

Prior to carrying out the crystallisation, a thermal analysis of the hybridisation behaviour of Au and UC NPs functionalised with complementary DNA strands was performed. Equimolar amounts of

AuNPs@Res2 and UCNPs@Res1 were mixed together and incubated at 60 °C in NaCl 0.5 M for 12 hours. The resulting pellet was transferred in a quartz cuvette and allowed to settle down. The absorption at 260 nm of this sample was recorded while the temperature was slowly increased. **Figure 5.1** shows that in the presence of NPs, the melting temperature is shifted to higher values (85 °C) compared to the DNA alone (56 °C).

The observed sigmoidal shape confirmed the successful cooperative hybridisation between heterogeneous particles, therefore the crystallisation by slow cooling was attempted.

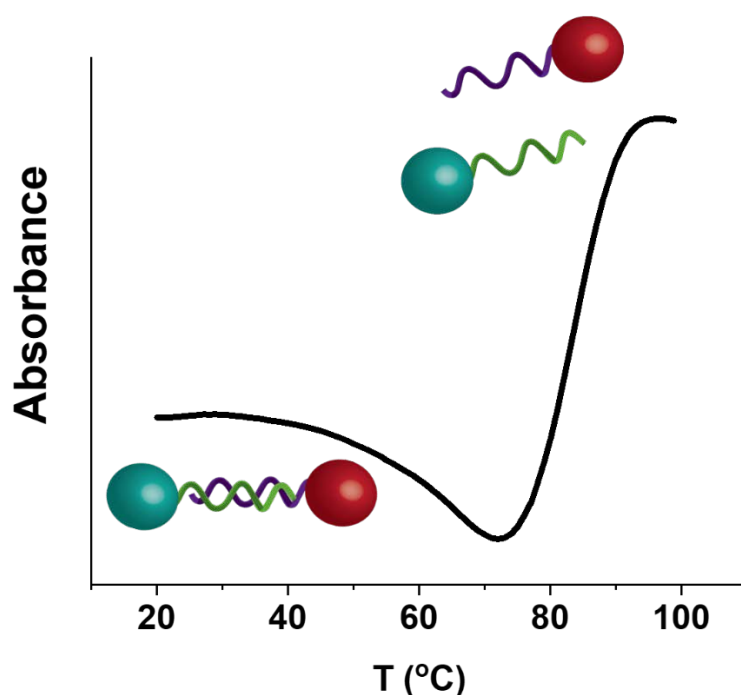


**Figure 5.1** Variation of the absorbance with increasing temperature. The melting temperature is defined at the inflection point of the curve and it resulted equal to 85 °C.

AuNPs and UCNPs functionalised with complementary oligonucleotides were mixed together in different proportion. The samples presented in **Table 5.1** were prepared as follows. In all the samples, the amount of UCNPs@Res2 was kept constant, while AuNPs@Res1 and UCNPs@Res1 were added in different relative ratios. The first sample (A0) was an aggregate of pure UCNPs, synthesised by mixing UCNPs@Res1 and UCNPs@Res2, hence the gold content corresponded to 0%. In the following samples, the amount of UCNPs@Res1 was gradually decreased while increasing AuNPs@Res1. This created a competition between the two different kinds of nanoparticles bearing the same ssDNA Res1 to bind the complementary Res2. This progressive variation allowed to achieve different gold content percentages in each sample, which were named after it as A12.5, A25, A37.5 and lastly A50. In A50 no UCNPs@Res1 was added, and the aggregate was an equal combination of UCNPs@Res2 and AuNPs@Res1. A similar rationale was used to prepare the

samples described in **Table 5.2**. Here, the content of AuNPs@Res2 was fixed, whereas AuNPs@Res1 and UCNPs@Res1 were added in different relative proportion. An aggregate of pure gold was fabricated by combining AuNPs@Res1 and AuNPs@Res2 (sample name U0). Then, the amount of AuNPs@Res1 was progressively reduced and UCNPs@Res1 was incremented. The samples were labelled after the UC percentage content as U12.5, U25, U37.5 and U50. Three different set of samples A and U were prepared using different sizes UCNPs (45 nm, 30 nm, 15 nm). Initially, standard NaYF<sub>4</sub>:Yb(20%),Er(2%) UCNPs 45 nm were used because of their very high fluorescent signal. Nevertheless, their large size, compared to the AuNPs, could complicate the formation of an ordered particles' arrangement. To tackle this issue, smaller UCNPs were produced by introducing gadolinium in the NaYF<sub>4</sub> matrix to decrease the NPs' size, thus obtaining 30 nm and 15 nm UCNPs. An extended discussion about this topic can be found in **Section 3.1.3**.

Prescribed amount of Au and UCNPs were mixed in phosphate buffer 0.01 M and NaCl 0.3 M. The samples were transferred to a thermal cycler machine, heated up and kept at the melting temperature of 80 °C for 1 hour and slowly cooled down at a rate of 0.1 °C/10 min. In this case, the crystallisation protocol was slightly modified to take into account the very high T<sub>m</sub> experimentally determined (80 °C). In the previous Chapters, the usual protocol involved heating up above the T<sub>m</sub> and an immediate slow cooling after the target temperature had been reached. In this case, heating up above the T<sub>m</sub> could have incurred into the detachment of the ssDNA from the NPs' surface, which is normally observed around 90 °C. To overcome this issue, the samples were brought at the T<sub>m</sub> and then kept for an hour to allow the quick dehybridisation-hybridisation of the oligonucleotides and favour the formation of an ordered lattice.

**Table 5.1** Summary of the A-series samples. The number after the 'A' represents the percentage of AuNPs doping added to the UCNPs aggregate.

Sample name	UCNPs@Res2	UCNPs@Res1	AuNPs@Res1	Gold %
A0	1	1	0	0
A12.5	1	0.75	0.25	12.5
A25	1	0.5	0.5	25
A37.5	1	0.25	0.75	37.5
A50	1	0	1	50

**Table 5.2** Summary of the U-series samples. The number after the 'U' represents the percentage of UCNPs doping added to the AuNPs aggregate.

Sample name	AuNPs@Res2	AuNP@Res1	UCNPs@Res1	UC %
U0	1	1	0	0
U12.5	1	0.75	0.25	12.5
U25	1	0.5	0.5	25
U37.5	1	0.25	0.75	37.5
U50	1	0	1	50

After the slow cooling from  $T_m$ , aggregates were observed at the bottom of the tubes and the supernatant solution was removed and replaced with fresh phosphate buffer 0.01 M and NaCl 0.3 M. **Figure 5.2** shows optical photographs of some homogeneous and mixed composition superlattices: in A, pure gold superlattices (sample U0), in B pure upconversion superlattices (sample A0), while in C a mixed composition superlattice (sample U50) formed by Au and UCNPs in 1:1 ratio are shown. As previously observed, when AuNPs are assembled together, their colour shifts from red to a dark violet hue, due to the effect of aggregation on the surface plasmon resonance. Conversely, the UCNPs do not show any absorption in the visible range and hence they remained white; aggregation did not affect their optical properties in the visible range, thus resulting in a white aggregate. Interestingly, heterogeneous assemblies showed a light pink colour, resulting from the combination of the Au and UC properties. In **D**, **E** and **F** the same samples are shown under supercontinuum (full wavelength range 400-1200 nm) laser illumination, showing different absorption and scattering. The pure gold sample U0 looked red (**Figure 5.2D**), the UCNPs aggregate A0 showed a yellow hue (**Figure 5.2E**), and the mixed composition U50 (**Figure 5.2F**) presented an orange colour due to the combination of both components' absorption. A deeper investigation of this phenomenon is carried out in the following **Section 5.2**.

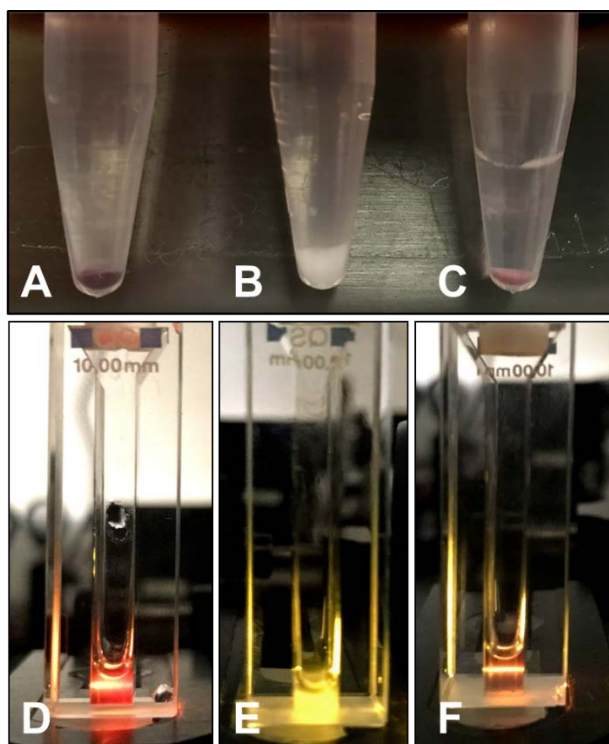


**Figure 5.2** Optical photographs of white light scattered from gold and upconversion. On the top, pure AuSLs (sample U0), pure UCLS (Sample A0) and a mixture of AuNPs and UCNPs (Sample U50) under ambient light, showing different hues. On the bottom, U0 (D), A0 (E) and U50 under supercontinuum laser light, showing different absorption.

## 5.2 UV-vis spectroscopy of heterogeneous assemblies

When two or more metallic NPs are placed in close proximity, their optical response changes from individual to collective.<sup>181–184</sup> The coupled structure displays different plasmon modes compared to the individual modes, due to the coupling of the building blocks. A commonly observed behaviour is the redshift of the plasmon peak.<sup>185</sup> For particle size in the nanoscale range, the shift trend is described by an exponential relationship, the plasmon ruler equation (**Equation 5.1**), which is valid for different particle's shapes and sizes.<sup>186</sup> In this equation, the plasmon shift is expressed as a function of particle size and interparticle distance.

**Equation 5.1** Plasmon ruler equation.  $\lambda_0$  is the resonance wavelength of the individual element,  $\Delta\lambda$  is the wavelength shift,  $l$  and  $s$  are the particle size and interparticle distance respectively.  $\sigma$  and  $\tau$  are two fitting parameters, depending on the medium.

$$\frac{\Delta\lambda}{\lambda_0} = \sigma e^{(-s/\tau l)}$$

Apart from the plasmonic contribution, the role of light scattering must also be taken into account in case of a large number of particles (or increasingly larger particles). When radiation passes through an absorbing and turbid medium, its extinction is the sum of both absorbance and scattering.<sup>187</sup> **Figure 5.3** displays the extinction spectrum for DNA-AuNPs SLs, compared to the absorbance of a colloidal solution of DNA-coated AuNPs, showing remarkable red-shift and peak broadening. Previous reports<sup>188</sup> have highlighted that the red-shift and broadening observed in the extinction spectra of DNA-nanoparticles aggregates are due to the development of a collective response of the electrons of assembled nanoparticles. The optical properties of DNA-networked NPs are sensitive to the aggregate size and to the metal fraction volume, but they are not particularly affected by the specific lattice arrangement.

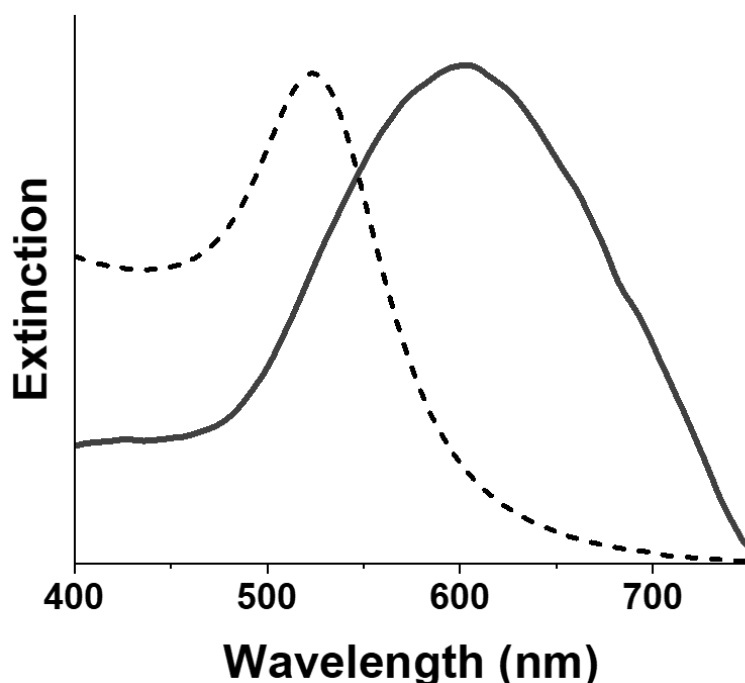


**Figure 5.3** Normalised extinction spectrum of a DNA-AuNPs superlattices sample (solid line) compared to the absorbance of DNA-coated Au colloidal solution. The maximum absorbance shifted from 523 nm to 601 nm.

The effect of the metal content on the extinction behaviour is particularly relevant in the context of heterogeneous SLs. According to published literature,<sup>188</sup> being the size of the aggregates approximately equal, the reduction of the metal content should translate into a blue-shifting and sharpening of the maximum optical density peak. This behaviour is the result of a diminished interaction among AuNPs due most likely to an increased distance between the NPs. This prediction found confirmation in the extinction spectra of mixed crystals with different percentages of gold (**Figure 5.4**). Analysed samples were prepared from 14 nm AuNPs and 15 nm UCNPs combined in

different proportion, as described in **Table 5.2**. As the percentage amount of gold is decreased, the extinction maximum is blue-shifted and the peaks appear sharper. This observation was attributed to an increased distance among the AuNPs due to the presence of UCNP. The wider distance reduced the entity of both the collective plasmon interaction and the scattering contribution. The plasmon ruler equation (**Equation 5.1**) was used to estimate the distance between AuNPs within the lattices. The fitting parameters  $\sigma$  and  $\tau$  were set respectively to 0.18 and 0.23, which were previously optimised for DNA-coated AuNPs in aqueous medium.<sup>189,190</sup> Considering 14 nm AuNPs spaced by 45 mer oligonucleotides, the predicted nearest neighbour spacing corresponds to  $27 \pm 3$  nm. The interparticle distance found in a SLs 100% gold (sample U0) was 34 nm, in relatively good agreement with the 27 nm obtained from SAXS data analysis (see **Section 3.4.1**).

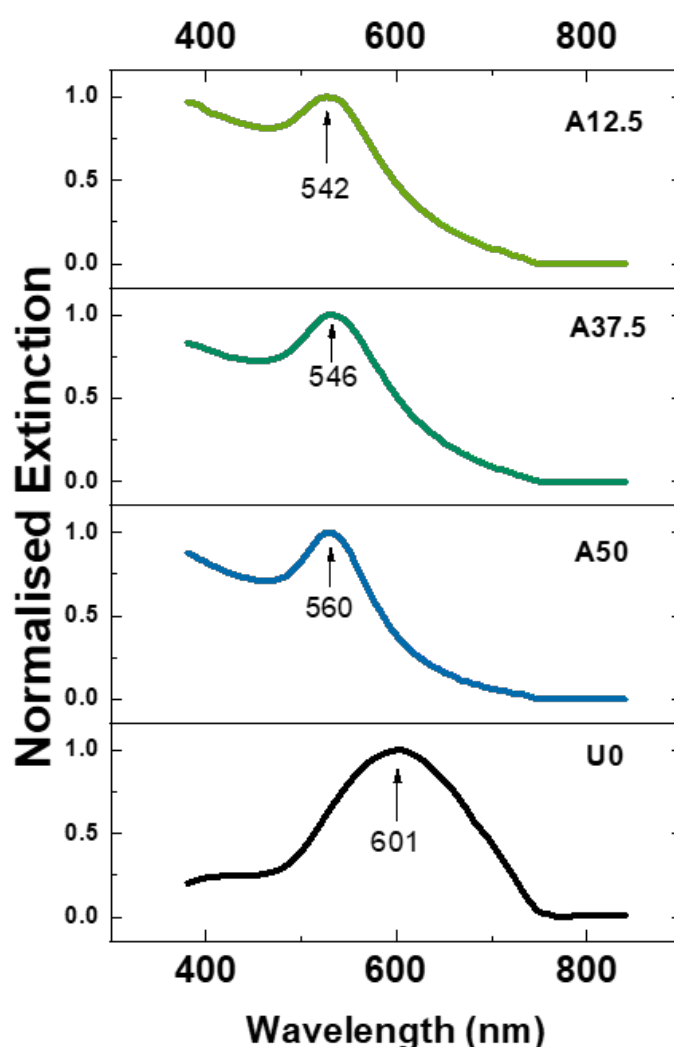


**Figure 5.4** Normalised extinction spectra for superlattices containing different percentage of gold. As the amount of gold increase from 12.5% in A12.5 to 100 in U0, the maximum peak broadens and shift to longer wavelengths, as result of increased interaction between AuNPs.

In **Table 5.3**, a summary of the calculated distance between AuNPs in lattices containing different percentages of gold. For a sample formed by AuNPs@Res1 and UCNPs@Res2 in a ratio 1:1 (sample A50), the interparticle spacing between two AuNPs was found equal to 53 nm. A predicted value of  $54 \pm 3$  nm was calculated considering two  $14 \pm 1$  nm AuNPs at the centre of a body centred cubic structure (see illustration in **Scheme 5.1**). This assumption was justified considering that each AuNP@Res1 would be surrounded by UCNPs@Res2, due to the complementarity between the ssDNA on the particles' surface and to the absence of competing UCNPs@Res1. The nearest neighbour distance ( $d_{nn}$ ) between an AuNP at the centre of the BCC and a UCNP at the corner of the cube was estimated by summing the Au and UCNP (including the silica shell, **Section 3.3.4.1.2**) radii plus the 45 base pair oligonucleotides between them. The lattice parameter  $a$  was then calculated from  $a = 2d_{nn}/\sqrt{3}$  and it resulted in  $54 \pm 3$  nm. The cell parameter  $a$  for a BCC lattice corresponds to the distance between two particles at the centre of two adjacent unit cells. This value is in excellent agreement with 53 nm, experimentally determined from the plasmon ruler equation.

**Scheme 5.1** Illustration of two adjacent body centred cubic unit cell, formed by spherical AuNPs at the centre of the cell and surrounded by hexagonal UCNPs. The core-to-core distance between two AuNPs is highlighted for clarity.

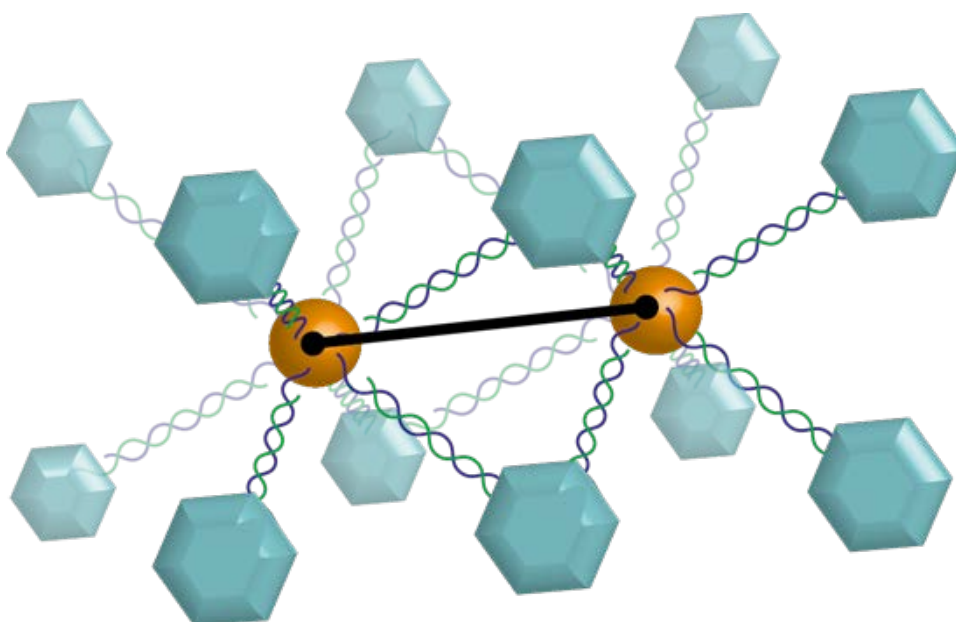




**Table 5.3** Estimated spacing between two adjacent AuNPs for superlattices containing different percentages of gold, as calculated from the plasmon ruler equation, showing good agreement with the expected values.

Sample	Peak Maximum (nm)	$\Delta\lambda$ (nm)	Interparticle distance (nm)
A12.5	542	19	60
A37.5	546	23	56
A50	560	27	53
U0	601	78	34

On the other hand, a comparison between experimental and theoretical distances between AuNPs within assemblies A37.5 and A12.5 was more challenging to conduct. Predicting the relative positioning of AuNPs within the lattice was unfeasible due to the competition between AuNPs@Res1 and UCNPs@Res1 to hybridise UCNPs@Res2. Despite this inherent difficulty, we can predict that the interparticle distance should increase as the gold content decrease. Calculations from the extinction data endorsed this hypothesis. Specifically, the distance varied from 53 nm in A50 to 56 nm (in A37.5) and 60 nm (in A12.5). These determined distances are wider than the theoretically calculated lattice parameter (53 nm) for a lattice containing equivalent amounts of UCNPs and AuNPs. This did not provide hints on the specific positioning of the AuNPs, but suggested that less than one AuNPs per unit cell is present, thus the gold can be regarded as an impurity in a UCNPs lattice.

### 5.3 Non-linear optical properties of heterogeneous assemblies

In this section the non-linear optical properties of heterogeneous assemblies of 14 nm AuNPs with either 45 nm or 30 nm UCNPs will be investigated. Both AuNPs and UCNPs show non-linear optical characteristics, in processes involving two-photon transitions.

As outlined in more detail in **1.1.1.4**, photon upconversion is a non-linear fluorescence process consisting in the sequential absorption of two lower energy photons, which are subsequently emitted at a higher energy wavelength, through a series of different transitions among different energy levels. Upconversion nanoparticles are inorganic crystalline structures composed by a matrix (typically NaYF<sub>4</sub>) hosting rare-earth elements, which act as sensitizers and activators for the upconversion of infrared photons. Usually, sensitizers are chosen so that they possess relatively

large photo-absorption cross-sections and appropriate energy levels to match the corresponding activators. These characteristics are well-met by lanthanide ions, due to the high number of energy levels in the 4f-5d energy levels, which provide multiple energy transfer pathways for upconversion emission. Ytterbium  $\text{Yb}^{3+}$  is a highly efficient photo-sensitizer with high absorption at 976 nm (transition  $^2F_{7/2} \rightarrow ^2F_{5/2}$ ). The absorbed energy is then transferred to an activator within the matrix (such as  $\text{Er}^{3+}$ ), which can then emit the energy in the visible spectrum.<sup>191,192</sup>

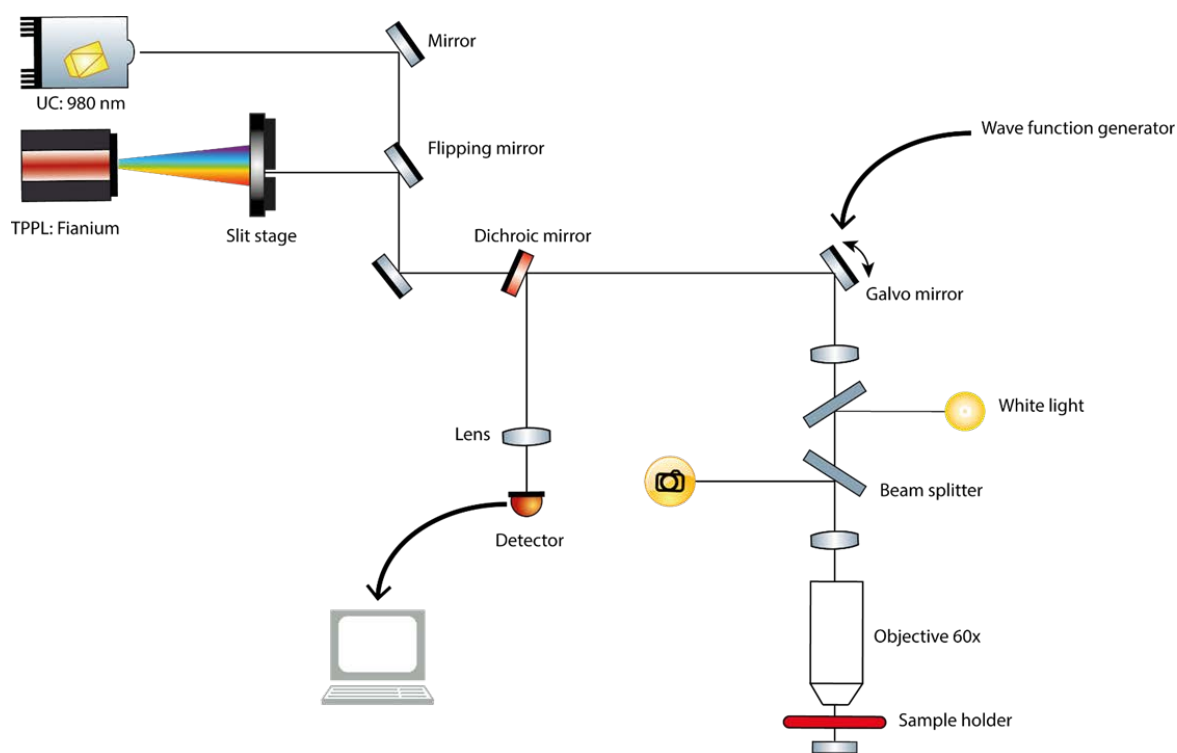
Two-photon photoluminescence (TPPL) is a third-order phenomenon involving the sequential absorption of two photons carrying approximately the same energy. As described in **Section 1.1.1.3**, this process involves the promotion of an electron from the ground state to an excited state located at energy equal to twice the energy of the irradiating photons. The energy absorbed is then radiatively emitted at half the wavelength of the exciting one. For AuNPs, the working wavelength is around 1060 nm and the emission is observed at 530 nm. Being a third-order nonlinear phenomenon, the signal is not exceedingly intense; however, it is sufficiently strong to be used in several applications, such as microscopy.<sup>53,193</sup>

### **5.3.1 Optical characterisation of heterogeneous assemblies of 15 nm AuNPs and 45 nm UCNPs**

A home-built setup was used to investigate the optical properties of the assemblies, specifically the TPPL arising from the AuNPs and the fluorescence from the UCNPs. The set-up was built with the help of Professor Otto Muskens, with the specific aim to alternatively measure the TPPL of the gold component and the fluorescence of the UCNPs on the same area of the aggregates, to evaluate if the co-presence of the two components had affected the co-localisation of the signals. The TPPL setup included a supercontinuum Yb-doped fibre laser (Fianium) with emission centred at 1060 nm, pulse duration of 11 ps, 20 MHz repetition rate and a laser power of 30 mW. The emission wavelength was selected by using a stage slit. The laser beam was directed through a series of mirrors on the sample and focused onto it by using a 60x objective lens. The sample's position was controlled with a 3-axis piezo motor and the nanoparticle assemblies were located by bright field imaging with a white light source. The measurement was then performed by scanning the laser beam on the identified area using a galvo mirror, which was connected to a wave function generator (scan rate 40 Hz). The emitted signal was finally collected on an avalanche photodetector (Excelitas SPCM-AQRH). Photon counts were collected as a function of position using a laser-scanning arrangement and a data-acquisition system (Becker&Hickl).

The upconversion fluorescence measurements were performed with a continuous wave (CW) 980 nm diode laser (Thorlabs) as excitation source with power of 10 mW, and an avalanche

photodetector (the same used for TPPL) as collector of the fluorescence signal. In **Scheme 5.2** a diagram of the TPPL/Fluorescence setup is reported.



**Scheme 5.2** Schematic illustration of the custom-made, home-built setup for the alternate detection of TPPL and fluorescence signals. The light coming from either the supercontinuum or 980 nm laser is directed through a number of mirrors into the objective where the sample is placed. The scattered light is then directed either to a camera or to a CCD detector. The white light source was used for the location of the aggregates by bright field imaging.

Preliminary experiments were conducted on a limited number of heterogeneous assemblies of 15 nm AuNPs and 45 nm UCNPs, prepared as described in **Table 5.2**. Briefly, samples U12.5, U25, U37.5 and U50 were assembled by keeping constant the amount of AuNPs@Res2 and adding different aliquots of AuNPs@Res1 and UCNPs@Res1, which competed to bind AuNPs@Res2 (a more detailed description can be found in **Section 5.1**). In a similar manner, a sample containing 62.5% UCNPs was prepared by keeping constant UCNPs@Res2 and replacing 12.5% of UCNPs@Res1 with AuNPs@Res1 (sample A12.5 described in **Table 5.2**).

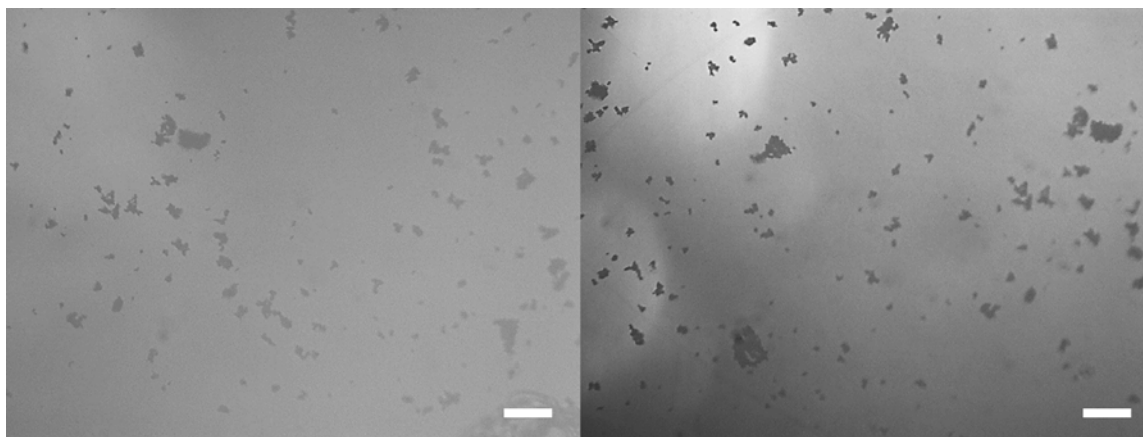


**Figure 5.5** Representative bright field microscope images of aggregates of particles (sample U0). Scale bars 200  $\mu\text{m}$ .

After self-assembly, the optical properties of the aggregates were assessed using the custom-made setup described above. Specimen were prepared by dropcasting ca. 20  $\mu\text{l}$  of each sample in an 18-wells  $\mu$ -slide and placed on the staged sample holder. A suitable area to perform optical measurements was roughly located using bright field microscopy (representative images of sample U0 are shown in **Figure 5.6**). Subsequently, the chosen region was positioned in the beam path and the laser (either the supercontinuum or the 980 nm) was focused onto it. The signals arising either from TPPL or fluorescence were collected by illuminating the same sample area with either the supercontinuum laser for TPPL or the 980 nm laser for fluorescence.

**Figure 5.7** shows examples of the images used for the pixel analysis. Each pair of images (A and B, C and D) corresponds to the same area, imaged with both lasers. In general, the fluorescence signal (**Figure 5.7B** and **D**) had a considerably higher intensity than the corresponding TPPL (**Figure 5.7A** and **C**), which can be explained considering that the TPPL is a low-intensity third-order physical phenomenon. From **Figure 5.7**, it is evident that the regions displaying higher intensity response in each pair of images were found at the same coordinates and presented the same features for both TPPL and fluorescence. Since AuNPs and UCNPs were functionalised with complementary oligonucleotides, the successful hybridisation between them would create a heterogeneous assembly. It follows that, if a mixed composition assembly was created, the TPPL and the fluorescence signals should originate from the same areas of the sample (co-localisation). Conversely, if the AuNPs did not mix with the UCNPs, segregation of the TPPL and upconversion fluorescence signals would be observed. The observation of similar features and positioning of TPPL and fluorescence outcome attested the co-localisation of gold and upconversion nanoparticles, confirming the fabrication of a mixed-composition aggregate.

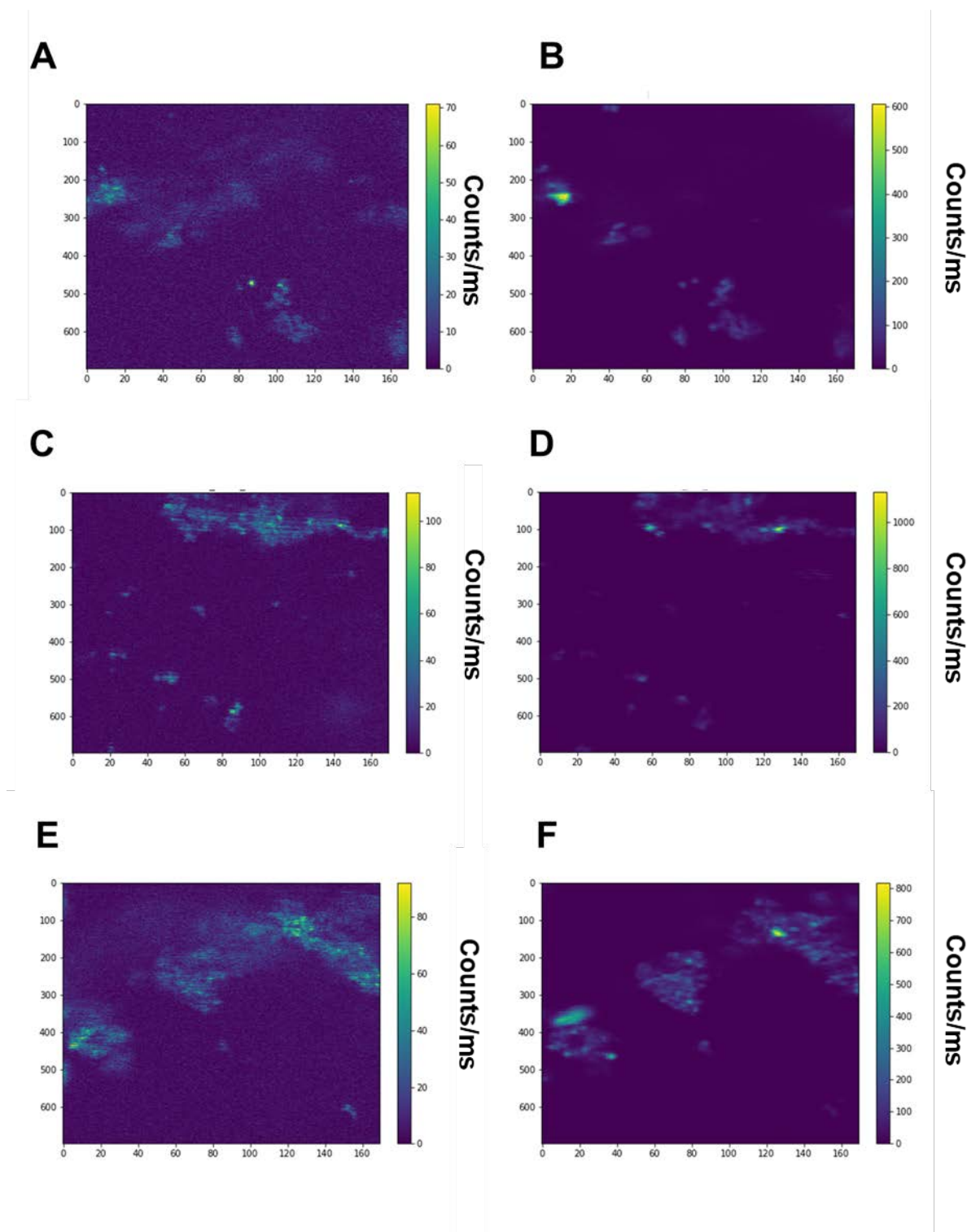


**Figure 5.6** TPPL (A, C and F) and fluorescence log scale maps (B, D and F) obtained from a typical heterogeneous sample. A and B correspond to the same area, imaged with 1060 nm and 980 nm laser, similarly to C-D and E-F pairs. The bright regions in each image is thought to represent a cluster of AuNPs and UCNP aggregates. The co-localisation of AuNPs and UCNP is highlighted by the presence of higher intensity signals in the same regions for both lasers.

The signal intensity ratio was obtained by summing the intensities of all the pixels in the TPPL measurement and dividing by the sum of all the pixels in the upconversion measurements on the same area, or in symbols: intensity ratio =  $\Sigma(\text{Pixel intensity UC})/\Sigma(\text{Pixel intensity TPPL})$ .

In **Figure 5.8**, a graph showing the relationship between the intensity ratio calculated as above and the percentage of UCNPs is reported. More specifically, it shows the data for samples U12.5, U25, U37.5, U50 and A37.5, in which the amount of UC is increased from 12.5% to 62.5%. These samples were chosen as they contained both AuNPs@Res1 and UCNPs@Res1 competing to bind the complementary strand on AuNPs@Res2. From the graph, it is clear that the fluorescence-to-TPPL ratio is relatively constant for UCNPs content  $\leq 37.5\%$ . After the UCNPs fraction was risen at 50% and above, the fluorescence predominated and a sharp increase in the signal ratio was observed.

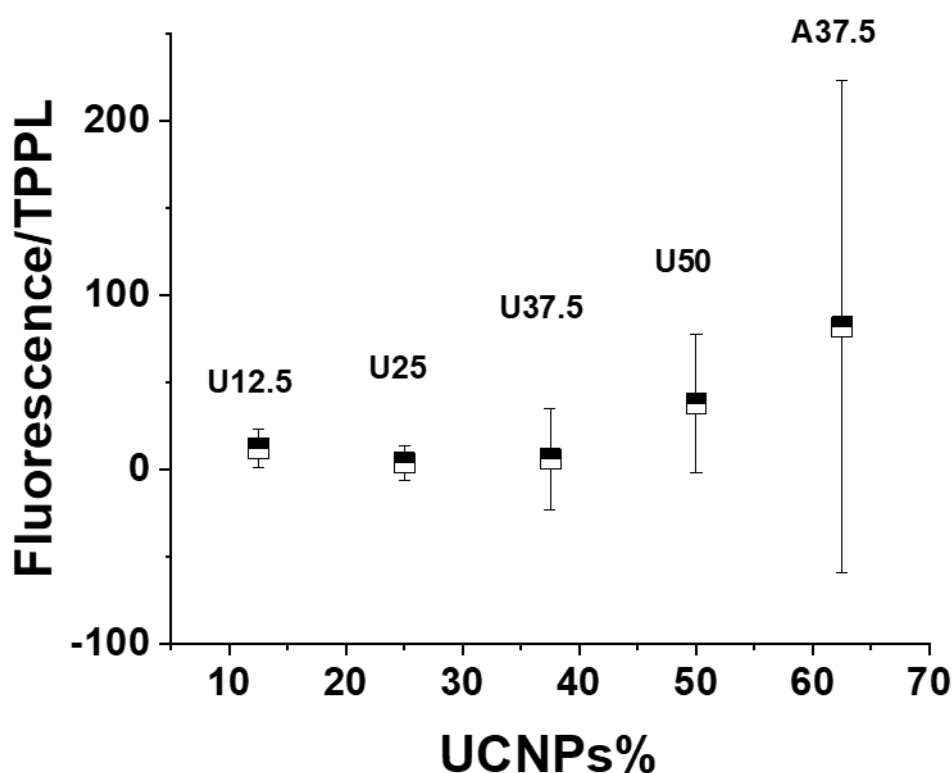


**Figure 5.7** Fluorescence to TPPL ratio for different UCNPs percentage, varying from 12.5% (sample U12.5) to 62.5% (sample A37.5). A sharp increase in the fluorescence signal takes place when the UCNPs fraction of the aggregate raised above 50%.

This substantial steadiness of the fluorescence signal at low ratio followed by a sharp increase could be attributed to the “hot-spot” effect in the TPPL response of plasmonic particles. A near-field enhancement of the optical response occurs in clusters of gold nanoparticles,<sup>194,195</sup> but when the NPs are distant, such as in samples with gold fraction  $< 50\%$ , the photoluminescence is rapidly reduced, causing a swift increase in the fluorescence-to-TPPL ratio.

### 5.3.2 Optical characterisation of heterogeneous assemblies of AuNPs and 30 nm UCNPs

An improved version of the previously presented setup was used to study the TPPL from gold nanoparticles and the fluorescence signal generated by 30 nm lanthanide-doped NaY:GdF<sub>4</sub> nanoparticles. To maximise the TPPL signal intensity and reducing the background signal from upconversion, the supercontinuum laser was replaced with a femtosecond pulsed laser with emission centred at 1064 nm  $\pm$  5 nm. The laser operated at 100 mW at a repetition rate of 5 MHz, and a pulsewidth of 200 fs, which allows to achieve higher pumping energies compared to the picosecond laser previously employed. The upconversion signal was detected using a continuous wave 980 nm diode laser (Thorlabs) as excitation source with power of 10 mW. The laser beam (either the 1064 nm or the 980 nm) was directed using a galvo scanning mirrors and was focused onto the sample using a 60x objective lens. After location of the nanoparticle assemblies by bright field imaging, the measurement was performed by scanning the laser beam with a galvo mirror (40 Hz). The emitted signal is finally collected on an avalanche photodetector (Excelitas SPCM-AQRH). The scheme of this setup is identical to the drawing reported in **Scheme 5.2**, except for the supercontinuum laser, which was replaced by the femtosecond one.

In this experiment, ca. 20  $\mu$ l of mixed composition aggregates prepared as in **Table 5.1** and **Table 5.2** were dropcasted on a  $\mu$ -slide and allowed to sediment at the bottom of the well. A white light source and an optical microscope were used to roughly locate the aggregate on the slide. The vertical position of the sample was then adjusted to optimise the focus on the sediment aggregate through a series of z-axis scans. An example of a series of z-stack images is reported in **Figure 5.9**. A series of ten images was collected on the same area of a heterogeneous aggregate of Au and UCNPs. The stage height was varied between 20 V and 40 V using a piezo controller and an image was collected for each 1V step. The height that yielded the highest intensity was selected and used for data collection.

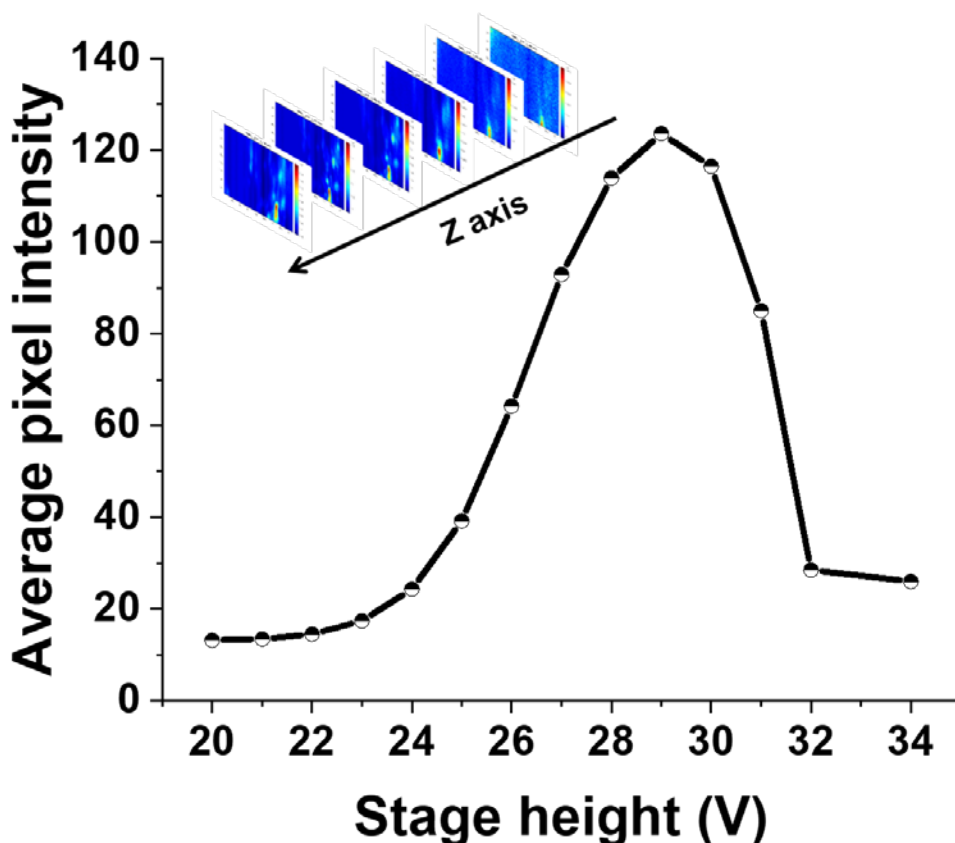


**Figure 5.8** Representative z-stack images series for a heterogeneous aggregate of AuNPs and UCNPs and corresponding plot of the average pixel intensity for each image. The intensity increases and the background noise is reduced as the stage height approaches the laser focus. The height that maximised the pixel intensity was chosen for data collection.

After a suitable area of the sample had been located and placed in the laser focus, two images were recorded, using alternatively the 980 nm and the 1064 nm laser. Images with both lasers were collected on five different areas of for each sample to test the consistency of their optical response. The intensity from each image was extracted and averaged on the number of pixels in each image.

In **Figure 5.10**, a graph of the mean intensity for every image of each sample versus the UCNPs percentage fraction is reported. The TPPL signal is represented by filled circles, while the fluorescence is symbolised by filled squares. The signal intensity variation across each image is represented by coloured bars for each sample. Concerning the photoluminescence behaviour (filled circles), the TPPL signal showed an overall decreasing trend with decreasing content of AuNPs. The highest absolute intensity was registered for a pure gold sample (U0). Following introduction of UCNPs within the gold clusters (U-series samples, orange circles), a dramatic drop of about an order of magnitude took place (U12.5). Further increase of UC percentage in parallel with the decrease in Au content, caused the TPPL intensity to progressively drop down to zero in a pure UCNPs sample.



This trend was rationalised considering that the introduction of UCNPs progressively perturbed the AuNPs coupling, and therefore it gradually reduced the TPPL intensity. When the concentration of UCNPs reached the 50% and above, the AuNPs were essentially diluted in an UC aggregate and the corresponding signal had low intensity in all the A-series samples. Coherently, the fluorescence response (filled squared), showed an opposite trend, as it raised with increasing UCNPs content. The fluorescence signal remained fairly constant in U-series samples (grey squares), as the UCNPs constituted a small fraction of the overall aggregate. A more pronounced increase in fluorescence was detected for A-series samples (black squares), consistent with the elevated percentage of UCNPs in the samples.

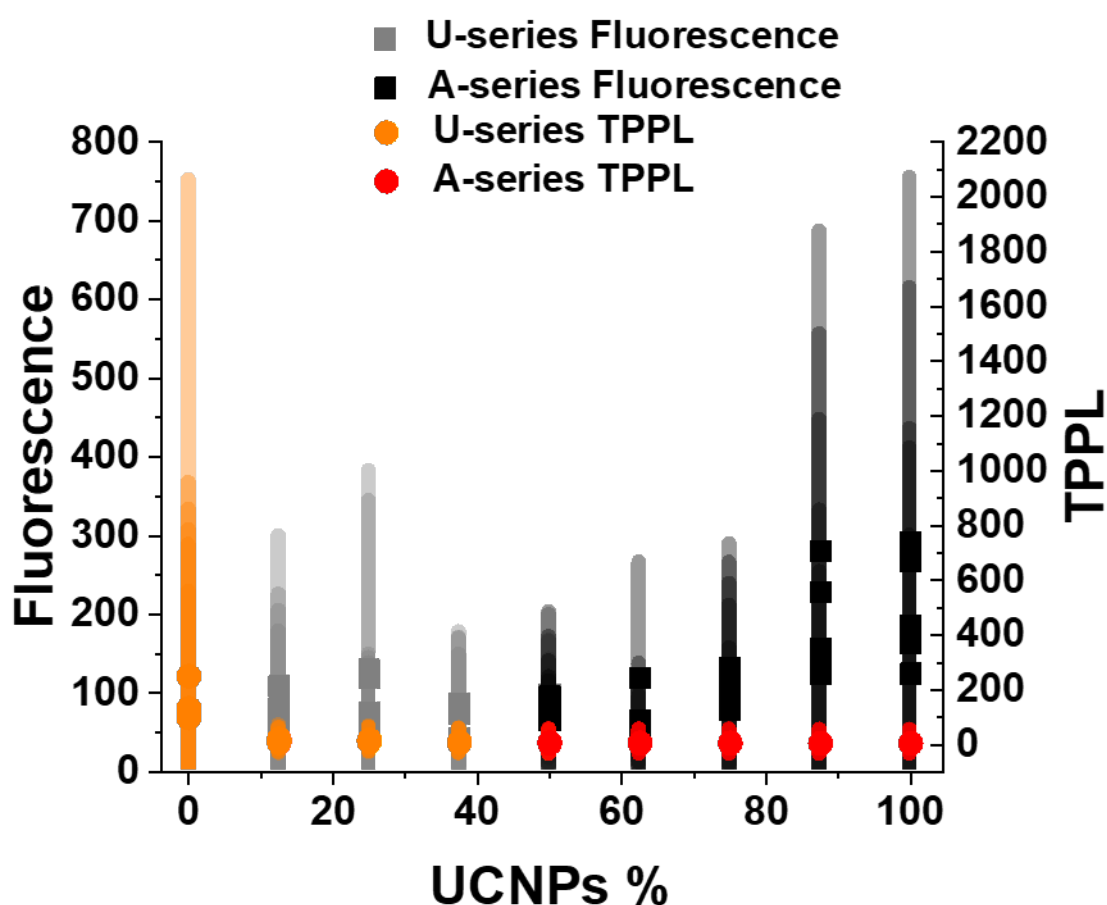


**Figure 5.9** Averaged pixel intensity and corresponding dispersion of the signal for each image of A- and U-series samples. TPPL measurements from the gold for U-series and A-series samples are represented by orange and red circles respectively. Average fluorescence intensity of the UCNPs is symbolised by grey (U samples) and black (A samples) squares. The variation of the signal across each sample is represented by coloured bars.

In **Figure 5.11**, the entity of the TPPL and fluorescent upconversion response for each sample is reported as an average of the pixel intensity over five images taken in different areas of the same sample. The fluorescence to TPPL ratio against the UCNPs percentage is then plotted for A- and U-

series samples. In the gold-doped UCNP aggregates (A-series, light blue triangles), a linear increase of the fluorescence response was detected. As the UCNP content raised from 50% to 100%, the fluorescence to TPPL ratio increased accordingly. This behaviour is in good agreement with the measurements performed on the A-series samples containing UCNP 45 nm (**Section 5.3.1**). Remarkably, the two samples A50 and U50 showed very similar ratios, coherently with their composition. In fact, these two samples were both prepared with the same ratio of Au and UCNP.

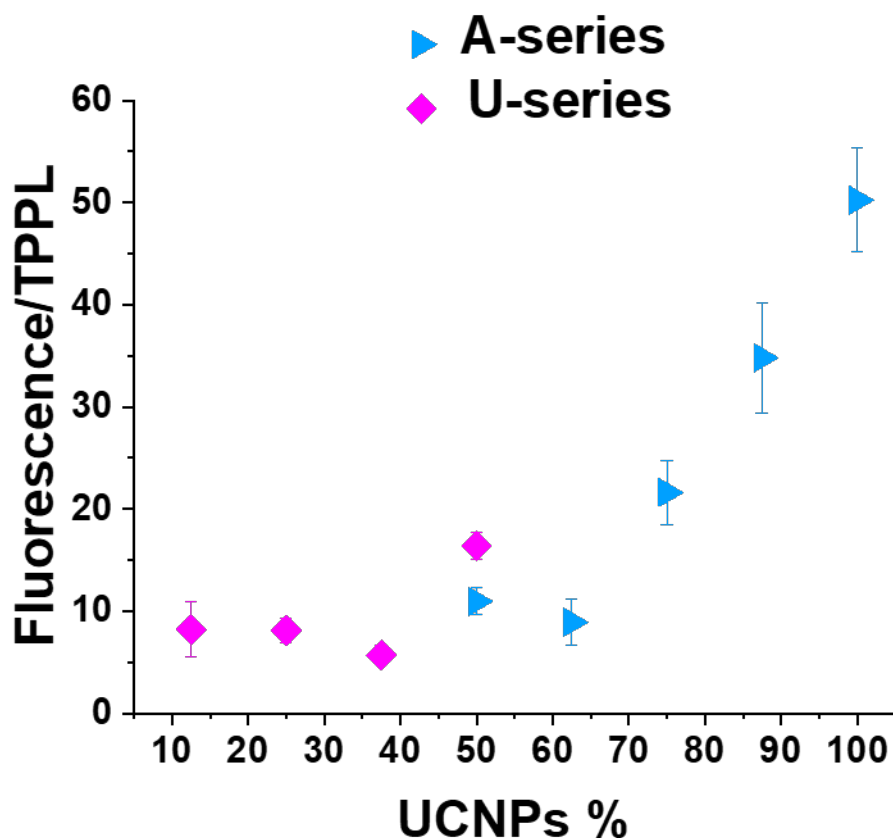


**Figure 5.10** Fluorescence to TPPL ratio against the UCNP percentage for U-series samples (magenta diamonds) and for A-series samples (light blue triangles). A sharp increase in the fluorescence signal takes place when the UCNP fraction of the aggregate raised above 50%.

A third set of A and U samples with AuNPs 14 nm and UCNP 15 nm was also fabricated and a thorough non-linear optical characterisation will be undertaken. Despite the lower fluorescence intensity observed for small UCNP (see **Section 3.1.3** and ref<sup>83</sup>), the use of particles with approximately the same size, should facilitate the achievement of an ordered lattice. Furthermore, small UCNP presents a more spherical shape compared to the hexagonal platelets observed for 45 nm UCNP. This shape matching could also contribute to a higher crystallinity sample. The obtainment of a crystalline material may improve the consistency of the optical response, since the

NPs would be found in predetermined positions. In case of extended single crystals ( $>10\ \mu\text{m}$ ), the optical response of a single crystal could be revealed.



## Chapter 6 Conclusion and Outlook

The long-term vision behind this project was to develop universal strategies for the accurate design and fabrication of reconfigurable three-dimensional mesoscopic materials. These materials are made of functional nanoparticles, assembled *via* DNA interactions. The nanoparticles endow the material with their intrinsic properties, such as plasmonics, fluorescence or magnetism. On the other hand, the specificity of the base-pair recognition makes synthetic oligonucleotides a unique and unsurpassed tool for the precise assembling and positioning of nanoparticles. The synergy between these two components was exploited in this work for the fabrication of stimuli responsive, three-dimensional arrays of nanoparticles. These materials are envisioned to originate unconventional properties, arising both from the composition of the material itself and from the architectural arrangement in space.

In this final Chapter, a summary of all the results obtained is given (**Section 6.1**). An outlook of the future perspective based on latest results, is outlined in **Section 6.2**.

### 6.1 Summary of results

In **Chapter 4**, different types of nanoparticles were synthesised and characterised with the final goal of employing them as self-assembly building blocks. Gold and silver nanoparticles were synthesised with classical citrate-reduction methods, and subsequently grown in different sizes using a seeded-mediated strategy. Fluorescent NaYF<sub>4</sub>:Yb<sup>3+</sup>,Er<sup>3+</sup> upconversion nanoparticles and magnetic iron oxide nanoparticles were synthesised using a co-precipitation method. The synthesised nanoparticles were characterised using a variety of techniques, including transmission electron microscopy, x-rays diffraction, zeta potential measurements, UV-visible and fluorescence spectroscopies.

Different approaches were used to cover the surface of the NPs with a dense layer of synthetic oligonucleotides. For gold and silver NPs, the direct surface attachment was performed by using thiol-modified ssDNA. Amino-terminated oligonucleotides were used to functionalise silica-coated upconversion and iron oxide nanoparticles via EDC/sulfo-NHS coupling.

Three-dimensional assemblies were fabricated using DNA-NPs units as building components. Temperature-regulated strategies were used to favour the ordered arrangement of the components in ordered superlattices. High-quality crystalline assemblies of gold and silver NPs were synthesised, and the structure was assessed via scanning electron microscopy and x-rays scattering. In **Chapter 4**, the expertise gained in the construction of such 3D architectures was applied to the synthesis of light-responsive micron-sized crystals. For this aim, engineered nucleic

## Conclusion and Outlook

acids were designed and characterised. A modified nucleobase containing a cyanovinyl carbazole molecule was introduced in the ssDNA sequences used for the fabrication of superlattices. This compound is a light-responsive molecule, which enables the formation of a covalent bond between two complementary DNA strands upon illumination with 365 nm wavelength. This bond is insensitive to environment changes, endowing the overall structure with extra-ordinary stability. This method of ligation is exceptionally versatile for several reasons. First, it can be activated at will following 365 nm irradiation, remaining silent otherwise. This is of utmost importance when crystalline assemblies are desired because many hybridisation/dehybridisation events must occur for the particles to arrange in the most thermodynamically stable form (the crystal structure). The possibility to selectively induce the carbazole reaction allows to “lock” the structure with covalent bonds only after the ordered lattice is formed.

Moreover, the carbazole crosslinking is a reversible reaction. By using a different wavelength (312 nm), the covalent bond can be opened, yielding the pristine, non-crosslinked oligonucleotides. Other crosslinking methods are usually irreversible, leading to the loss of the dynamicity provided by the hybridisation/dehybridisation of DNA. This is not the case for the carbazole ligation: the reversibility of the covalent bond allows to take advantage of the flexible properties of DNA to achieve completely reversible, dynamic structures.

In **Chapter 5**, heterogeneous aggregates of gold and upconversion nanoparticles were synthesised. Preliminary measurements were carried out to investigate the linear and non-linear optical properties of these assemblies, providing a novel insight on the interplay between plasmonic and fluorescent nanomaterials.

## 6.2 Future work

The last ten years have witnessed intense research of DNA-driven nanoparticle assembly. Since 2008, achievable crystal structures have advanced from a BCC structure to a library consisting of crystals with dozens of different symmetries. The rapid development of this field has benefit from further research in other fields, but it has also stimulated it. New techniques were developed to produce highly monodisperse inorganic nanoparticles with different sizes and shapes, novel strategies were invented to functionalise the NPs' surface with oligonucleotides and other bio-molecules, and the DNA nanotechnology has far exceeded the original function of nucleic acids as genetic materials.

However, despite the extensive work done so far in the field of DNA-NPs assembly, there is more to explore. In particular, the applicability of these systems in real-life devices still needs to be demonstrated.

The lack of inherent stability has so far limited the actual applications of superlattices. The method of DNA ligation demonstrated in this thesis has allowed for the first time to create a range of ultra-stable, dynamic, mesoscale materials which will be investigated as photonic materials.<sup>19 117</sup> The home-built setup described in **Chapter 5** will be further optimised to allow the investigation of the backscattering and reflection behaviour of the superlattices. The “breathing” effect observed for crosslinked crystals (**Section 4.2**), which caused the variation of the distance between NPs in the lattice, will be explored for dynamic plasmon coupling/de-coupling.

Additionally, the scalability of the fabrication technique needs to be addressed. Improved understanding of thermodynamic and kinetic processes at the nanoscale is expected to aid the development of more complex structures at a larger scale. In future, a potential processing technique involving the use of an external force or field (for example high pressure) will be explored to accelerate the DNA-mediated self-assembly process. Building on the preliminary work done on the seed-mediated superlattices growth (**Section 4.4**) we plan to perform pressure-guided crystallisation of DNA-coated gold nanoparticles in combination with real-time X-rays scattering measurements. We predict that the possibility to track the crystals formation and growth *in situ* via SAXS measurements while applying different pressures is of utmost importance to enable the optimisation of the experimental conditions and maximise the crystal yield. Indeed, part of the challenge of scaling-up the production of functional nanomaterials consists in obtaining high yields of production. To tackle this issue, new design of DNA strands has also been considered. All the work presented in this thesis relied on the employment of a 2-strands system, each of them loaded on the surface of a batch of nanoparticles. However, multiple strands systems can be also engineered to yield single crystal domains. In **Figure 6.1** an example of the working principle of a four strands system is presented. Two batches of AuNPs are functionalised with thiolated DNA strands, which are not complementary to each other. The assembly is triggered by the addition of two linker strands which are complementary to each other and each of them is also complementary to the oligonucleotides conjugated to the NPs’ surface. This strategy was employed for some preliminary crystallisation experiments. Two four-strands system were designed, one containing conventional oligonucleotides (system A), while the other was a rather complex, engineered system, consisting of 4 sequences modified with three carbazole nucleobases (details on the chemistry of the carbazole can be found in **Chapter 4**). All the employed sequences are reported in **Table 6.1** (System A, conventional strands) and **Table 6.2** (System B, engineered strands).

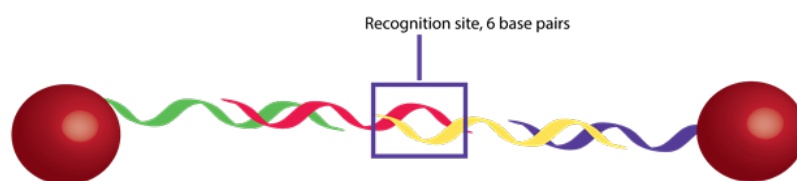


**Figure 6.1** Schematic illustration of the working principle of a four-strands system within a dimer of particles.

**Table 6.1** Oligonucleotides sequences for System A. The Res3thiol and Res4thiol have a thiol modification at the 3' end to conjugate the surface of the AuNPs. Res3linker is designed to bind Res3thiol with 18 bases complementarity. In the same way, Res4linker is designed to bind Res4thiol. When mixed together, Res3linker hybridises with Res4linker with a complementarity of 6 bases. Sp18 indicates a polyethylene glycol spacer adding 18 atoms.

Abbreviation	Sequence and Modification
Res3thiol	5'-Thiol-(Sp18) <sub>2</sub> -CATCCATCCTTATCAACT-3'
Res4thiol	5'-Thiol-(Sp18) <sub>2</sub> -AACGACTCATACTCACCT-3'
Res3linker	5'-TTCCTT-A-AGTTGATAAGGATGGATG-3'
Res4linker	5'-AAGGAA-A-AGGTGAGTATGAGTCGTT-3'

**Table 6.2** Details of the sequences designed for System B, an engineered system containing three cyanoviny carbazole nucleobases (position indicated by an 'X'). The Res5thiol and Res6thiol have a thiol modification at the 3' end to conjugate the surface of the AuNPs. Res5linker is designed to bind Res5thiol with 18 bases complementarity. In the same way, Res6linker is designed to bind Res6thiol. When mixed together, Res3linker hybridises with Res4linker with a complementarity of 6 bases. Under UV-B irradiation,



the three carbazole are activated and will form a covalent bond with a facing thymine base in the opposite strand.

Abbreviation	Sequence and Modification
Res5thiol	5'Thiol (Sp18) <sub>2</sub> AAC GAC TCA TGT CTC ACC T 3'
Res6thiol	5'Thiol (Sp18) <sub>2</sub> CAT CCA TCC TGT ATC AAC T 3'
Res5linker	5' AA GGA XAA GGT GAG AXA TGA GTC GTT 3'
Res6linker	5' TGT CCT T AGT TGA TAXA GGA TGG ATG 3'

The recognition site between the linker strands (Res3linker with Res4linker, and Res5linker with Res6linker) consists of 6 complementary base pairs, against to the 15 bases in the case of Res1 and Res2. We postulated that the decreased level of complementarity would help the re-arrangement in an ordered manner, as less energy would be required to de-hybridised and re-hybridised. For this reason, the annealing temperature was lowered to 55 °C (compared to the 70 °C used in **Chapter 3** and **4**), while the cooling rate profile was kept to 0.1 °C/10 min. The obtained samples were morphologically characterised by SEM imaging. The images reported in **Figure 6.2A** and **B** clearly show the abundance of single crystals, while in **C** and **D** the sharp crystal faces and the ordered arrangement of the NPs can be appreciated.

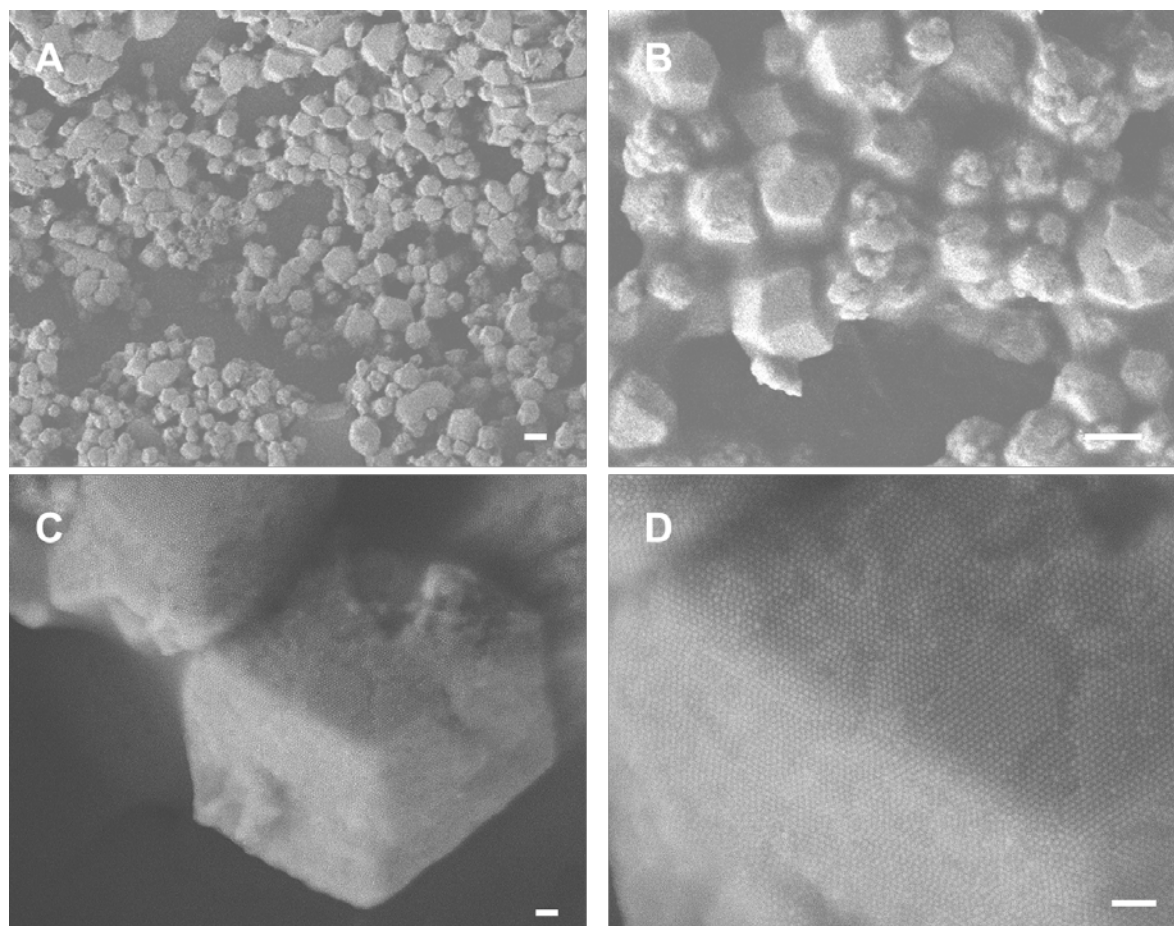


**Figure 6.2** Different magnification SEM micrographs of AuNPs superlattices obtained by NPs functionalised with Res3thiol and Res4thiol, assembled together by the addition of Res3linker and Res4linker *via* the slow (0.1 °C/10 min) cooling from 55 °C. Scale bars in A and B 1  $\mu\text{m}$ , scale bars in C and D 100 nm.

In addition to conventional DNA strands, also engineered oligonucleotides were employed. Due to the presence of three carbazole modifications, System B (**Table 6.2**) can crosslink the four oligonucleotides, thus resulting in a system stable to denaturing conditions. The assembly was carried out under the same conditions as System A, and micron-sized crystals were obtained (SEM shown in **Figure 6.3A**). Following successful crystallisation, the efficiency of the carbazole crosslinking was tested. An aliquot of as-synthesised crystals in phosphate buffer 0.01 M, SDS 0.01% and NaCl 0.3 M was placed in an ice bath under a UV lamp and irradiated for 30 minutes. The crosslinked crystals were purified by a gentle centrifugation (1 min, 700 rpm, 3x) and resuspended in water. SEM images of irradiated crystals in buffered conditions are shown in **Figure 6.3B**, showing no significant changes compared to the superlattices prior irradiation. Following transfer to pure water, the crystal structure was also preserved (**Figure 6.3C**), proving the ability of this new DNA design in retaining the crystal structure in destabilising conditions.

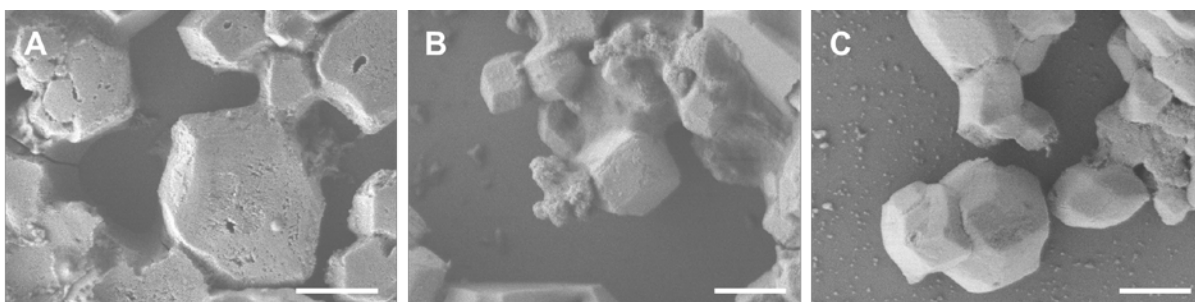


**Figure 6.3** SEM micrographs of AuNPs superlattices obtained by NPs functionalised with Res5thiol and Res6thiol, assembled together by the addition of Res5linker and Res6linker. In A, the as-synthesised crystals in phosphate buffer and NaCl 0.3 M. After the assembly, the same crystals were irradiated with 365 nm light for 30 minutes to activate the carbazole and induce the crosslinking between the complementary sequences. In B the crosslinked crystals are shown in the assembly buffer. In C, the superlattices were purified from the salt and transferred to pure water, showing that the crystal structure was retained even in low ionic strength medium.

In the long-term, the feasibility of application in nano-electronics will be considered. Although the intrinsic conductance properties of DNA might not be suitable for this task, metallisation strategies have been proved successful in fabricating conducting nanowires and metal cluster nanostructures onto DNA.<sup>113,196–198</sup> For this aim, DNA can be modified either by incorporating single metal atoms into its duplex or by continuously metallizing the whole duplex in between NPs. Development along this direction may unveil new potential to research areas such as micro- and nanofabrication and information storage.

To conclude, the field of DNA-nanoparticles technology is breaking the boundaries of chemistry, biology, physics, and material science and it is branching out to reach the industry implementation stage, with the promise to create novel solutions to this century's grand challenges.



## Appendix A

### A.1 List of reagents and suppliers

All reagents were used without further purification.

Sigma-Adrich: sodium tetrachloroaurate (III) (99% purity), sodium citrate ( $\geq 99\%$  purity), sodium chloride (99% purity), silver nitrate (98% purity), iron(III) chloride hexahydrate (97% purity), tannic acid ( $\geq 99\%$  purity), tris(2-carboxyethyl)phosphine hydrochloride (TCEP, powder), potassium cyanide ( $\geq 96\%$  purity), urea ( $\geq 99\%$  purity), yttrium (III) chloride hexahydrate, ytterbium(III) chloride hexahydrate, erbium(III) chloride hexahydrate, thulium(III) chloride hexahydrate, oleic acid (90%), 1-octadecene (90%), sodium hydroxide ( $\geq 98\%$  purity), absolute alcohol, phosphate buffered saline (PBS), sodium dodecyl sulfate ( $\geq 98\%$  purity), monobasic phosphate (99%), dibasic phosphate (99%), 4-(2-Hydroxyethyl)piperazine-1-ethanesulfonic acid, N-(2-Hydroxyethyl)piperazine-N'-(2-ethanesulfonic acid) (HEPES,  $\geq 99.5\%$  purity), tetraethyl orthosilicate (TEOS,  $\geq 99\%$  purity), Polyoxyethylene (5) nonylphenylether (IGEPAL CO-520), polyacrylic acid (PAA, 1.8 kDa), tetrahydrofuran (THF,  $\geq 99\%$  purity), N-(3-Dimethylaminopropyl)-N'-ethylcarbodiimide hydrochloride (EDC,  $\geq 99\%$  purity), N-Hydroxysulfosuccinimide sodium salt (sulfo-NHS,  $> 98\%$  purity), (3-Aminopropyl)trimethoxysilane (APTMS, 97% purity), 2-(N-Morpholino)ethanesulfonic acid (MES,  $\geq 99\%$  purity).

VWR: syringe (20G), syringe filter (0.2  $\mu\text{m}$ ), methanol (99% purity), hexane (90% purity), N,N-Dimethylformamide (DMF, 99% purity), acrylamide: bis-acrylamide 1:29 (40% solution).

Agar scientific: 200 mesh copper/nickel grid, silicon wafer chips (2 mm).

Alfa Aesar: Succinic anhydride (99% purity), 1-octadecene (96%), oleic acid (90%).

### A.2 Description of the characterisation techniques

#### A.2.1 UV-Visible spectroscopy

The concentration of gold and silver NPs as well as oligonucleotides were determined by monitoring the absorption maximum over a wavelength range of 200 to 800 nm. In case of dilute samples (optical density  $\leq 1$ ) and negligible scattering, the concentration can be determined by using the Beer-Lambert law (**Equation A.1**). This equation correlates the maximum optical density, defined as the negative logarithm of the transmitted intensity divided by the incident intensity, with the

concentration of the analyte. Molar concentrations can be obtained using the molar extinction coefficient, a measure of the absorption efficiency of a species for a specific wavelength. Extinction coefficients for different sizes of gold and silver colloids are tabulated,<sup>199,200</sup> while the coefficients for the DNA strands were determined by Dr. Afaf El-Sagheer. Spectra were collected using a black Low Volume Quartz Cuvette (optical path length 1 cm) using a UV – 2600 Shimadzu UV-vis spectrophotometer.

$$C = \frac{OD_{max}}{\varepsilon \cdot l}$$

**Equation A.1** Rearranged Beer-Lambert equation for the determination of sample concentration.

*C*: Concentration (mol/L), *OD<sub>max</sub>*: Maximal Optical Density, *l*: path length of light (cm) and *ε*: extinction coefficient (L·mol<sup>-1</sup>·cm<sup>-1</sup>) obtained from reference.<sup>199</sup>

### A.2.2 Microscopy techniques

The morphology of materials can be visualised using microscopy techniques. Different microscopies have different resolutions, depending on the imaging wavelength as  $\lambda/NA$ , where NA is the numerical aperture of the microscope, a dimensionless number that characterises the range of angles over which the system can accept or emit light, and it depends on the refractive index of the medium. In order to image objects at the nanoscale, wavelengths shorter than visible light must be used; in this case electron microscopes are employed. In this technique, specimens are visualised using an electron beam as imaging source rather than visible light, as in the case of optical microscopy. The use of electrons as incident beam also presents as additional advantage the generation of characteristic X-rays from the inner shells of the analyte, thus allowing for elemental analysis of the specimen by measuring the energies of the emitted X-ray, which can be unambiguously assigned to specific chemical elements. This technique is called Energy Dispersive X-ray Spectrometry (EDX or EDS), and can be coupled with both transmission and scanning electron microscopies.

### A.2.3 Transmission electron microscopy

In Transmission Electron Microscopy (TEM), the visualisation is possible by collecting the electrons transmitted through the specimen and collected on a fluorescent screen. This technique relies on the appropriate specimen preparation, as a thick layer of the sample will impede the transmittance of any electrons. Therefore, a diluted specimen droplet was deposited and evaporated on a 400 Mesh Copper grid coated with a Formvar and a carbon film to make the surface hydrophobic.

Visualisation of gold nanoparticles and their assemblies was performed using a Hitachi H7000 TEM, operating voltage: 75kV or Hitachi H7700, operating voltage 100kV. Images of the particles were analysed using the ImageJ software and the data were plotted using Origin software to obtain size distribution histograms.

#### **A.2.4 Scanning electron microscopy**

In Scanning Electron Microscopy (SEM) the image is formed by rastering the surface of the specimen with an electron beam and collecting the electron coming from the sample. According to which kind of electrons are collected, different types of detector are available. In the case of SEI, Secondary Electron Image, SEI, or Low secondary Electron Image, LEI, electrons emitted from the valence levels of the analyte are collected. Whereas these electrons possess low energy, only the ones emitted at the top surface of the specimen can escape and be collected; therefore, SEI is mostly used to observe the topography of the specimen surface. Backscattered Electron Images (BEI) are obtained by collection of incident electrons from the raster beam which are scattered backward elastically from the sample. These electrons have higher energy, thus information about the deeper structure of the sample can be gathered.

#### **A.2.5 Dynamic light scattering and zeta potential**

Dynamic light scattering measurements was used to estimate the hydrodynamic radii of nanomaterial in suspension. This technique relies on the Brownian motion of the particles and the Rayleigh scattering provoked by the particles being intercepted by a light beam. A measurement is performed using a coherent and monochromatic light source, such as a laser, on a sample of particles in a liquid medium and recording the interference pattern created by the when light is scattered in all directions by multiple objects. This measurement is performed in a liquid medium, implying that the scatters are in a constant Brownian motion, which causes fluctuations in the interference pattern. The time scale of these fluctuations can be correlated to the diffusion coefficient, which, in turn, can be used to calculate the hydrodynamic radius with the Stokes-Einstein **Equation A.2**.

$$d_H = \frac{k T}{3 \pi \eta D}$$

**Equation A.2** Stokes-Einstein equation, where  $d_H$  is the hydrodynamic radius,  $k$  is the Boltzmann's constant,  $T$  the absolute temperature,  $D$  is the diffusion coefficient and  $\eta$  the viscosity of the medium.

The zeta potential is the net charge of a particle at the Stern layer, the internal region of the electrical double layer which is created between a particle and the counterions strongly bounded to its surface. The magnitude of the zeta potential is associated with the colloidal stability of the system, as particles with a high zeta potential value (either strongly negative or positive) are highly charged and will repel each other and thus reducing the tendency to aggregate. Determination of zeta potential is performed by measuring the velocity of the particles exposed to an electric field (electrophoretic mobility); these two quantities are related by the Henry equation (**Equation A.3**). Electrophoretic mobility is measured by a laser light source which is split to provide an incident and reference beam. The incident laser beam passes through the centre of the sample cell, and the scattered light at an angle of about  $13^\circ$  is detected. When an electric field is applied to the cell, any particles moving through the measurement volume will cause fluctuations proportional to the particle speed. Finally, the application of the Smoluchowky approximation of the Henry equation, allows the calculation of the zeta potential, which is hence defined as “apparent zeta potential”.

$$U_E = \frac{2 \varepsilon \zeta f(\kappa a)}{3\eta}$$

**Equation A.3** Henry equation showing the relationship between zeta potential ( $\zeta$ ) and electrophoretic mobility ( $U_E$ ). The other terms in the equation are  $\varepsilon$ , the dielectric constant,  $\eta$ , the viscosity of the medium, and  $f(\kappa a)$ , the Henry’s function which takes into account the radius  $a$  of the particles, and the Debye length  $\kappa$  of the electrolytes.

Electrophoretic mobility and zeta potential calculations were performed using the same instrument as for the DLS, a Malvern Zetasizer Nano ZS with a He-Ne light source at 633 nm wavelength. Each measurement was performed loading 1 mL of the colloidal sample in a disposable folded capillary cell and recording 10 sub-runs for three times.

### A.2.6 Powder X-rays scattering

X-ray diffraction is a technique employed for the determination of crystal structures by recording the elastic scattering of X-rays in a by atoms in a periodic lattice in the angular range  $10$ - $80^\circ$ . The scattered monochromatic x-rays that are in phase give constructive interference. **Figure A. 1A** shows the diffraction of x-rays by crystal planes formed by an array of scatterers. allows Using the Bragg's law  $2d_{hkl} = n\lambda \sin\theta$ , where  $d$  is the plane spacing and  $n$  is an integer number, the crystal spacings can be determined.



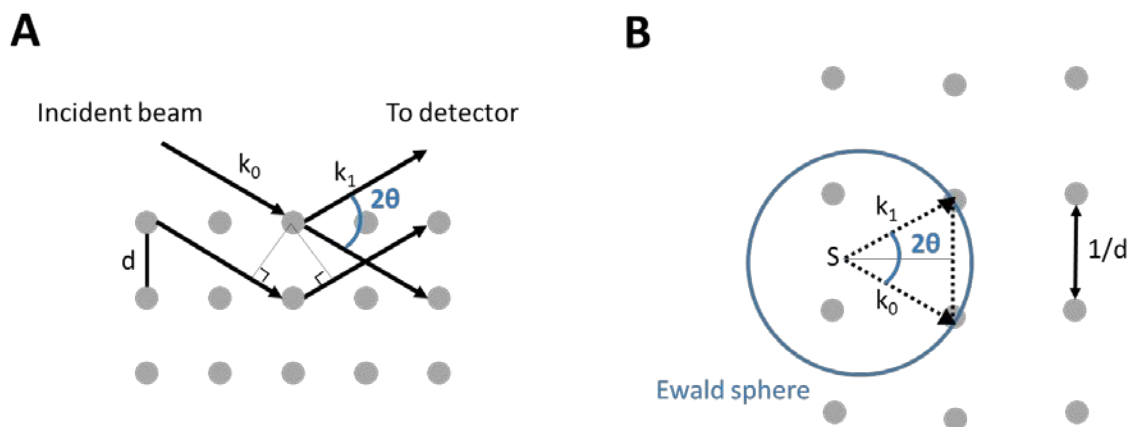


**Figure A. 1** Schematic representation of a series of xy crystalline planes formed by scattering elements, in the real (A) and reciprocal (B) space.

In the reciprocal space (**Figure A. 1B**), an array of xy atomic planes spaced along z becomes a row of reciprocal-lattice points spaced along z with a periodicity of  $1/d$ .<sup>201</sup> The Ewald sphere is a geometrical construction with radius equal to  $1/\lambda$ ; the Bragg's condition is satisfied and wherever the scattering points are found on the surface of this sphere. In XRD measurements the wavelength of the incident beam is usually fixed meaning that the radius of the Ewald sphere is constant. A polycrystalline specimen contains many crystallites in all possible orientations and so the probability that many reciprocal lattice points coincide with the surface of the Ewald sphere is high. Therefore, diffraction from the crystalline plane can be collected by moving the detector to the right positions. This collection method is called Bragg-Brentano geometry.

### A.2.7 Small-angle X-rays scattering

Small-Angle X-ray Scattering (SAXS) is a scattering technique which detects the differences in electron densities within a specimen, by recording the elastic scattering of X-rays in a small angular range (typically from  $0.1^\circ$  to  $10^\circ$ ). While XRD investigates the atomic structure of the material, SAXS is helpful in determining structures at the nanoscale. This is due to the angular range of X-rays collection. Being in the reciprocal space, the collection of photons elastically scattered at small angle provides information at a lower resolution and *viceversa*.

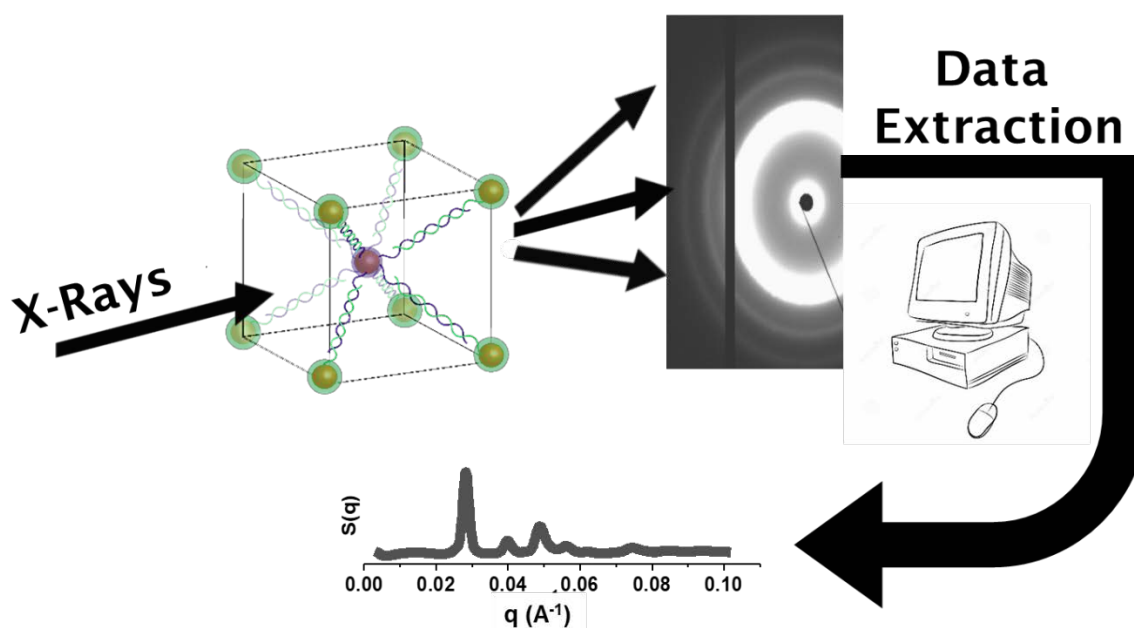


**Figure A 2** Schematic illustration of the SAXS data collection and processing. A monochromatic X-rays source hits the sample. The diffracted X-rays are collected, and an image is formed. The data are extracted and digitally processed.

**Figure A 2** shows a schematic illustration of the SAXS data collection. An X-rays beam impinges on the sample and the photons scattered at low angles are collected on a CCD detector. An image is obtained and converted to 1D scattering intensity vs. wave vector transfer,  $q$ , defined as in **Equation A.4**.

$$q = \frac{4\pi}{\lambda} \sin\left(\frac{\theta}{2}\right)$$

**Equation A.4** Definition of the wave vector  $q$  in function of the incident wavelength  $\lambda = 0.8551 \text{ \AA}$  and scattering angle  $\theta$ .

In order to be able to refer the SAXS pattern to a crystalline lattice, the intensity of the signal  $I(q)$  is converted in the corresponding structure factor  $S(q)$  and plotted against the scattering vector  $q$ . For identical NPs with spherical symmetry, the  $I(q)$  can be assumed equal to the product between the structure factor  $S(q)$  and the form factor  $P(q)$ .<sup>202</sup> For DNA-NPs assembly at high  $q$  values the contribution of  $S(q)$  to  $I(q)$  is negligible so it can be assumed as  $P(q)$  is the only contribute. However, in some cases diffuse scattering, resulting from lattice defects, will smear the fine features at high  $q$ , preventing this type of analysis. Consequently, it may be necessary to melt the superlattice into its distinct components to obtain this ratio, so the  $P(q)$  is actually measured as the  $I(q)$  of free NP(s). At this point, it is possible to assign the obtained pattern to a specific crystalline system.

### A.3 Conditions investigated for nanoparticles assemblies




Temperature, ionic strength and cooling rate were the parameters varied to optimise the superlattices yield and crystal quality. In tables the different investigated conditions are tabulated.

**Table A. 1** Condition investigated for the crystallisation of AuNPs with a thermal annealing strategy. Different salts (NaCl, MgCl<sub>2</sub>) at different concentration and different annealing temperature were tested.

		✘ No aggregate observed	NaCl (M)						MgCl <sub>2</sub> (M)					
			0.04	0.08	0.1	0.2	0.3	0.4	0.04	0.08	0.1	0.2	0.3	0.4
Annealing Temperature (°C)	48	✘	✘	✘	✘	✘	✘	↘	↘	↘	↘	↘	↘	↘
	50	✘	✘	✓	✓	✓	✓	↘	✓	✓	✓	✓	✓	↘
	52	✘	✘	✓	✓	✓	✓	↘	✓	✓	✓	✓	✓	↘
	54	✘	✘	✓	✓	✓	✓	↘	✓	✓	✓	✓	✓	↘
	56	✘	✘	✓	✓	✓	✓	↘	✓	✓	✓	✓	✓	↘




**Table A. 2** Condition investigated for the crystallisation of AuNPs with a slow cooling strategy.

NaCl at different concentration and different cooling rates were tested.






















 No aggregate observed  Aggregates observed  Not attempted		NaCl (M)					
		0.04	0.08	0.1	0.2	0.3	0.4
Cooling rate (°C/min)	0.1	✘	✘	✘	✘	✘	✘
	0.01	✘	✘	✓	✓	✓	✓
	0.1 (70-65 °C) 0.01 (65-40 °C) 0.1 (40-24 °C)	✘	✘	✓	✓	✓	✓
	0.1 (70-65 °C) 0.001 (65-45 °C) 0.1 (45-24 °C)	✘	✘	✓	✓	✓	✓
	0.001	↘	↘	↘	✓	✓	✓

**Table A. 3** Condition investigated for the crystallisation of AgNPs with a slow cooling strategy.

NaCl at different concentration and different cooling rates were tested.

 No aggregate observed  Aggregates observed  Not attempted		NaCl (M)					
		0.04	0.08	0.1	0.2	0.3	0.4
Cooling rate (°C/min)	0.1	✓	✓	✓	✓	✓	↘
	0.01	↘	↘	✓	✓	✓	↘
	0.001	↘	↘	✓	✓	✓	↘

**Table A. 4** Condition investigated for the crystallisation of UCNPs with a slow cooling strategy. NaCl at different concentration (with or without a surfactant) and different cooling rates were tested.

 No aggregate observed  Aggregates observed  Not attempted		NaCl (M)					
		0.1	0.2	0.3	0.3 + SDS 0.01%	0.4	0.4 + SDS 0.01%
Cooling rate (°C/min)	0.1						
	0.01						
	0.001						



## List of References

- (1) Conference, L. The Lund Declaration. In *New Worlds – New Solutions – Research and Innovation as a Basis for Developing Europe in a Global Context*; **2009**; 1–2.
- (2) European Commission Directorate-General for Research and Innovation. NanoData Landscape Compilation; **2016**.
- (3) Royal Society (Great Britain); Royal Academy of Engineering (Great Britain). *Nanoscience and Nanotechnologies : Opportunities and Uncertainties*; Royal Society, **2004**.
- (4) European Commission. White Paper: Strategy for a Future Chemicals Policy; Brussels, **2001**.
- (5) Commission of the European Communities. Horizon 2020 - Nanotechnologies <https://ec.europa.eu/programmes/horizon2020/en/h2020-section/nanotechnologies#Article>.
- (6) Seeman, N. C. Nucleic Acid Junctions and Lattices. *J. Theor. Biol.* **1982**, *99*, 237–247.
- (7) Seeman, N. C.; Kallenbach, N. R. Design of Immobile Nucleic Acid Junctions. *Biophys. J.* **1983**, *44*, 201–209.
- (8) Rothmund, P. W. K. Folding DNA to Create Nanoscale Shapes and Patterns. *Nature* **2006**, *440*, 297–302.
- (9) Kanaras, A. G.; Wang, Z.; Bates, A. D.; Cosstick, R.; Brust, M. Towards Multistep Nanostructure Synthesis: Programmed Enzymatic Self-Assembly of DNA/Gold Systems. *Angew. Chem. Int. Ed. Engl.* **2003**, *42*, 191–194.
- (10) Winfree Erik; Liu Furong; Wenzler Lisa A.; Seeman Nadrian C. Design and Self-Assembly of Two-Dimensional DNA Crystals. *Nature* **1998**, *394*, 539–544.
- (11) Seeman, N. Assembly of Borromean Rings from DNA. *Nature* **1997**, *386*, 137–138.
- (12) Chen, J.; Seeman, N. C. Synthesis from DNA of a Molecule with the Connectivity of a Cube. *Nature* **1991**, *50*, 133–139.
- (13) Mao, C.; Sun, W.; Shen, Z.; Seeman, N. C. A Nanomechanical Device Based on the B–Z Transition of DNA. *Nature* **1999**, *397*, 144–146.
- (14) Yurke, B.; Turberfield, A. J.; Mills, A. P.; Simmel, F. C.; Neumann, J. L. A DNA-Fuelled

## List of References

- Molecular Machine Made of DNA. *Nature* **2000**, *406*, 605–608.
- (15) Qian, L.; Winfree, E.; Bruck, J. Neural Network Computation with DNA Strand Displacement Cascades. *Nature* **2011**, *475*, 368–372.
- (16) Seelig, G.; Yurke, B.; Winfree, E. Catalyzed Relaxation of a Metastable DNA Fuel. *J. Am. Chem. Soc.* **2006**, *128*, 12211–12220.
- (17) Alivisatos, A. P.; Johnsson, K. P.; Peng, X.; Wilson, T. E.; Loweth, C. J.; Bruchez, M. P.; Schultz, P. G. Organization of 'Nanocrystal Molecules' Using DNA. *Nature* **1996**, *382*, 609–611.
- (18) Mirkin, C. A.; Letsinger, R. L.; Mucic, R. C.; Storhoff, J. J. A DNA-Based Method for Rationally Assembling Nanoparticles into Macroscopic Materials. *Nature* **1996**, *382*, 607–609.
- (19) Tan, S. J.; Campolongo, M. J.; Luo, D.; Cheng, W. Building Plasmonic Nanostructures with DNA. *Nat. Nanotechnol.* **2011**, *6*, 268–276.
- (20) Coffey, J. L.; Bigam, S. R.; Li, X.; Pinizzotto, R. F.; Rho, Y. G.; Pirtle, R. M.; Pirtle, I. L. Dictation of the Shape of Mesoscale Semiconductor Nanoparticle Assemblies by Plasmid DNA. *Appl. Phys. Lett.* **1996**, *69*, 3851–3853.
- (21) Braun, E.; Eichen, Y.; Sivan, U.; Ben-Yoseph, G. DNA-Templated Assembly and Electrode Attachment of a Conducting Silver Wire. *Nature* **1998**, *391*, 775–778.
- (22) Faraday, M. Experimental Relations of Gold (and Other Metals) to Light. *Philos. Trans.* **1857**, *147*, 145–181.
- (23) Turkevich, J.; Stevenson, P. C.; Hillier, J. A Study of the Nucleation and Growth Processes in the Synthesis of Colloidal Gold. *Discuss. Faraday Soc.* **1951**, *55*, 55–75.
- (24) Frens, G. Controlled Nucleation for the Regulation of the Particle Size in Monodisperse Gold Suspensions. *Nat. Phys. Sci.* **1973**, *241*, 20–22.
- (25) Schulz, F.; Homolka, T.; Bastús, N. G.; Puentes, V.; Weller, H.; Vossmeier, T. Little Adjustments Significantly Improve the Turkevich Synthesis of Gold Nanoparticles. *Langmuir* **2014**, *30*, 10779–10784.
- (26) Ji, X.; Song, X.; Li, J.; Bai, Y.; Yang, W.; Peng, X. Size Control of Gold Nanocrystals in Citrate Reduction: The Third Role of Citrate. *J. Am. Chem. Soc.* **2007**, *129*, 13939–13948.
- (27) Kumar, S.; Gandhi, K. S.; Kumar, R. Modeling of Formation of Gold Nanoparticles by Citrate



- Method. *Ind. Eng. Chem. Res.* **2007**, *46*, 3128–3136.
- (28) Xia, H.; Bai, S.; Hartmann, J.; Wang, D. Synthesis of Monodisperse Quasi-Spherical Gold Nanoparticles in Water via Silver(I)-Assisted Citrate Reduction. *Langmuir* **2010**, *26*, 3585–3589.
- (29) Biggs, S.; Chow, M. K.; Zukoski, C. F.; Grieser, F. The Role of Colloidal Stability in the Formation of Gold Sols. *J. Colloid Interface Sci.* **1993**, *160*, 511–513.
- (30) Privman, V.; Goia, D. V.; Park, J.; Matijević, E. Mechanism of Formation of Monodispersed Colloids by Aggregation of Nanosize Precursors. *J. Colloid Interface Sci.* **1999**, *213*, 36–45.
- (31) Jana, N. R.; Gearheart, L.; Murphy, C. J. Evidence for Seed-Mediated Nucleation in the Chemical Reduction of Gold Salts to Gold Nanoparticles. *Chem. Mater.* **2001**, *13*, 2313–2322.
- (32) Ziegler, C.; Eychmüller, A. Seeded Growth Synthesis of Uniform Gold Nanoparticles with Diameters of 15–300 Nm. *J. Phys. Chem. C* **2011**, *115*, 4502–4506.
- (33) Bastús, N. G.; Comenge, J.; Puentes, V. V. Kinetically Controlled Seeded Growth Synthesis of Citrate-Stabilized Gold Nanoparticles of up to 200 Nm: Size Focusing versus Ostwald Ripening. *Langmuir* **2011**, *27*, 11098–11105.
- (34) Lee, P. C.; Meisel, D. Adsorption and Surface-Enhanced Raman of Dyes on Silver and Gold Sols. *J. Phys. Chem.* **1982**, *60439*, 3391–3395.
- (35) Janata, E.; Henglein, A.; Ershov, B. G. First Clusters of Ag<sup>+</sup> Ion Reduction in Aqueous Solution; **1994**; Vol. 98.
- (36) Henglein, A.; Giersig, M. Formation of Colloidal Silver Nanoparticles: Capping Action of Citrate. *J. Phys. Chem. B* **1999**, *103*, 9533–9539.
- (37) Dadosh, T. Synthesis of Uniform Silver Nanoparticles with a Controllable Size. *Mater. Lett.* **2009**, *63*, 2236–2238.
- (38) Bastús, N. G.; Merkoçi, F.; Piella, J.; Puentes, V. Synthesis of Highly Monodisperse Citrate-Stabilized Silver Nanoparticles of up to 200 Nm: Kinetic Control and Catalytic Properties. *Chem. Mater.* **2014**, *26*, 2836–2846.
- (39) Conde, J.; Dias, J. T.; Grazú, V.; Moros, M.; Baptista, P. V.; de la Fuente, J. M. Revisiting 30 Years of Biofunctionalization and Surface Chemistry of Inorganic Nanoparticles for Nanomedicine. *Front. Chem.* **2014**, *2*, 48.

## List of References

- (40) Mie, G. Beitrage Zur Optik Triiber Medien, Speziell Colloidaler Metallosungen. *Ann. Phys.* **1908**, *25*, 377–445.
- (41) Link, S.; El-Sayed, M. A. Size and Temperature Dependence of the Plasmon Absorption of Colloidal Gold Nanoparticles. **1999**.
- (42) Noguez, C. Surface Plasmons on Metal Nanoparticles: The Influence of Shape and Physical Environment. *J. Phys. Chem. C* **2007**, *111*, 3606–3619.
- (43) Amendola, V.; Pilot, R.; Frasconi, M.; Maragò, O. M.; Iatì, M. A. Surface Plasmon Resonance in Gold Nanoparticles: A Review. *J. Phys. Condens. Matter* **2017**, *29*, 1–48.
- (44) Liz-Marzan, L. M. Nanomaterials Formation and Color. *Mater. Today* **2004**, *7*, 26–31.
- (45) Kreibig, U.; Genzel, L. Optical Absorption of Small Metallic Particles. *Surf. Sci.* **1985**, *156*, 678–700.
- (46) Malinsky, M. D.; Lance Kelly, K.; Schatz, G. C.; van Duyne, R. P. Nanosphere Lithography: Effect of Substrate on the Localized Surface Plasmon Resonance Spectrum of Silver Nanoparticles. *J. Phys. Chem. B* **2001**, *105*, 2343–2350.
- (47) Ghosh, S. K.; Pal, T. Interparticle Coupling Effect on the Surface Plasmon Resonance of Gold Nanoparticles: From Theory to Applications. *Chem. Rev.* **2007**, *107*, 4797–4862.
- (48) Mooradian, A. Photoluminescence of Metals. *Phys. Rev. Lett.* **1969**, *22*, 185–187.
- (49) Boyd, G. T.; Yu, Z. H.; Shen, Y. R. Photoinduced Luminescence from the Noble Metals and Its Enhancement on Roughened Surfaces. *Phys. Rev. B* **1986**, *33*, 7923–7936.
- (50) Bouhelier, A.; Beversluis, M. R.; Novotny, L. Characterization of Nanoplasmonic Structures by Locally Excited Photoluminescence. *Appl. Phys. Lett.* **2003**, *83*, 5041–5043.
- (51) Olesiak-Banska, J.; Waszkielewicz, M.; Obstarczyk, P.; Samoc, M. Two-Photon Absorption and Photoluminescence of Colloidal Gold Nanoparticles and Nanoclusters. *Chem. Soc. Rev.* **2019**, *48*, 4087–4117.
- (52) Beversluis, M.; Bouhelier, A.; Novotny, L. Continuum Generation from Single Gold Nanostructures through Near-Field Mediated Intraband Transitions. *Phys. Rev. B - Condens. Matter Mater. Phys.* **2003**, *68*, 115433-1–10.
- (53) Helmchen, F.; Denk, W. Deep Tissue Two-Photon Microscopy. *Nat. Methods* **2005**, *2*, 932–940.

- (54) Kano, H.; Kawata, S. Two-Photon-Excited Fluorescence Enhanced by a Surface Plasmon. *Opt. Lett.* **1996**, *21*, 1848–1850.
- (55) Lamprecht, B.; Krenn, J. R.; Leitner, A.; Aussenegg, F. R. Resonant and Off-Resonant Light-Driven Plasmons in Metal Nanoparticles Studied by Femtosecond-Resolution Third-Harmonic Generation. *Phys. Rev. Lett.* **1999**, *83*, 4421–4424.
- (56) Yelin, D.; Oron, D.; Thiberge, S.; Moses, E.; Silberberg, Y. Multiphoton Plasmon-Resonance Microscopy. *Opt. Express* **2003**, *11*, 1385–1391.
- (57) Beermann, J.; Bozhevolnyi, S. I. Two-Photon Luminescence Microscopy of Field Enhancement at Gold Nanoparticles. *Phys. Status Solidi C Conf.* **2005**, *2*, 3983–3987.
- (58) Yao, S.; Belfield, K. D. Two-Photon Fluorescent Probes for Bioimaging. *European J. Org. Chem.* **2012**, No. 17, 3199–3217.
- (59) Menyuk, N.; Dwight, K.; Pierce, J. W. NaYF<sub>4</sub>: Yb,Er - An Efficient Upconversion Phosphor. *Appl. Phys. Lett.* **1972**, *21*, 159–161.
- (60) Kano, T.; Yamamoto, H.; Otomo, Y. NaLnF<sub>4</sub>:Yb,Er (Ln:Y,Gd,La): Efficient Green-Emitting Infrared-Excited Phosphors. *J. Electrochem. Soc.* **1972**, *119*, 1561–1564.
- (61) Heer, S.; Lehmann, O.; Haase, M.; Güdel, H. U. Blue, Green, and Red Upconversion Emission from Lanthanide-Doped LuPo<sub>4</sub> and YbPO<sub>4</sub> Nanocrystals in a Transparent Colloidal Solution. *Angew. Chemie - Int. Ed.* **2003**, *42*, 3179–3182.
- (62) Liang, L.; Wu, H.; Hu, H.; Wu, M.; Su, Q. Enhanced Blue and Green Upconversion in Hydrothermally Synthesized Hexagonal NaY<sub>1-x</sub>Yb<sub>x</sub>F<sub>4</sub>:Ln<sup>3+</sup> (Ln<sup>3+</sup> = Er<sup>3+</sup> or Tm<sup>3+</sup>). *J. Alloys Compd.* **2004**, *368*, 94–100.
- (63) Zhou, J.; Liu, Q.; Feng, W.; Sun, Y.; Li, F. Upconversion Luminescent Materials: Advances and Applications. *Chem. Rev.* **2015**, *115*, 395–465.
- (64) Wang, F.; Liu, X. Multicolor Tuning of Lanthanide-Doped Nanoparticles by Single Wavelength Excitation. *Acc. Chem. Res.* **2014**, *47*, 1378–1385.
- (65) Sun, Q. C.; Ding, Y. C.; Sagar, D. M.; Nagpal, P. Photon Upconversion towards Applications in Energy Conversion and Bioimaging. *Prog. Surf. Sci.* **2017**, *92*, 281–316.
- (66) Chen, G.; Qiu, H.; Prasad, P. N.; Chen, X. Upconversion Nanoparticles: Design, Nanochemistry, and Applications in Theranostics. *Chem. Rev.* **2014**, *114*, 5161–5214.

## List of References

- (67) Liu, C.; Chen, D. Controlled Synthesis of Hexagon Shaped Lanthanide-Doped LaF<sub>3</sub> Nanoplates with Multicolor Upconversion Fluorescence. *J. Mater. Chem.* **2007**, *17*, 3875–3880.
- (68) Guo, H.; Dong, N.; Yin, M.; Zhang, W.; Lou, L.; Xia, S. Visible Upconversion in Rare Earth Ion-Doped Gd<sub>2</sub>O<sub>3</sub> Nanocrystals. *J. Phys. Chem. B* **2004**, *108*, 19205–19209.
- (69) Wang, G.; Qin, W.; Wang, L.; Wei, G.; Zhu, P.; Zhang, D.; Ding, F. Enhanced Ultraviolet Upconversion in YF<sub>3</sub>:Yb<sup>3+</sup>/Tm<sup>3+</sup> Nanocrystals. *J. Rare Earths* **2009**, *27*, 330–333.
- (70) Krämer, K. W.; Biner, D.; Frei, G.; Güdel, H. U.; Hehlen, M. P.; Lüthi, S. R. Hexagonal Sodium Yttrium Fluoride Based Green and Blue Emitting Upconversion Phosphors. *Chem. Mater.* **2004**, *16*, 1244–1251.
- (71) Suyver, J. F.; Aebischer, A.; Biner, D.; Gerner, P.; Grimm, J.; Heer, S.; Krämer, K. W.; Reinhard, C.; Güdel, H. U. Novel Materials Doped with Trivalent Lanthanides and Transition Metal Ions Showing Near-Infrared to Visible Photon Upconversion. *Opt. Mater. (Amst)*. **2005**, *27*, 1111–1130.
- (72) Wang, M.; Liu, J.-L.; Zhang, Y.-X.; Hou, W.; Wu, X.-L.; Xu, S.-K. Two-Phase Solvothermal Synthesis of Rare-Earth Doped NaYF<sub>4</sub> Upconversion Fluorescent Nanocrystals. *Mater. Lett.* **2009**, *63*, 325–327.
- (73) Mi, C.; Tian, Z.; Cao, C.; Wang, Z.; Mao, C.; Xu, S. Novel Microwave-Assisted Solvothermal Synthesis of NaYF<sub>4</sub>:Yb,Er Upconversion Nanoparticles and Their Application in Cancer Cell Imaging. *Langmuir* **2011**, *27*, 14632–14637.
- (74) Xiong, L. Q.; Chen, Z. G.; Yu, M. X.; Li, F. Y.; Liu, C.; Huang, C. H. Synthesis, Characterization, and in Vivo Targeted Imaging of Amine-Functionalized Rare-Earth up-Converting Nanophosphors. *Biomaterials* **2009**, *30*, 5592–5600.
- (75) Yi, G. S.; Chow, G. M. Synthesis of Hexagonal-Phase NaYF<sub>4</sub>:Yb,Er and NaYF<sub>4</sub>:Yb,Tm Nanocrystals with Efficient up-Conversion Fluorescence. *Adv. Funct. Mater.* **2006**, *16*, 2324–2329.
- (76) Mai, H. X.; Zhang, Y. W.; Si, R.; Yan, Z. G.; Sun, L. D.; You, L. P.; Yan, C. H. High-Quality Sodium Rare-Earth Fluoride Nanocrystals: Controlled Synthesis and Optical Properties. *J. Am. Chem. Soc.* **2006**, *128*, 6426–6436.
- (77) Boyer, J.-C.; Cuccia, L. A.; Capobianco, J. A. Synthesis of Colloidal Upconverting Monodisperse Nanocrystals. *Nano Lett.* **2007**, *7*, 847–852.

- (78) Heer, S.; Kömpe, K.; Güdel, H. U.; Haase, M. Highly Efficient Multicolour Upconversion Emission in Transparent Colloids of Lanthanide-Doped NaYF<sub>4</sub> Nanocrystals. *Adv. Mater.* **2004**, *16*, 2102–2105.
- (79) Yi, G. S.; Chow, G. M. Colloidal LaF<sub>3</sub>:Yb,Er, LaF<sub>3</sub>:Yb,Ho and LaF<sub>3</sub>:Yb,Tm Nanocrystals with Multicolor Upconversion Fluorescence. *J. Mater. Chem.* **2005**, *15*, 4460–4464.
- (80) Li, Z.; Zhang, Y. An Efficient and User-Friendly Method for the Synthesis of Hexagonal-Phase NaYF<sub>4</sub>:Yb, Er/Tm Nanocrystals with Controllable Shape and Upconversion Fluorescence. *Nanotechnology* **2008**, *19*, 345606.
- (81) Huang, X. Tuning the Size and Upconversion Luminescence of NaYbF<sub>4</sub>:Er<sup>3+</sup>/Tm<sup>3+</sup> Nanoparticles through Y<sup>3+</sup> or Gd<sup>3+</sup> Doping. *Opt. Mater. Express* **2016**, *6*, 2165.
- (82) Zhai, X.; Wang, Y.; Liu, X.; Liu, S.; Lei, P.; Yao, S.; Song, S.; Zhou, L.; Feng, J.; Zhang, H. A Simple Strategy for the Controlled Synthesis of Ultrasmall Hexagonal-Phase NaYF<sub>4</sub>:Yb,Er Upconversion Nanocrystals. *ChemPhotoChem* **2017**, *1*, 369–375.
- (83) Wang, F.; Han, Y.; Lim, C. S.; Lu, Y.; Wang, J.; Xu, J.; Chen, H.; Zhang, C.; Hong, M.; Liu, X. Simultaneous Phase and Size Control of Upconversion Nanocrystals through Lanthanide Doping. *Nature* **2010**, *463*, 1061–1065.
- (84) Pei, W. B.; Chen, B.; Wang, L.; Wu, J.; Teng, X.; Lau, R.; Huang, L.; Huang, W. NaF-Mediated Controlled-Synthesis of Multicolor Na<sub>x</sub>ScF<sub>3+x</sub>:Yb/Er Upconversion Nanocrystals. *Nanoscale* **2015**, *7*, 4048–4054.
- (85) DaCosta, M. V.; Doughan, S.; Han, Y.; Krull, U. J. Lanthanide Upconversion Nanoparticles and Applications in Bioassays and Bioimaging: A Review. *Anal. Chim. Acta* **2014**, *832*, 1–33.
- (86) Dong, H.; Sun, L. D.; Yan, C. H. Basic Understanding of the Lanthanide Related Upconversion Emissions. *Nanoscale* **2013**, *5*, 5703–5714.
- (87) Haase, M.; Schäfer, H. Upconverting Nanoparticles. *Angew. Chemie - Int. Ed.* **2011**, *50*, 5808–5829.
- (88) Aldaye, F. A.; Palmer, A. L.; Sleiman, H. F. Assembling Materials with DNA as the Guide. *Science (80-. )*. **2008**, *321*, 1795–1799.
- (89) Berg, J. M.; Tymoczko, J. L.; Stryer, L. *Biochemistry*, 7th ed.; W H Freeman: New York, **2011**.
- (90) Watson, J. D.; Crick, F. H. C. Molecular Structure of Nucleic Acids: A Structure for Deoxyribose Nucleic Acid. In *50 Years of DNA*; Nature Publishing Group, **2016**; Vol. 171,

## List of References

83–84.

- (91) Sinden, R. R. DNA Structure and Function; Elsevier, Ed.; Academic Press: London, **2012**.
- (92) Damha, M. J.; Giannaris, P. A.; Zabarylo, S. V. An Improved Procedure for Derivatization of Controlled-Pore Glass Beads for Solid-Phase Oligonucleotide Synthesis. *Nucleic Acids Res.* **1990**, *18*, 3813–3821.
- (93) Pon, R. T.; Yu, S. Linker Phosphoramidite Reagents for the Attachment of the First Nucleoside to Underivatized Solid-Phase Supports. *Nucleic Acids Res.* **2004**, *32*, 623–631.
- (94) Pon, R. T.; Yu, S. Tandem Oligonucleotide Synthesis Using Linker Phosphoramidites. *Nucleic Acids Res.* **2005**, *33*, 1940–1948.
- (95) Iyer, R. P.; Beaucage, S. L. Oligonucleotide Synthesis. In *Comprehensive Natural Products Chemistry*; Piet Herdewijn, Ed.; Humana Press: Totowa, New Jersey, **1999**; 105–152.
- (96) Häkkinen, H. The Gold-Sulfur Interface at the Nanoscale. *Nat. Chem.* **2012**, *4*, 443–455.
- (97) Lee, J. S.; Lytton-Jean, A. K. R.; Hurst, S. J.; Mirkin, C. A. Silver Nanoparticle - Oligonucleotide Conjugates Based on DNA with Triple Cyclic Disulfide Moieties. *Nano Lett.* **2007**, *7*, 2112–2115.
- (98) Dougan, J. A.; Karlsson, C.; Smith, W. E.; Graham, D. Enhanced Oligonucleotide-Nanoparticle Conjugate Stability Using Thioctic Acid Modified Oligonucleotides. *Nucleic Acids Res.* **2007**, *35*, 3668–3675.
- (99) Alonso-Cristobal, P.; Vilela, P.; El-Sagheer, A.; Lopez-Cabarcos, E.; Brown, T.; Muskens, O. L.; Rubio-Retama, J.; Kanaras, A. G. Highly Sensitive DNA Sensor Based on Upconversion Nanoparticles and Graphene Oxide. *ACS Appl. Mater. Interfaces* **2015**, *7*, 12422–12429.
- (100) Yoshimura, Y.; Fujimoto, K. Ultrafast Reversible Photo-Cross-Linking Reaction: Toward in Situ DNA Manipulation. *Org. Lett.* **2008**, *10*, 3227–3230.
- (101) Fujimoto, K.; Yamada, A.; Yoshimura, Y.; Tsukaguchi, T.; Sakamoto, T. Details of the Ultrafast DNA Photo-Cross-Linking Reaction of 3-Cyanovinylcarbazole Nucleoside: Cis-Trans Isomeric Effect and the Application for SNP-Based Genotyping. *J. Am. Chem. Soc.* **2013**, *135*, 16161–16167.
- (102) Sakamoto, T.; Tanaka, Y.; Fujimoto, K. DNA Photo-Cross-Linking Using 3-Cyanovinylcarbazole Modified Oligonucleotide with Threoninol Linker. *Org. Lett.* **2015**, *17*, 936–939.

- (103) Harimech, P. K.; Gerrard, S. R.; El-Sagheer, A. H.; Brown, T.; Kanaras, A. G. Reversible Ligation of Programmed DNA-Gold Nanoparticle Assemblies. *J. Am. Chem. Soc.* **2015**, *137*, 9242–9245.
- (104) Brent, T. P.; Remack, J. S. Formation of Covalent Complexes between Human O6 Alkyltransferase and BCNU-Treated Defined Length Synthetic Oligodeoxynucleotides. *Nucleic Acids Res.* **1988**, *16*, 6779–6788.
- (105) Zhao, L.; Li, L.; Xu, J.; Zhong, R. Comparative Investigation of the DNA Inter-Strand Crosslinks Induced by ACNU, BCNU, CCNU and FTMS Using High-Performance Liquid Chromatography- Electrospray Ionization Tandem Mass Spectrometry. *Int. J. Mass Spectrom.* **2014**, *368*, 30–36.
- (106) Cao, H.; Hearst, J. E.; Corash, L.; Wang, Y. LC-MS/MS for the Detection of DNA Interstrand Cross-Links Formed by 8-Methoxypsoralen and UVA Irradiation in Human Cells. *Anal. Chem.* **2008**, *80*, 2932–2938.
- (107) Lee, S.; Zheng, C. Y.; Bujold, K. E.; Mirkin, C. A. A Cross-Linking Approach to Stabilizing Stimuli-Responsive Colloidal Crystals Engineered with DNA. *J. Am. Chem. Soc.* **2019**, *141*, 11827–11831.
- (108) Hemming, K. Organic Chemistry. By J. P. Clayden, N. Greeves, S. Warren, and P. D. Wothers; Oxford University Press, 2001, ISBN 0 19 850346 6, 53 Chapters, 1508 Pages. Cost Is. *Chem. Educ.* **2001**, *6*, 396–398.
- (109) De Fazio, A. F.; El-Sagheer, A. H.; Kahn, J. S.; Nandhakumar, I.; Burton, M. R.; Brown, T.; Muskens, O. L.; Gang, O.; Kanaras, A. G. Light-Induced Reversible DNA Ligation of Gold Nanoparticle Superlattices. *ACS Nano* **2019**, *13*, 5771–5777.
- (110) Hu, Q.; Li, H.; Wang, L.; Gu, H.; Fan, C. DNA Nanotechnology-Enabled Drug Delivery Systems. *Chem. Rev.* **2019**, *119*, 6459–6506.
- (111) Kuzyk, A.; Schreiber, R.; Fan, Z.; Pardatscher, G.; Roller, E. M.; Högele, A.; Simmel, F. C.; Govorov, A. O.; Liedl, T. DNA-Based Self-Assembly of Chiral Plasmonic Nanostructures with Tailored Optical Response. *Nature* **2012**, *483*, 311–314.
- (112) Yan, W.; Xu, L.; Xu, C.; Ma, W.; Kuang, H.; Wang, L.; Kotov, N. A. Self-Assembly of Chiral Nanoparticle Pyramids with Strong R/S Optical Activity. *J. Am. Chem. Soc.* **2012**, *134*, 15114–15121.
- (113) Liu, J.; Geng, Y.; Pound, E.; Gyawali, S.; Ashton, J. R.; Hickey, J.; Woolley, A. T.; Harb, J. N.

## List of References

- Metallization of Branched DNA Origami for Nanoelectronic Circuit Fabrication. *ACS Nano* **2011**, *5*, 2240–2247.
- (114) Kuzyk, A.; Yang, Y.; Duan, X.; Stoll, S.; Govorov, A. O.; Sugiyama, H.; Endo, M.; Liu, N. A Light-Driven Three-Dimensional Plasmonic Nanosystem That Translates Molecular Motion into Reversible Chiroptical Function. *Nat. Commun.* **2016**, *7*, 10591.
- (115) Sun, L.; Lin, H.; Kohlstedt, K. L.; Schatz, G. C.; Mirkin, C. A. Design Principles for Photonic Crystals Based on Plasmonic Nanoparticle Superlattices. *Proc. Natl. Acad. Sci.* **2018**, *115*, 7242–7247.
- (116) Samai, S.; Choi, T. L. Y.; Guye, K. N.; Yan, Y.; Ginger, D. S. Plasmonic Nanoparticle Dimers with Reversibly Photoswitchable Interparticle Distances Linked by DNA. *J. Phys. Chem. C* **2018**, *122*, 13363–13370.
- (117) Park, D. J.; Zhang, C.; Ku, J. C.; Zhou, Y.; Schatz, G. C.; Mirkin, C. A. Plasmonic Photonic Crystals Realized through DNA-Programmable Assembly. *Proc. Natl. Acad. Sci. U. S. A.* **2015**, *112*, 977–981.
- (118) Huschka, R.; Zuloaga, J.; Knight, M. W.; Brown, L. V.; Nordlander, P.; Halas, N. J. Light-Induced Release of DNA from Gold Nanoparticles: Nanoshells and Nanorods. *J. Am. Chem. Soc.* **2011**, *133*, 12247–12255.
- (119) Zhan, P.; Dutta, P. K.; Wang, P.; Song, G.; Dai, M.; Zhao, S. X.; Wang, Z. G.; Yin, P.; Zhang, W.; Ding, B.; et al. Reconfigurable Three-Dimensional Gold Nanorod Plasmonic Nanostructures Organized on DNA Origami Tripod. *ACS Nano* **2017**, *11*, 1172–1179.
- (120) Hurst, S. J.; Lytton-Jean, A. K. R.; Mirkin, C. A. Maximizing DNA Loading on a Range of Gold Nanoparticle Sizes. *Anal. Chem.* **2006**, *78*, 8313–8318.
- (121) Heuer-Jungemann, A.; Feliu, N.; Bakaimi, I.; Hamaly, M.; Alkilany, A.; Chakraborty, I.; Masood, A.; Casula, M. F.; Kostopoulou, A.; Oh, E.; et al. The Role of Ligands in the Chemical Synthesis and Applications of Inorganic Nanoparticles. *Chem. Rev.* **2019**, *119*, 4819–4880.
- (122) Giljohann, D. A.; Seferos, D. S.; Daniel, W. L.; Massich, M. D.; Patel, P. C.; Mirkin, C. A. Gold Nanoparticles for Biology and Medicine. *Angew. Chemie - Int. Ed.* **2010**, *49*, 3280–3294.
- (123) Zhang, X.; Servos, M. R.; Liu, J. Fast PH-Assisted Functionalization of Silver Nanoparticles with Monothiolated DNA. *Chem. Commun.* **2012**, *48*, 10114.



- (124) Liu, B.; Liu, J. Freezing Directed Construction of Bio/Nano Interfaces: Reagentless Conjugation, Denser Spherical Nucleic Acids, and Better Nanoflares. *J. Am. Chem. Soc.* **2017**, *139*, 9471–9474.
- (125) Pakiari, A. H.; Jamshidi, Z. Nature and Strength of M–S Bonds (M = Au, Ag, and Cu) in Binary Alloy Gold Clusters. *J. Phys. Chem. A* **2010**, *114*, 9212–9221.
- (126) Battocchio, C.; Meneghini, C.; Fratoddi, I.; Venditti, I.; Russo, M. V.; Aquilanti, G.; Maurizio, C.; Bondino, F.; Matassa, R.; Rossi, M.; et al. Silver Nanoparticles Stabilized with Thiols: A Close Look at the Local Chemistry and Chemical Structure. *J. Phys. Chem. C* **2012**, *116*, 19571–19578.
- (127) Hermanson, G. *Bioconjugate Techniques*, 3rd ed.; Academic Press: London, **2013**.
- (128) Grzelczak, M.; Vermant, J.; Furst, E. M.; Liz-Marzán, L. M. Directed Self-Assembly of Nanoparticles. *ACS Nano* **2010**, *4*, 3591–3605.
- (129) Pileni, M. P. Self-Assembly of Inorganic Nanocrystals: Fabrication and Collective Intrinsic Properties. *Acc. Chem. Res.* **2007**, *40*, 685–693.
- (130) Boles, M. A.; Engel, M.; Talapin, D. V. Self-Assembly of Colloidal Nanocrystals: From Intricate Structures to Functional Materials. *Chem. Rev.* **2016**, *116*, 11220–11289.
- (131) Park, S. Y.; Lytton-Jean, A. K. R.; Lee, B.; Weigand, S.; Schatz, G. C.; Mirkin, C. A. DNA-Programmable Nanoparticle Crystallization. *Nature* **2008**, *451*, 553–556.
- (132) Nykypanchuk, D.; Maye, M. M.; van der Lelie, D.; Gang, O. DNA-Guided Crystallization of Colloidal Nanoparticles. *Nature* **2008**, *451*, 549–552.
- (133) Sun, D.; Gang, O. Binary Heterogeneous Superlattices Assembled from Quantum Dots and Gold Nanoparticles with DNA. *J. Am. Chem. Soc.* **2011**, *133*, 5252–5254.
- (134) Auyeung, E.; Li, T. I. N. G.; Senesi, A. J.; Schmucker, A. L.; Pals, B. C.; de la Cruz, M. O.; Mirkin, C. A. DNA-Mediated Nanoparticle Crystallization into Wulff Polyhedra. *Nature* **2013**, *505*, 73–77.
- (135) Auyeung, E.; Macfarlane, R. J.; Choi, C. H. J.; Cutler, J. I.; Mirkin, C. A. Transitioning DNA-Engineered Nanoparticle Superlattices from Solution to the Solid State. *Adv. Mater.* **2012**, *24*, 5181–5186.
- (136) Zhang, C.; Macfarlane, R. J.; Young, K. L.; Choi, C. H. J.; Hao, L.; Auyeung, E.; Liu, G.; Zhou, X.; Mirkin, C. A. A General Approach to DNA-Programmable Atom Equivalents. *Nat. Mater.*

## List of References

- 2013**, *12*, 741–746.
- (137) Auyeung, E.; Morris, W.; Mondloch, J. E.; Hupp, J. T.; Farha, O. K.; Mirkin, C. a. Controlling Structure and Porosity in Catalytic Nanoparticle Superlattices with DNA. *J. Am. Chem. Soc.* **2015**, *137*, 1658–1662.
- (138) O'Brien, M. N.; Brown, K. A.; Mirkin, C. A. Critical Undercooling in DNA-Mediated Nanoparticle Crystallization. *ACS Nano* **2016**, *10*, 1363–1368.
- (139) Kim, Y.; Macfarlane, R. J.; Jones, M. R.; Mirkin, C. A. Transmutable Nanoparticles with Reconfigurable Surface Ligands. *Science (80-. )*. **2016**, *351*, 579–582.
- (140) Macfarlane, R. J.; Lee, B.; Jones, M. R.; Harris, N.; Schatz, G. C.; Mirkin, C. A. Nanoparticle Superlattice Engineering with DNA. *Science (80-. )*. **2011**, *334*, 204–208.
- (141) Jones, M. R.; Macfarlane, R. J.; Lee, B.; Zhang, J.; Young, K. L.; Senesi, A. J.; Mirkin, C. a. DNA-Nanoparticle Superlattices Formed from Anisotropic Building Blocks. *Nat. Mater.* **2010**, *9*, 913–917.
- (142) O'Brien, M. N.; Jones, M. R.; Lee, B.; Mirkin, C. a. Anisotropic Nanoparticle Complementarity in DNA-Mediated Co-Crystallization. *Nat. Mater.* **2015**, *14*, 833–839.
- (143) Liu, W.; Tagawa, M.; Xin, H. L.; Wang, T.; Emamy, H.; Li, H.; Yager, K. G.; Starr, F. W.; Tkachenko, A. V; Gang, O. Diamond Family of Nanoparticle Superlattices. *Science (80-. )*. **2016**, *351*, 582–586.
- (144) Seo, S. E.; Girard, M.; De La Cruz, M. O.; Mirkin, C. A. The Importance of Salt-Enhanced Electrostatic Repulsion in Colloidal Crystal Engineering with DNA. *ACS Cent. Sci.* **2019**, *5*, 186–191.
- (145) Oh, T.; Ku, J. C.; Lee, J.-H.; Hersam, M. C.; Mirkin, C. A. Density-Gradient Control over Nanoparticle Supercrystal Formation. *Nano Lett.* **2018**, *18*, 6022–6029.
- (146) Seo, S. E.; Wang, M. X.; Shade, C. M.; Rouge, J. L.; Brown, K. A.; Mirkin, C. A. Modulating the Bond Strength of DNA–Nanoparticle Superlattices. *ACS Nano* **2015**, *10*, 1771–1779.
- (147) Oh, T.; Park, S. S.; Mirkin, C. A. Stabilization of Colloidal Crystals Engineered with DNA. *Adv. Mater.* **2018**, *31*, 1805480 (1-5).
- (148) Macfarlane, R. J.; O'Brien, M. N.; Petrosko, S. H.; Mirkin, C. A. Nucleic Acid-Modified Nanostructures as Programmable Atom Equivalents: Forging a New “Table of Elements.” *Angew. Chemie Int. Ed.* **2013**, *52*, 5688–5698.

- (149) Park, J.; An, K.; Hwang, Y.; Park, J. E. G.; Noh, H. J.; Kim, J. Y.; Park, J. H.; Hwang, N. M.; Hyeon, T. Ultra-Large-Scale Syntheses of Monodisperse Nanocrystals. *Nat. Mater.* **2004**, *3*, 891–895.
- (150) Giust, D.; Lucío, M. I.; El-Sagheer, A. H.; Brown, T.; Williams, L. E.; Muskens, O. L.; Kanaras, A. G. Graphene Oxide–Upconversion Nanoparticle Based Portable Sensors for Assessing Nutritional Deficiencies in Crops. *ACS Nano* **2018**, *12*, 6273–6279.
- (151) Maier, S. A.; Kik, P. G.; Atwater, H. A.; Meltzer, S.; Harel, E.; Koel, B. E.; Requicha, A. A. G. Local Detection of Electromagnetic Energy Transport below the Diffraction Limit in Metal Nanoparticle Plasmon Waveguides. *Nat. Mater.* **2003**, *2*, 229–232.
- (152) Jain, P. K.; Huang, X.; El-Sayed, I. H.; El-Sayed, M. A. Noble Metals on the Nanoscale: Optical and Photothermal Properties and Some Applications in Imaging, Sensing, Biology, and Medicine. *Acc. Chem. Res.* **2008**, *41*, 1578–1586.
- (153) Zhang, H.; Li, Y.; Ivanov, I. A.; Qu, Y.; Huang, Y.; Duan, X. Plasmonic Modulation of the Upconversion Fluorescence in NaYF<sub>4</sub>:Yb/Tm Hexaplate Nanocrystals Using Gold Nanoparticles or Nanoshells. *Angew. Chem. Int. Ed. Engl.* **2010**, *49*, 2865–2868.
- (154) Yin, Y.; Alivisatos, A. P. Colloidal Nanocrystal Synthesis and the Organic–Inorganic Interface. *Nature* **2005**, *437*, 664–670.
- (155) Bealing, C. R.; Baumgardner, W. J.; Choi, J. J.; Hanrath, T.; Hennig, R. G. Predicting Nanocrystal Shape through Consideration of Surface-Ligand Interactions. *ACS Nano* **2012**, *6*, 2118–2127.
- (156) Johnson, N. J. J.; Oakden, W.; Stanisz, G. J.; Scott Prosser, R.; Van Veggel, F. C. J. M. Size-Tunable, Ultrasmall NaGdF<sub>4</sub> Nanoparticles: Insights into Their T<sub>1</sub> MRI Contrast Enhancement. *Chem. Mater.* **2011**, *23*, 3714–3722.
- (157) Wang, F.; Wang, J.; Liu, X. Direct Evidence of a Surface Quenching Effect on Size-Dependent Luminescence of Upconversion Nanoparticles. *Angew. Chemie - Int. Ed.* **2010**, *49*, 7456–7460.
- (158) Park, J.; An, K.; Hwang, Y.; Park, J. E. G.; Noh, H. J.; Kim, J. Y.; Park, J. H.; Hwang, N. M.; Hyeon, T. Ultra-Large-Scale Syntheses of Monodisperse Nanocrystals. *Nat. Mater.* **2004**, *3*, 891–895.
- (159) Bronstein, L. M.; Huang, X.; Retrum, J.; Schmucker, A.; Pink, M.; Stein, B. D.; Dragnea, B. Influence of Iron Oleate Complex Structure on Iron Oxide Nanoparticle Formation. *Chem.*

## List of References

- Mater.* **2007**, *19*, 3624–3632.
- (160) Ding, H. L.; Zhang, Y. X.; Wang, S.; Xu, J. M.; Xu, S. C.; Li, G. H. Fe<sub>3</sub>O<sub>4</sub>@SiO<sub>2</sub>core/Shell Nanoparticles: The Silica Coating Regulations with a Single Core for Different Core Sizes and Shell Thicknesses. *Chem. Mater.* **2012**, *24*, 4572–4580.
- (161) Wang, S. B.; Min, Y. L.; Yu, S. H. Synthesis and Magnetic Properties of Uniform Hematite Nanocubes. *J. Phys. Chem. C* **2007**, *111*, 3551–3554.
- (162) Ge, J.; Hu, Y.; Biasini, M.; Beyermann, W. P.; Yin, Y. Superparamagnetic Magnetite Colloidal Nanocrystal Clusters. *Angew. Chemie Int. Ed.* **2007**, *46*, 4342–4345.
- (163) Macfarlane, R. J.; Jones, M. R.; Senesi, A. J.; Young, K. L.; Lee, B.; Wu, J.; Mirkin, C. A. Establishing the Design Rules for DNA-Mediated Programmable Colloidal Crystallization. *Angew. Chemie - Int. Ed.* **2010**, *49*, 4589–4592.
- (164) Nucleic Acids in Chemistry and Biology; Blackburn, G. M., Gait, M. J., Loakes, D., Williams, D. M., Eds.; Royal Society of Chemistry: Cambridge, **2007**.
- (165) Chrambach, A.; Rodbard, D. Polyacrylamide Gel Electrophoresis. *Science (80-. )*. **1971**, *172*, 440–451.
- (166) Burns, J. A.; Butler, J. C.; Moran, J.; Whitesides, G. M. Selective Reduction of Disulfides by Tris(2-Carboxyethyl)Phosphine; **1991**; Vol. 56.
- (167) Li, X.; Jiang, L.; Zhan, Q.; Qian, J.; He, S. Localized Surface Plasmon Resonance (LSPR) of Polyelectrolyte-Functionalized Gold-Nanoparticles for Bio-Sensing. *Colloids Surfaces A Physicochem. Eng. Asp.* **2009**, *332*, 172–179.
- (168) Qi, P. H.; Hiskey, J. B. Electrochemical Behavior of Gold in Iodide Solutions. *Hydrometallurgy* **1993**, *32*, 161–179.
- (169) Nakao, Y.; Soneb, K. Reversible Dissolutioddeposition of Gold in Iodine-Iodide-Acetonitrile Systems. *Chem. Commun* **1996**, No. 8, 897–898.
- (170) Fu, Y.; Ng, S. P.; Qiu, G.; Hung, T. F.; Wu, C. M. L.; Lee, C. S. A Redox-Controlled Electrolyte for Plasmonic Enhanced Dye-Sensitized Solar Cells. *Nanoscale* **2017**, *9*, 10940–10947.
- (171) Hajizadeh, S.; Farhadi, K.; Forough, M.; Sabzi, R. E. Silver Nanoparticles as a Cyanide Colorimetric Sensor in Aqueous Media. *Anal. Methods* **2011**, *3*, 2599–2603.
- (172) Brinker, C. J.; Scherer, G. W. Sol-Gel Science; Brinker, C. J., Scherer, G. W., Eds.; Academic

Press: San Diego, **1990**.

- (173) Heuer-Jungemann, A.; Kirkwood, R.; El-Sagheer, A. H.; Brown, T.; Kanaras, A. G. Copper-Free Click Chemistry as an Emerging Tool for the Programmed Ligation of DNA-Functionalised Gold Nanoparticles. *Nanoscale* **2013**, *5*, 7209–7212.
- (174) Coomber, D.; Bartczak, D.; Gerrard, S. R.; Tyas, S.; Kanaras, A. G.; Stulz, E. Programmed Assembly of Peptide-Functionalized Gold Nanoparticles on DNA Templates. *Langmuir* **2010**, *26*, 13760–13762.
- (175) Niemeyer, C. M.; Ceyhan, B.; Hazarika, P. Oligofunctional DNA–Gold Nanoparticle Conjugates. *Angew. Chemie Int. Ed.* **2003**, *42*, 5766–5770.
- (176) Parak, W. J.; Pellegrino, T.; Micheel, C. M.; Gerion, D.; Williams, S. C.; Alivisatos, A. P. Conformation of Oligonucleotides Attached to Gold Nanocrystals Probed by Gel Electrophoresis. *Nano Lett.* **2003**, *3*, 33–36.
- (177) Midelet, J.; El-Sagheer, A. H.; Brown, T.; Kanaras, A. G.; Débarre, A.; Werts, M. H. V. Spectroscopic and Hydrodynamic Characterisation of DNA-Linked Gold Nanoparticle Dimers in Solution Using Two-Photon Photoluminescence. *ChemPhysChem* **2018**, *19*, 827–836.
- (178) Auyeung, E.; Cutler, J. I.; Macfarlane, R. J.; Jones, M. R.; Wu, J.; Liu, G.; Zhang, K.; Osberg, K. D.; Mirkin, C. a. Synthetically Programmable Nanoparticle Superlattices Using a Hollow Three-Dimensional Spacer Approach. *Nat. Nanotechnol.* **2011**, *7*, 24–28.
- (179) Mackenzie, L. E.; Goode, J. A.; Vakurov, A.; Nampi, P. P.; Saha, S.; Jose, G.; Millner, P. A. The Theoretical Molecular Weight of NaYF<sub>4</sub>:RE Upconversion Nanoparticles. *Sci. Rep.* **2018**, *8*, 1106.
- (180) Wu, D. M.; García-Etxarri, A.; Salleo, A.; Dionne, J. A. Plasmon-Enhanced Upconversion. *J. Phys. Chem. Lett.* **2014**, *5*, 4020–4031.
- (181) De Abajo, F. J. G. Nonlocal Effects in the Plasmons of Strongly Interacting Nanoparticles, Dimers, and Waveguides. *J. Phys. Chem. C* **2008**, *112*, 17983–17987.
- (182) Chen, F.; Alemu, N.; Johnston, R. L. Collective Plasmon Modes in a Compositionally Asymmetric Nanoparticle Dimer. *AIP Adv.* **2011**, *1*, 032134–14.
- (183) Woo, K. C.; Shao, L.; Chen, H.; Liang, Y.; Wang, J.; Lin, H. Q. Universal Scaling and Fano Resonance in the Plasmon Coupling between Gold Nanorods. In *ACS Nano*; **2011**; Vol. 5,

## List of References

5976–5986.

- (184) Pasquale, A. J.; Reinhard, B. M.; Dal Negro, L. Engineering Photonic-Plasmonic Coupling in Metal Nanoparticle Necklaces. *ACS Nano* **2011**, *5*, 6578–6585.
- (185) Link, S.; El-Sayed, M. A. Size and Temperature Dependence of the Plasmon Absorption of Colloidal Gold Nanoparticles. *J. Phys. Chem. B* **2002**, *103*, 4212–4217.
- (186) Sönnichsen, C.; Reinhard, B. M.; Liphardt, J.; Alivisatos, A. P. A Molecular Ruler Based on Plasmon Coupling of Single Gold and Silver Nanoparticles. *Nat. Biotechnol.* **2005**, *23*, 741–745.
- (187) Bohren, C. F.; Huffman, D. R. Absorption and Scattering of Light by Small Particles; John Wiley & Sons: Hoboken, NJ, USA, **1998**.
- (188) Lazarides, A. A.; Schatz, G. C. DNA-Linked Metal Nanosphere Materials: Structural Basis for the Optical Properties. *J. Phys. Chem. B* **2000**, *104*, 460–467.
- (189) Jain, P. K.; Huang, W.; El-Sayed, M. A. On the Universal Scaling Behavior of the Distance Decay of Plasmon Coupling in Metal Nanoparticle Pairs: A Plasmon Ruler Equation. *Nano Lett.* **2007**, *7*, 2080–2088.
- (190) Samai, S.; Choi, T. L. Y.; Guye, K. N.; Yan, Y.; Ginger, D. S. Plasmonic Nanoparticle Dimers with Reversibly Photoswitchable Interparticle Distances Linked by DNA. *J. Phys. Chem. C* **2018**, *122*, 13363–13370.
- (191) Dong, H.; Sun, L. D.; Yan, C. H. Energy Transfer in Lanthanide Upconversion Studies for Extended Optical Applications. *Chem. Soc. Rev.* **2015**, *44*, 1608–1634.
- (192) Zhou, J.; Liu, Q.; Feng, W.; Sun, Y.; Li, F. Upconversion Luminescent Materials: Advances and Applications. *Chem. Rev.* **2015**, *115*, 395–465.
- (193) Denk, W.; Strickler, J. H.; Webb, W. W. Two-Photon Laser Scanning Fluorescence Microscopy. *Science (80-. )*. **1990**, *248*, 73–76.
- (194) Coronado, E. A.; Encina, E. R.; Stefani, F. D. Optical Properties of Metallic Nanoparticles: Manipulating Light, Heat and Forces at the Nanoscale. *Nanoscale* **2011**, *3*, 4042–4059.
- (195) Mondes, V.; Antonsson, E.; Plenge, J.; Raschpichler, C.; Halfpap, I.; Menski, A.; Graf, C.; Kling, M. F.; Rühl, E. Plasmonic Electric Near-Field Enhancement in Self-Organized Gold Nanoparticles in Macroscopic Arrays. *Appl. Phys. B Lasers Opt.* **2016**, *122*.

- (196) Richter, J.; Seidel, R.; Kirsch, R.; Mertig, M.; Pompe, W.; Plaschke, J.; Schackert, H. K. Nanoscale Palladium Metallization of DNA. *Adv. Mater.* **2000**, *12*, 507–510.
- (197) Richter, J. Metallization of DNA. *Phys. E Low-Dimensional Syst. Nanostructures* **2003**, *16*, 157–173.
- (198) Hossen, M. M.; Bendickson, L.; Palo, P. E.; Yao, Z.; Nilsen-Hamilton, M.; Hillier, A. C. Creating Metamaterial Building Blocks with Directed Photochemical Metallization of Silver onto DNA Origami Templates. *Nanotechnology* **2018**, *29*, 355603.
- (199) Haiss, W.; Thanh, N. T. K.; Aveyard, J.; Fernig, D. G. Determination of Size and Concentration of Gold Nanoparticles from UV-Vis Spectra. *Anal. Chem.* **2007**, *79*, 4215–4221.
- (200) Paramelle, D.; Sadovoy, A.; Gorelik, S.; Free, P.; Hopley, J.; Fernig, D. G. A Rapid Method to Estimate the Concentration of Citrate Capped Silver Nanoparticles from UV-Visible Light Spectra. *Analyst* **2014**, *139*, 4855–4861.
- (201) Warren, B. E. X-Ray Diffraction, 2nd ed.; Dover Publications: New York, NY, **1990**.
- (202) Li, T.; Senesi, A. J.; Lee, B. Small Angle X-Ray Scattering for Nanoparticle Research. *Chem. Rev.* **2016**, *116*, 11128–11180.





